



**DÜZCE  
ÜNİVERSİTESİ**

**BİLİM ve TEKNOLOJİ  
DERGİSİ**

Düzce University  
Journal of  
Science & Technology

e-ISSN: 2148-2446

---

Cilt  
Volume

**11**

Sayı  
Issue

**5**

Aralık / December  
**2023**

---

**Düzce Üniversitesi**  
**BİLİM ve TEKNOLOJİ DERGİSİ**  
**DÜBİTED**

<http://dergipark.org.tr/dubited>



**Düzce University**  
**JOURNAL of SCIENCE & TECHNOLOGY**  
**DUBITED**

<http://dergipark.org.tr/dubited>

**Sahibi**

*Owner*

Uğur GÜVENÇ (Lisansüstü Eğitim Enstitüsü Müdürü)

(D. Ü. Lisansüstü Eğitim Enstitüsü adına)

(On behalf of D. U. Institute of Graduate Programs)

**Editör**

*Editor*

Suat SARIDEMİR

Erdem ELİBOL

Ümit AĞBULUT

**Yardımcı Editörler**

*Assistant Editors*

Berfin ŞENİK

Vesile YALÇIN

Anıl DEMİRCAN

Ahmet AYTEĞİN

Nisa KAPLAN ERGÜL

**Sorumlu Yazı İşleri Müdürü**

*Publishing Manager*

Uğur GÜVENÇ

**Yayın Kurulu**

*Editorial Board*

Ahmet Bora KIRKLIKÇI, Karamanoğlu Mehmet Bey  
Üniversitesi, Türkiye

Ali ÇALHAN, Düzce Üniversitesi, Türkiye

Ali Etem GÜREL, Düzce Üniversitesi, Türkiye

Alper ERGÜN, Karabük Üniversitesi, Türkiye

Ali ÖZDEMİR, Muş Alparslan Üniversitesi, Türkiye

Ali ÖZTÜRK, Düzce Üniversitesi, Türkiye

Ahmet DEMİR, Düzce Üniversitesi, Türkiye

Arif ÖZKAN, Kocaeli Üniversitesi, Türkiye

Aytaç AYDIN, Karadeniz Teknik Üniversitesi,  
Türkiye

Barış KARAKAYA, Fırat Üniversitesi, Türkiye

Emre AVCI, Düzce Üniversitesi, Türkiye

Engin EROĞLU, Düzce Üniversitesi, Türkiye  
Fatih TAŞPINAR, Düzce Üniversitesi, Türkiye  
Fatih YILMAZ, Bayburt Üniversitesi, Türkiye  
Fikret POLAT, Düzce Üniversitesi, Türkiye  
Alev ÖZKÖK, Hacettepe Üniversitesi, Türkiye  
Gökhan YILDIZ, Düzce Üniversitesi, Türkiye  
Hakan ARSLAN, Düzce Üniversitesi, Türkiye  
Harun BAYRAKDAR, Düzce Üniversitesi, Türkiye  
Hüseyin BUDAK, Düzce Üniversitesi, Türkiye  
Hüseyin BAKIR, Doğu Üniversitesi, Türkiye  
İrem DÜZDAR ARGUN, Düzce Üniversitesi, Türkiye  
Koray ŞARKAYA, Pamukkale Üniversitesi, Türkiye  
Mecit AKSU, Düzce Üniversitesi, Türkiye  
Mehmet SÖNMEZ, Osmaniye Korkut Ata  
Üniversitesi, Türkiye  
Melahat Sevgül BAKAY AĞBULUT, Düzce  
Üniversitesi, Türkiye  
Melike ERDOĞAN, Düzce Üniversitesi, Türkiye  
Mert YILDIRIM, Düzce Üniversitesi, Türkiye  
Metin TOZ, Karamanoğlu Mehmetbey Üniversitesi,  
Türkiye  
Mevlüt ERSOY, Süleyman Demirel Üniversitesi, Türkiye  
Muhammet Emin ŞAHİN, Yozgat Bozok Üniversitesi,  
Türkiye  
Muhammet GÜL, Munzur Üniversitesi, Türkiye  
Mustafa KARAGÖZ, Karabük Üniversitesi, Türkiye  
Murat AYDEMİR, Erzurum Teknik Üniversitesi, Türkiye  
Murat Kadir YEŞİLYURT, Bozok Üniversitesi,  
Türkiye  
Murat EYVAZ, Gebze Teknik Üniversitesi, Türkiye  
Mustafa DAYI, Düzce Üniversitesi, Türkiye  
Musa Çadırcı, Düzce Üniversitesi, Türkiye  
Nuray Benli YILDIZ, Düzce Üniversitesi, Türkiye  
Nihat Hakan AKYOL, Kocaeli Üniversitesi, Türkiye  
Nuri ŞEN, Düzce Üniversitesi, Türkiye  
Osman DİKMEN, Düzce Üniversitesi, Türkiye  
Osman KANDARA, Southern University,  
Özge Tüzün ÖZMEN, İzmir Bakırçay Üniversitesi,  
Türkiye  
Özlem ÖZKAN ÖNÜR, Düzce Üniversitesi, Türkiye  
Pınar GÜLTEKİN, Düzce Üniversitesi, Türkiye  
Revna ACAR VURAL, Yıldız Teknik Üniversitesi, Türkiye  
Salih Tunç KAYA, Düzce Üniversitesi, Türkiye  
Semih ÖZDEN, Milli Savunma Üniversitesi, Türkiye  
Sercan SERİN, Osmaniye Korkut Ata Üniversitesi,  
Türkiye  
Serdar BİROĞUL, Düzce Üniversitesi, Türkiye

Serhat DUMAN, Bandırma Onyedil Eylül  
Üniversitesi, Türkiye  
Suat SARIDEMİR, Düzce Üniversitesi, Türkiye  
Şerife Gülsün KIRANKAYA, Düzce Üniversitesi, Türkiye  
Taner YOLDAŞ, Düzce Üniversitesi, Türkiye  
Tarık GEDİK, Düzce Üniversitesi, Türkiye  
Tikendra Nath VERMA, Maulana Azad National  
Institute of Technology, Hindistan  
Turgay BİRTÜRK, Düzce Üniversitesi, Türkiye  
Uğur GÜVENÇ, Düzce Üniversitesi, Türkiye  
Ümit AĞBULUT, Düzce Üniversitesi, Türkiye  
Ümit ERGUN, Düzce Üniversitesi, Türkiye  
Ümit YURT, Düzce Üniversitesi, Türkiye  
Yasin ŞALE, Gebze Teknik Üniversitesi, Türkiye  
Yaşar Selman GÜLTEKİN, Düzce Üniversitesi, Türkiye  
Zehra KARAPINAR ŞENTÜRK, Düzce Üniversitesi,  
Türkiye

---

**Ulusal Danışma Kurulu**  
*National Advisory Board*

Adem ACIR, Gazi Üniversitesi, Türkiye  
Adem ÇİÇEK, Yıldırım Beyazıt Üniversitesi, Türkiye  
Arif ÖZKAN, Kocaeli Üniversitesi, Türkiye  
Devrim AKGÜN, Sakarya Üniversitesi, Türkiye  
Elif UZ, Uludağ Üniversitesi, Türkiye  
Ercan ÖZGAN, Düzce Üniversitesi, Türkiye  
Erol BURDURLU, Gazi Üniversitesi, Türkiye  
Ethem TOKLU, Düzce Üniversitesi, Türkiye  
Fahri VATANSEVER, Uludağ Üniversitesi, Türkiye  
Fatih TAŞPINAR, Düzce Üniversitesi, Türkiye  
H.Hüseyin CİRİTCİOĞLU, Düzce Üniversitesi, Türkiye  
Hakan AKTAŞ, Süleyman Demirel Üniversitesi, Türkiye  
Hakan ALTINÇEKİÇ, İstanbul Üniversitesi, Türkiye  
Hakan HOCAOĞLU, Gebze Teknik Üniversitesi, Türkiye  
İbrahim YÜCEDAĞ, Düzce Üniversitesi, Türkiye  
İlyas UYGUR, Düzce Üniversitesi, Türkiye  
İsmail TORÖZ, İstanbul Teknik Üniversitesi, Türkiye  
İsmet YILDIZ, Düzce Üniversitesi, Türkiye  
Mehmet BUDAKÇI, Düzce Üniversitesi, Türkiye  
Memiş IŞIK, Karabük Üniversitesi, Türkiye  
Meral KEKEÇOĞLU, Düzce Üniversitesi, Türkiye  
Muharrem GÖKÇEN, Düzce Üniversitesi, Türkiye  
Murat KALE, Düzce Üniversitesi, Türkiye  
Murat SİPAHİOĞLU, Yüzüncü Yıl Üniversitesi, Türkiye  
Mustafa OKUTAN, Yıldız Teknik Üniversitesi, Türkiye  
Raşit TURAN, Orta Doğu Teknik Üniversitesi, Türkiye  
Salih TOSUN, Düzce Üniversitesi, Türkiye

Selçuk ÖZMEN, Düzce Üniversitesi, Türkiye  
Seyhan FIRAT, Gazi Üniversitesi, Türkiye  
Suat SARIDEMİR, Düzce Üniversitesi, Türkiye  
Şerife Gülsün KIRANKAYA, Düzce Üniversitesi, Türkiye  
Uğur GÜVENÇ, Düzce Üniversitesi, Türkiye  
Yasin KİŞİOĞLU, Kocaeli Üniversitesi, Türkiye  
Yusuf AVCI, Bahçeşehir Üniversitesi, Türkiye  
Zeki DEMİR, Düzce Üniversitesi, Türkiye

**Uluslararası Danışma Kurulu**  
*International Advisory Board*

Abdelilah SLAOUI, Universite de Strasbourg, France  
Clay S. GLOSTER, North Caroline A&T University,  
USA  
A.S. El-Shafay, Prince Sattam bin Abdulaziz Üniversitesi,  
Suudi Arabistan  
Nicoleta BREAZ, University of Alba Lulia, Romania  
Luis ROSEIRO, Coimbra Institute of Engineering,  
Portugual  
Mohamed Saber Gad, Fayoum University, Egypt  
Marwan BIKDASH, North Carolina A & T State  
University, USA  
Sadık ARTUNÇ, Mississippi State University, USA  
Salim HIZIROĞLU, Oklahoma State University, USA  
Thomas C. CULBRETH, North Carolina State  
University, USA

**Cilt**  
*Volume*

**11**

**Sayı**  
*Issue*

**5**

**Aralık/December**  
**2023**

**Ürün Bilgisi**  
*Product Information*

**Yayıncı**  
*Publisher*

Düzce Üniversitesi Lisansüstü Eğitim Enstitüsü  
*Düzce University Institute of Graduate Programs*

**Sahibi**  
*Owner*

Uğur GÜVENÇ (Lisansüstü Eğitim Enstitüsü Müdürü)  
(D. Ü. Lisansüstü Eğitim Enstitüsü adına)  
*(On behalf of D. U. Institute of Graduate Programs)*

**Sorumlu Yazı İşleri Müdürü**  
*Publishing Manager*

Uğur GÜVENÇ

**Web Sayfası**

<http://dergipark.org.tr/dubited>

*Web Page*

**Basım Tarihi**  
*Date of Publication*

Aralık 2023  
*December 2023*

**Yayın Dili**  
*Language*

Türkçe / İngilizce  
*Turkish / English*

**Yayın Aralığı**  
*Frequency*

Yılda dört kez yayınlanır  
*Published four times in a year*

**Yayın Türü**  
*Type of Publication*

Sürelî yayın  
*Periodical*

**e-ISSN Numarası**  
*e-ISSN Number*

2148-2446

---

**Yazışma Adresi**

Düzce Üniversitesi Lisansüstü Eğitim  
Enstitüsü Rektörlük Binası 3. Kat 81620  
Düzce/TÜRKİYE

Telefon: +90 380 542 12 08

Fax: +90 380 542 12 38

E-posta: [dubitedyayin@duzce.edu.tr](mailto:dubitedyayin@duzce.edu.tr)

<http://dergipark.org.tr/dubited>  
adresinden dergiye ilişkin bilgilere ve  
makalelerin tam metnine ulaşılabilir.

***Correspondence Address***

*Düzce University Institute of  
Graduate Programs Rectorship  
Building 3rd Floor 81620  
Düzce/TURKEY*

*Phone: +90 380 542 12 08*

*Fax: +90 380 542 12 38*

*E-mail: [dubitedyayin@duzce.edu.tr](mailto:dubitedyayin@duzce.edu.tr)*

*Instructions for authors and all  
articles in this journal can be  
reached at  
<http://dergipark.org.tr/dubited>*

---

# **İÇİNDEKİLER**

**Sayfa**

**Makale**

## **BİYOLOJİ/BİYOKİMYA/MOLEKÜLER BİYOLOJİ VE GENETİK/SU ÜRÜNLERİ**

### **Araştırma Makalesi/ Research Article**

2255-2264 Investigation of Some Quality Criteria in Chestnut Honey of Düzce Province  
Düzce İli Kestane Balında Bazı Kalite Kriterlerinin Araştırılması  
Taner YOLDAŞ, Bora KARAGÜL, Elif Sine DÜVENCİ

## **BİLGİSAYAR / YAZILIM MÜHENDİSLİĞİ/BİLİŞİM SİSTEMLERİ VE TEKNOLOJİLERİ**

### **Araştırma Makalesi/ Research Article**

2373-2381 Measuring the Thickness of Fiber Mats Using Light Transmittance via Image Processing  
Fiber Matların Kalınlığının Görüntü İşleme Yoluyla Işık Geçirgenliği Kullanılarak Ölçülmesi  
Burcu YILMAZEL, Dilara ÖZTÜRK, Hercan YAVUZTÜRK, Halit Kaan CAN, Emre KAÇMAZ, Gamze KARANFİL KAÇMAZ

## **ELEKTRİK/ELEKTRONİK / ELEKTRİK ELEKTRONİK/ MEKATRONİK/ENERJİ MÜHENDİSLİĞİ**

### **Araştırma Makalesi/ Research Article**

2283-2292 Correlation of Destructive and Non-Destructive Tests with Electrical Resistance in Cementless Composites

Çimentosuz Kompozitlerde Tahribatlı ve Tahribatsız Testlerin Elektriksel Direnç ile İlişkilendirilmesi  
**Ümit YURT, Barış KIR, Yunus BİÇEN**

2419-2444 Comparison of Payback Periods of Solar Power Plant in Türkiye and Europe  
Güneş Enerjisi Santrallerinin Türkiye ve Avrupa'daki Geri Ödeme Sürelerinin Karşılaştırması  
**Mohannad GYAM, İlhan CEYLAN, Ali Etem GÜREL, Gökhan YILDIZ**

### **İNŞAAT / METALURJİ ve MALZEME / ÇEVRE MÜHENDİSLİĞİ**

#### **Araştırma Makalesi/ Research Article**

2321-2340 Surface Analysis of Magnesium AZ31 Samples Immersed in Various Aqueous Solutions  
Çeşitli Sulu Çözeltilerde Tutulan Magnezyum AZ31 Numunelerinin Yüzey Analizi  
**Erdem ŞAHİN, Meltem ALP, Ahmed ŞEREF**

### **MAKİNE / MEKATRONİK / MALZEME / ENDÜSTRİ / İMALAT / OTOMOTİV MÜHENDİSLİĞİ**

#### **Araştırma Makalesi/ Research Article**

2341-2351 Evaluation Of Foreign Object Damage On The Fan Blades with Microscopic Techniques  
Mikroskopik Tekniklerle Pale Hasarının Değerlendirilmesi  
**Ayhan İsmail KIRCA, Seyid Fehmi DİLTEMİZ, Sezer YUMRUKAYA, Aykut BATAR**

2352-2364 Experimental Analysis of The Impacts of Biodiesel-Diesel Fuel Mixtures on Engine Vibration, Noise and Combustion  
Biyodizel-Dizel Yakıt Karışımlarının Motor Titreşimi, Gürültü ve Yanma Üzerindeki Etkilerinin Deneysel Analizi  
**Suat SARIDEMİR, Fikret POLAT**

2365-2372 Inspection of Surface Damage in Composite Materials with Different Techniques  
Kompozit Malzemelerde Yüzey Hasarlarının Farklı Tekniklerle İncelenmesi  
**Seyid Fehmi DİLTEMİZ, Ersin EROĞLU, Aykut BATAR, Sezer YUMRUKAYA**

2293-2308 The Analysis of Next-Generation Refrigerants in Terms of Energy, Exergy, and LCCP Perspective  
Yeni Nesil Soğutucu Akışkanların Enerji, Ekserji ve LCCP Perspektifinde Analizi



**Merve ÖZER ŞİMŞEK, Mehmet Onur KARAAĞAÇ, Alper ERGÜN, Mustafa AKTAŞ**

- 2309-2320 Determination of Modified Mohr-Coulomb Damage Model Parameters for DH780 Steel in Finite Element Analysis  
DH780 Çeliği için Modifiye Edilmiş Mohr-Coulomb Hasar Model Parametrelerinin Belirlenmesi  
**Tolgahan CİVEK, Nuri SEN, Oktay ELKOCA**
- 2382-2390 Structural Health Monitoring Application of Aviation Composite Materials Using Microscopic Techniques  
Havacılık Kompozit Malzemelerinde Mikroskopik Teknikler Kullanılarak Yapısal Sağlık İzleme Uygulamalar  
**Seyid Fehmi DİLTEMİZ, Saliha MUSTAFAOĞLU, Furkan KAYA**
- 2391-2396 Microstructural Characterization of Hot Shortness in Steels  
Çeliklerde Sıcak Yırtılmanın Mikroyapısal Analizi  
**Selçuk YEŞİLTEPE**
- 2409-2418 Experimental Investigation of the Effects of Paraffin as a Phase Change Material on the Cooling Performance of a Battery Thermal  
Faz Değişim Malzemesi Olarak Parafinin Bir Batarya Termal Yönetim Sisteminin Soğutma Performansı Üzerindeki Etkisinin Deneysel Olarak İncelenmesi  
**Fikret POLAT, Suat SARIDEMİR**

**ORMAN/ORMAN ENDÜSTRİ MÜHENDİSLİĞİ/PEYZAJ MİMARLIĞI/ZİRAAT MÜHENDİSLİĞİ**

**Araştırma Makalesi/ Research Article**

- 2265-2282 Honey Plants of Düzce University Ornamental and Medicinal Plants Botanical Garden  
Düzce Üniversitesi Süs ve Tıbbi Bitkiler Botanik Bahçesinin Ballı Bitkileri  
**Necmi AKSOY, Haldun MÜDERRİSOĞLU, Engin EROĞLU, Neval GÜNEŞ ÖZKAN, Turgay BİRTÜRK, Nihan KOÇER, Bilge TUNÇKOL, Özgür YERLİ, Şemsettin KULAÇ, Bilal ÇETİN, Murat SARGINCI, Sertaç KAYA, Serdar ASLAN, Salih Sercan KANOĞLU, Nermin BAŞARAN, Tuba GÜL DOĞAN, Ahmet**
- AYTEĞİN**
- 2397-2408 Evaluation of Honey Bees within the Scope of Sustainable Development Goals and Ecosystem Services  
Bal Arılarının Sürdürülebilir Kalkınma Hedefleri ve Ekosistem Hizmetleri Kapsamında Değerlendirilmesi  
**Melek YILMAZ KAYA, Yaşar Selman GÜLTEKİN, Pınar GÜLTEKİN**



# Düzce University Journal of Science & Technology

Research Article

## Investigation of Some Quality Criteria in Chestnut Honey of Düzce Province<sup>1</sup>

 Taner YOLDAŞ<sup>a,\*</sup>,  Bora KARAGÜL<sup>a</sup>,  Elif Sine DÜVENÇİ<sup>a</sup>

<sup>a</sup> Düzce University Scientific and Technological Research Application and Research Center, Düzce, TÜRKİYE

\* Corresponding author: taneryoldas@duzce.edu.tr

DOI: 10.29130/dubited.1383148

### ABSTRACT

Honey is a natural food source that has been consumed by humans for thousands of years and has an important place in various cultures. Chestnut honey is an important type of honey produced in Düzce province. Determining the quality and purity of honey ensures that consumers have access to safe, high-quality honey. The control criteria for the suitability of honey for human health consumption are defined in the Turkish Food Codex Communiqué on Honey (2020/7). Düzce University Scientific and Technological Research Application and Research Center (DÜBİT) responds to requests for honey analysis for non-commercial, internal quality control purposes. In this study, the results of honey samples produced in the province of Düzce and analyzed in the laboratories of DÜBİT were examined according to the criteria of the Turkish Food Codex Communiqué on Honey and an evaluation of the results was carried out. According to the test results, 38%, 20% and 16% of the samples were found to be unsuitable for the quality criteria, especially for the sugar profile, conductivity and proline parameters, respectively. Additionally, pollen analysis of 13% of the honey samples revealed pollen densities that did not match the declared plant family. From a public health point of view, it is important to consume high-quality, reliable and natural honey products. Therefore, quality control of bee products should be carried out from the producer to the consumer.

**Keywords:** chestnut honey, natural product, honey analyses, bee product, quality criteria

## Düzce İli Kestane Balında Bazı Kalite Kriterlerinin Araştırılması

### Öz

Bal, binlerce yıldır insanlar tarafından tüketilen ve çeşitli kültürlerde önemli bir yere sahip olan doğal bir besin kaynağıdır. Kestane balı Düzce ilinde üretilen önemli bir bal türüdür. Balın kalitesinin ve saflığının belirlenmesi, tüketicilerin güvenli, yüksek kaliteli bala erişimini sağlar. Balın insan sağlığı açısından tüketime uygunluğuna ilişkin kontrol kriterleri Türk Gıda Kodeksi Bal Tebliği'nde (2020/7) tanımlanmıştır. Düzce Üniversitesi Bilimsel ve Teknolojik Araştırmalar Uygulama ve Araştırma Merkezi (DÜBİT), ticari olmayan, iç kalite kontrol amaçlı bal analizi taleplerine yanıt vermektedir. Bu çalışmada Düzce ilinde üretilen ve DÜBİT laboratuvarlarında analiz edilen bal numunelerinin sonuçları Türk Gıda Kodeksi Bal Tebliği kriterlerine göre incelenmiş ve sonuçların bir değerlendirmesi yapılmıştır. Test sonuçlarına göre örneklerin %38'i şeker profili, %20'si iletkenlik ve %16'sı prolin

<sup>1</sup> This study was presented as an abstract at the "1st International Congress of Apitherapy" held on 2-4th October 2023.

parametreleri başta olmak üzere kalite kriterlerine uygun bulunmamıştır. Buna ek olarak, balların %13'ünde yapılan polen analizinde, beyan edilen bitki familyasına uymayan polen yoğunlukları tespit edilmiştir. Halk sağlığı açısından bakıldığında, yüksek kaliteli, güvenilir ve doğal bal ürünlerinin tüketilmesi önemlidir. Bu nedenle arı ürünlerinin kalite kontrolü üreticiden tüketiciye kadar yapılmalıdır.

*Anahtar Kelimeler: kestane balı, doğal ürün, bal analizleri, arı ürünü, kalite kriterleri*

## **I. INTRODUCTION**

The latest legislation concerning honey is the Turkish Food Codex Honey Communiqué (Communiqué No: 2020/7) which was published in 2020. Honey is defined in this Communiqué as a natural substance that can naturally crystallize. It is created when honey bees collect plant nectars, secretions from living plant components, or secretions from plant-sucking insects living on the living components of plants and then modify them by combining them with exclusive substances, reducing the water content, and maturing by storing them in the honeycomb. The earliest discoveries of honey production date back to 7000-8000 BC. Archaeological evidence suggests that as hunter-gatherer societies adopted a sedentary lifestyle, they began developing tools and containers specifically for honey production [1]. Honey holds significant importance for humanity with regard to its historical significance. Its journey can be traced back to the ancient civilizations of Egypt, Greece and Mesopotamia, and continues to be relevant today. The industrial revolution, advancements in honey production and beekeeping, and the utilization of innovative technology and techniques have led to the modern form of beekeeping [2].

Honey can be classified into two types based on its plant source: secretion honey and flower honey. Worker bees collect nectar from flowers to produce flower honey, while secretion honey is made by bees collecting resin and sweet secretions from insects living in forest trees. Honey can also be categorized based on the type of flowers bees visit while collecting nectar: polyfloral (multi-flowered) honey and monofloral (single-flowered) honey. The most well-known varieties of monofloral honeys are lavender honey, chestnut honey, carob honey, orange blossom honey, and lemon blossom honey [3]. Differences in the plant source significantly affect the smell, taste and color of honey. Other physical properties and chemical content of honey also vary according to the type of bee, the climatic characteristics of the geographical region where it is collected and the harvest season. All these factors contribute to determining the quality of honey. Multi-flowered honeys are produced in high altitude plateaus and depending on the flower diversity of the region [4], [5].

Turkey plays a significant role in honey production. With its unique geographical features, rich flora housing endemic plant species, and diverse honeybee breeds, Turkey has high potential for beekeeping and producing high-quality honey [6]. Chestnut honey matures as it is derived from collecting nectar from chestnut trees that start to bloom at the start of the summer season. The use of chestnut as a raw material is notable due to its chemical and biological benefits in traditional medicine. In Turkey, *Castanea sativa* Miller (European chestnut) produces a monofloral variety of honey when chestnut trees in the Marmara, Aegean, and Black Sea regions flower in June [7], [8].

Monofloral chestnut honey is abundant in C and B vitamins, along with iron and potassium minerals. Its dark color distinguishes chestnut honey from other honey varieties. Studies have shown that chestnut honey improves immunity through its vitamin, mineral, and antioxidant content. Additionally, it possesses antiviral and antibacterial properties [9].

In conclusion, honey and chestnut honey hold significant economic and cultural significance in Turkey. They are widely consumed within the country and exported abroad. Additionally, the health benefits of chestnut honey are increasingly recognized. Producers seeking to ascertain the quality of their product and maintain internal control seek out laboratories that conduct honey analyses. DÜBİT, the Scientific

and Technological Research Application and Research Center at Düzce University, conducts honey analyses upon request. The analyses are intended for non-commercial internal quality control purposes and to support local honey producers. The honey samples from the Düzce province, which were analyzed in the DÜBİT laboratory, were evaluated based on the TGK Honey Communiqué criteria in this study.

## **II. MATERIAL AND METHODS**

### **A. MATERIAL**

The study discusses the conformity of the analyses conducted by Düzce University Scientific and Technological Research Application and Research Centre (DÜBİT) using the honey analysis methods determined by the Turkish Standards Institute with the Turkish Food Codex Honey Communiqué. Only data of customers who authorized its use were utilized. Technical abbreviations were explained when first used. The analyses performed in DÜBİT between 2020-2023 served as the database.

### **B. METHODS**

Turkish Standard methods and certain International Honey Commission (IHC) methods were utilized to perform analyses specified in the Turkish Food Codex Honey Communiqué [10], [11].

#### **B. 1. Determination of Moisture Content**

The lens of the digital honey refractometer was initially calibrated by introducing pure water. Afterwards, a small quantity of honey sample was inserted, and the moisture level was measured. This sequence was repeated thrice. The water content of honey was quantified as the mass of water per 100 g of honey. The refractive index of liquidized honey was calculated [5], [12].

#### **B. 2. Determination of Diastasis Number**

The diastase activity of honey samples is conducted in accordance with TS 13364 guidelines. The amylase enzymes present in 100 grams of honey facilitate starch breakdown at a specific temperature range (38 to 40 degrees Celsius) and under predetermined experimental conditions. This method measures the enzyme activity in 1 gram of honey, ascertained by observing the blue value at the endpoint, after exposing it to 0.01 grams of starch at a temperature of 40 degrees Celsius for an hour [13], [14].

#### **B. 3. Measurement of Electrical Conductivity**

The experiment was conducted in accordance with TS 13366 standards. Subsequently, 20 g of dry honey was weighed and dissolved in 100 ml of distilled water using the method outlined in TS 13365. The electrical conductivity of the mixture was measured with a conductivity cell to determine its resistance [15], [16].

#### **B. 4. Determination of Free Acidity**

The free acidity of the honey samples was determined according to the guidelines outlined in TS 13360. Specifically, the free acid content of the honey sample was dissolved in water and was measured through potentiometric titration with the use of sodium bicarbonate solution until the endpoint was at pH 8.3. Results were then expressed as mmol/kg in sodium hydroxide for every 100 g of honey using the method specified in this standard [13], [17].

## B. 5. Determination of Proline Content

Proline assays follow harmonized methods as specified by the IHC and serve as crucial parameters in detecting honey adulteration. Proline content represents a quality indicator, forming a colored complex with ninhydrin. Detection of this complex involves the addition of 2-propanol, followed by observation for color change at the maximum wavelength of the sample solution and the reference solution [10], [12].

## B. 6. Determination of Sugar Profile

Fructose, glucose, sucrose, and maltose were identified in honey through sugar profile analysis, which utilized IHC. High-performance liquid chromatography (HPLC) was employed for the analyses. To prepare, 5 grams of honey was dissolved in 40 Milliliters of ultrapure water and the solution was filled up to 100 ml with ultrapure water. The filtered and vialled sample was subsequently analyzed using HPLC. Acetonitrile: water (80:20) was utilized as the mobile phase for the experiment. In addition, a column of NH<sub>2</sub> (5 µm, 250 mm x 4.6 mm, 100 Å) was selected as the desired separation column [5], [10], [13], [18].

## B. 7. Determination of Hydroxymethylfurfural

HMF analysis was carried out according to the IHC-determined method. The HMF value was measured in the samples using HPLC with a C-18 column. The measurements were compared to HMF standards that were measured at 258 nm [10], [13].

## B. 8. Pollen Analysis

Relative pollen analysis was conducted following TS 13363 with minor adjustments. Initially, approximately 10 grams of honey were dissolved in 20 Milliliters of distilled water. The honeycombs were filtered through a 0.5 mm sieve prior to dissolution to eliminate significant solid particles and residual honeycomb materials. The supernatant was discarded after centrifugation at 4,000 rpm for 10 minutes. The pellet is again dissolved with 20 mL of distilled water and centrifuged once more to completely dissolve the sugar crystals. The pellet was then re-dissolved in 200 µl of pure water, and the hydrated pollen was examined under light microscopy at a magnification of 10-40X [19]–[21]. Pollen atlases and literature were utilized to determine the pollen species [22]–[24].

## III. RESULTS AND DISCUSSION

We examined some quality criteria in honeys from the Düzce region that were applied to DÜBİT for analysis. We evaluated the conformity of the results we obtained according to the limit values in the annex of the Turkish Food Codex (TFC) Honey Communiqué (Table 1). Depending on the parameter requested, the number of samples analyzed was between 16-30. Although the majority of the samples were found to be suitable according to the criteria of the TFC Honey Communiqué, samples outside the limit values were also detected.

*Table 1. Analysis results for chestnut honey from the Düzce and the TFC Honey Communiqué limit values.*

Test Parameters	NOS (NUS)	Minimum (min.)	Maximum (max.)	Mean + SD	Limits and Units**
Fructose / Glucose	16 (1)	1,17	1,97	1,40±0,17	1,0-1,85
Fructose + Glucose	16 (6)	34,30	70,22	58,75±9,80	min. 60 g/100g
Sucrose	16 (0)	0,13	3,90	1,37±1,30	max. 5 g / 100g

Maltose	16 (0)	0,65	3,19	1,75±0,83	max. 4 g / 100g
Hydroxymethylfurfural (HMF)	18 (0)	1,10	2,05	1,63±0,40	max. 40 mg/kg
Diastase	18 (2)	7,00	50,00	15,28±11,11	min. 8
Proline	19 (3)	81,60	1202,40	736,80±286,24	min. 500 mg/kg
Conductivity	20 (4)	0.07	1.75	1.00±0.48	min. 0,8 mS/cm
Free acidity	20 (0)	12,00	46,00	27,86±9,63	max. 50 meq/kg
Moisture content	26 (4)	12,50	29,40	18,40±2,86	max. %20
Chestnut pollen ratio	30 (4)	40,00	97,00	80,29±15,44	min. %70

NOS: Number of samples, NUS: Number of unsuitable samples

\*\*Limit values are determined according to the Turkish Food Codex Honey Communiqué.

A low moisture content in honey signifies its maturity and enables its long-term storage without spoilage. Abbreviations for technical terms will be clearly explained upon first use. The water content of honey, also called moisture content, is an important criterion for assessing honey quality. The moisture level of honey differs during the ripening process, depending on environmental conditions, the water content of the nectar that creates the honey, and storage conditions after extraction. High levels of moisture can accelerate crystallization in some varieties of honey, resulting in an increase in water activity that could lead to yeast growth and eventual fermentation. Honey with elevated moisture levels is particularly susceptible to fermentation. In accordance with the TFC Honey Communiqué, the acceptable moisture content for flower honey (excluding puree and heather honey) should not exceed 20%.

Out of the 26 samples of honey that were analyzed in our laboratory, 22 had a moisture content that fell below the limit value of 20%. However, four samples were identified as having values exceeding 20%, with a range of 20.5% to 29.4%. The average moisture content of the analyzed chestnut honey from the Düzce region was determined to be  $18.40 \pm 2.86\%$ . In 2018, Bayram and Demir found that the moisture content of six chestnut honey samples from the Giresun and Rize regions ranged between 17.8% and 22% [12]. Only one of the tested samples exceeded the limit of 20%, indicating potential issues. The moisture content of chestnut honey from the Kocaeli region was found to be 18.2% in a separate study evaluating quality criteria across 12 types of honey, including chestnut honey [13], which is comparable to our average moisture value. In a previous analysis of honeys from the Düzce region, Kambur *et al.* [25] found moisture levels in two samples dominated by chestnut pollen to be less than 20%, which is consistent with our own findings.

Organic acids such as gluconic acid, acetic acid, butyric acid, citric acid, formic acid, lactic acid, and malic acid can be found in honey. The free acidity of honey represents the total amount of organic acids in it. This parameter is crucial as it affects the taste and quality of honey. When the free acidity level is too high, the honey is considered to be of low quality. The free acidity level in honey may vary depending on the type of honey, production method, and storage conditions. According to the TFC Honey Regulations, the free acidity level for flower honey should not exceed 50 meq/kg. The entire set of 20 samples subjected to the free acidity parameter test revealed results below the prescribed limit. The samples exhibited an average value of free acidity at 27.86 meq/kg, with the lowest and highest recorded levels at 12.5 meq/kg and 46.0 meq/kg, respectively. In 2016, a study examined 10 samples of honey sourced from the Yığılca district of Düzce province. Only one sample did not meet the TFC Honey Regulations criteria for the free acidity parameter, with a value of 70 meq/kg [25].

The electrical conductivity of honey is determined by the quantity of organic acids, proteins, sugars, and minerals present in it. When the electrical conductivity of honey is high, the concentration of these components is also high. Certain types of honey are anticipated to have low conductivity, whereas others

like chestnut honey are expected to have high conductivity. According to the TFC Honey Communiqué, the electrical conductivity of flower honey should not exceed 0.8 mS/cm, whereas that of chestnut honey should be at least 0.8 mS/cm. The electrical conductivity of honey may be contingent upon the type of honey, the mode of production, and storage conditions. For instance, heat-treated honeys exhibit higher conductivity than natural honeys, while temperature or extended storage duration may elevate conductivity. Four out of the 20 samples tested for conductivity failed to meet the minimum chestnut honey limit of 0.8 mS/cm. Upon analyzing all samples, the average conductivity value was found to be  $1.00 \pm 0.48$  mS/cm. The four samples that did not meet the required value had conductivity values ranging from 0.07 to 0.60 mS/cm. In a study where one chestnut honey was compared to twelve other flower honeys, the conductivity value was determined to be 1.97 mS/cm. The study highlights chestnut honey's distinctive conductivity parameter in contrast to other flower honeys [13]. Furthermore, a study analyzing honey samples from the Yığılca region found that one of the two honey samples with dominant chestnut pollen had a conductivity of 0.8 mS/cm, while the other had a conductivity of 0.39 mS/cm [25].

The diastase enzyme is responsible for converting starch to sugar in honey. The diastase level in honey indicates its freshness, with honey high in diastase considered fresh. Additionally, the diastase level provides information about the purity and nutritional value of honey. Adulterated or blended honey has lower diastase levels compared to pure and natural honey. Honey with high diastase levels is considered higher quality than honey with low diastase levels. Enzyme activity in honey analysis reports is calculated based on its potential to convert starch and is expressed as diastase units. According to the TFC Honey Communiqué, this value must be at least 8 for blossom honey. Of the 18 honey samples analyzed, two did not meet the criterion and had a value of 7. The remaining 16 samples had values of 8 or above, with three exhibiting diastase numbers above the average, featuring values of 23, 39, and 50. According to a study conducted in the Düzce region, eight out of ten honey samples examined had diastase numbers exceeding 8, while two lacked diastase [25].

Proline is a fundamental amino acid that constitutes the building blocks of protein. Its significance in honey quality control standards is crucial due to its production solely by honeybees. Proline serves as one of the most relevant indicators that confirm natural and pure honey production by bees. The concentration of proline in honey can fluctuate depending on the honey type, production technique, and storage conditions. Heated honey has lower proline content than traditionally produced honey, and prolonged storage in high-temperature conditions can also decrease its proline levels. According to the TFC Honey Communiqué, chestnut honey must contain a minimum of 500 mg/kg of proline. Of the nineteen honey samples analyzed in this study, sixteen had proline levels above 500 mg/kg (with a maximum of 1202.4 mg/kg), while three samples showed proline levels below the limit value (minimum 81.6 mg/kg). In a study examining various flower honeys from the Erzurum, Giresun, Hakkari, and Rize regions, Giresun and Rize honeys were identified as chestnut honey through palynological evaluation. The study reported proline levels between 503.46-692.88 mg/kg, highlighting the low proline content in samples determined as chestnut honey [12]. In a recent study conducted by Özgüven *et al.* [13], the quantity of proline present in chestnut honey sourced from the Kocaeli region was determined to be 711 mg/kg.

Hydroxymethylfurfural (HMF) is a compound naturally present in honey and molasses. HMF forms through the enzymatic degradation of fructose in honey under high temperatures or during extended storage periods. The HMF concentration in honey serves as a measure of its quality. According to the TFC Honey Communiqué, the acceptable HMF level in honey should not exceed 40 mg/kg. Furthermore, the HMF level may increase due to the storage environment, particularly at high temperatures or prolonged storage. None of the 18 samples analyzed by the HPLC method had a value of 40 mg/kg or higher in terms of HMF content. Only 3 samples were found to contain HMF, with the highest HMF value recorded at 2.05 mg/kg. In their study, Özgüven *et al.* [13] found HMF content in chestnut honey to be less than 0.1 mg/kg, and in other floral honeys, values were found to be up to 1.22 mg/kg. Kambur *et al.* [25] found that the HMF values of 10 types of honey examined were within the limit values. However, the results (ranging from 17.93-36.02 mg/kg) were considerably higher than the literature values.

Approximately 80% of honey's contents are sugars. The main sugars found in honey are fructose and glucose, but sucrose, maltose, galactose, and xylose can also be present. Honey's sugar profile provides detailed information on quality, purity, and adulteration. Sugar quantities in honey can be affected by the type of honey, production method, heat treatment, and storage conditions. The TFC Honey Communiqué outlines four parameters and limit values for sugar content in flower honey. These parameters include the ratio of fructose to glucose (between 0.9-1.4; for chestnut honey, between 1.0-1.85), the total amount of fructose and glucose (minimum of 60 g per 100 g), maximum amount of sucrose (5 g per 100 g), and maximum percentage of maltose (4%). One of the 16 honey samples analyzed using the HPLC has a fructose/glucose ratio of 1.98, with fructose and glucose values of 41.14 g/100g and 20.8 g/100g, respectively, falling outside the limit range. Six samples with fructose and glucose values ranging from 34.3 g/100g to 57.45 g/100g, below the minimum expected total of 60 g/100g, also failed to meet the requirement. All samples were evaluated as suitable with respect to the limit values of sucrose and maltose sugars. The detection and separation of sugars and HMF in the HPLC chromatogram can be seen in Figure 1.

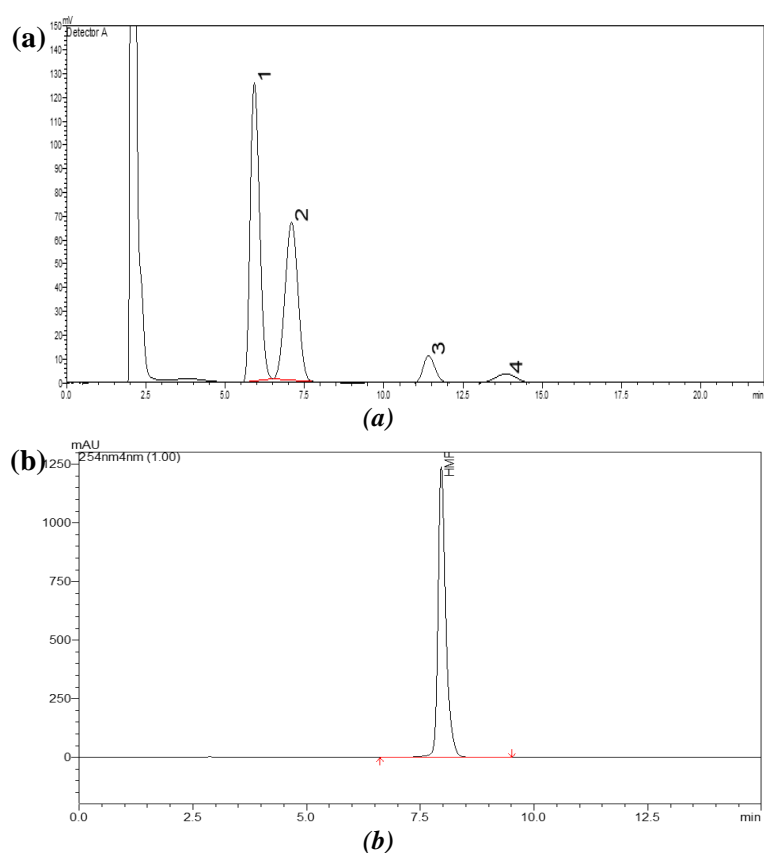


**Figure 1.** (a) Sugars and (b) HMF – chromatograms of honey HPLC analyses. The numerical digits in Figure (a) indicate 1: fructose, 2: glucose, 3: sucrose, and 4: maltose.

When analyzing recent studies, comparable outcomes are noticed. Ten honey samples from the surroundings of Yiğilca were analyzed, indicating fructose/glucose ratios ranging from 1.18 to 1.32 within the limit values. Furthermore, nine of these samples were found to contain maltose in amounts lower than 1.25 g/100 g [25]. In a study analyzing chestnut and rhododendron honey samples obtained from regions including Bartın, Kastamonu, İstanbul, and Düzce (6 samples), the results of sugar analysis by HPLC for 18 samples indicate fructose/glucose ratios ranging from 1.17 to 1.80. In terms of the sum of fructose and glucose parameters, half of the tested samples did not reach the 60g/100g limit value [18]. In another study conducted on flower honeys, the ratio of fructose/glucose in chestnut honey was recorded as 1.49 and the total amount of the sum of fructose and glucose was 78.58. In addition, the sucrose sugar amount was also determined as 0.44 g/100g [13].



Relative pollen determination in honey is a technique utilized to identify the plant-based pollen present in honey. Melissopalynology, the scientific study of pollen and spores in honey, utilizes the melissopalynological approach to ascertain the amount, family, taxon or species of pollen grains found in honey. According to the TFC Honey Communiqué (2020/7) Annex-2, the minimum pollen content for honeys whose botanical source is declared is specified. Chestnut honey must contain at least 70% *Castanea sativa* pollen to be declared as such. After conducting a melissopalynological analysis of 30 honey samples submitted to our laboratory as chestnut honey, it was discovered that six of these samples did not meet the threshold of 70% in regard to Fagaceae and *C. sativa* pollen content (Figure 2). While chestnut pollen is dominant in all other honeys, secondary or minor levels of pollen belonging to other families such as Fabaceae, Ericaceae, and Tiliaceae, which are part of the dominant vegetation in the area, were detected (Figure 2).

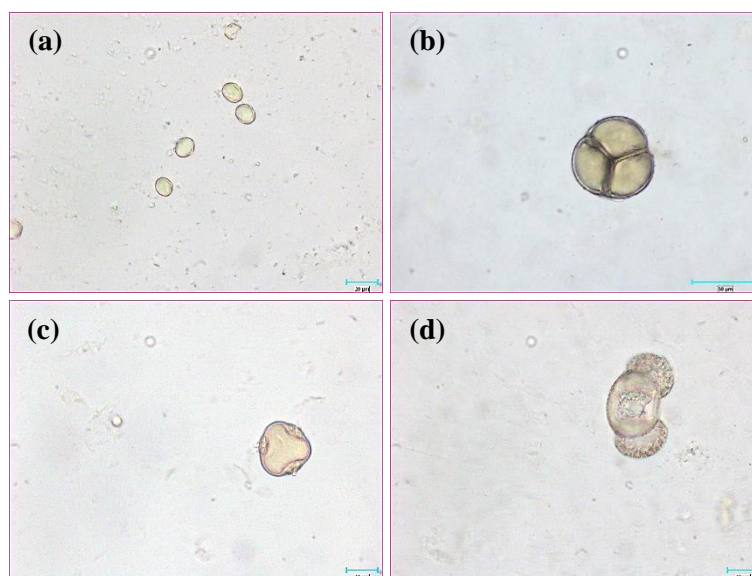


**Figure 2.** (a) Fagaceae, (b) Ericaceae, (c) Tiliaceae, and (d) Pinaceae – Examples of microscopic photographs of hydrated pollen grains from different plant families.

Upon examining prior studies on Düzce region honeys, comparable outcomes were observed to our own findings. Kambur *et al.* [25] identified three monofloral honeys through the analysis of honey samples from the Yığılca region. Two of them were chestnut honeys (with pollen ratios of 48.2% and 45.75%, respectively), while the other was honeysuckle honey (with a pollen ratio of 46.2%). In another study that included six samples from Düzce and examined the palynology of honey from four cities, it was reported that out of 18 samples, 10 were monofloral chestnut. Four of the honeys from Düzce have been identified as monofloral chestnut honey, with pollen ratios ranging from 48% to 68% [18]. In another study examining the honey from the Düzce Yığılca region, pollen detection of 43 different taxa from 26 families was conducted. In two of the seven samples, *C. sativa* pollen was recorded dominantly with percentages of 91.5% and 92.5% [20]. Another palynological study conducted in the Yığılca region examined chestnut honey propolis, and identified *C. sativa* pollen at a rate of 80.5% [26]. A separate study analyzed 34 honey samples collected from Düzce province and districts in 2019 and 2020, detecting pollen from 109 taxa belonging to 20 different families. *C. sativa* had the highest pollen rate among all identified taxa. It has been reported that 8 out of 12 monofloral honey samples collected were chestnut honey, with a pollen ratio of 70% or higher [19]. Similar to many studies, the prevalent pollen species identified in honey from the Düzce region are associated with the vegetation in the area, namely Fagaceae and Ericaceae families. Furthermore, pollen from numerous other families, including Fabaceae, Apiaceae, Malvaceae, Asteraceae, Boraginaceae, Poaceae, Rosaceae, and Campanulaceae, were also detected but classified as secondary or minor.

## **IV. CONCLUSION**

In this study, we evaluated the quality criteria of chestnut honey from the Düzce region, which were analyzed at DÜBİT laboratories. The TFC Honey Communiqué was used to ensure conformity. While most samples met the quality criteria, some exhibited inappropriate values.

Honey is a fundamental foodstuff in human life, with the quality of honey being critical when assessing its nutritional value. Although society has yet to fully comprehend the significance of determining and regulating quality criteria when purchasing honey, it plays a vital role in ensuring access to high-quality, natural honey. Information campaigns should be initiated by local and general authorities to raise public awareness. These campaigns should encourage producers to test and analyze their products, while also urging consumers to be mindful when making purchases. It is more accurate to evaluate honey using quality criteria data rather than relying on the belief that every expensive product is of good quality, and every cheap product is of poor quality. This approach would protect both parties involved.

**ACKNOWLEDGEMENTS:** We would like to express our gratitude to the management of Düzce University Scientific and Technological Research Application and Research Center (DÜBİT), as well as Ph.D. Tuna Demirci and Ph.D. Şeref Karadeniz, for their invaluable contributions to this study.

## **V. REFERENCES**

- [1] A. Coşkun, “Türkiye’de bal sektörünün mevcut durum değerlendirilmesi ve tüketici eğilimleri,” Yüksek lisans, Tarım Ekonomisi, Tekirdağ Namık Kemal Uni., Tekirdağ, Türkiye, 2019.
- [2] A. N. Morkoç, “Eski Ön Asya Tıbbında Bal,” *Mersin Üniversitesi Tıp Fakültesi Lokman Hekim Tıp Tarihi ve Folklorik Tıp Dergisi*, c. 12, s. 3, ss. 450–455, 2022.
- [3] E. Terzi, “Bilecik ve çevresinde üretilen ballarda bulunan polenlerin araştırılması,” Yüksek Lisans, Biyoloji, Anadolu Uni., Eskisehir, 2009.
- [4] M. Kekeçoğlu, S. Bir, and M. K. Acar, “Determination of anatolian honeybee biodiversity by wing characters,” *Sociobiology*, vol. 70, no. 3, pp. 8333, 2023.
- [5] S. A. El Sohaimy, S. H. D. Masry, and M. G. Shehata, “Physicochemical characteristics of honey from different origins,” *Ann. Agric. Sci.*, vol. 60, no. 2, pp. 279–287, 2015.
- [6] A. Özkök and N. Ecem Bayram, “Kestane (*Castanea sativa*) balı örneklerinin botanik orjinlerinin doğrulanması ve toplam polen sayıları,” *U. Bee J.*, c. 21, s. 1, ss. 54–65, 2021.
- [7] F. Villani, M. Pigliucci, and M. Cherubini, “Evolution of *Castanea sativa* mill, in Turkey and Europe,” *Genet Res*, vol. 63, no. 2, pp. 109–116, 1994.
- [8] M. Conedera, W. Tinner, P. Krebs, D. De Rigo, and G. Caudullo, “*Castanea sativa* in Europe: distribution, habitat, usage and threats” in *European Atlas of Forest Tree Species*, 1st ed., Luxembourg, EU: Publication Office of the European Union, 2016, pp-78-79
- [9] K. Yılmaz, E. Ceylan, and G. Derelioğlu, “Determination of chestnut honey consumption characteristics as a traditional treatment method and its effect on protection from covid-19,” *Complement Med Res*, vol. 29, no. 3, pp. 205–212, 2022.
- [10] S. Bogdanov. (2009, September 21). *Harmonised Methods of The International Honey*

Commission [Online]. Available: <https://www.ihc-platform.net/ihcmethods2009.pdf>.

- [11] Türk Gıda Kodeksi Bal Tebliği. *T.C. Resmi Gazete*, Sayı: 31107, 22 Nisan 2020.
- [12] N. E. Bayram and E. Demir, "Specifying some quality characteristics of monofloral and multifloral honey samples," *HJBC*, vol. 3, no. 46, pp. 417–423, 2018.
- [13] M. Özgüven, E. Demircan, and B. Özçelik, "Çeşitli Yörelerimizde Üretilen Çiçek Ballarının Fizikokimyasal Özelliklerinin Belirlenmesi ve Türk Gıda Kodeksi'ne Uygunluğunun Değerlendirilmesi," *Avrupa Bilim ve Teknoloji Dergisi*, s. 20, ss. 321–326, 2020.
- [14] *Bal - Diastaz Aktivitesi Tayini*, Türk Standartlar Enstitüsü TS 13364, 2008.
- [15] *Bal - Elektrik İletkenliği Tayini*, Türk Standartlar Enstitüsü TS 13366, 2008.
- [16] *Bal - Su Muhtevası Tayini - Refraktometrik Metot*, Türk Standartlar Enstitüsü TS 13366, 2008.
- [17] *Bal – Serbest Asit Muhtevasının Tayini*, Türk Standartlar Enstitüsü TS 13360, 2008.
- [18] N. Mayda, A. Özkök, and K. Sorkun, "Some characteristic properties of chestnut and rhododendron honeys in Turkey," *HJBC*, vol. 1, no. 46, pp. 135–145, 2018.
- [19] Ç. Atsay and E. Altundağ Çakır, "Düzce yöresi ballarında polen analizi," *Eurasian J. Forest Sci.* c. 10, s. 2, ss. 42–63, 2022.
- [20] E. A. Yıldırım, N. Karlıoğlu Kılıç, and N. Güneş Özkan, "Pollen analysis of honeys from Yığılca region (Düzce), Turkey," *Eurasian J. Forest Sci.*, vol. 9, no. 3, pp. 259–271, 2021.
- [21] *Bal - Nispi Polen Muhtevası Tayini*, Türk Standartlar Enstitüsü TS 13363, 2008.
- [22] K. Sorkun, *Türkiye'nin nektarlı bitkileri, polenleri ve balları*. 1.baskı, Ankara, Türkiye: Palme Yayıncılık, 2008.
- [23] Ş. Cınbırtoğlu, *Bal arıları (Apis mellifera L.) için Türkiye florasına ait önemli bitkiler ve polenleri*. 1.baskı, Ankara, Türkiye: TAGEM, 2022.
- [24] Nurten Türkarıslan. (2022, 22 Mart). *Polen Kütüphanesi*, T.C. Tarım ve Orman Bakanlığı. 2022. [Çevrimiçi]. Erişim: <https://gidalab.tarimorman.gov.tr/gidareferans/Menu/129/Polen-Kutuphanesi>
- [25] M. Kambur, M. Kekeçoğlu, and İ. Yıldız, "Düzce ili yığılca ilçesinde üretilen balların kimyasal ve palinolojik analiz yöntemleri ile değerlendirilmesi," *Uludağ Bee J.*, c. 15, s. 2, ss. 67–79, 2015.
- [26] M. Kekeçoğlu, E. Sonmez, M. K. Acar, and S. A. Karaoğlu, "Pollen analysis, chemical composition and antibacterial activity of Anatolian chestnut propolis collected from Yığılca region," *Biol. Bull.*, vol. 48, no. 6, pp. 721–728, 2021.



# Düzce University Journal of Science & Technology

Research Article

## Honey Plants of Düzce University Ornamental and Medicinal Plants Botanical Garden

Necmi AKSOY<sup>a,\*</sup>, Haldun MÜDERRİSOĞLU<sup>b</sup>, Engin EROĞLU<sup>b</sup>, Neval GÜNEŞ ÖZKAN<sup>a</sup>, Turgay BİRTÜRK<sup>a</sup>, Nihan KOÇER<sup>c</sup>, Bilge TUNÇKOL<sup>d</sup>, Özgür YERLİ<sup>b</sup>, Şemsettin KULAÇ<sup>a</sup>, Bilal ÇETİN<sup>a</sup>, Murat SARGINCI<sup>a</sup>, Sertaç KAYA<sup>b</sup>, Serdar ASLAN<sup>a</sup>, Salih Sercan KANOĞLU<sup>c</sup>, Nermin BAŞARAN<sup>b</sup>, Tuba GÜL DOĞAN<sup>b</sup>, Ahmet AYTEĞİN<sup>f</sup>

<sup>a</sup> Department of Forest Engineering, Faculty of Forestry, Düzce University, Düzce, TURKEY

<sup>b</sup> Department of Landscape Architecture, Faculty of Forestry, Düzce University, Düzce, TURKEY

<sup>c</sup> Vocational School of Forestry, Düzce University, Düzce, TURKEY

<sup>d</sup> Vocational School of Forestry, Bartın University, Bartın, TURKEY

<sup>e</sup> Nezahat Gökyiğit Botanical Garden, İstanbul, TURKEY

<sup>f</sup> Institute of Graduate Education, Düzce University, Düzce, TURKEY

\* Corresponding author's e-mail address: necmiaksoy@duzce.edu.tr

DOI: 10.29130/dubited.1383321

### ABSTRACT

In this study, melliferous plants that the honey bee (*Apis mellifera* L.) can benefit from among the taxa planted in Düzce University Ornamental and Medicinal Plants Botanical Garden, are presented. Among the 451 taxa planted in the botanical garden, those with these characteristics were determined by reviewing studies on the subject. Of the 165 taxa (36.58%) included in the honey plant class; 119 contain both nectar and pollen, 25 contain pollen, 13 contain nectar, 4 contain both pollen and insect secretion (IS) or sweet sap (SS), 2 contain pollen, nectar and IS or SS, 1 contain both nectar and SS, 1 contain only IS. In order to prevent the decrease in pollinator and pollinator insects, whose numbers are decreasing due to global climate change, a "Bee and Insect Hotel" was placed in the botanical garden. For this reason, the majority of the plants selected for planting were chosen from taxa with honey plant properties. The main purpose here is both to pollinate the plants in the botanical garden and to show and explain the effects of insect species on pollination through nature education.

**Keywords:** Botanical garden, Honey plants, Nectar, Pollen, Bee and insect hotel.

## Düzce Üniversitesi Süs ve Tıbbi Bitkiler Botanik Bahçesinin Ballı Bitkileri

### Öz

Bu çalışmada Düzce Üniversitesi Süs ve Tıbbi Bitkiler Botanik Bahçesi'ne dikilen taksonlardan bal arısının (*Apis mellifera* L.) yararlanabileceği ballı bitkiler sunulmuştur. Botanik bahçesine dikimi gerçekleştirilen 451 taksondan bu özelliklere sahip olanlar konuyla ilgili çalışmalar incelenerek belirlenmiştir. Ballı bitki sınıfına giren 165 taksondan (%36,58); 119'u hem nektar hem de polen, 25'i polen, 13'ü nektar, 4'ü hem polen hem de böcek salgısı (BS) veya tatlı özsu (TÖS), 2'si polen, nektar ve BS veya TÖS, 1'i hem nektar hem de TÖS, 1'i yalnızca BS içerir. Küresel iklim değişikliği nedeniyle sayıları azalan polen ve polen taşıyıcı böceklerin azalmasını önlemek amacıyla

botanik bahçesine bir "Arı ve Böcek Oteli" yerleştirildi. Bu nedenle dikim için seçilen bitkilerin büyük çoğunluğu ballı bitki özelliği taşıyan taksonlardan seçildi. Buradaki temel amaç hem botanik bahçesindeki bitkilerin tozlaşmasını sağlamak hem de böcek türlerinin tozlaşma üzerindeki etkilerini doğa eğitimi yoluyla göstermek ve anlatmaktır.

*Anahtar Kelimeler: Botanik bahçesi, Ballı bitki, Nektar, Polen, Arı ve böcek hoteli*

## **I. INTRODUCTION**

Animal pollination plays a vital role as a regulating ecosystem service in nature. Most of the world's wild flowering plants (87.5%) are pollinated by insects and other animals. The importance of animal pollination varies substantially among crops, and, therefore among regional crop economies [1]. The vast majority of pollinator species are wild, including more than 20,000 species of bees, some species of flies, butterflies, moths, wasps, beetles, thrips, birds, bats and other vertebrates [2].

A few species of bees are widely managed, including the western honey bee (*Apis mellifera*), the eastern honey bee (*Apis cerana*), some bumble bees, some stingless bees and a few solitary bees [3]. However wild pollinators have declined in occurrence and diversity (and abundance for certain species) at local and regional scales in North West Europe and North America [4]. The abundance, diversity, and health of pollinators and the provision of pollination are threatened by direct drivers that generate risks to societies and ecosystems [5].

The ranges, abundances, and seasonal activities of some wild pollinator species (e.g., bumble bees and butterflies) have changed in response to observed many of our pollinators are currently suffering declines due to land use changes, land management, pesticides, disease, invasive species, and climate change [6]. Ecological infrastructure needed to improve pollination includes patches of semi-natural habitats distributed throughout productive landscapes, providing nesting and floral resources [7]. Providing artificial habitats for pollinators can significantly increase their number and diversity. It is known for certain that more nectar and pollen sources will help increase their health and numbers. For this reason, it is known that efforts to develop and create alternative habitats for pollinators continue in some countries [8, 9, 10].

Currently, in the context of biodiversity losses, Botanical gardens have assumed a new role as repositories for the conservation of the plant biological diversity at global level. The Botanical Gardens are habitats that highly structured with many very different biotope types and a permanently high flower diversity, for bees [11].

Düzce University Ornamental and Medicinal Plants Botanical Garden was established in order to protect the plant biological diversity of Düzce province and the Western Black Sea Region, to transfer it to future generations by ensuring its sustainability, and to serve integrated nature conservation and education. While selecting species for the botanical garden, care was taken to plant species that contain nectar and pollen in order to provide food for pollinators, as well as species that have visual appeal that can attract the attention of visitors.

In this study, it was aimed to determine food plants for bees in Düzce University Ornamental and Medicinal Plants Botanical Garden, which is a living nature museum, and to give information about the application that will attract bees.

## II. MATERIAL METHOD

### A. STUDY AREA

Euro-Siberian (Euxine) Flora, Mediterranean Flora and Irano-Turanian Flora are dominant in the northwestern Black Sea region in Düzce province. Thus, biodiversity is very high in Düzce.

Düzce flora has 102 families, 471 genera, 1200 species and subspecies taxa. On the north-facing slopes of the region, there is forest vegetation consisting of beech, chestnut, oak, hornbeam, linden, maple, ash and other leafy trees belonging to the Black Sea vegetation. On the south-facing slopes, there is a pseudo-macchia vegetation consisting of shrubs such as laurel (*Laurus nobilis* L.), Oak (*Quercus* sp.), and heather (*Erica arborea* L.) belonging to the local Mediterranean vegetation. Düzce's rich flora is habitat for various pollinators. Chestnut (*Castanea sativa* Miller), linden (*Tilia* spp.), thyme (*Thymus* spp.) and heather (*Ericaceae*) are the main species of honey forests. The study area is located within the borders of Düzce University Konuralp Campus, located in the north of Düzce province (Fig. 2).

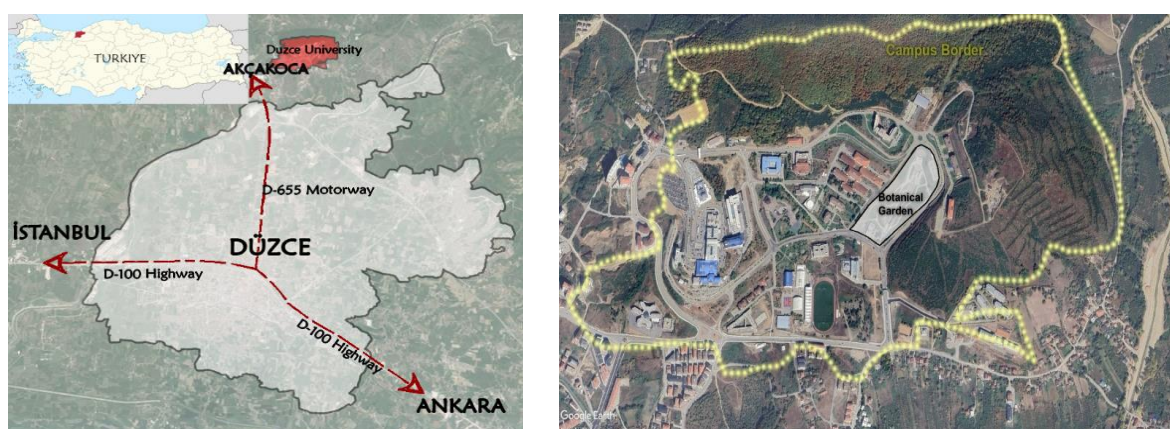


Figure 1. Location of study area

The botanical garden is a valley located within the borders of Düzce University, with an area of approximately 51,450 m<sup>2</sup>, from the bottom of which a weak water flows, and the amount of green area consists of a total of 38293 m<sup>2</sup>.

The Botanical Garden is a rectangular area extending from the north-northeast direction to the south-southwest axis and is surrounded by internal roads. The Black Sea climate is generally dominant in the project area.

Düzce University Ornamental and Medicinal Plants Botanical Garden is a living nature museum built on 43 main consisting of terraced gardens, rock gardens, waterfalls, streams, streams, pond ecological systems, amphitheater, nature and botanical museum education systems, collections and garden exhibitions where living biomes on earth are defined: arboretum and recreation area, medicinal aromatic plants garden, *Ex-situ* Düzce plants, Central Anatolian steppe plants, rock garden, Mediterranean plants, herbaceous-woody plants, geophyte garden, exotic species, pond and aquatic plants, moist stream vegetation and welcome gardens (Fig. 3).



*Figure 2. Plant collections of Düzce University Ornamental and Medicinal Plants Botanical Garden*

## **B. DETERMINING HONEY PLANTS PLANTED IN THE BOTANICAL GARDEN**

Among the plants planted in the botanical garden, taxa that can provide food sources for various pollinators by containing nectar, pollen, insect secretions and sweet sap were determined by examining various literature on the subject (Figs. 7 and 8) [12, 13, 14, 15, 16, 17, 18, 19, 20, 21].

## **C. BEE AND INSECT HOTEL DESIGN**

A bee and insect hotel has been designed to host various pollinators, especially solitary wild bees, that will benefit from the honey plants in the Botanical Garden. Log pieces, timber and briquette bricks were used as materials in the design of the Bee Hotel (Fig. 4).



*Figure 3. Bee and insect hotel located in Düzce University Ornamental and Medicinal Plants Botanical Garden*

### **III. RESULT**

Aromatic- medicinal gardens plants in the botanical garden, are a type of garden designed with the intent of growing used as natural medicines also specific nectar and pollen-producing plants. This designed garden is approximately 80 meters long and 2 m wide. 18 different species were preferred in this garden. Each parcel is approximately 4 m.

18 different species were preferred in this garden. Most of these species attract bees with their scent and flower characteristics. For the planting project carried out in the Botanical Garden, 13852 plants belonging to 451 taxa were procured through purchases and grants from various nurseries in Turkey. In this context, approximately; Grant from 4444 Nezahat Gökyiğit Botanical Gardens and Eskişehir and Bolu Regional Directorates of Forestry, 9408 plants were procured through purchasing. Seeds of medicinal plants obtained by donation from Afyonkarahisar Medicinal and Herbal Plants Center and Zeytinburnu Medicinal Plants Garden are stored in the seed bank until the germination process begins. Among the taxa planted in the botanical garden, the life forms of 165 taxa determined to be honey plants were determined. Accordingly, 147 taxa (89.09%) are Phanerophyt (Trees and shrubs), 9 taxa (5.45%) are Chamaephytes (woody plants with perennating buds), 5 taxa (3.03%) are Lianas (climbing woody plants), 4 taxa (2.42%) are Hemicryptophytes (rosette plants) (Fig. 5).



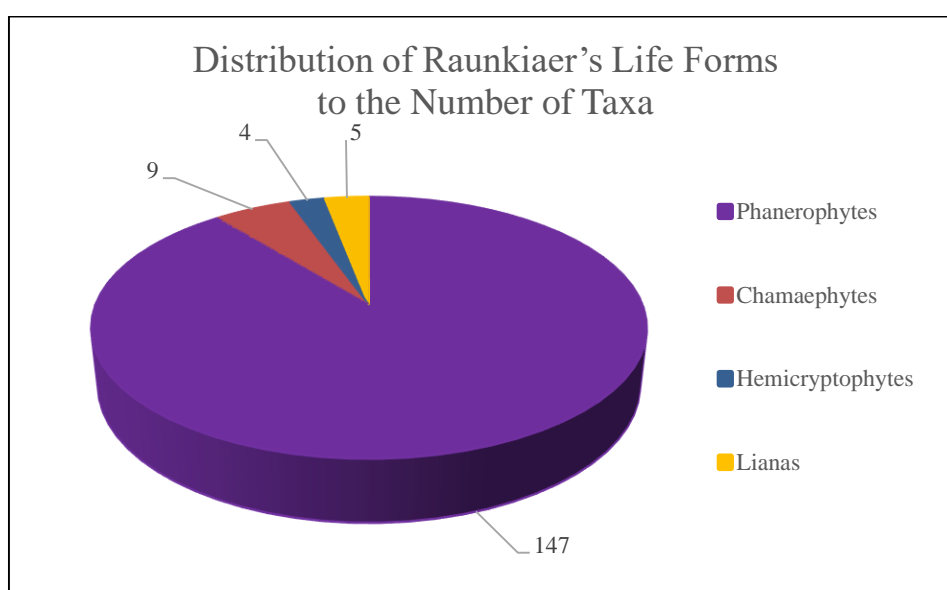


**Figure 4.** Distribution of Number of Taxa according to Raunkiaer's Life Forms

The majority of the plants selected for planting were chosen from taxa with honey plant properties. The main purpose here is both to pollinate the plants in the botanical garden and to show and explain the effects of insect species on pollination through nature education.

Melliferous plant characteristics of 451 taxa planted in the Botanical Garden were determined. Accordingly, 165 taxa (36.58%) are important for beekeeping. 119 contain both nectar and pollen, 25 contain pollen, 13 contain nectar, 4 contain both pollen and insect secretion (IS) or sweet sap (SS), 2 contain pollen, nectar and IS or SS, 1 contain both nectar and SS, 1 contain only IS (Table 1), (Fig. 6).

**Table 1.** Honey Plants Planted in Düzce University Ornamental and Medicinal Plants Botanical Garden

Family	Takson	Nectar	Pollen	IS/SS	Life Form
Caprifoliaceae	<i>Abelia × grandiflora</i> (Rovelli ex André) Rehder	N	P		Phanerophyt
Caprifoliaceae	<i>Abelia × grandiflora</i> 'Compacta Nana'	N	P		Phanerophyt
Caprifoliaceae	<i>Abelia × grandiflora</i> 'Kaleidoscope'	N	P		Phanerophyt
Fabaceae	<i>Acacia dealbata</i> Link	N	P		Phanerophyt
Sapindaceae	<i>Acer buergerianum</i> Miq.	N			Phanerophyt
Sapindaceae	<i>Acer campestre</i> L.	N	P		Phanerophyt
Sapindaceae	<i>Acer negundo</i> 'Flamingo'	N	P		Phanerophyt
Sapindaceae	<i>Acer negundo</i> L.	N	P		Phanerophyt
Sapindaceae	<i>Acer palmatum</i> 'Dissectum'	N	P		Phanerophyt
Sapindaceae	<i>Acer platanoides</i> 'Crimson King'	N	P		Phanerophyt

<b>Sapindaceae</b>	<i>Acer platanoides</i> 'Drummondii'	N	P		Phanerophyt
<b>Sapindaceae</b>	<i>Acer platanoides</i> 'Fairview'	N	P		Phanerophyt
<b>Sapindaceae</b>	<i>Acer platanoides</i> 'Globosum'	N	P		Phanerophyt
<b>Sapindaceae</b>	<i>Acer platanoides</i> L.	N	P		Phanerophyt
<b>Sapindaceae</b>	<i>Acer platanoides</i> 'Royal Red'	N	P		Phanerophyt
<b>Sapindaceae</b>	<i>Acer pseudoplatanus</i> L.	N	P		Phanerophyt
<b>Sapindaceae</b>	<i>Acer pseudoplatanus</i> 'Leopoldii'	N	P		Phanerophyt
<b>Sapindaceae</b>	<i>Acer pseudoplatanus</i> 'Spaethii'	N	P		Phanerophyt
<b>Sapindaceae</b>	<i>Acer rubrum</i> L.	N	P		Phanerophyt
<b>Sapindaceae</b>	<i>Acer saccharinum</i> L.	N	P		Phanerophyt
<b>Sapindaceae</b>	<i>Acer saccharinum</i> 'Laciniatum Wieri'	N	P		Phanerophyt
<b>Sapindaceae</b>	<i>Acer tataricum</i> L.	N	P		Phanerophyt
<b>Sapindaceae</b>	<i>Aesculus</i> × <i>carnea</i> Hayne	N	P		Phanerophyt
<b>Sapindaceae</b>	<i>Aesculus hippocastanum</i> L.	N	P		Phanerophyt
<b>Ericaceae</b>	<i>Arbutus unedo</i> 'Compacta'	N	P		Phanerophyt
<b>Berberidaceae</b>	<i>Berberis</i> × <i>media</i> 'Red Jewel'	N	P		Phanerophyt
<b>Berberidaceae</b>	<i>Berberis juliana</i> C.K.Schneid.	N	P		Phanerophyt
<b>Berberidaceae</b>	<i>Berberis ottawensis</i> 'Superba'	N	P		Phanerophyt
<b>Berberidaceae</b>	<i>Berberis thunbergii</i> 'Coronita'	N	P		Phanerophyt
<b>Berberidaceae</b>	<i>Berberis thunbergii</i> DC.	N	P		Phanerophyt
<b>Berberidaceae</b>	<i>Berberis thunbergii</i> f. <i>atropurpurea</i>	N	P		Phanerophyt
<b>Berberidaceae</b>	<i>Berberis thunbergii</i> f. <i>atropurpurea</i> 'Nana'	N	P		Phanerophyt
<b>Berberidaceae</b>	<i>Berberis thunbergii</i> 'Maria'	N	P		Phanerophyt
<b>Berberidaceae</b>	<i>Berberis thunbergii</i> 'Tinny Gold'	N	P		Phanerophyt
<b>Berberidaceae</b>	<i>Berberis vulgaris</i> L.	N	P		Phanerophyt
<b>Betulaceae</b>	<i>Betula pendula</i> Roth		P	IS	Phanerophyt
<b>Scrophulariaceae</b>	<i>Buddleja davidii</i> Franch.	N			Phanerophyt
<b>Fagaceae</b>	<i>Castanea sativa</i> Mill.	N	P	SS	Phanerophyt
<b>Cannabaceae</b>	<i>Celtis australis</i> L.	N	P		Phanerophyt

<b>Fabaceae</b>	<i>Ceratonia siliqua</i> L.	N	P	Phanerophyt
<b>Fabaceae</b>	<i>Cercis siliquastrum</i> L.	N	P	Phanerophyt
<b>Cistaceae</b>	<i>Cistus creticus</i> L.	N	P	Chamaephyt
<b>Cistaceae</b>	<i>Cistus salviifolius</i> 'Crispus'	N	P	Chamaephyt
<b>Ranunculaceae</b>	<i>Clematis vitalba</i> L.		P	Lian
<b>Fabaceae</b>	<i>Colutea arborescens</i> L.	N	P	Phanerophyt
<b>Cornaceae</b>	<i>Cornus alba</i> 'Aurea'	N		Phanerophyt
<b>Cornaceae</b>	<i>Cornus alba</i> 'Sibirica'	N		Phanerophyt
<b>Cornaceae</b>	<i>Cornus florida</i> L.	N		Phanerophyt
<b>Cornaceae</b>	<i>Cornus kousa</i> Bürger ex Hance	N		Phanerophyt
<b>Cornaceae</b>	<i>Cornus mas</i> L.	N	P	Phanerophyt
<b>Cornaceae</b>	<i>Cornus sanguinea</i> L.	N	P	Phanerophyt
<b>Rosaceae</b>	<i>Cotoneaster dammeri</i> C.K.Schneid.	N	P	Phanerophyt
<b>Rosaceae</b>	<i>Cotoneaster dammeri</i> 'Evergreen'	N	P	Phanerophyt
<b>Rosaceae</b>	<i>Cotoneaster franchetii</i> Boiss.	N	P	Phanerophyt
<b>Rosaceae</b>	<i>Cotoneaster frigida</i> 'Cornubia'	N	P	Phanerophyt
<b>Rosaceae</b>	<i>Cotoneaster horizontalis</i> Decne.	N	P	Phanerophyt
<b>Rosaceae</b>	<i>Cotoneaster microphyllus</i> Wall. ex Lindl.	N	P	Phanerophyt
<b>Rosaceae</b>	<i>Cotoneaster salicifolius</i> Franch.	N	P	Phanerophyt
<b>Rosaceae</b>	<i>Crataegus lavalleyi</i> 'Carrierei'	N	P	Phanerophyt
<b>Cupressaceae</b>	<i>Cupressus sempervirens</i> L.		P	Phanerophyt
<b>Cupressaceae</b>	<i>Cupressus sempervirens</i> subsp. <i>horizontalis</i>		P	Phanerophyt
<b>Cupressaceae</b>	<i>Cupressus sempervirens</i> subsp. <i>pyramidalis</i>		P	Phanerophyt
<b>Hydrangeaceae</b>	<i>Deutzia gracilis</i> Siebold & Zucc.		P	Phanerophyt
<b>Ebenaceae</b>	<i>Diospyros kaki</i> L.f.	N	P	Phanerophyt
<b>Elaeagnaceae</b>	<i>Elaeagnus angustifolia</i> L.	N	P	Phanerophyt
<b>Escalloniaceae</b>	<i>Escallonia rubra</i> (Ruiz & Pav.) Pers.	N	P	Phanerophyt
<b>Fagaceae</b>	<i>Fagus orientalis</i> Lipsky		P	Phanerophyt
<b>Oleaceae</b>	<i>Forsythia</i> × <i>intermedia</i> Zabel	N	P	Phanerophyt

<b>Oleaceae</b>	<i>Fraxinus excelsior</i> 'Altena'	N	P		Phanerophyt
<b>Oleaceae</b>	<i>Fraxinus excelsior</i> 'Diversifolia'	N	P		Phanerophyt
<b>Oleaceae</b>	<i>Fraxinus excelsior</i> 'Jaspidea'	N	P		Phanerophyt
<b>Oleaceae</b>	<i>Fraxinus excelsior</i> L.	N	P		Phanerophyt
<b>Oleaceae</b>	<i>Fraxinus excelsior</i> 'Westhof Glorie'	N	P		Phanerophyt
<b>Fabaceae</b>	<i>Genista tinctoria</i> 'Royal Gold'	N	P		Chamaephyt
<b>Araliaceae</b>	<i>Hedera helix</i> 'Alba Marginata'	N	P		Lian
<b>Araliaceae</b>	<i>Hedera helix</i> 'Aurea Variegata'	N	P		Lian
<b>Araliaceae</b>	<i>Hedera helix</i> L.	N	P		Lian
<b>Araliaceae</b>	<i>Hedera hibernica</i> Poit.	N	P		Lian
<b>Hydrangeaceae</b>	<i>Hydrangea macrophylla</i> (Thunb.) Ser.	N	P		Phanerophyt
<b>Hydrangeaceae</b>	<i>Hydrangea quercifolia</i> Bartram	N	P		Phanerophyt
<b>Juglandaceae</b>	<i>Juglans regia</i> L.		P	SS	Phanerophyt
<b>Lauraceae</b>	<i>Laurus nobilis</i> L.	N	P		Phanerophyt
<b>Lauraceae</b>	<i>Laurus nobilis</i> 'Pyramidalis'	N	P		Phanerophyt
<b>Lamiaceae</b>	<i>Lavandula angustifolia</i> Mill. subsp. <i>angustifolia</i>	N			Chamaephyt
<b>Lamiaceae</b>	<i>Lavandula dentata</i> L.	N			Chamaephyt
<b>Lamiaceae</b>	<i>Lavandula stoechas</i> subsp. <i>cariensis</i> (Boiss.) Rozeira	N	P		Chamaephyt
<b>Oleaceae</b>	<i>Ligustrum vulgare</i> L.	N	P		Phanerophyt
<b>Caprifoliaceae</b>	<i>Lonicera etrusca</i> Santi	N	P		Phanerophyt
<b>Caprifoliaceae</b>	<i>Lonicera japonica</i> Thunb.	N	P		Phanerophyt
<b>Caprifoliaceae</b>	<i>Lonicera nitida</i> E.H.Wilson	N	P		Phanerophyt
<b>Caprifoliaceae</b>	<i>Lonicera pileata</i> Oliv.	N	P		Phanerophyt
<b>Caprifoliaceae</b>	<i>Lonicera tatarica</i> L.	N	P		Phanerophyt
<b>Magnoliaceae</b>	<i>Magnolia grandiflora</i> 'Gallisoniensis'		P		Phanerophyt
<b>Magnoliaceae</b>	<i>Magnolia grandiflora</i> 'Pyramidalis'		P		Phanerophyt
<b>Magnoliaceae</b>	<i>Magnolia</i> × <i>soulangeana</i> 'Nana'		P		Phanerophyt
<b>Magnoliaceae</b>	<i>Magnolia</i> × <i>soulangeana</i> Soul.-Bod.		P		Phanerophyt
<b>Berberidaceae</b>	<i>Mahonia aquifolium</i> (Pursh) Nutt. (≡ <i>Berberis aquifolium</i> Pursh)	N	P		Phanerophyt

<b>Berberidaceae</b>	<i>Mahonia aquifolium</i> 'Charty'	N	P		Phanerophyt
<b>Rosaceae</b>	<i>Malus sylvestris</i> Mill.	N	P		Phanerophyt
<b>Lamiaceae</b>	<i>Melissa officinalis</i> L.	N	P		Hemicryptophyt
<b>Lamiaceae</b>	<i>Mentha</i> × <i>piperita</i> L.	N			Hemicryptophyt
<b>Moraceae</b>	<i>Morus alba</i> L.		P		Phanerophyt
<b>Moraceae</b>	<i>Morus alba</i> 'Pendula'		P		Phanerophyt
<b>Lamiaceae</b>	<i>Origanum onites</i> L.	N	P		Chamaephyt
<b>Oleaceae</b>	<i>Osmanthus</i> × <i>burkwoodii</i> (Burkwood & Skipwith) P.S.Green	N	P		Phanerophyt
<b>Oleaceae</b>	<i>Osmanthus heterophyllus</i> (G.Don) P.S.Green	N	P		Phanerophyt
<b>Oleaceae</b>	<i>Osmanthus ilicifolius</i> 'Tricolor'	N	P		Phanerophyt
<b>Hydrangeaceae</b>	<i>Philadelphus coronarius</i> L.	N	P		Phanerophyt
<b>Oleaceae</b>	<i>Phillyrea latifolia</i> L.		P		Phanerophyt
<b>Pinaceae</b>	<i>Pinus brutia</i> Ten.			IS	Phanerophyt
<b>Anacardiaceae</b>	<i>Pistacia lentiscus</i> L.	N	P		Phanerophyt
<b>Platanaceae</b>	<i>Platanus orientalis</i> L.		P	SS	Phanerophyt
<b>Rosaceae</b>	<i>Prunus avium</i> (L.) L. (≡ <i>Cerasus avium</i> (L.) Moench)	N	P		Phanerophyt
<b>Rosaceae</b>	<i>Prunus laurocerarus</i> L. (≡ <i>Laurocerasus officinalis</i> M.Roem.)	N	P		Phanerophyt
<b>Rosaceae</b>	<i>Prunus laurocerarus</i> 'Nana'	N	P		Phanerophyt
<b>Rosaceae</b>	<i>Prunus laurocerarus</i> 'Otto Luyken'	N	P		Phanerophyt
<b>Rosaceae</b>	<i>Prunus laurocerarus</i> 'Rotundifolia'	N	P		Phanerophyt
<b>Rosaceae</b>	<i>Pyracantha coccinea</i> 'Aurea'	N	P		Phanerophyt
<b>Rosaceae</b>	<i>Pyracantha coccinea</i> M.Roem.	N	P		Phanerophyt
<b>Rosaceae</b>	<i>Pyracantha coccinea</i> 'Mohave'	N	P		Phanerophyt
<b>Rosaceae</b>	<i>Pyracantha coccinea</i> 'Nana'	N	P		Phanerophyt
<b>Rosaceae</b>	<i>Pyracantha coccinea</i> 'Navaho'	N	P		Phanerophyt
<b>Rosaceae</b>	<i>Pyracantha coccinea</i> 'Orange Glow'	N	P		Phanerophyt
<b>Rosaceae</b>	<i>Pyracantha coccinea</i> 'Soleil D'or'	N	P		Phanerophyt
<b>Rosaceae</b>	<i>Pyrus communis</i> L. subsp. <i>communis</i>	N	P		Phanerophyt
<b>Rosaceae</b>	<i>Pyrus elaeagrifolia</i> Pall.	N	P		Phanerophyt

<b>Fagaceae</b>	<i>Quercus brantii</i> Lindl.		P	Phanerophyt
<b>Fagaceae</b>	<i>Quercus ilex</i> L.		P	Phanerophyt
<b>Fagaceae</b>	<i>Quercus macranthera</i> subsp. <i>sypirensis</i> (K.Koch) Menitsky		P	Phanerophyt
<b>Fagaceae</b>	<i>Quercus palustris</i> Münchh.		P	Phanerophyt
<b>Fagaceae</b>	<i>Quercus robur</i> 'Fastigiata'		P	Phanerophyt
<b>Fagaceae</b>	<i>Quercus robur</i> L.		P	Phanerophyt
<b>Fagaceae</b>	<i>Quercus virgiliana</i> (Ten.) Ten.	N		SS Phanerophyt
<b>Fagaceae</b>	<i>Quercus vulcanica</i> Boiss. & Heldr. ex Kotschy		P	Phanerophyt
<b>Ericaceae</b>	<i>Rhododendron ponticum</i> 'Grazella'	N		Phanerophyt
<b>Rosaceae</b>	<i>Rosa canina</i> L.	N	P	Phanerophyt
<b>Rosaceae</b>	<i>Rosa</i> L.		P	Phanerophyt
<b>Rosaceae</b>	<i>Rosa multiflora</i> Thunb.	N	P	Phanerophyt
<b>Salicaceae</b>	<i>Salix babylonica</i> L.	N	P	Phanerophyt
<b>Salicaceae</b>	<i>Salix babylonica</i> var. <i>matsudana</i> (Koidz.) H. Ohashi & Yonek.	N	P	Phanerophyt
<b>Lamiaceae</b>	<i>Salvia officinalis</i> L.	N	P	Hemicryptophyt
<b>Lamiaceae</b>	<i>Salvia rosmarinus</i> Schleid. (= <i>Rosmarinus officinalis</i> L.)	N	P	Chamaephyt
<b>Lamiaceae</b>	<i>Salvia sclarea</i> L.	N	P	Hemicryptophyt
<b>Viburnaceae</b>	<i>Sambucus nigra</i> L.	N	P	Phanerophyt
<b>Rosaceae</b>	<i>Sorbus aucuparia</i> L.	N	P	Phanerophyt
<b>Rosaceae</b>	<i>Sorbus torminalis</i> (L.) Crantz	N	P	Phanerophyt
<b>Oleaceae</b>	<i>Syringa vulgaris</i> L.	N	P	Phanerophyt
<b>Tamaricaceae</b>	<i>Tamarix africana</i> Poir.	N		Phanerophyt
<b>Tamaricaceae</b>	<i>Tamarix smyrnensis</i> Bunge	N	P	Phanerophyt
<b>Taxaceae</b>	<i>Taxus baccata</i> 'Compacta'		P	Phanerophyt
<b>Taxaceae</b>	<i>Taxus baccata</i> 'Fastigiata'		P	Phanerophyt
<b>Taxaceae</b>	<i>Taxus baccata</i> L.		P	Phanerophyt
<b>Taxaceae</b>	<i>Taxus baccata</i> 'Media Hillii'		P	Phanerophyt
<b>Malvaceae</b>	<i>Tilia cordata</i> Mill.	N	P	Phanerophyt
<b>Malvaceae</b>	<i>Tilia dasystyla</i> subsp. <i>multiflora</i> (Ledeb.) Pigott	N	P	Phanerophyt

<b>Malvaceae</b>	<i>Tilia platyphyllos</i> Scop.	N	P		Phanerophyt
<b>Malvaceae</b>	<i>Tilia platyphyllos</i> subsp. <i>corinthiaca</i> (Bosc ex K.Koch) Pigott	N	P		Phanerophyt
<b>Malvaceae</b>	<i>Tilia tomentosa</i> Moench	N	P	SS	Phanerophyt
<b>Ulmaceae</b>	<i>Ulmus minor</i> Mill.		P	SS	Phanerophyt
<b>Ericaceae</b>	<i>Vaccinium myrtillus</i> L.	N	P		Phanerophyt
<b>Plantaginaceae</b>	<i>Veronica odora</i> Hook.f.	N	P		Phanerophyt
<b>Plantaginaceae</b>	<i>Veronica</i> × <i>andersonii</i> Lindl. & Paxton	N			Phanerophyt
<b>Rhamnaceae</b>	<i>Ziziphus jujuba</i> Mill.	N	P		Phanerophyt

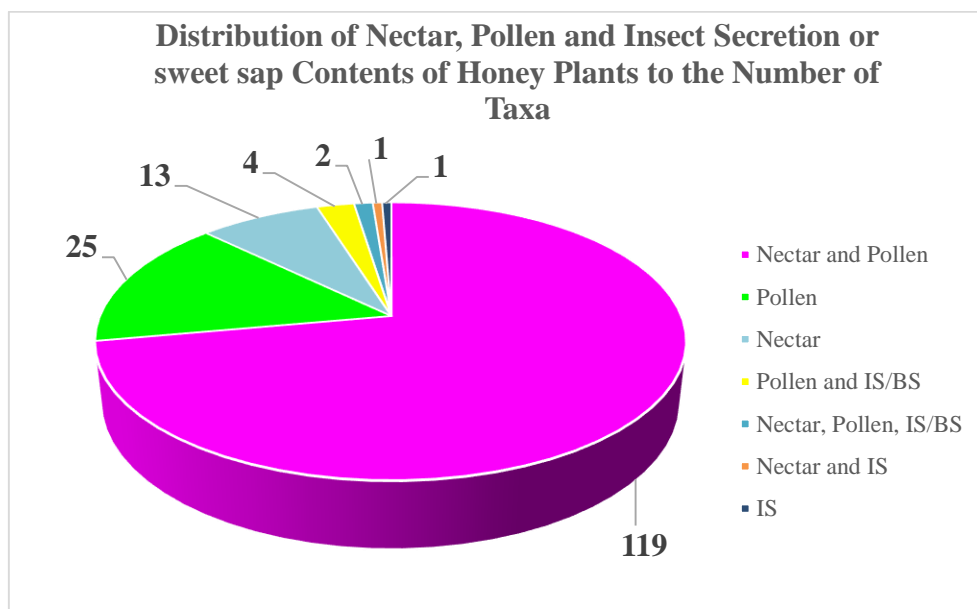
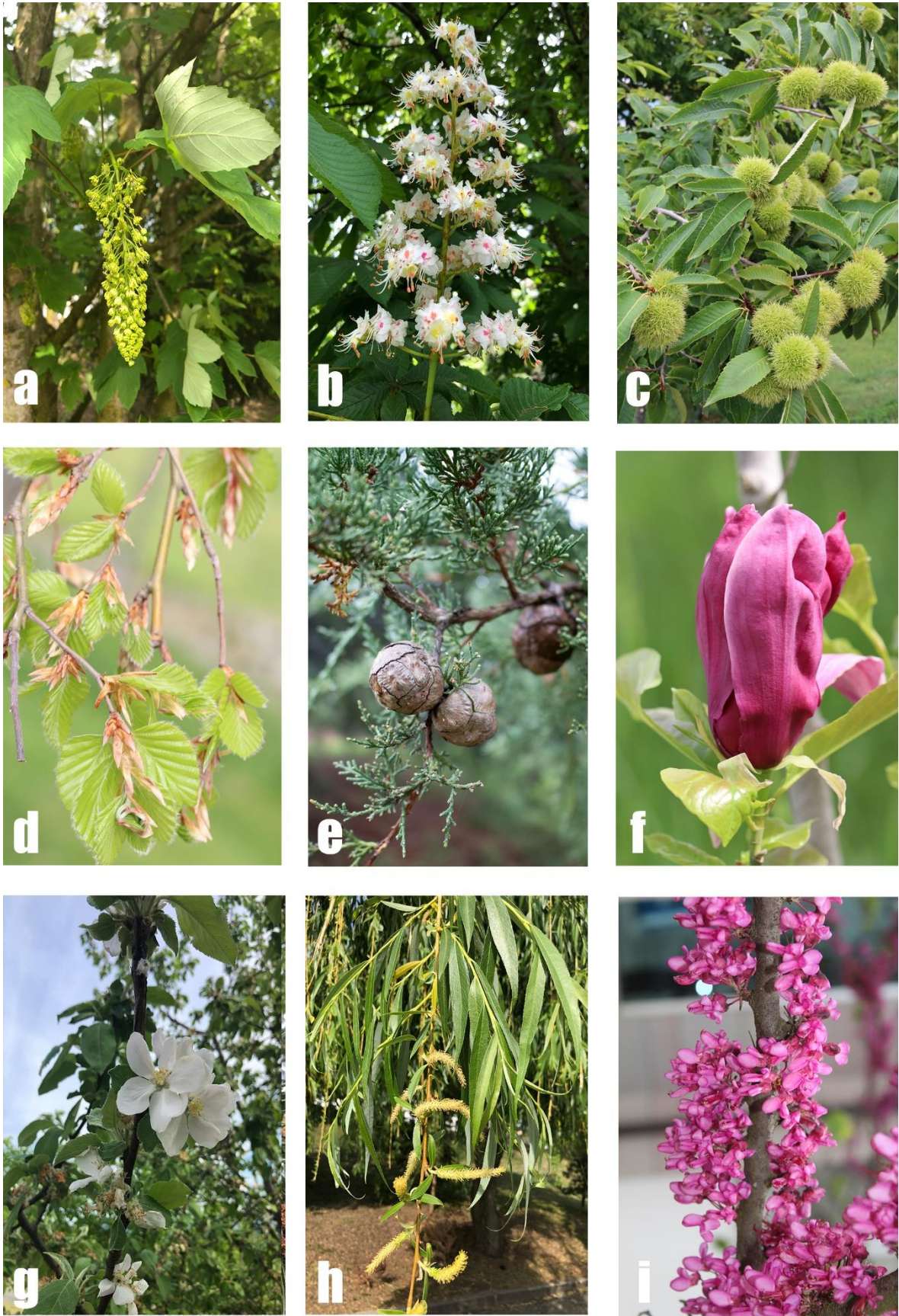


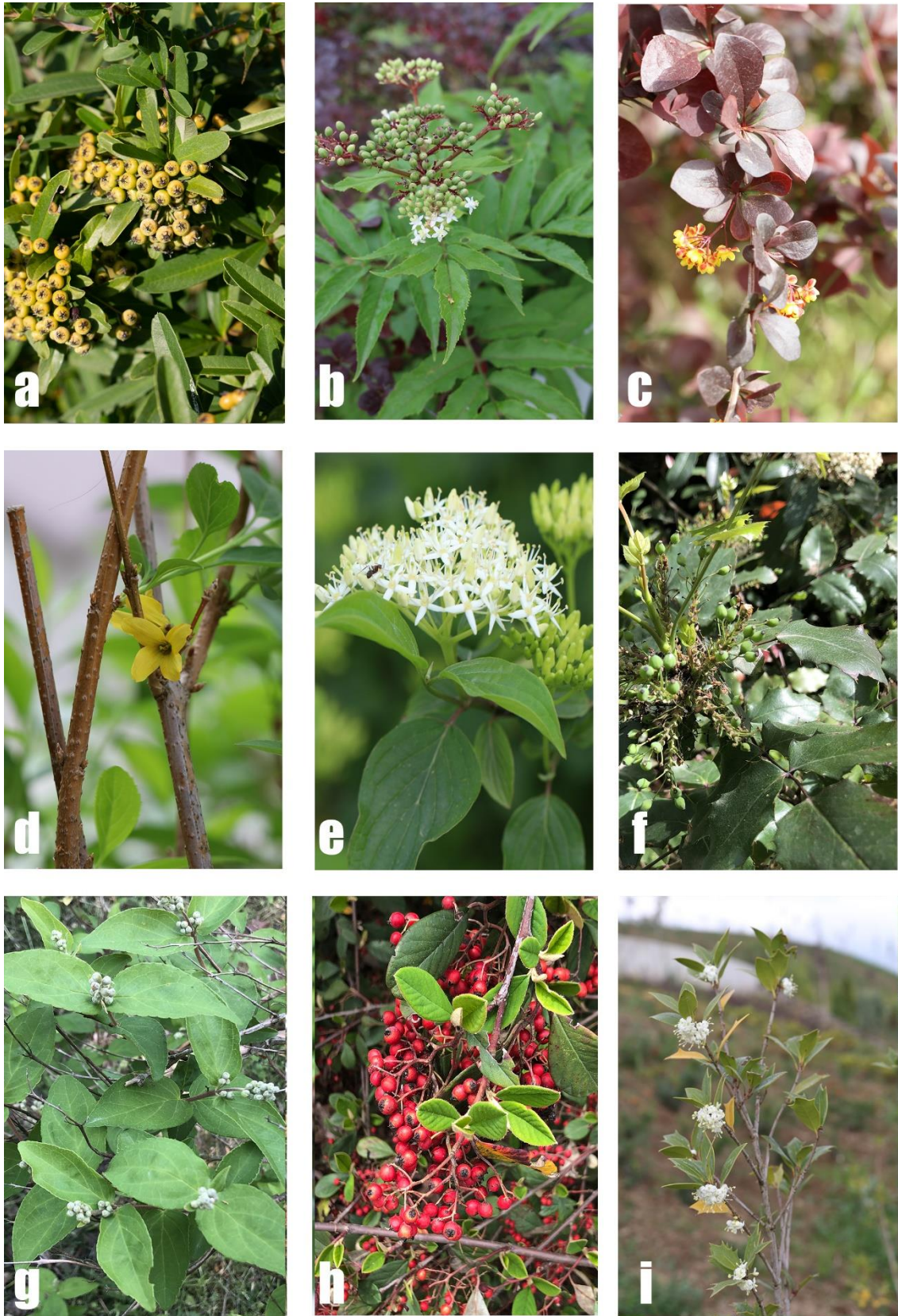
**Figure 5.** Distribution of Nectar, Pollen and Insect Secretion or Sweet Sap Contents of Honey Plants to the Number of Taxa



a- *Acer pseudoplatanus*, b- *Aesculus hippocastanum*, c-*Castanea sativa*, d-*Fagus orientalis*, e-*Cupressus sempervirens*, f-*Magnolia* × *soulangeana*, g- *Malus sylvestris*, h- *Salix babylonica*, i- *Cercis siliquastrum*

**Figure 6.** Some tree plant species used for pollen in the botanical garden.





a-*Pyracantha coccinea*, b- *Sambucus ebulus*, c-*Berberis thunbergii*, d-*Forsythia × intermedia*, e-*Cornus sanguinea*, f-*Mahonia aquifolium*, g- *Deutzia gracilis*, h- *Cotoneaster franchetii*, i- *Osmanthus heterophyllus*

**Figure 7.** Some shrub plant species used for pollen in the botanical garden.

## **IV. CONCLUSION**

Many functions of botanical gardens emphasize the scientific basis of botanical gardens, focusing on research, education, and conservation. Botanical gardens responded to the necessary habitat for wildlife. Because botanical gardens have a rich floristic diversity.

Botanical gardens provide for and facilitate the pollinators continuing their lives in disintegrated urban habitats through applications that increase the richness of natural and endemic species (such as fragrance garden, rock garden, water garden, roof and terrace garden) [22]. Botanical gardens evaluate, improve, and maintain effective pollinator breeding practices to improve genetic diversity and maintain traits. Botanical gardens help to identify and address spatiotemporal gaps in forage, habitat, and nutrition and their relation to the health and sustainability of managed and wild pollinators.

Depending on what sorts of pollinators a gardener is hoping to attract, be it birds, bees, or butterflies, nectar, pollen, and larval-host plants appropriate for these species should be chosen [23, 24]. Decision makers are also encouraged to choose native plant species. A plant is considered to be a native species if it occurs naturally in a particular region or habitat without human introduction. Native plants have evolved to be best adapted and suited for the particular climate and growing conditions in which they are found and have often developed pollinator-specific relationships [25]. Additionally, choosing native plants ensures that surrounding native plant populations will not be outcompeted by introduced species. Garden maintenance, such as mulching, weeding, and clearing, should also be timed appropriately so as not to interrupt particular pollinator life stages. Further, it is important that pollinator gardens include structural elements such as nesting boxes and water sources to further support the complex life cycle of pollinators.

Nectar and pollen characteristics of 451 taxa planted in the Botanical Garden were determined. Accordingly, 165 taxa (36.58%) are important for beekeeping. 119 contain both nectar and pollen, 25 contain pollen, 13 contain nectar, 4 contain both pollen and insect secretion (IS) or sweet sap (SS), 2 contain pollen, nectar and IS or SS, 1 contain both nectar and SS, 1 contain only IS. It is important for the integrity of the ecosystem that the taxa planted in the botanical garden have honeyed plant characteristics. Attracting pollinators to the area is important for the pollination of the plants in the area, as well as providing nutrients to the pollinators.

Bees are a very diverse group with very different lifestyles and nesting habits. Some bees live in society, while some bees live alone. Solitary bees build their nests on their own and lay their eggs in tunnels such as dead trees or hard soil. In nature, solitary species often nest in hollow plant trunks, holes in dead wood, or other natural crevices. Man-made cavities can also easily provide nesting habitat [10, 26, 27]. Bee hotels provide nesting sites for certain solitary bumblebee and wasps. A bee hotel is designed with hollow reeds, stems or perforated wooden blocks, aiming to simulate a nesting environment. These nesting tunnels can be protected from weather and predators by using a variety of guards [10, 26]. For this goal, a bee hotel was placed in the botanical garden and a poster was prepared to inform visitors about the bee hotel and placed in front of the bee hotel (Fig. 9).

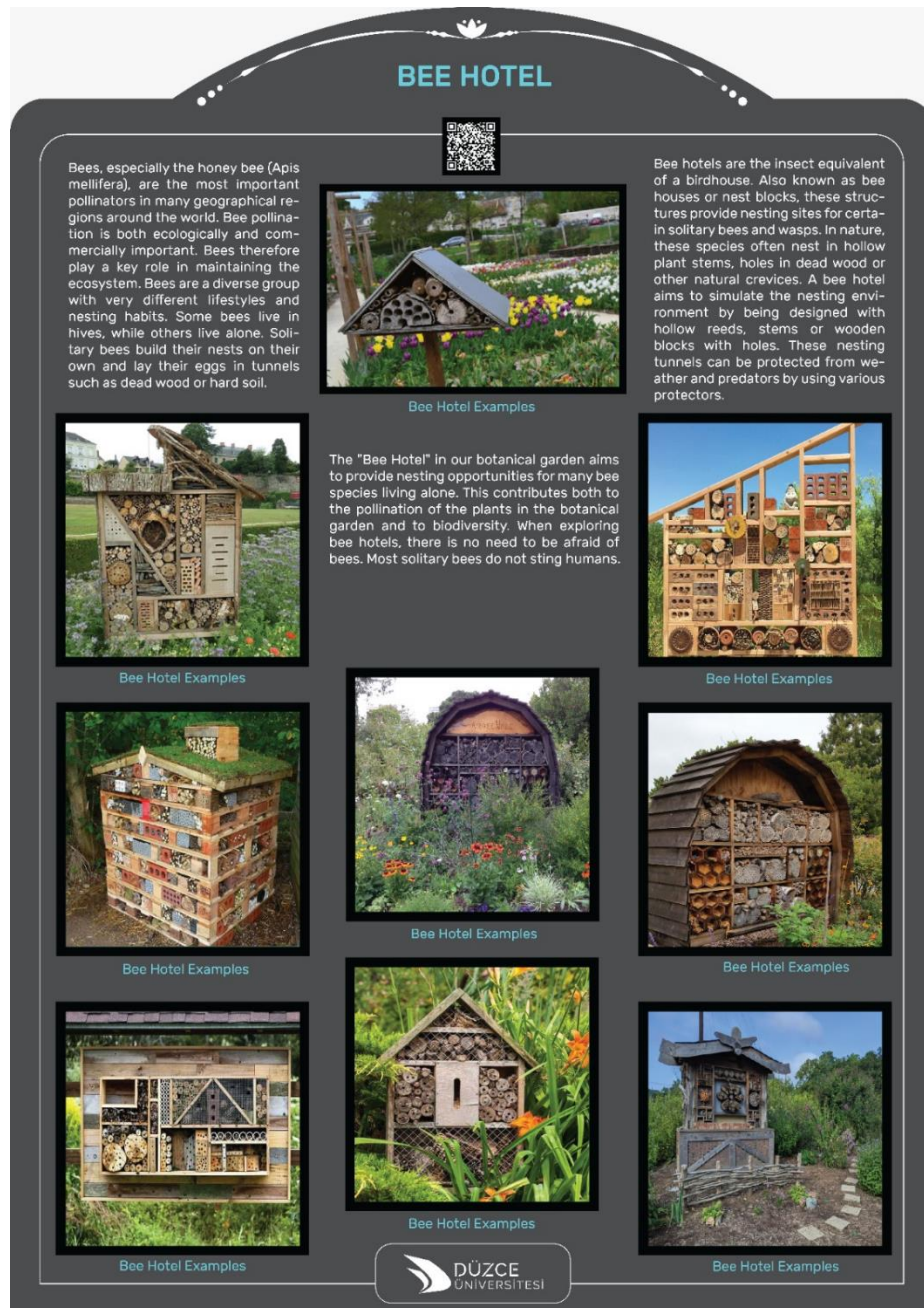


**Figure 8.** Information poster about the bee hotel placed in the Botanical Garden

**ACKNOWLEDGEMENTS:** This study was supported by Düzce University Scientific Research Projects Coordination Office with project number 2021.02.02.1254.

## V. REFERENCES

- [1] M. Rundlöf, G.K. Andersson, R. Bommarco, R.I. Fries, V. Hederström, L. Herbertsson, and H.G. Smith, "Seed coating with a neonicotinoid insecticide negatively affects wild bees". *Nature*, vol. 521, no. 7550, pp. 77-80, 2015.

- [2] N. Kaur, and A.S. Kaleka, “Diversity, importance and decline of pollinating insects in present era”, in *Global Decline of Insects*, H.A.F. El-Shafie, Ed., IntechOpen, 2022, pp. 85-99.
- [3] L.A. Garibaldi, I. Steffan-Dewenter, R. Winfree, M.A. Aizen, R. Bommarco, S.A. Cunningham, and A.M. Klein, “Wild pollinators enhance fruit set of crops regardless of honey bee abundance”, *Science*, vol. 339, no. 6127, pp. 1608-1611, 2013.
- [4] B.M. Freitas, A.J. Pacheco Filho, P.B. Andrade, C.Q. Lemos, E.E.M. Rocha, N.O. Pereira, and K.S. Mendonça, “Forest remnants enhance wild pollinator visits to cashew flowers and mitigate pollination deficit in NE Brazil”, *J. Pollinat. Ecol.*, vol. 12, pp. 22-30, 2014.
- [5] T. Petanidou, A.S. Kallimanis, J. Tzanopoulos, S.P. Sgardelis, and J.D. Pantis, “Long-term observation of a pollination network: fluctuation in species and interactions, relative invariance of network structure and implications for estimates of specialization”, *Ecol. Lett.*, vol. 11, no. 6, pp.564-575, 2008.
- [6] R. Rader, J. Reilly, I. Bartomeus, and R. Winfree, “Native bees buffer the negative impact of climate warming on honey bee pollination of watermelon crops”, *Global Change Biology*, vol.19, no. 10, pp. 3103-3110, 2013.
- [7] A. Kovács-Hostyánszki, A. Espíndola, A.J. Vanbergen, J. Settele, C. Kremen, and L.V. Dicks, “Ecological intensification to mitigate impacts of conventional intensive land use on pollinators and pollination”, *Ecology Letters*, vol. 20, no. 5, pp. 673-689, 2017.
- [8] J. Sadler, A. Bates, J. Hale, and P. James, “Bringing cities alive: the importance of urban green spaces for people and biodiversity”, *Urban Ecology*, pp. 230-260, 2010.
- [9] M.H. Sirohi, J. Jackson, M. Edwards, and J. Ollerton, “Diversity and abundance of solitary and primitively eusocial bees in an urban centre: a case study from Northampton (England)”, *Journal of Insect Conservation*, vol. 19, no. 3, pp. 487-500, 2015.
- [10] H.H. Wang, D. Bhattacharya, E. Evans, and P. Jirik, “Building bee houses”, *Science Scope*, vol.41, no. 3, pp.41-49, 2017.
- [11] I.B. Vilella-Arnizaut, D.V. Roeder, and C.B. Fenster, “Use of botanical gardens as arks for conserving pollinators and plant-pollinator interactions: a case study from the United States Northern Great Plains”, *The Journal of Pollination Ecology*, vol. 31, pp.53-69, 2022.
- [12] How beekeeping can restore degraded land and improve livelihoods– FAO report. (2023). Accessed: August 15, 2023. [Online]. Available: <https://www.fao.org/forestry/news/en/>.
- [13] N.A. Zariman, N.A. Omar, A.N. Huda, “Plant Attractants and Rewards for Pollinators: Their Significance to Successful Crop Pollination”, *International Journal of Life Sciences and Biotechnology*, vol.5, no.2, pp.270-293.
- [14] Melliferous flower. (2023). Accessed: August 15, 2023. [Online]. Available: [http://en.wikipedia.org/wiki/Melliferous\\_flower](http://en.wikipedia.org/wiki/Melliferous_flower).
- [15] M. Bilgen, “Batı Antalya yöresi Florasında Bulunan Tıbbi ve Aromatik Bitkilerin Belirlenmesi ve Arıcılık Açısından Değerlendirilmesi”. TÜBİTAK TOGTAG Proje 2674, 2004: 1-45, 2004.
- [16] N. Grozeva, “Possibilities For Providing Bee Pasture From Nectariferous Plants in Sinite Kamani Natural Park Sliven”, *Trakia J. Sci.*, vol. 9, no. 2, pp. 15-21, 2011.
- [17] N.G. Özkan, N. Aksoy, and A.S. Değermenci, “Hasanlar Barajı (Düzce-Yığılca) ve Çevresinin Ballı Bitkileri”, *Düzce Üniversitesi Orman Fak. Ormancılık Dergisi*, vol. 12, no. 2, pp.44-65, 2016.

- [18] A. Karaca, “Aydın Yöresinde Bal Arılarının (*Apis mellifera* L.) Yararlanabileceği Bitkiler ve Bazı Özellikleri”, *Adnan Menderes Üniv. Ziraat Fak. Derg.*, vol. 5, no. 2, pp. 39-66, 2008.
- [19] C.H. Paschalis, “The Honey bee and the beekeeping Techniques”, Agricultural University of Athens, Greece, 1997.
- [20] P. Sıralı, and M. Deveci, “Balarısı (*Apis mellifera* L.) İçin Önemli Olan Bitkilerin Trakya Bölgesinde İncelenmesi”, *Uludağ Arıcılık Derg.*, vol.2, no. 1, pp.17-26, 2002.
- [21] N. Özhatay, M. Koçyiğit, and M. Bona, “İstanbul'un ballı bitkileri”, İstanbul: BAL-DER, 2012.
- [22] M. Giovanetti, C. Giuliani, S. Boff, G. Fico, and D. Lupi, “A botanic garden as a tool to combine public perception of nature and life-science investigations on native/exotic plants interactions with local pollinators”, *PLoS One*, vol. 15, no. 2, 2020
- [23] S. Reel and N. Seiler. Attracting Pollinators to Your Garden Using Native Plants. (2023) Accessed: September 25, 2023. [Online]. Available: [http://www.nancyseiler.com/wp-content/uploads/2010/09/Pollination\\_FINAL1-Lo-Res.pdf](http://www.nancyseiler.com/wp-content/uploads/2010/09/Pollination_FINAL1-Lo-Res.pdf)
- [24] A. Majewska, and S. Altizer, "Planting gardens to support insect pollinators", *Conserv. Biol.*, vol. 34, no. 1, pp.15–25, 2018.
- [25] C.L. Morales, and A. Traveset, “A meta-analysis of impacts of alien vs. native plants on pollinator visitation and reproductive success of co-flowering native plants”, *Ecol. Lett.*, vol. 12, no. 7, pp.716-728, 2009.
- [26] J. Brokaw, and R. Isaacs. *Building and Managing Bee Hotels For Wild Bees*. Accessed: September 25, 2023. [Online]. Available: <http://icpbees.org/wp-content/uploads/2014/05/Brokaw-and-Isaacs-E-3337-final-PDF-for-printing.pdf>
- [27] E.C. Bauer, L.I. Lynch, D.A. Golick, and T.J. Weissling, *Creating a Solitary Bee Hotel*. Accessed: September 25, 2023. [Online]. Available: <https://entomology.unl.edu/scilit/Creating%20a%20Solitary%20Bee%20Hotel.pdf>



# Düzce University Journal of Science & Technology

Research Article

## Correlation of Destructive and Non-Destructive Tests with Electrical Resistance in Cementless Composites

 Ümit YURT<sup>a</sup>,  Barış KIR<sup>b</sup>,  Yunus BİÇEN<sup>b,\*</sup>

<sup>a</sup>Construction Technology, Düzce University, Türkiye

<sup>b,\*</sup>Faculty of Engineering, Electrical and Electronics Engineering, Düzce University, Türkiye

\* Corresponding author's e-mail address: yunusbicen@duzce.edu.tr

DOI: 10.29130/dubited.1364092

### ABSTRACT

In the construction industry, tests such as compressive strength, density porosity, and water absorption porosity are frequently used to determine material properties. In general, experimental studies are divided into two categories: destructive and non-destructive testing methods. According to the common consensus, destructive testing methods produce more dependable results than non-destructive testing methods. However, it is not possible to reuse the samples in destructive tests, and there are difficulties in taking samples from the building whose construction process has been completed. In addition, the experimental implementation of destructive tests creates time and cost disadvantages. Within the scope of this study, destructive and non-destructive experiments have been carried out on alkali-activated concrete composites, which have attracted interest as sustainable environmentally friendly composite building materials in recent years. Compressive strength, density, porosity, water absorption, etc. traditional test methods have been associated with electrical resistance measurements. Electrical measurements have been taken with the MEGGER equipment, and resistance values have been directly correlated with the other parameters. The positive results indicate that different structures of materials used in the construction industry can be evaluated regardless of sample size or localization.

**Keywords:** Alkali-activated composite; Electrical resistance; Non-destructive test

## Çimentosuz Kompozitlerde Tahribatlı ve Tahribatsız Testlerin Elektriksel Direnç ile İlişkilendirilmesi

### Öz

İnşaat sektöründe, malzeme özelliklerini belirlemek için basınç dayanımı, yoğunluk, su emme ve prozite gibi testler sıklıkla kullanılmaktadır. Genel olarak deneysel çalışmalar tahribatlı ve tahribatsız muayene yöntemleri olarak iki kategoriye ayrılır. Ortak görüşe göre, tahribatlı muayene yöntemleri tahribatsız muayene yöntemlerine göre daha güvenilir sonuçlar üretir. Ancak tahribatlı testlerde numunelerin tekrar kullanılması mümkün olmamakta ve inşaat süreci tamamlanan binadan numune alınmasında zorluklar yaşanmaktadır. Ayrıca tahribatlı testlerin deneysel olarak uygulanması zaman ve maliyet açısından dezavantajlar doğurmaktadır. Bu çalışma kapsamında, son yıllarda sürdürülebilir çevre dostu kompozit yapı malzemeleri olarak ilgi gören alkali aktivasyonlu beton kompozitler üzerinde tahribatlı ve tahribatsız deneyler yapılmıştır. Basınç dayanımı, yoğunluk, prozite, su emme vb. geleneksel test yöntemleri elektriksel direnç ölçümleriyle ilişkilendirilmiştir. MEGGER ekipmanı ile elektriksel ölçümler alınmış ve direnç değerleri diğer parametrelerle doğrudan ilişkilendirilmiştir. Elde edilen olumlu sonuçlar, inşaat sektöründe kullanılan malzemelerin numune boyutu veya lokalizasyondan bağımsız olarak önerilen yöntemle değerlendirilebileceğini göstermektedir.

**Anahtar Kelimeler:** Alkali aktivasyonlu kompozit; Elektrik direnci, Tahribatsız test

# **I. INTRODUCTION**

The harmful effects of global warming are increasing in parallel with the development of industry [1, 2]. Besides, the construction sector is held directly or indirectly responsible for a significant part of global warming [3]. Pozzolans and industrial wastes used as cement substitutes contribute to reducing cement production quantities. However, this practice is not sufficient. The need for alternative solutions for this sector, which is held responsible for 8% of CO<sub>2</sub> emissions, has been increasing gradually. In recent years, studies on the production of building materials from different wastes by using alkali activators have increased [4-12]. Alkali-activated composite products may have different physical and mechanical properties compared to cementitious composites due to the variety of materials entering the mixture [13]. The most commonly used methods for determining mechanical properties include compressive strength, flexural strength, splitting tensile strength, and so on. In addition to mechanical properties, density, water absorption, porosity, etc. physical properties are also among the most basic properties of building materials [14]. Changes in material properties affect mechanical and physical properties as well as electrical properties [15, 16]. Defects such as capillary spaces, microstructural cracks, pore solution etc. in the material can affect the electrical conductivity [17, 18]. Micro cracks and defects may occur during or after the production process in composites that have a heterogeneous structure such as building material [19]. Tests used to classify building materials are often associated with these defects.

A change in any parameter in a matter or system causes changes in different parameters. Therefore from the changes in the physical properties of the matter, evaluations can be made about the different properties. The electrical properties of each of the natural or artificially produced materials also differ according to the other. The electrical characteristics of materials may vary depending on the effects of different stresses to be applied to the material [20-22]. If the material undergoes permanent deterioration due to the applied stress, the change in the electrical characteristic of the material may be permanent. In this case, the change can be associated with the rating of the degradation of the material. However, the material may deteriorate during the process of applying stress and return to its former state when the stress is removed. In this case, the temporary changes in the electrical characteristics of the material allow making sense of the applied stress.

One of these methods is the electrical resistivity measurements of the structures [23, 24]. In this method, the relationships between the mechanical properties of the building material, the porosity or void ratio in the material and/or the additive ratios can be determined [25-27]. Resistivity is not affected by the size and geometry of the sample for a homogeneous structure. However, it is not always possible to provide absolute homogeneity for structures such as mortars, concrete with additives and alkali activated composites. Therefore, testing on a particular sample may not always describe the overall structure. Instead, it may be necessary to test on more samples. However, this time, problems arise in terms of cost increase and sustainability.

In this study, we aimed to measure the resistance of the structure directly instead of the electrical resistivity. For this purpose, we preferred the MEGGER measurement system, which is used to measure very large resistance values. In this way, the resistance values of not only samples but also larger structures can be measured directly.

Thus, the obligation to produce samples suitable for the measurement system is eliminated, and the resistance values taken from the measurement points of the structure of the desired shape and size are directly used. Therefore, more generalized results regarding the structure can be produced. Based on the preferred approach, the relationship between the electrical properties and strength properties of sustainable environmentally friendly alkali-activated composites has been investigated, in this study. Four different alkali-activated composite mixtures containing ground granulated blast furnace slag (GGBFS), zeolite, aggregate, NaOH (sodium hydroxide), and Na<sub>2</sub>SiO<sub>3</sub> (sodium silicate) have been prepared. Prepared fresh alkali-activated composite mixtures have been placed in cube molds (70,7 mm) with the help of vibration. Samples with different mix properties have been subjected to activation temperatures of 90°C and 120°C for 20 hours. Compressive strength, water absorption, porosity, density,

and electrical resistance measurements have been performed on the specimens left to water cure for 28 days after the activation temperature.

## II. THEORETICAL DESCRIPTION AND MEASUREMENT SYSTEM

During the preparation of alkali activated composites, it is desired to have as homogeneous a mixture as possible as shown in Fig. 1(a). In this case, since the resistivity ( $\rho$ ) values in each region are equal to each other, the resistance values ( $R$ ) in the equi-sectioned regions are also equal to each other, theoretically. Therefore, equations (1) and (2) can describe the model in Fig. 1(a). Where  $d$  is the length and  $S$  is the cross-sectional area of the sample, and  $n$  is the number of equi-sections. However, this is hardly possible in practice. In such structures, there are cracks and voids at micro levels, or fractures under stress can also be observed as shown in Fig. 1(b). Or the fabricated building sample may differ from one another in terms of its properties or additive material, as in Fig. 1(c). Therefore, the resistivity values at each small volume location will also be different. This will change the resistances in the equi-sections. Therefore, the total equivalent resistance value of the realistic model  $R_{1 \rightarrow j}$  will differ from the total equivalent resistance value obtained with the theoretically homogeneous sample  $R_{1 \rightarrow n}$ .

$$R_1 = \frac{\rho d}{S} , \quad \text{and} \quad R_1 = \dots = R_{n-1} = R_n \quad (1)$$

$$R_{1 \rightarrow n} = \frac{\rho d}{Sn} \quad (2)$$

For a realistic model;

$$R_1 \neq \dots \neq R_{n-1} \neq R_n , \quad \text{and also} \quad R_{1 \rightarrow j} \neq R_{1 \rightarrow n} \quad (3)$$

$$\text{If, } \frac{d}{S} = \delta \therefore R_{1 \rightarrow j} = 1 / \left( \frac{1}{\rho_1 \delta} + \dots + \frac{1}{\rho_n \delta} \right) \quad (4)$$



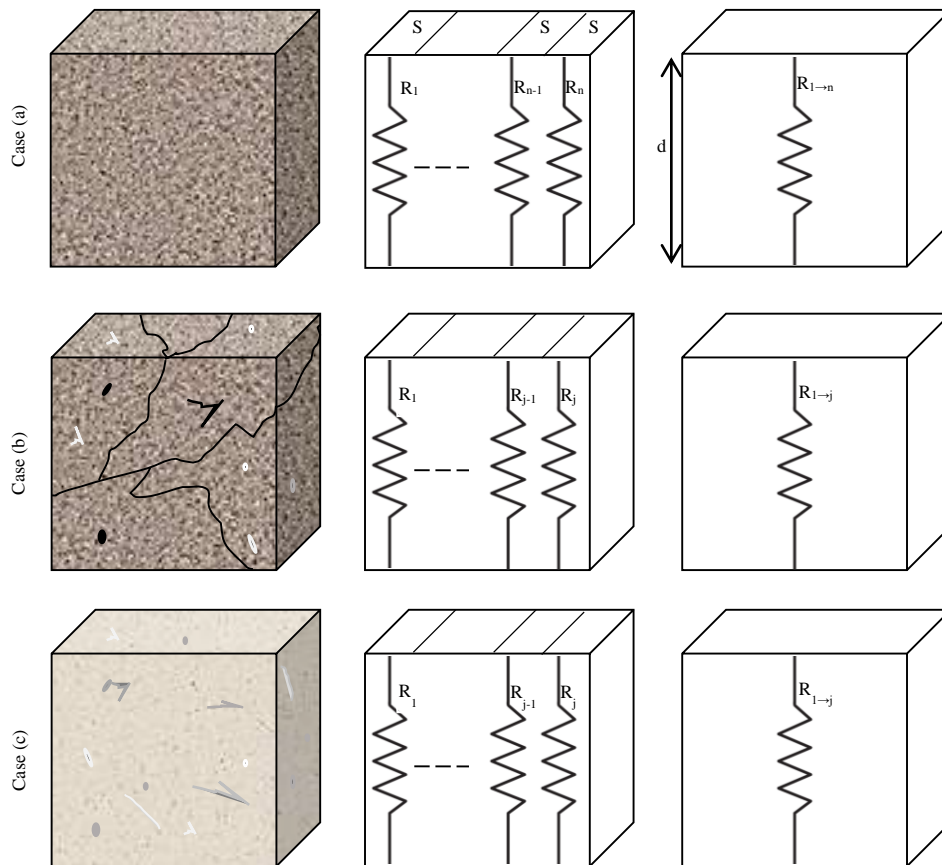


**Figure 1.** Different alkali activated composites, (a) theoretically homogeneous structure; (b) cracked structure; (c) robust but different types of alkali activated composite.

Testing of the proposed approach is possible with MEGGER equipment where high resistances can be measured. It is normally used for testing grounding and/or high electrical insulations in electrical systems. Meggers have a structure that can produce DC voltage between 250V and 5000V. These voltage values are applied to the resistance value to be measured and it is possible to measure up to 5 Tohm by applying the largest value. In Fig. 2, the measuring setup is presented. Prepared alkali-activated composite samples are placed between pertinaxes, one surface of which is covered with copper. Thus, full contact with the sample surface is ensured. The surface area of the pertinaxes ( $0.03\text{m}^2$ ) has been kept wider than the sample in order to take the measuring tip. After connecting the determined connector tips to the MEGGER device, tests have been carried out under 1000V DC voltage. Measurements have been recorded at the end of the 15th second from the moment the voltage has been applied for each sample. The materials required for the mixture have been prepared according to the values determined as a result of the trial mixtures carried out before. NaOH has been first turned into an aqueous solution during the preparation of alkaline-activated concrete mixes. More detailed information about NaOH and  $\text{Na}_2\text{SiO}_3$  can be obtained from previous studies [4, 7-13]. Then, coarse and fine aggregates have been placed in the mixer and mixed until a homogeneous distribution is obtained. Afterward, GGBFS and zeolite have been added to the mixer sequentially, and the mixing process has been continued. Finally, the process has been completed with the addition of alkaline activators. The fresh alkali-activated concrete mixtures obtained have been placed in molds with the help of vibration, and their upper surfaces have been covered for temperature activation and placed in the oven. In order to examine the effect of activation temperature on physical and mechanical properties, the specimens were subjected to 2 different activation temperatures ( $90^\circ\text{C}$  and  $120^\circ\text{C}$  for 20 hours). After the activation process that lasted for 20 hours under constant temperature, it has been taken out of the molds and taken into the standard curing pool. The standard curing process has been applied for 28 days. After the curing period, mechanical, physical, and electrical measurements have been carried out.

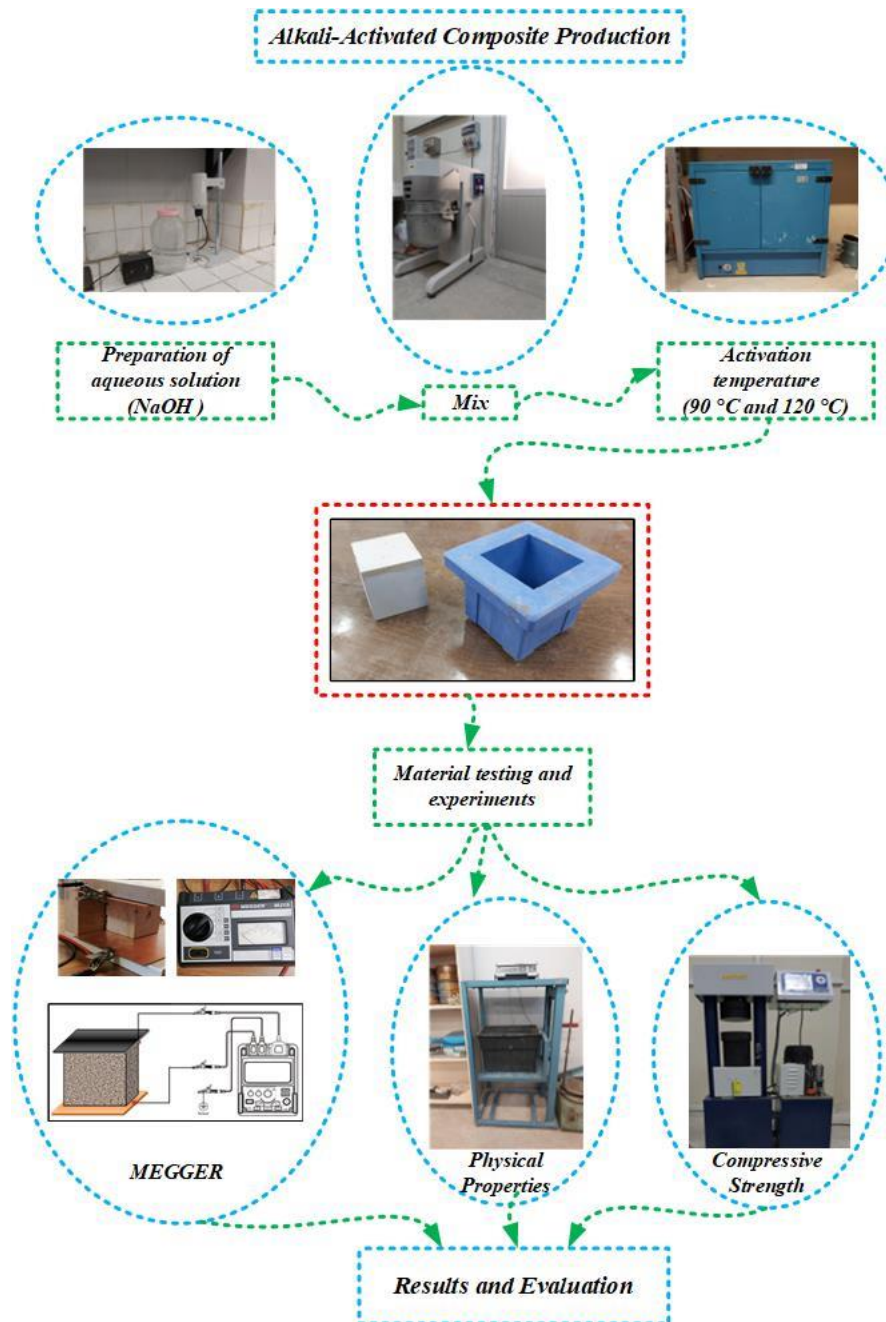


*Figure 2. Experimental study stages*

### **III. MEASUREMENT RESULTS AND EVALUATIONS**

The resistance values obtained by the proposed method have been obtained for different alkali activated composite types. Then, the relationships between these measurement results and conventional test methods have been examined. In alkali-activated concrete mixtures, decreases in electrical resistance values have been observed with the increase of the zeolite ratio, as shown in Fig. 3. The ideal activation temperature is one of the most important parameters for strength development, depending on the

properties of the materials entering the mixture in alkali-activated composite mixtures. It has been reported in previous studies that the activation temperature contributes to the polymerization process [7, 9, 13, 28].

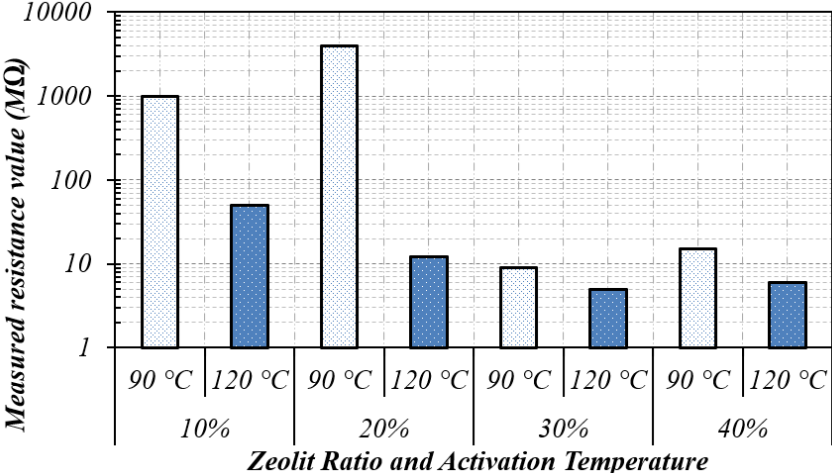


Figure 3. Measured resistance values of different samples

When Figure 4 is examined, it is seen that the maximum compressive strength value is obtained from mixtures with a 10% zeolite replacement rate. It can be concluded that the activation cure temperature is an important parameter for alkali activated composites [7] and the ideal activation temperature for this study is 90 C. The electrical resistance values of the samples with high compressive strength also reach high values. There is a substantial correlation between compressive strength and electrical resistance levels. And this correlation is shown in Fig. 5(a). This positive correlation has been obtained by considering only the data independently of the sample types. It is noticed that the positive association between the compressive strength values and the electrical resistance values is related to the water absorption values of the material and hence the pore distribution (please consider figures 5(a) and (b) together). Fig. 5(b) depicts an inverse relationship between the water absorption value and the measured resistance values.

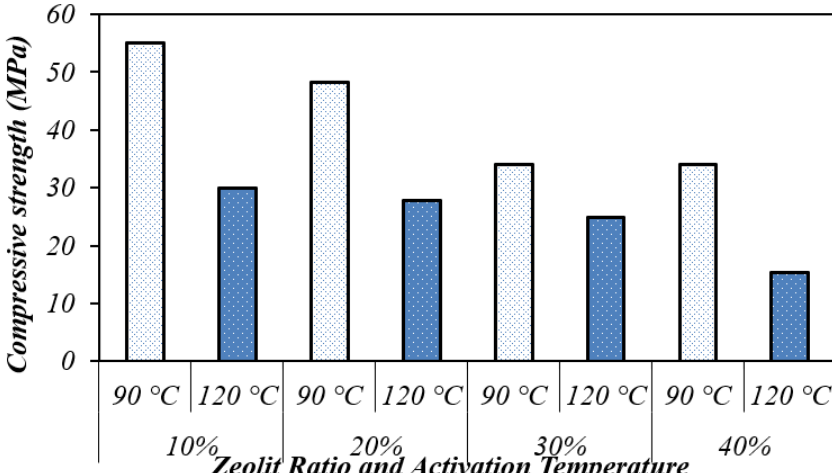
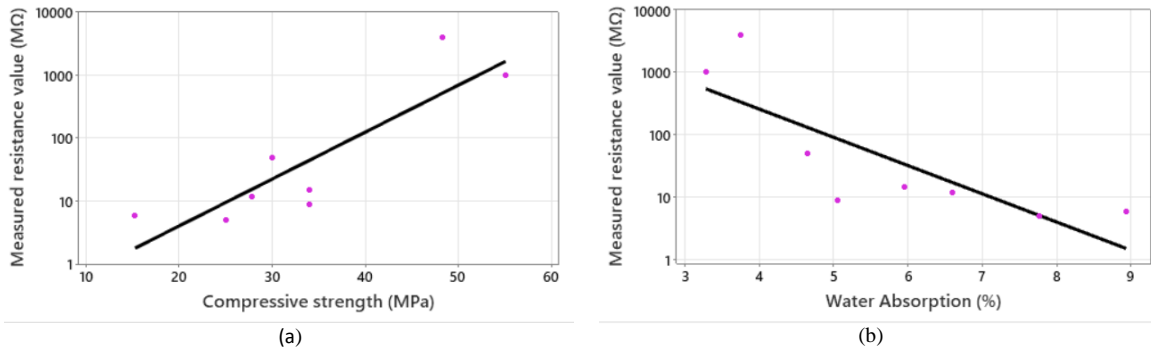
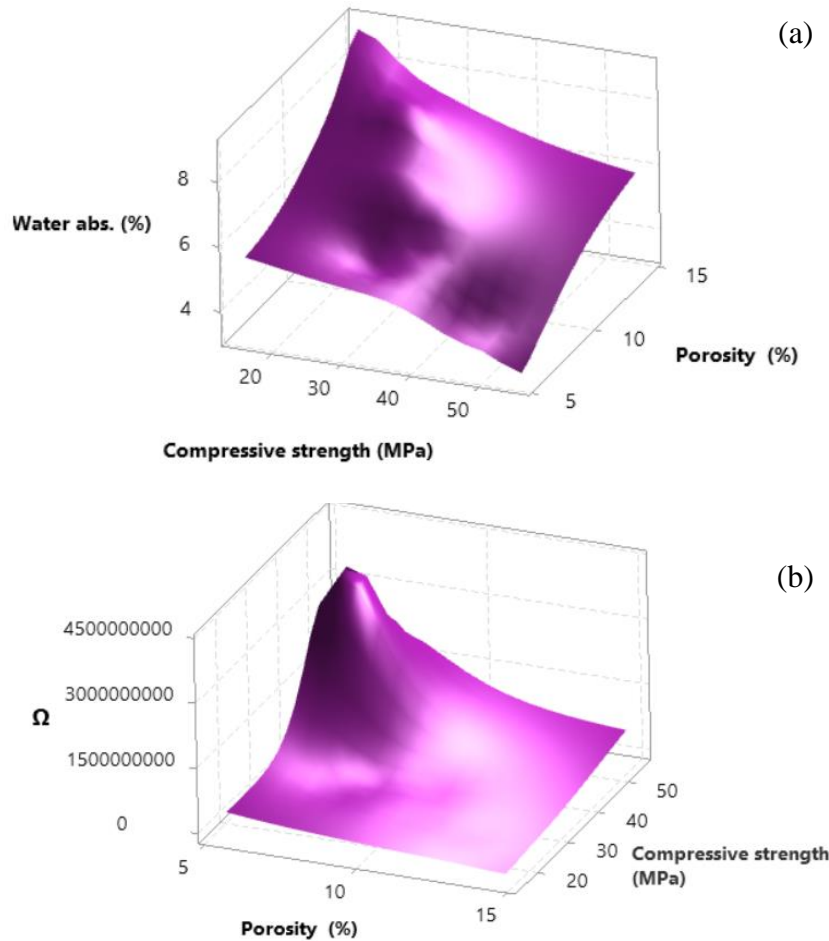


Figure 4. Compressive strength values of different samples



**Figure 5.** Correlations for different samples: (a) between measured resistance value and compressive strength values; (b) measured resistance value and water absorption values

Surface graphs have been drawn to better define the relationship of the measured parameters with the samples, in Fig. 6. Fig. 6(a) proves that the resistance value and the porosity are negatively correlated. This graph clearly shows that as porosity increases, compressive strength falls. In Fig. 6(b), the water absorption rate, compressive strength, and porosity parameters have been compared on the surface plot. As expected, the water absorption rate changes in a positive relationship with porosity. In addition, a very similar situation is observed between the values of water absorption and compressive strength.



**Figure 6.** Surface plots, (a) measured resistance – compressive strength – porosity; (b) water absorption – compressive strength – porosity

## **IV. CONCLUSION**

Within the scope of this study, sustainable environmentally friendly alkali-activated concrete composite mixture designs have been carried out. Additionally, the relationships between electrical resistance values and physical and mechanical properties of cementless composites produced from hybrid wastes were examined. Mechanical and physical tests have been carried out on alkali activation concrete composites prepared with 4 different mixing ratios of zeolite, with GGBFS which is an important waste of the iron and steel industry. Compressive strength, density, porosity, water absorption, and electrical resistance measurements have been correlated with each other. MEGGER device has been used for electrical resistance measurement. The results obtained as a result of the experimental study are summarized below.

\* It has been concluded that there is a strong relationship between the compressive strength test results, which is one of the destructive testing methods, and the electrical resistance values.

\* Moreover, the strength values in alkali-activated concrete have been shown to decline as the zeolite replacement ratio increases.

\* It has been concluded that the proportions and chemical compositions of the materials entering the mixture for cementless composites with alkali activation hybrid binders have a significant effect on the physical and mechanical properties.

\* It has been observed that maximum pressure and electrical resistivity values can be obtained at low porosity values.

\* It has been concluded that the activation temperature has a significant effect on the physical and mechanical properties of alkali-activated composites.

\* It has been inferred that determining the optimum activation temperature is an important parameter for strength development, especially in cement-free composites, due to the difference in the physical and chemical properties of the hybrid materials entering the mixture.

**ACKNOWLEDGEMENTS:** This study was supported within the scope of Düzce University Scientific Research Projects Support Program. Project Number: 2021.21.08.1226.

## **V. REFERENCES**

[1] N. Wunderling et al., "Global warming overshoots increase risks of climate tipping cascades in a network model," *Nature Climate Change*, vol. 13, no. 1, pp. 75-82, 2023.

[2] R. Wu, Z. Tan, and B. Lin, "Does carbon emission trading scheme really improve the CO2 emission efficiency? Evidence from China's iron and steel industry," *Energy*, vol. 277, p. 127743, 2023.

[3] H. Elhegazy et al., "An exploratory study on the impact of the construction industry on climate change," *Journal of Industrial Integration and Management*, online, doi:10.1142/S2424862222500282, pp. 1-23, 2023.

[4] Ü. Yurt and F. Bekar, "Comparative study of hazelnut-shell biomass ash and metakaolin to improve the performance of alkali-activated concrete: A sustainable greener alternative," *Construction and Building Materials*, vol. 320, p. 126230, 2022.

[5] H. R. Gavali, A. Bras, P. Faria, and R. V. Ralegaonkar, "Development of sustainable alkali-activated bricks using industrial wastes," *Construction and Building Materials*, vol. 215, pp. 180-191, 2019.

- [6] G. F. Huseien and K. W. Shah, "Durability and life cycle evaluation of self-compacting concrete containing fly ash as GBFS replacement with alkali activation," *Construction and Building Materials*, vol. 235, p. 117458, 2020.
- [7] G. Dokuzlar, B. Dündar, and Ü. Yurt, "Effect of recycled asphalt waste on mechanical properties of alkali-activated mortars," *Proceedings of the Institution of Mechanical Engineers, Part E: Journal of Process Mechanical Engineering*, Online, doi:10.1177/09544089231191621, 2023.
- [8] Ü. Yurt, "An experimental study on fracture energy of alkali activated slag composites incorporated different fibers," *Journal of Building Engineering*, vol. 32, p. 101519, 2020.
- [9] Ü. Yurt, "High performance cementless composites from alkali activated GGBFS," *Construction and Building Materials*, vol. 264, p. 120222, 2020.
- [10] Ü. Yurt, B. Dündar, and E. Çınar, "Investigation of Sulfuric Acid Effect in Geopolymer Concrete," *Düzce University Journal of Science and Technology*, vol. 8, no. 2, pp. 1548-1561, 2020.
- [11] Ü. Yurt and M. Emiroğlu, "The Effects of Curing Condition on Geopolymers Incorporating Zeolit," *Academic Platform-Journal of Engineering Science*, vol. 8, no. 2, pp. 396-402, 2020.
- [12] Ü. Yurt, "Effect of Curing Temperature on Fracture Properties of Alkali-Activated Fiber Concrete," *Osmaniye Korkut Ata University Journal of The Institute of Science and Technology*, vol. 5, no. 1, pp. 176-188, 2022.
- [13] Ü. Yurt and M. Emiroğlu, "Alkali Aktivasyonlu Kompozitlerde Hibrit Bağlayıcıların Etkileri," *Beton 2023 Hazır Beton Fuarı ve Kongresi*, İstanbul, Türkiye, Nov. 8-10, 2023.
- [14] H. Ulugöl, M. F. Günal, İ. Ö. Yaman, G. Yıldırım, and M. Şahmaran, "Effects of self-healing on the microstructure, transport, and electrical properties of 100% construction- and demolition-waste-based geopolymer composites," *Cement and Concrete Composites*, vol. 121, p. 104081, 2021.
- [15] P. Payakaniti, S. Pinitsoonthorn, P. Thongbai, V. Amornkitbamrung, and P. Chindaprasirt, "Effects of carbon fiber on mechanical and electrical properties of fly ash geopolymer composite," *Materials Today: Proceedings*, vol. 5, no. 6, Part 1, pp. 14017-14025, 2018.
- [16] M. Kupke, K. Schulte, and R. Schüller, "Non-destructive testing of FRP by d.c. and a.c. electrical methods," *Composites Science and Technology*, vol. 61, no. 6, pp. 837-847, 2001.
- [17] C. Shi, "Effect of mixing proportions of concrete on its electrical conductivity and the rapid chloride permeability test (ASTM C1202 or ASSHTO T277) results," *Cement and Concrete Research*, vol. 34, no. 3, pp. 537-545, 2004.
- [18] P. Gao, J. Wei, T. Zhang, J. Hu, and Q. Yu, "Modification of chloride diffusion coefficient of concrete based on the electrical conductivity of pore solution," *Construction and Building Materials*, vol. 145, pp. 361-366, 2017.
- [19] P. Duchene, S. Chaki, A. Ayadi, and P. Krawczak, "A review of non-destructive techniques used for mechanical damage assessment in polymer composites," *Journal of Materials Science*, vol. 53, no. 11, pp. 7915-7938, 2018.
- [20] H. Liu, K. Liu, Z. Lan, and D. Zhang, "Mechanical and Electrical Characteristics of Graphite Tailing Concrete," *Advances in Materials Science and Engineering*, vol. 2018, p. 9297628, 2018.

- [21] X. Quan et al., "Influence of iron ore tailings by-product on the mechanical and electrical properties of carbon fiber reinforced cement-based composites," *Journal of Building Engineering*, vol. 45, p. 103567, 2022.
- [22] Y. Ding, Z. Chen, Z. Han, Y. Zhang, and F. Pacheco-Torgal, "Nano-carbon black and carbon fiber as conductive materials for the diagnosing of the damage of concrete beam," *Construction and Building Materials*, vol. 43, pp. 233-241, 2013.
- [23] L. Li, Q. Zheng, S. Dong, X. Wang, and B. Han, "The reinforcing effects and mechanisms of multi-layer graphenes on mechanical properties of reactive powder concrete," *Construction and Building Materials*, vol. 251, p. 118995, 2020.
- [24] A. O. Monteiro, P. B. Cachim, and P. M. F. J. Costa, "Electrical Properties of Cement-based Composites Containing Carbon Black Particles," *Materials Today: Proceedings*, vol. 2, no. 1, pp. 193-199, 2015.
- [25] J. H. Kim, H.-K. Yoon, and J.-S. Lee, "Void ratio estimation of soft soils using electrical resistivity cone probe," *Journal of Geotechnical and Geoenvironmental Engineering*, vol. 137, no. 1, pp. 86-93, 2011.
- [26] R. Ranade, J. Zhang, J. P. Lynch, and V. C. Li, "Influence of micro-cracking on the composite resistivity of Engineered Cementitious Composites," *Cement and Concrete Research*, vol. 58, pp. 1-12, 2014.
- [27] H. K. Kim, I. W. Nam, and H. K. Lee, "Enhanced effect of carbon nanotube on mechanical and electrical properties of cement composites by incorporation of silica fume," *Composite Structures*, vol. 107, pp. 60-69, 2014.
- [28] S. Çelikten, M. Sarıdemir, and İ. Ö. Deneme, "Mechanical and microstructural properties of alkali-activated slag and slag + fly ash mortars exposed to high temperature," *Construction and Building Materials*, vol. 217, pp. 50-61, 2019.



# Düzce University Journal of Science & Technology

Research Article

## The Analysis of Next-Generation Refrigerants in Terms of Energy, Exergy, and LCCP Perspective

Merve ÖZER ŞİMŞEK<sup>a</sup>, Mehmet Onur KARAAĞAÇ<sup>b,c,\*</sup>, Alper ERGÜN<sup>d</sup>, Mustafa AKTAŞ<sup>e</sup>

<sup>a</sup> Department of Energy Systems Engineering, Faculty of Technology, Karabük University, Karabük, TÜRKİYE

<sup>b</sup> Department of Energy Systems Engineering, Faculty of Engineering and Architecture, Sinop University, Sinop, TÜRKİYE

<sup>c</sup> Energy Research and Application Center, Sinop University, Sinop, TÜRKİYE

<sup>d</sup> Department of Mechanical Engineering, Faculty of Engineering Karabük University, Karabük, TÜRKİYE

<sup>e</sup> Department of Energy Systems Engineering, Faculty of Technology, Gazi University, Ankara, TÜRKİYE

\* Corresponding author's e-mail address: [okaraagac@sinop.edu.tr](mailto:okaraagac@sinop.edu.tr)

DOI: 10.29130/dubited.1388565

### ABSTRACT

In this study, commonly used hydrofluorocarbon (HFC)-based refrigerants R404A and R410A, as well as hydrofluoroolefin (HFO)-based environmentally friendly next-generation refrigerant R1234yf with a low global warming potential (GWP), were analyzed in terms of energy, exergy, and life cycle climate performance (LCCP) in refrigeration and air conditioning systems. All three refrigerants were examined at four different evaporation temperatures (-30°C, -15°C, -5°C, 0°C) with a constant condenser temperature of 50°C using a simulation program. For different evaporation temperatures, the performance of the refrigerants was evaluated using the first and second laws of thermodynamics, and performance coefficients, exergy efficiency, and exergy destruction were calculated. Additionally, the amount of kgCO<sub>2</sub>e equivalent was calculated using the LCCP method. In the study, it was found that the compressor energy consumption of R410A and R1234yf refrigerants was similar and approximately 7% lower than that of the R404A refrigerant. The highest coefficient of performance (COP) value was determined for R1234yf. It was observed that R1234yf refrigerant had the highest exergy efficiency starting from -15°C. The kgCO<sub>2</sub>e equivalent emission values calculated using the LCCP method revealed that R404A had the highest CO<sub>2</sub> emissions, while R1234yf had the lowest. Furthermore, based on the simulation study and theoretical calculations, it was determined that R410A and R1234yf refrigerants could be considered as alternative choices to R404A refrigerants in systems where two refrigerants are used.

**Keywords:** Energy, Exergy, GWP, LCCP, Refrigerant

## Yeni Nesil Soğutucu Akışkanların Enerji, Ekserji ve LCCP Perspektifinde Analizi

### Öz

Bu çalışmada, soğutma ve iklimlendirme sistemlerinde yaygın olarak kullanılan hidroflorokarbon (HFC) tabanlı R404A, R410A akışkanları ile hidrofluoroolefin (HFO) tabanlı düşük küresel ısınma potansiyel oranına sahip ve ozon tabasına dost yeni nesil soğutucu akışkan olan R1234yf enerji, ekserji ve yaşam döngüsü iklim performansı (LCCP) açısından incelenmiştir. Her üç soğutucu akışkan dört farklı buharlaşma sıcaklığı (-30°C, -15°C, -5°C, 0°C) ile sabit kondenser sıcaklığında (50°C) simülasyon programı kullanılarak gerçekleştirilmiştir. Farklı buharlaşma sıcaklıkları için, soğutucu akışkanların performansları termodinamiğin birinci ve ikinci kanunu kullanılarak değerlendirilmiş ve sistemlere ait performans katsayıları, ekserji verimi, ekserji yıkımı hesaplanmış, LCCP yöntemiyle de kgCO<sub>2</sub>eşd. miktarı hesaplanmıştır. Çalışmanın sonunda R410A ve R1234yf soğutucu akışkanlarının kompresör enerji tüketimlerinin birbirine yakın ve R404A soğutucu akışkanına göre yaklaşık %7 daha düşük olduğu tespit edilirken en yüksek COP değeri R1234yf olarak belirlenmiştir. R1234yf soğutucu

<sup>1</sup>11. Uluslararası Meslek Yüksekokulları Sempozyumu'nda (UMYOS) sunulmuştur.

Received: 09/11/2023, Revised: 25/11/2023, Accepted: 09/12/2023



akışkanın  $-15^{\circ}\text{C}$ 'den itibaren en yüksek ekserji verimine sahip olduğu görülmüştür. LCCP yöntemi ile hesaplanan  $\text{kgCO}_2\text{eşd.}$  emisyon değerlerinde  $\text{CO}_2$  emisyonu yüksek olan soğutucu akışkanın R404A, en düşüğün ise R1234yf olduğu tespit edilmiştir. Ayrıca yapılan simülasyon çalışması ve teorik hesaplamalar sonucunda ele alınan soğutucu akışkanlardan R404A soğutucu akışkanı yerine R410A ve R1234yf soğutucu akışkanlarının kullanılmasında iki soğutucu akışkanın kullanıldığı sistemlerde alternatif olarak kullanılabilir olduğu tespit edilmiştir.

*Anahtar Kelimeler: Enerji, Ekserji, GWP, LCCP, Soğutucu Akışkan*

## **I. INTRODUCTION**

Reducing greenhouse gas emissions from energy consumption is a key objective in combating climate change and promoting environmental sustainability. One effective approach is using renewable energy sources and high-efficiency technologies instead of conventional energy sources. However, more than these measures are required. In this context, the energy consumption and environmental impact of refrigeration and air conditioning systems operating on vapor compression refrigeration cycles have emerged as significant concerns. Conventional refrigerants, such as chlorofluorocarbons (CFCs) and hydrofluorocarbons (HFCs), have been recognized for their adverse effects on the environment because of their global warming potential and, ozone-depleting potential (ODP). To mitigate the adverse environmental impacts of refrigerants, various laws, and regulations, including the Montreal Protocol, the Kyoto Protocol, and the Paris Agreement, have been enacted. Therefore, alternative, or next-generation refrigerants for vapor compression systems have become a critical issue. With technological advances, a wide array of cooling systems has been developed to enhance climate control and cooling solutions by incorporating eco-friendly next-generation refrigerants. These include hydrofluoroolefins (HFOs) and hydrocarbons (HCs), which help reduce the negative environmental impacts, fostering more sustainable and environmentally friendly cooling technologies.

Key criteria for next-generation refrigerants include a low ozone depletion potential, low global warming potential (GWP), high efficiency, and safety in usage [1]. To minimize energy consumption and greenhouse gas emissions, there is a need for environmentally friendly refrigerants with low GWP and zero ODP.

Numerous studies have been conducted on production and performance assessment of next-generation and alternative refrigerants. When reviewing these studies, one conducted by Berk stands out. In Berk's study, a 2.05 kW cooling capacity air conditioner operating with R22 refrigerant was compared to using R422A and R424A refrigerants. Experimental research focused on energy parameters, particularly cooling capacity, and coefficient of performance (COP). The experiments were carried out using an outdoor duct, an insulated room, a condenser, and an indoor split air conditioning unit that maintained a constant outdoor temperature. The study concluded that using R422A and R424A refrigerants in place of R22 resulted in lower COP values compared to the system using R22. However, it was noted that the temperature conditions simulated in this study, representing various climate conditions, could be beneficial for air conditioning. Therefore, the study recommended using R422A or R424A instead of R22 in hot climate regions. [2]

Kılıç and Arabacı conducted an energy analysis on the use of LPG (R1270 propylene) as a refrigerant in a vapor compression refrigeration system. They employed the Coolpack program to perform calculations and investigate the effects of LPG (R1270-Propylene) on the system's performance under various operating conditions. Findings revealed that an increase in the evaporator temperature enhanced the COP. Conversely, when the condenser temperature increased, the COP value decreased. It achieved the highest COP value under operating conditions with a  $25^{\circ}\text{C}$  condenser and a  $-1^{\circ}\text{C}$  evaporator temperature. This study highlights the impact of temperature variations on the system's performance. The potential advantages of using R1270 propylene as a refrigerant in vapor compression refrigeration systems are shown [3].

In another study, Yıldız and Yıldırım conducted a theoretical analysis was carried out to examine the performance of refrigerants R134A and R513A. It also evaluated the environmental impact of the used refrigerants through a Life Cycle Climate Performance (LCCP) analysis. The energy performance of refrigerants was assessed at different evaporator and condenser temperatures. In the refrigeration system, R134A and R513A refrigerants performed approximately equally. Furthermore, it was noted that R513A had a lower Direct Emission (DE) value compared to R134A. Since R513A does not possess flammable properties, it can be used in systems designed for R134A without needing any modifications [4].

Choi et al., a novel method was developed to evaluate the environmental impacts of household refrigerators in terms of LCCP. This study provided an energy consumption model for this study refrigerator covering three typical single evaporator refrigerators. The authors used experimental data from series, bypass, and parallel circuit refrigerators to calculate energy consumption in dual evaporator refrigerators. The study underlined that in terms of LCCP, the performance of the system and equipment production emissions were influential factors in the lifetime CO<sub>2</sub> emissions. Several findings were discussed, including the approximate 14% reduction in CO<sub>2</sub> emissions when a dual evaporator cycle was used instead of a single evaporator in the refrigeration cycle in the results. Additionally, they noted that using aluminum instead of steel for condenser materials could result in approximately a 2.5% reduction in CO<sub>2</sub> emissions, applying vacuum insulation panels on both sides of the refrigerator for insulation could lead to about a 7% reduction in CO<sub>2</sub> emissions, and using renewable energy sources for energy consumption could potentially reduce emissions by approximately 20%. These findings underscore the significance of design choices and technologies in mitigating the environmental impact of household refrigerators [5].

Wan et al., were investigated 11 different cities and five different refrigerants in conjunction with various impact parameters using a 10.5 kW air conditioner. They evaluated these parameters through Life Cycle Climate Performance (LCCP) analysis and compared the results. The study explored the potential of using low GWP refrigerants, such as R-290, R-32, R-452B, and R-466A, as alternatives to R410A. Experimental findings concluded that emission factors were important for countries with high annual energy consumption. R-290, R-32, R-452B, and R-466A were determined as excellent alternative refrigerants to R-410A for countries with low emission factors. It was also noted that R-32, R-452B, and R-466A for LCCP results were similar, while R-410A had the highest LCCP value. The study estimated that LCCP values could be reduced by up to 60% by replacing R-410A with R-290. These findings highlighted the importance of choosing environmentally friendly refrigerants and the important role can play in reducing carbon emissions [6].

In another study, Choi et al. carried out on LCCP for cooling and heating systems in five different cities in South Korea. The study investigated using refrigerant systems for cooling, gas boilers for heating, and heat pumps for space heating. It has been found that using refrigerant systems for cooling, a gas boiler for heating, and a heat pump for space heating, can reduce CO<sub>2</sub> emissions by approximately 11-17%. Additionally, the use of refrigerants with low global energy potential was also observed, along with various cycle parameters and weather conditions. The study noted that low-GWP refrigerants would reduce direct emissions by reducing the charge amount compared to R410A. Besides, adding a flash tank to the vapor cycle using R410A has been shown to increase energy efficiency and reduce CO<sub>2</sub> emissions by 7-10% [7].

Ergün et al. investigated R-417A and R-438A refrigerants as alternatives to R-22 refrigerant, which is widely used in cooling systems. Additionally, the performance of these refrigerants was compared by evaluating the energy, exergy, and COP values of the system for different evaporation temperatures. The results indicated that among the three refrigerants evaluated, R-438A had higher COP values than R-417A and R-22. Therefore, R-438A is the best alternative to R-22 refrigerant in terms of performance [8].

Özgür analyzed the exergy efficiency and performance of R-1234yf and R-1234ze refrigerants, which are alternatives to R134a refrigerant in the refrigerant cycle. The efficiency and exergy performance of R-134a, R-1234yf, and R-1234ze refrigerants were compared in the same cycle and operating range.

The results showed that the cycle efficiency and exergy performance values of R-134a and R-1234ze refrigerants were the same. However, when R-1234yf refrigerant was used, higher values were obtained compared to the other two refrigerants. The study also reported that R-1234yf more efficient and effective alternative to R-134a in cooling systems [9].

Additionally, Leck investigated the design of cooling systems and heat pumps for residential and light commercial vehicles and medium-temperature cooling applications in the simulation program. R22, R407C, R32, HFO-1234yf, DR-11, DR-4, DR-3, DR-5, and DR-9 were tested, and an energy and LCCP assessment was conducted. The study found that HFO-1234yf had a lower LCCP than R410A and R404A due to its low GWP. However, DR-5 provided the best energy and LCCP performance among the tested refrigerants. [10].

Various protocols indicated that CFC (Chlorofluorocarbon) and HCFC (Hydrochlorofluorocarbon) refrigerants will be restricted in the future, and alternatives to these refrigerants must be developed. In this regard, a study was conducted to evaluate HFC (hydrofluorocarbon)-based R404A and R410A refrigerants, as well as HFO (hydrofluoroolefin)-based R1234yf refrigerant, for different evaporative temperatures in cooling systems. For this purpose, calculations of kgCO<sub>2</sub> equivalent were conducted by utilizing the first and second laws of thermodynamics, performance coefficients, exergy efficiency, and exergy destruction, along with the LCCP method, and the results were compared.

## II. MATERIAL METHOD

Due to changing conditions since 1830, including environmental impacts and legal obligations, many refrigerants have been developed and used in systems depending on the desired characteristics [11]. When examining first-generation refrigerants, any available refrigerant was used for cooling. In second-generation refrigerants, characteristics like safety and durability became prominent. Third-generation refrigerants focused on protecting the ozone layer, leading to the use of refrigerants that do not harm the ozone layer. Due to increasing concerns about global warming, fourth-generation refrigerants currently in use are required to have conditions such as an ODP of 0, low GWP, high efficiency, and disappears into the atmosphere quickly [13].

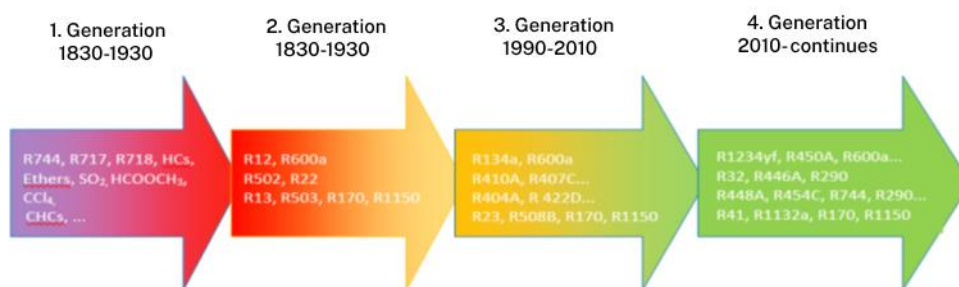


*Figure 1. Development of Refrigerants Over the Historical Period [12]*

The chemical composition, mass quantities, Ozone Depletion Potential, and Global Warming Potential values of the refrigerants used are provided in Table 1.

**Table 1.** Physical and Thermodynamic Properties of Refrigerants Classified as HFC and HFO [14]

	<b>R404A</b>	<b>R410A</b>	<b>R1234yf</b>
Chemical Composition	CF <sub>3</sub> CHF <sub>3</sub> , CF <sub>3</sub> CH <sub>3</sub> , CF <sub>2</sub> CH <sub>2</sub> F (52% R-143a / 44% R-125 / 4% R-134a)	CH <sub>2</sub> F <sub>2</sub> , CF <sub>3</sub> CHF <sub>2</sub> (50% R-125 / 50% R-32)	CF <sub>3</sub> CF=CH <sub>2</sub>
Molecular Weight (g/mol)	97.6	72.4	114.04
Critical Temperature (°C)	72.05	71.36	95
Critical Pressure (MPa)	37.29	49.02	3.382
Standard Boiling Point (°C)	-51.2	-60.6	-29
Safety Class	A1	A1	A2L
ODP	0	0	0
GWP	3922	2088	4

In this study, refrigerants with high Global Warming Potential, such as R404A and R410A, as well as the so-called new generation refrigerant with low GWP, R1234yf, were used with the design parameters specified in Table 2. The Genetron Properties software was employed, and a simple refrigeration cycle was selected within the program to analyze this system's energy, exergy, and LCCP. The system's coefficient of cooling performance and exergy efficiency were calculated under the same operating conditions using different refrigerants. Figure 2 provides a schematic representation of the system, and the exergy losses of the system components were calculated.

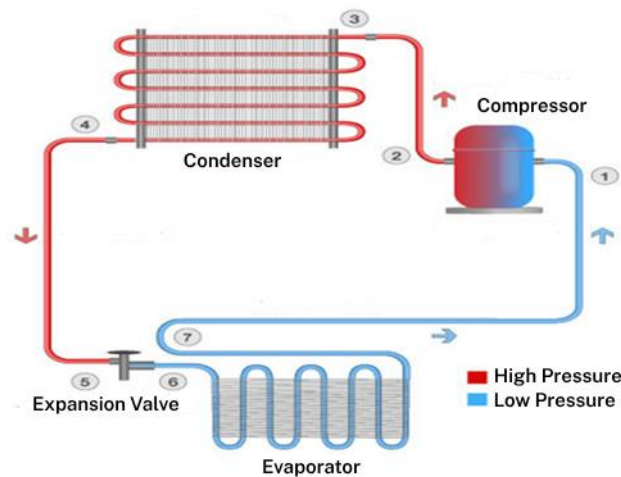


**Figure 2.** Schematic view of the refrigeration cycle

The simulation program selected a 2 kW refrigeration system. The electrical and mechanical efficiency of the compressors in the system was assumed to be 98% and 88%, respectively. It was assumed that the system operates in an open channel flow and that there is no pressure drop in the pipes used. The condenser temperature in the system was kept constant at 50°C, and the evaporator temperature was varied at -30, -15, -5, and 0°C according to the Eurovent standard for separate refrigerant analysis [8].

### **III. ANALYSIS**

#### **A. Thermodynamic Analysis**

The energy equations applied to the system components, considering the cycle points shown in Figure 2, for the first-law analysis of the cooling system are provided below.

Condenser heat load:

$$\dot{Q}_{kond} = \dot{m} \cdot (h_3 - h_4) \quad (1)$$

Evaporator heat load:

$$\dot{Q}_{evap} = \dot{m} \cdot (h_7 - h_6) \quad (2)$$

Power of compressor:

$$\dot{W}_{komp} = \dot{m} \cdot (h_2 - h_1) \quad (3)$$

Electrical power consumed by the compressor:

$$\dot{W}_{komp,el} = \frac{\dot{W}_{komp}}{\eta_{el} \cdot \eta_{mek}} \quad (4)$$

Coefficient of performance of the refrigeration system:

$$COP_C = \frac{\dot{Q}_{evap}}{\dot{W}_{komp,el}} \quad (5)$$

Heating performance coefficient of the refrigeration system:

$$COP_H = \frac{\dot{Q}_{kond}}{\dot{W}_{komp,el}} \quad (6)$$

Exergy is defined as the potential work of a system concerning its surroundings. When the system is balanced with its surroundings, useful work is obtained. The exergy of a system in equilibrium with its surroundings is zero. Exergy transfer between systems occurs through mass, energy, entropy, and power. When a system cannot perform work thermodynamically, the state of the environment is referred to as a "steady state" [15,16]. The steady state of a system implies that the system is in thermodynamic equilibrium with its surroundings. A steady system has the temperature and pressure of its surroundings. It has zero kinetic and potential energy relative to its surroundings and does not react to them. Additionally, no imbalanced magnetic, electrical, or surface tension effects exist between the system and its surroundings. The steady state's characteristics are denoted by zero subscripts, such as,  $P_0$ ,  $T_0$ ,  $h_0$ ,  $u_0$ ,  $s_0$ . Unless otherwise specified, the steady state temperature and pressure are assumed to be  $T_0 = 25 \text{ °C}$  and  $P_0 = 1 \text{ atm}$  (101.325 kPa) [15].

In the case where kinetic and potential energy are neglected for a flowing system, the specific exergy per unit mass is calculated as follows:

$$\psi = h - h_0 - T_0(s - s_0) \quad (7)$$

The equation, when multiplied by the mass flow rate of the refrigerant, is as follows:

$$\dot{E}x = \dot{m}[(h - h_0) - T_0(s - s_0)] \quad (8)$$

The exergy balance and exergy loss of the components in the cooling system can be calculated as follows. The exergy balance equation for the condenser is as follows:

$$\dot{E}x_{yik.kond.} = \dot{E}x_3 - \dot{E}x_4 - Q_{kond} \left(1 - \frac{T_0}{T_{kond}}\right) \quad (9)$$

The exergy balance equation for the evaporator is as follows:

$$\dot{E}x_{y1k.evap.} = \dot{E}x_7 - \dot{E}x_6 - Q_{evap}\left(1 - \frac{T_0}{T_{evap}}\right) \quad (10)$$

The exergy balance equation for the compressor is as follows:

$$\dot{E}x_{y1k.komp.} = \dot{E}x_2 - \dot{E}x_1 - \dot{W}_{komp,el} \quad (11)$$

Expansion valve's exergy balance equation:

$$\dot{E}x_{y1k.GV.} = \dot{E}x_5 - \dot{E}x_6 \quad (12)$$

The second-law exergy efficiency of the refrigeration system is expressed by the following equation:

$$\eta_{Ex} = \frac{\dot{E}x_3 - \dot{E}x_4}{\dot{W}_{komp,el}} \quad (13)$$

The equation for the total exergy destruction in the system can be expressed as follows:

$$\dot{E}x_{y1k.Toplam} = \dot{E}x_{y1k.kond.} + \dot{E}x_{y1k.komp.} + \dot{E}x_{y1k.evap.} + \dot{E}x_{y1k.GV.} \quad (14)$$

### B. LCCP Analysis

LCCP is a valuation method used to assess the impact of HVAC (Heating, Ventilation, and Air Conditioning) systems on global warming over their entire lifecycle. It considers both direct and indirect emissions incurred throughout the system's life, from production to use, maintenance, and final disposal. Direct emissions include all effects of the refrigerant released into the atmosphere during the system's lifespan, encompassing annual leaks and losses that occur when the device is disposed of. Indirect emissions, on the other hand, cover emissions originating from production processes, energy consumption, and facility disposal [16]. LCCP is divided into two main groups: direct emissions and indirect emissions. Figure 3 illustrates the LCCP categories. Each category within the given main groups is calculated separately, and the results are expressed in kgCO<sub>2</sub> equivalent.

$$LCCP = DE(CO_{2,Direct}) + EE (CO_{2,Indirect}) \quad (15)$$

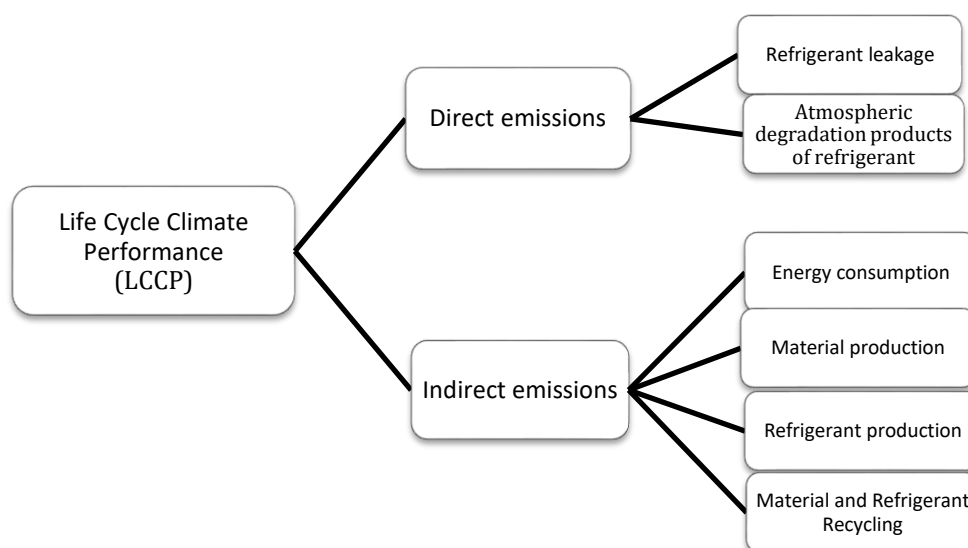


Figure 3. Life Cycle Climate Performance (LCCP) Categories

Direct emissions arise from the use of vapor compression systems. They result from the effects of the refrigerant released into the atmosphere during the system's operational life (annual refrigerant leakage due to leaks, refrigerant losses at the end of the system's life, and reaction products from a refrigerant breakdown in the atmosphere). Direct emissions from vapor compression systems ( $CO_{2,Direct}$ ) can be calculated using the following equation [16]:

$$CO_{2,Direct} = C * (L * ALR + EOL) * (GWP + GWP_{adp}) \quad (16)$$

Where C represents the refrigerant charge used (kg), L is the operating lifetime of the system (years), ALR is the annual refrigerant leakage rate of the refrigerant used (%), and EOL is the refrigerant leakage rate at the end of the device's lifetime (%). GWP denotes the global warming potential of the refrigerant ( $kgCO_2eq/kg$ ), and  $GWP_{adp}$  stands for the global warming potential arising from the breakdown of the refrigerant in the atmosphere ( $kgCO_2eq/kg$ ). Indirect emissions encompass all emissions from the production to disposal of a unit and this includes all emissions during manufacturing, usage, and recycling processes. Indirect emissions are calculated as per Equation 17.

$$CO_{2,Indirect} = L * AEC * EM + \Sigma(m MM) + \Sigma(m_r RM) + C * (1 + L * ALR) * RFM + C * (1 - EOL) \quad (17)$$

Where AEC represents the annual energy consumption of the system (kWh/year), EM denotes the emission factor for electricity production ( $kgCO_2eq/kWh$ ), m signifies the mass of the cooling unit used (kg), MM is the material manufacturing emissions ( $kgCO_2eq/kg$ ),  $m_r$  stands for the mass of recycled material (kg), RM represents the emissions from recycled material ( $kgCO_2eq/kg$ ), and RFM signifies the emissions from refrigerant manufacturing.

In this study, R404A, R410A, and R1234yf were used for each refrigerant, and experimental data were obtained by inputting the following assumptions into the simulation program. Energy, exergy, and LCCP analyses were conducted using the obtained data. The assumptions taken are provided in Table 3.

**Table 3. Assumptions Made for Energy, Exergy, and LCCP Analyses**

Description	Value
Cooling capacity	2 kW
System service life (L)	15 Years
Annual refrigerant leakage rate (ALR)	2.5%
Refrigerant leakage rate at the end of device life (EOL)	15%
Heat pump unit mass (m)	100 kg
Condenser temperature	50°C
Evaporator temperature	-30, -15, -5, 0°C
Compressor electrical efficiency	98%
Compressor mechanical efficiency	88%
Superheating	5°C
Subcooling	5°C

## IV. RESULTS

Analyses were performed for R404A, R410A, and R1234yf refrigerants in a vapor compression refrigeration cycle under the same operating conditions. Genetron Properties software was used to calculate the thermodynamic properties of the refrigerants. The analysis results, including energy, exergy, and Life Cycle Climate Performance (LCCP) parameters, were obtained. These results were evaluated and presented in tables and graphs.

The change in compressor power when the evaporation temperatures of R404A, R410A, and R1234yf refrigerants were varied between  $-30\text{ }^{\circ}\text{C}$  and  $0\text{ }^{\circ}\text{C}$  is shown in Figure 4. As can be seen from the figure, in this range of evaporation temperatures, R404A refrigerant has the highest compressor power consumption. At  $-30\text{ }^{\circ}\text{C}$  evaporation temperature, the refrigerant compressor energy consumptions are as follows: 1.328 kW for R404A, 1.245 kW for R1234yf, and 1.199 kW for R410A. Compared to R1234yf, R404A consumes 6.24% more power, and compared to R410A, it consumes 9.71% more power. For R404A, at  $-30\text{ }^{\circ}\text{C}$ , it consumes 1.328 kW, and at  $0\text{ }^{\circ}\text{C}$ , it consumes 0.596 kW, resulting in a difference of 0.732 kW. R410A consumes 1.199 kW at  $-30\text{ }^{\circ}\text{C}$  and 0.574 kW at  $0\text{ }^{\circ}\text{C}$ , with a difference of 0.625 kW. R1234yf consumes 1.245 kW at  $-30\text{ }^{\circ}\text{C}$  and 0.555 kW at  $0\text{ }^{\circ}\text{C}$ , resulting in a difference of 0.69 kW. As the evaporation temperature increases, the power consumption of all refrigerants decreases.

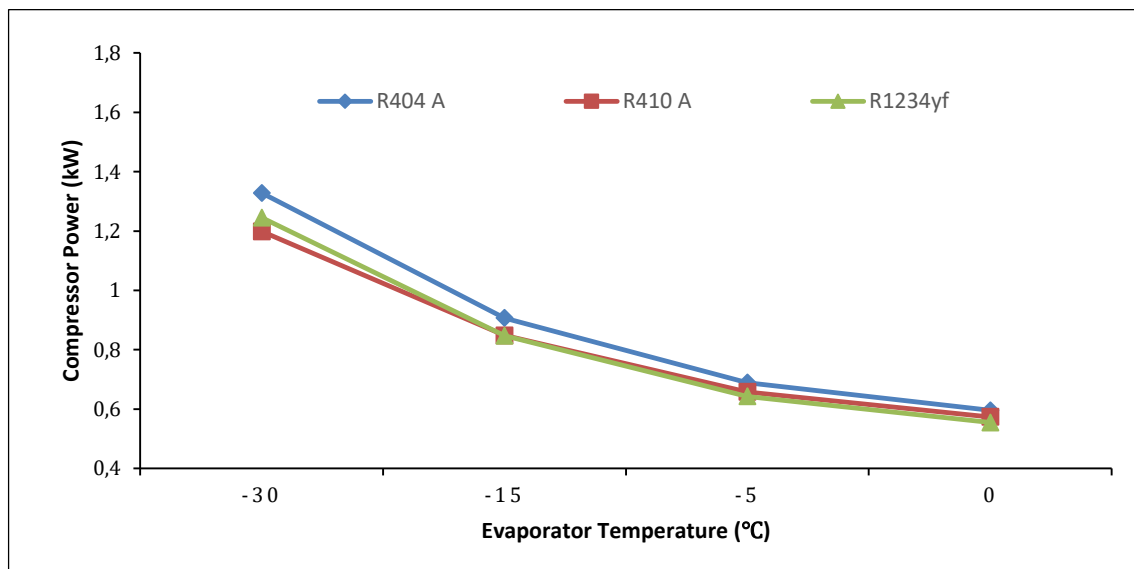


*Figure 4. Compressor energy consumption of refrigerants*

When the evaporation temperatures of R404A, R410A, and R1234yf refrigerants are varied between  $-30\text{ }^{\circ}\text{C}$  and  $0\text{ }^{\circ}\text{C}$ , COP for heating and cooling are shown in Figure 5. When investigating the heating and cooling COP values, it can be observed that R404A has a 10% increase, and R1234yf has a 7% increase compared to R410A. These COP values are directly proportional to the evaporation temperature, and the compressor energy consumption is inversely proportional. For R404A, the cooling COP values range between 1.5 and 3.3, and the heating COP values range between 2.5 and 4.3. For R410A, the cooling COP values range between 1.66 and 3.48, and the heating COP values range between 2.66 and 4.48. As for R1234yf, the cooling COP values range between 1.60 and 3.60, and the heating COP values range between 2.60 and 4.60.



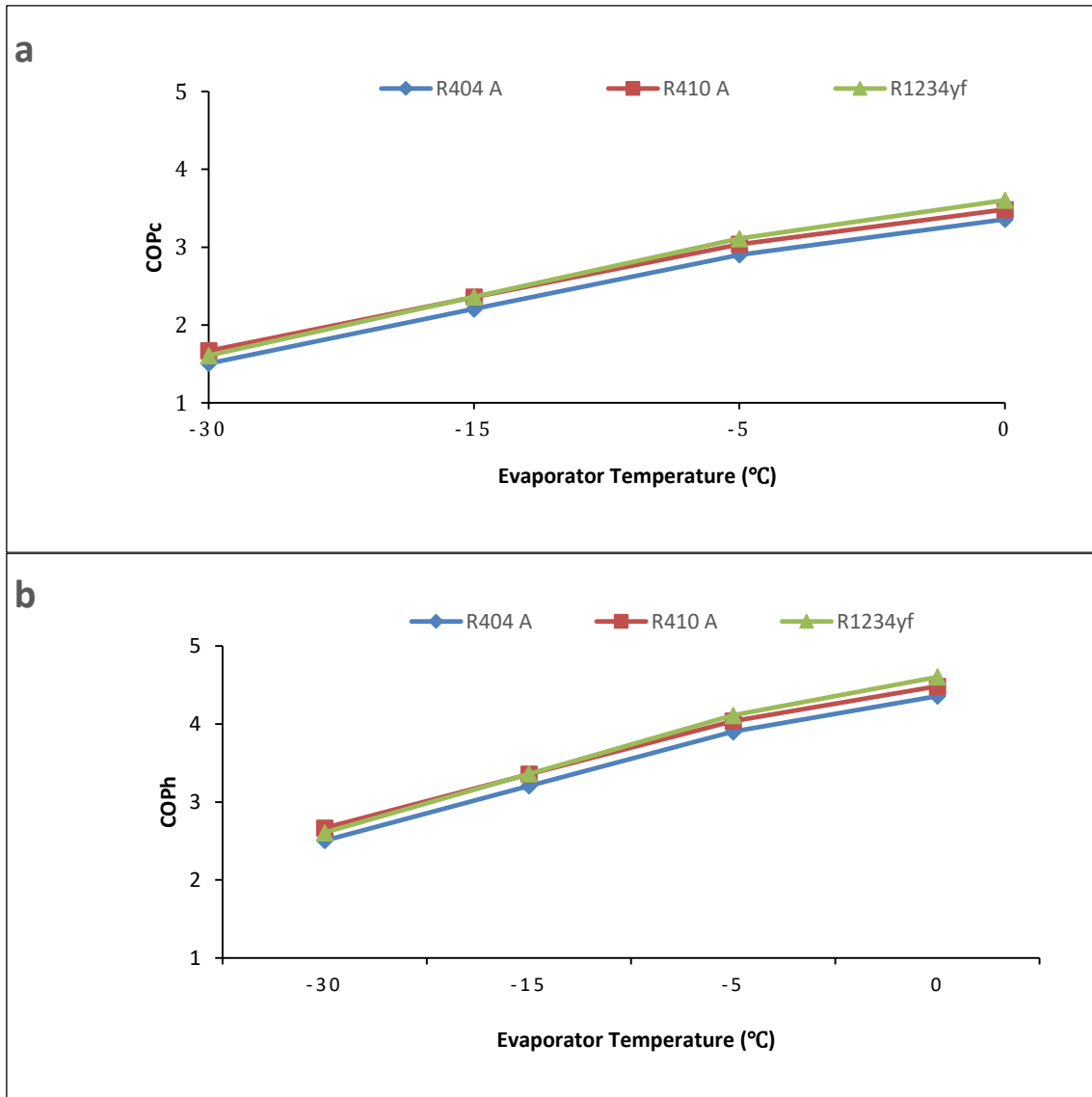


**Figure 5.** Change in cooling COP values (a) and heating COP values (b) of the refrigeration system

When the evaporation temperatures of R404A, R410A, and R1234yf refrigerants are changed between  $-30^{\circ}\text{C}$  and  $0^{\circ}\text{C}$ , the change in the system's condenser power is shown in Figure 6. As seen in the figure, the highest condenser load was found to be 3.3 kW for R404A refrigerant, 3.244 kW for R1234yf refrigerant, and 3.199 kW for R410A refrigerant at  $-30^{\circ}\text{C}$ . Increasing the evaporation temperature of the refrigerants resulted in a decrease in the condenser capacities. With an increase in the condensation temperature, the compression ratio of the compressor will increase, and the flow rate of the refrigerant circulating in the system will decrease, leading to a partial decrease in the cooling capacity.

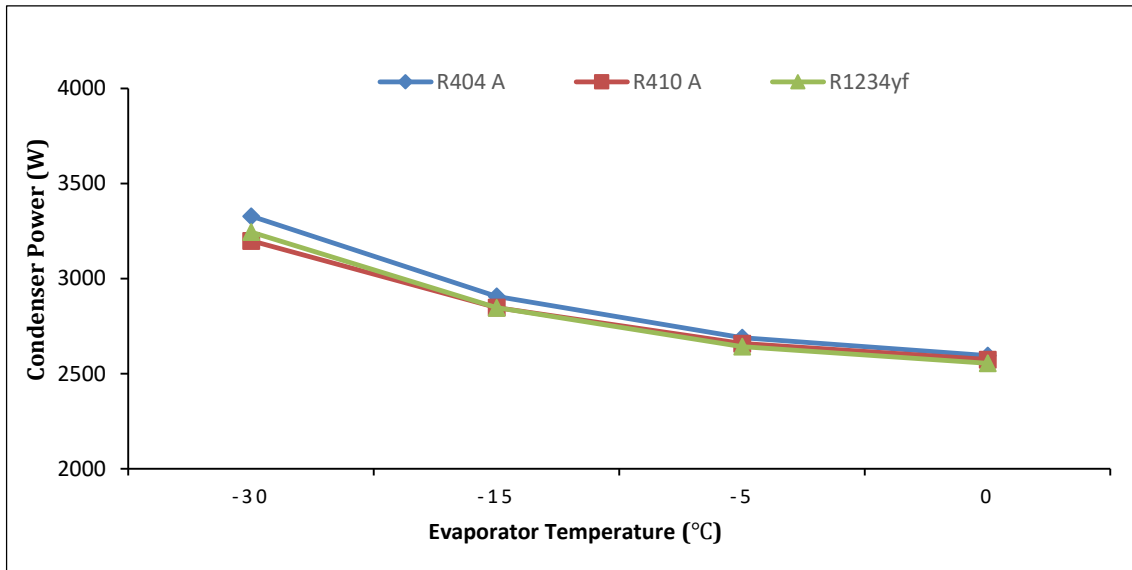


*Figure 6. Condenser powers for refrigerants in the system*

Figure 7 illustrates the change in the total exergy destruction of the system when R404A, R410A, and R1234yf refrigerant evaporation temperatures are varied between  $-30^{\circ}\text{C}$  and  $0^{\circ}\text{C}$ . The highest total exergy destruction is 3.13 kW for R404A, 2.96 kW for R1234yf, and 2.775 kW for R410A at  $-30^{\circ}\text{C}$ . As the evaporation temperatures decrease, the total exergy destruction in the system increases. The total exergy destruction is inversely proportional to the evaporation temperature.

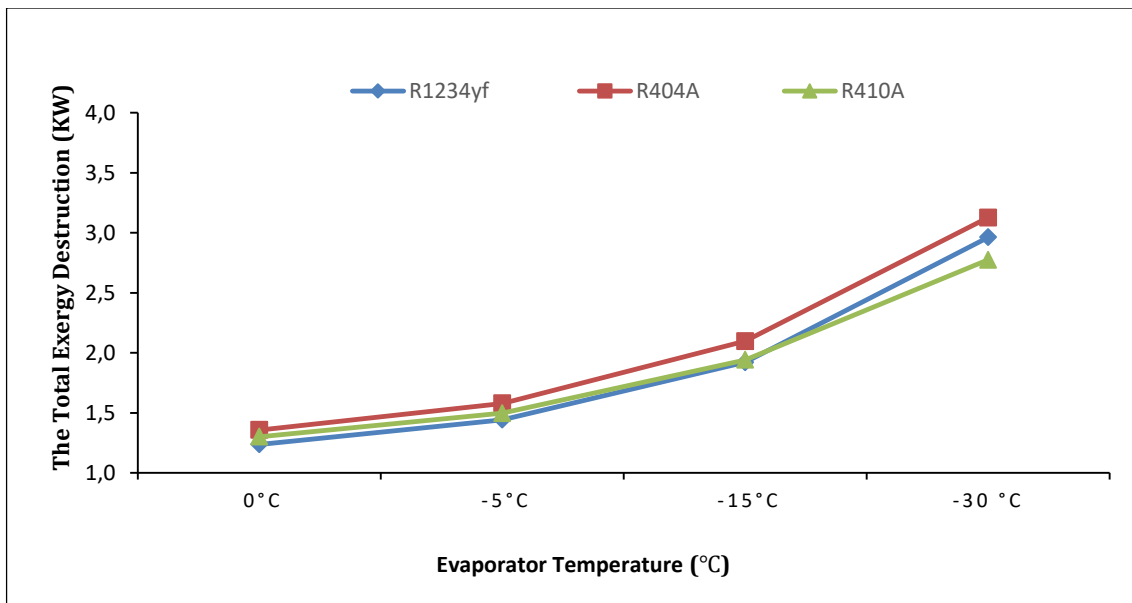


*Figure 7. Exergy destruction of the systems*

When R404A, R410A, and R1234yf refrigerants evaporation temperatures between changed  $-30^{\circ}\text{C}$  and  $0^{\circ}\text{C}$ , exergy efficiency changes are shown in Figure 8. The exergy efficiency of the refrigeration system is observed to vary between 26% to 29.4% for R404A refrigerant, between 27% to 32.5% for R410A refrigerant, and between 28% to 31.5% for R1234yf refrigerant.

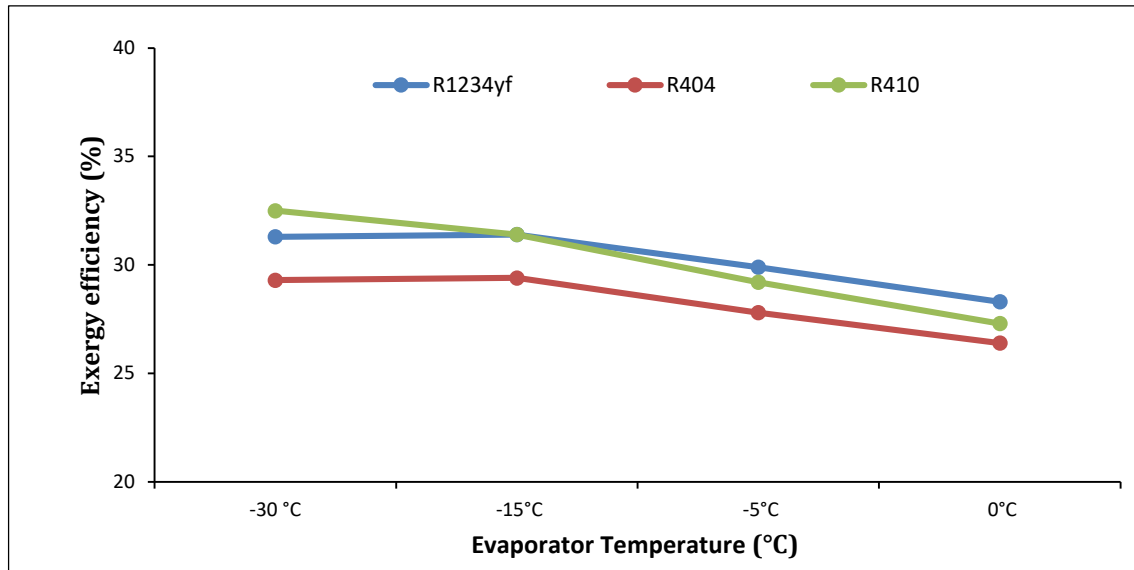


Figure 8. Exergy efficiency of the systems

LCCP analysis based on the evaporation temperatures of the refrigerants is shown in Figure 9. As the evaporation temperature decreases, an increase in the LCCP value is observed. When the evaporation temperature is changed between 0 °C and -30 °C, the LCCP values for R404A refrigerant range from 13102 kgCO<sub>2</sub> to 23611 kgCO<sub>2</sub>, for R410A refrigerant range from 10650 kgCO<sub>2</sub> to 19622 kgCO<sub>2</sub>, and R1234yf refrigerant range from 8370 kgCO<sub>2</sub> to 18275 kgCO<sub>2</sub>. The direct emission ratios in the total emission values of R404A, R410A, and R1234yf refrigerants are approximately 20.3%, 11.7%, and 0.05%, respectively.

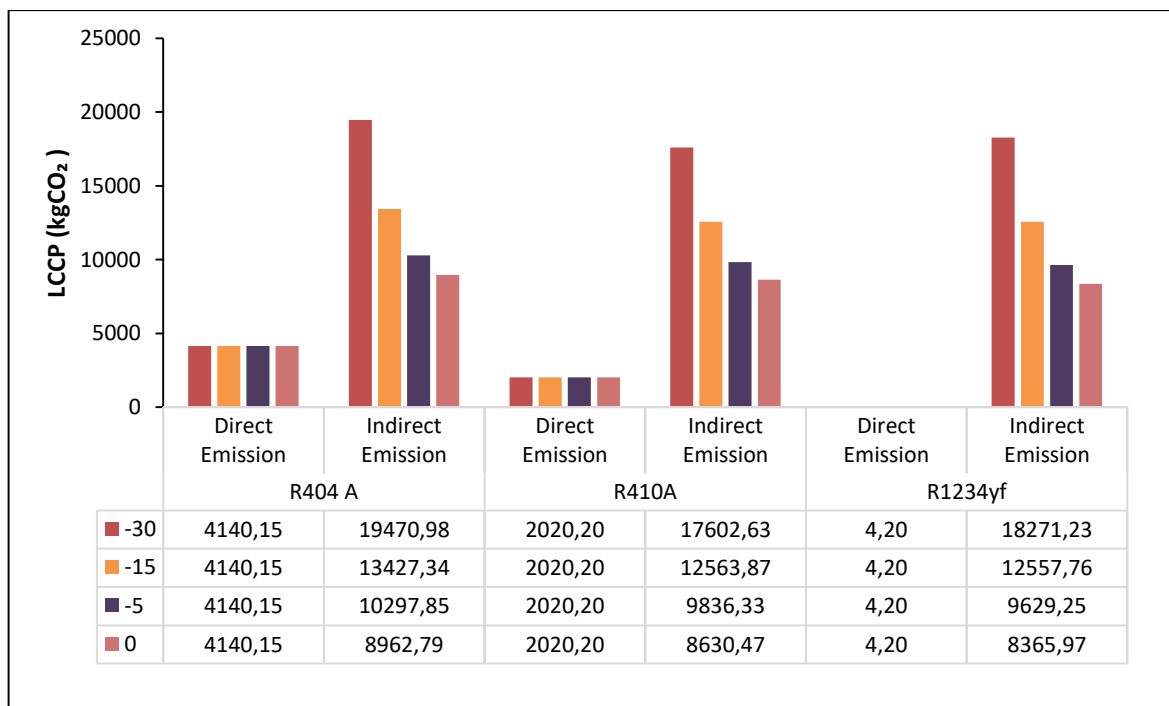
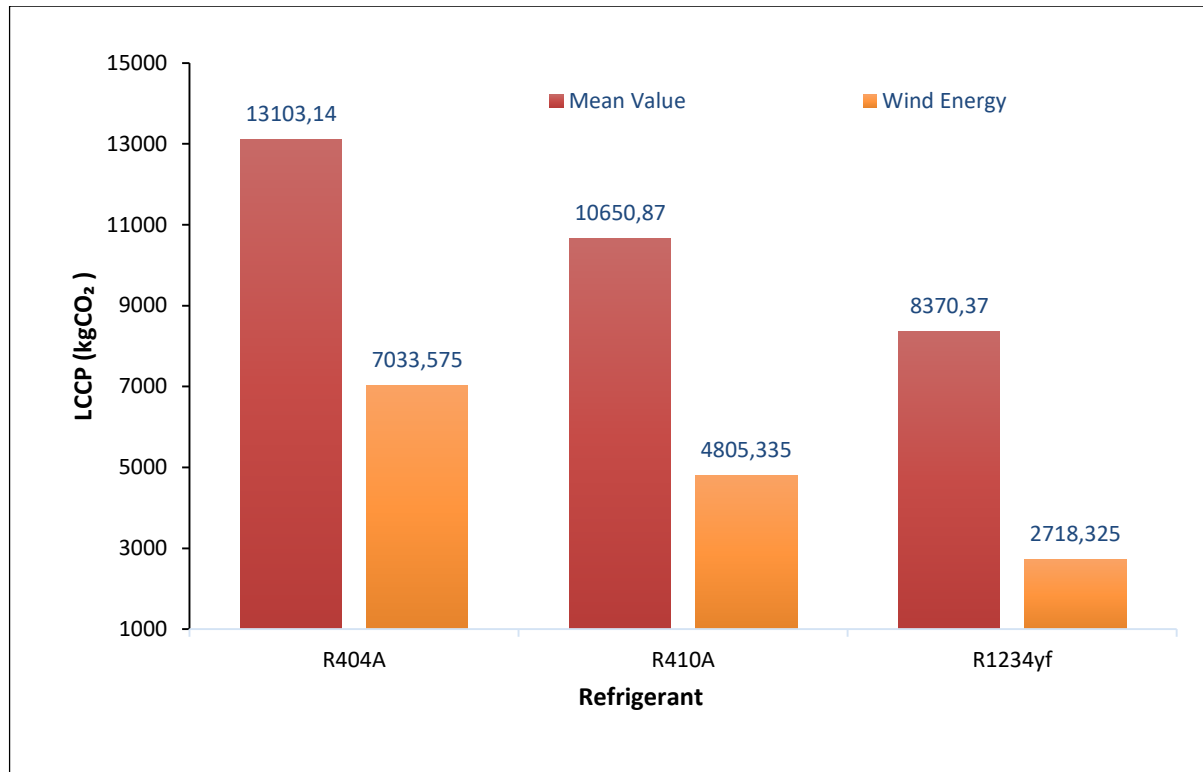


Figure 9. Detailed comparison of LCCP analysis according to refrigerant evaporation temperatures

The LCCP analysis used wind energy, a renewable energy source, to demonstrate its indirect emissions impact on the cooling cycle. The emission value for wind energy was considered to be 0.1237 kgCO<sub>2</sub>

per kWh, with an average emission value of 0.440 kgCO<sub>2</sub> per kWh. Keeping the evaporation temperature at 0°C and the condenser temperature at 50°C constant, a comparison was made between the average and emission values for wind energy. According to the comparison in Figure 10, when wind energy is used for electricity generation, there is a reduction of 17.79% kgCO<sub>2</sub> in R404A refrigerant, 41.68% in R410A refrigerant, and 65.88% in R1234yf refrigerant.



*Figure 10. LCCP comparison based on average emission values and wind energy emission values*

## V. CONCLUSION

In this study, a simple vapor compression refrigeration cycle system was designed using the Genetron simulation program. Due to the phase-out of high GWP refrigerant R404A in new devices, an energy, exergy, and life cycle climate performance (LCCP) analysis was conducted for the lower GWP refrigerant R410A and the new-generation refrigerant R1234yf, in comparison with R404A. The results are summarized below, and recommendations have been made.

- The COP values for heating and cooling are highest at an evaporation temperature of -30°C for R410A refrigerant and at an evaporation temperature range of -15°C to 0°C for R1234yf. As the evaporation temperature of refrigerants increases, the heating and cooling COP of refrigerants also increases.
- While the highest exergy efficiency was calculated for R410A at -30°C evaporation temperature, the highest exergy efficiency was found in R1234yf refrigerant between -15°C and 0°C evaporation temperature.
- The lowest exergy efficiency is observed for the refrigerant R404A. The exergy efficiency of R404A refrigerant is approximately 6.6% lower than that of R1234yf and R410A refrigerants.

- Total exergy destruction of all systems was at the lowest level with R1234yf at -30°C, followed by R410A and R404A. As the evaporation temperature decreases, the exergy destruction of the system increases. Exergy destruction was inversely proportional to the evaporation temperature.
- LCCP analysis, the direct emission values of all refrigerants are approximately less than 1% for R1234yf, approximately 12% for R410A, and approximately 20% for R404A. More than 80% of the total emission value of refrigerants is due to indirect emissions.
- There is approximately a 17% reduction in kgCO<sub>2</sub> emissions for R404A compared to R410A at an evaporation temperature of -30°C and approximately a 23% reduction compared to R1234yf. A comparison was made using an LCCP analysis with parameters held constant at an evaporation temperature of 0°C and a condenser temperature of 50°C, comparing the average emission value with the wind energy emission value. A comparison of the average emission value with the wind energy emission value reveals reductions in kgCO<sub>2</sub>e emissions of approximately 18% for R404A, 42% for R410A, and 66% for R1234yf.
- Almost all of the indirect emissions are attributed to the energy consumption of the compressor in the cooling system. It is essential to use refrigerants with low charge amounts and low GWP values to improve efficiency and reduce the energy the compressor. Additionally, utilizing environmentally friendly energy sources like renewable energy for generating the electricity needed to work the compressor is crucial.

In conclusion, based on the energy, exergy, and LCCP analysis results, it is feasible to use R410A or R1234yf refrigerants as alternative refrigerants in cooling systems currently using R404A. The necessary adjustments and appropriate equipment selection are required for these transitions. According to the data obtained, R1234yf refrigerant exhibits lower energy consumption and higher exergy efficiency compared to R404A and R410A. Furthermore, R1234yf has a lower LCCP value than R404A and R410A. Therefore, R1234yf refrigerant is considered a better alternative regarding energy efficiency and environmental impact.

## **VI. REFERENCES**

- [1] A. Keogh, “Soğutucu Akışkan Seçimi ve Su Soğutma Grubu Tasarımı Paket Tip Su Soğutma Gruplarında R410A Kullanımı,” Alarko, Türkiye, Rap. 4, 2005.
- [2] U. Berk, “R422A Ve R424A Soğutucu Akışkanlarıyla Çalışan Bir Soğutma Sisteminin Deneysel İncelenmesi,” Yüksek lisans, Makina Mühendisliği, Dicle Üniversitesi, Diyarbakır, Türkiye, 2019.
- [3] B. Kılıç, E. Arabacı, “Lpg (R1270-Propilen) Soğutucu Akışkan Kullanılan Buhar Sıkıştırma Soğutma Sisteminin Enerji Analizi,” *Mehmet Akif Ersoy Üniversitesi Uygulamalı Bilimler Dergisi*, c. 2., ss. 75–81, 2018.
- [4] A. Yıldız, R. Yıldırım, “R134a’ya Alternatif Bir Soğutucu Akışkan (R513A) Kullanan Buhar Sıkıştırma Soğutma Sistemlerinin Enerji ve Çevresel Analizi,” *Düzce Üniversitesi Bilim ve Teknoloji Dergisi*, c. 8, s. 2, ss. 1817–1828, 2020.
- [5] S. Choi, Y. Jung, Y. Kim, H. Lee, Y. Hwang, “Environmental effect evaluation of refrigerator cycle with life cycle climate performance”, *International Journal of Refrigeration*, vol. 122, pp. 134–146, 2021.

- [6] H. Wan, T. Cao, Y. Hwang, R. Radermacher, S. Chin, “Comprehensive investigations on Life Cycle Climate Performance of unitary air-conditioners,” *International Journal of Refrigeration*, vol. 129, pp. 332–341, 2021.
- [7] T. Menlik, A. Demircioğlu, M.G. Özkaya, “Energy and exergy analysis of R22 and its alternatives in a vapour compression refrigeration system,” *International Journal of Exergy*, vol. 12, pp. 11–30, 2013.
- [8] A. Ergün, A.E. Gürel, İ. Ceylan, “Ticari Soğutma Sistemlerinde R22 Akışkanının Alternatifi Olarak R438A ve R417A Akışkanlarının Performansının İncelenmesi,” *Gazi Üniversitesi Fen Bilimleri Dergisi Part C: Tasarım ve Teknoloji*, c.6, s.4, ss. 824–833, 2018.
- [9] A.E. Özgür, “HFC-134a ve Alternatifi Soğutkanların (HFO-1234yf ve HFO-1234ze) Soğutma Çevrimi Performansı Açısından Karşılaştırması,” *Gazi Üniv. Müh. Mim. Fak. Der.*, c. 28, s. 2, ss. 465–472, 2013.
- [10] T.J. Leck, “New High Performance, Low GWP Refrigerants for Stationary AC and Refrigeration,” *International Refrigeration and Air Conditioning Conference*, 2010, pp. 1–8.
- [11] J.M. Calm, “The next generation of refrigerants-Historical review, considerations, and outlook,” *International Journal of Refrigeration*, vol. 31, pp. 1123–1133, 2008.
- [12] E. Demirci, M. Özkaymak, M. Koşan, A.M. Akkoç ve D. Aktaş, “Soğutucu Akışkan Kullanımında Gelişmeler, G. Mühendislik Bilimleri, *Gazi Mühendislik Bilimleri Dergisi*, c. 6, ss. 184–199, 2015.
- [13] M. Araz, A. Güngör, A. Hepbaşı, “Düşük Küresel Isınma Potansiyeline Sahip Soğutucu Akışkanların Soğutma Uygulamalarındaki Kullanımının Değerlendirilmesi,” 11. Ulusal Tesisat Mühendisliği Kongresi, İzmir, Türkiye, 2013, pp. 575–602.
- [14] Genetron® AZ-20 (R-410A) | European Refrigerants, *Bilgisayar Programı*, MSDOS version, 2023.
- [15] Y.A. Çengel, M.A. Boles, A. Pınarbaşı, *Mühendislik yaklaşımıyla termodinamik*, 5. baskı, İstanbul, Türkiye: Güven Bili, Palme, 2011.
- [16] M.O. Karaağaç, A. Kabul, F. Yiğit, “Kombine Doğalgaz Çevrim Santralinin Performans Analizi,” *Politeknik Dergisi*, c. 22, s. 2, ss. 319–325, 2019.

#### NOMENCLATURE

CO <sub>2</sub>	: Carbon Dioxide
m	: Mass
Al	: Aluminum
T	: Temperature
ψ	: Specific Energy
Ex	: Exergy
Q	: Heat
0	: Steady State Reference Point
W	: Work
η	: Efficiency
s	: Entropy
h	: Enthalpy

#### ABBREVIATIONS

GWP	: Global Warning Potential
GWP <sub>adp</sub>	: Global Warning Potential of Refrigerants Degrading in the Atmosphere

ODP : Ozane Depletion Potential  
LCCP : Life Cycle Climate Performance  
COP : Coefficient of Performance  
HVAC : Heating Ventilation Air Conditioning  
HC : Hydrocarbon  
CFC : Chlorofluorocarbon  
HCFC : Hydrochlorofluorocarbon  
HFC : Hydrofluorocarbon  
HFO : Hydrofluoroolefin  
UNEP :United Nations Environment Programme  
WMO : World Meteorological Organization  
UNCED : United Nations Conference on Environment and Development  
UNFCCC :United Nations Framework Convention on Climate Change  
DE : Direct Emission  
EE : Indirect Emission  
C : Refrigerant Charge Amount  
L : System Operating Life  
ALR : Annual Refrigerant Leakage Rate  
EOL : End of Life Refrigerant Leakage Rate  
AEC : Annual Energy Consumption  
EM : Electricity Generation Emission Value  
MM : Material Manufacturing Emissions  
mr : Recycled Material Mass  
RM : Recycled Material Emissions  
RFM : Refrigerant Manufacturing Emissions  
RFD : Refrigerant Disposal-Related Emissions



# Düzce University Journal of Science & Technology

Research Article

## Determination of Modified Mohr-Coulomb Damage Model Parameters for DH780 Steel in Finite Element Analysis

Tolgahan CİVEK<sup>a</sup>, Nuri SEN<sup>a,\*</sup>, Oktay ELKOCA<sup>a</sup>

<sup>a</sup> Department of Mechanical Engineering, Faculty of Engineering, Düzce University, Düzce, TURKEY

\* Corresponding author's e-mail address: nurisen@duzce.edu.tr

DOI: 10.29130/dubited.1390682

### ABSTRACT

In sheet metal forming processes, tearing problems might be occasionally encountered due to many reasons such as incorrect forming parameters. The trial and error methods that are used to solve such problems, on many occasions, are time-consuming and inefficient in terms of finding the correct forming parameters or die design for the forming process. The finite element analysis method, on the other hand, can be used as a tool that is both time and cost-saving. However, in order to effectively exploit the use of finite element analysis in sheet metal forming operations, the material that is used to be formed needs to be well characterized in terms of its hardening behaviour and failure criteria. In this study, a TRIP-aided DP steel (DH780) has been tensile tested in three different deformation conditions (uniaxial, plane stress and shear) and the parameters of its hardening model (Hollomon) and failure criteria (Modified Mohr-Coulomb) have been determined. According to the simulation results, obtained hardening parameters are able to describe the flow behaviour of the steel and the used failure criterion is able to predict the experimental failure correctly in each deformation condition.

**Keywords:** Finite element analysis, damage models, optimization, tensile test

## DH780 Çeliği için Modifiye Edilmiş Mohr-Coulomb Hasar Model Parametrelerinin Belirlenmesi

### ÖZ

Sac metal malzemelerin şekillendirilmesinde uygulanan prosesler sırasında karşılaşılan çeşitli hata veya kusurlar üretim maliyetini ciddi seviyelerde arttırmaktadır. Metal şekillendirme prosesinin sonlu elemanlar aracılığı ile önceden analiz edilmesi, üretimde deneme yanılma sayılarını ciddi oranda azaltıp, üretim maliyetinin önemli bir seviyede düşmesine yardımcı olmaktadır. Bu bağlamda, sonlu elemanlar analizlerinde deneysel sonuçlara yakınsamanın sağlanması için analizlerde malzemenin plastik davranışını tanımlayan akış modelinin ve aynı zamanda hasar tespiti için yararlanılan hasar modellerinin doğru bir şekilde tanımlanması ve parametrelerinin optimize edilmesi gerekmektedir. Bu çalışmada DH780 çelik malzeme için üç farklı deformasyon durumundaki (Kesme, tek eksenli çekme ve saf gerinim) numuneler çekme testine tabii tutulmuştur. Elde edilen verilerden yararlanılarak, Hollomon sertleşme modelinin ve modifiye edilmiş Mohr Coloumb hasar modellerinin parametreleri belirlenmiş ve optimize edilmiştir. Analiz ortamında yapılan çekme testlerinin sonuçları deneysel verilerle karşılaştırıldığında sonuçlar arasında yüksek oranda bir uyumun sağlandığı gözlemlenmiştir.

**Anahtar Kelimeler:** Sonlu Elemanlar Analizi, Hasar Modelleri, Optimizasyon, Çekme Testi

<sup>1</sup>11. Uluslararası Meslek Yüksekokulları Sempozyumu'nda (UMYOS) sunulmuştur.



# **I. INTRODUCTION**

Sheet metal forming methods involve stretching or drawing of sheets by a punch into a desired shape through a counter die [1]. However, even small changes in the forming parameters such as die radius, the amount of blankholder force, drawing bead design and etc. can have a significant impact on whether the forming process will be successful or not [2]. Hence, optimizing the forming parameters through trial and error method might cause significant waste both in time and cost [3]. Implementing the Finite Elements Method (FEM) in the forming processes, can drastically improve the forming process since it allows to visualize the problems and let the related parameters to be changed earlier in the die design process [3].

In order to use FEM effectively to observe the possible forming problems, it is required to well characterize the forming sheet metal [4]. The hardening model of the sheet metal is one of the most important parameters that is essential to correctly determine since it describes how the sheet metal flows during a forming operation. Hollomon, Swift, Fields & Backofen and Voce are some examples of isotropic hardening models that are commonly used in sheet metal forming simulations [5]–[10]. Depending on the flow behaviour of the sheet metal, the hardening model needs to be selected accordingly and its parameters need to be optimized. For some materials, the flow resistance might be different along the rolling direction (RD), diagonal direction (DD), and transversal direction (TD) of the sheet metal, which is called anisotropy [11], [12]. The anisotropic behaviour can cause an earing profile in the drawn sheet metals, changing the height of the drawn shapes to be different along the different directions of the sheet metal [13], [14]. For such materials, a kinematic hardening model may need to be selected and their parameters need to be optimized in order to visualize the correct flow behaviour of the sheet metal [15], [16]. To visualize the regions, where the sheet metal is likely to suffer from critical damage, in FEM simulations, it is necessary to implement a failure criterion for the defined sheet metal. Forming Limit Diagram (FLD) is one of the most known popular failure criterion that is used in FEM simulations [17]–[19]. FLD is simply a diagram which separates the safe straining zone from the critical straining zone, where the splitting occurs. By defining the FLD in the FEM simulation, critical zones in the sheet metal can be observed during a forming simulation. However, this method requires excessive amounts of tests in order to fully create a FLD [20]. Additionally, the accuracy of the FLD lowers for forming processes in which the strain path changes [21]. In order to overcome the inaccuracy related to the strain path changes in FLD, stress-based FLD methods can be used [22], [23].

Damage models are used to predict the onset of fracture in the sheet metal by relating various parameters such as hydrostatic stress, stress triaxiality, lode angle, etc. to the failure strain [24]. In its un-deformed state, the damage variable,  $D$ , in the sheet metal is assumed to be zero,  $D=0$ . As the forming process progresses, the damage accumulates in the sheet metal and if it reaches unity,  $D=1$ , or a critical damage value  $D = D_{critical}$ , the fracture takes place [24]. The damage variable can either be coupled or uncoupled to the strain hardening curve of the sheet metal [25], [26]. In coupled models, the damage variable affects the strain hardening curve and deteriorates the strain hardening of the sheet metal, while in uncoupled models the damage variable does not affect the strain hardening of the sheet metal and the damage accumulates independently from the strain hardening. While coupled models are more accurate in their prediction capabilities, the implementation of the uncoupled damage models and the determination of their parameters are much easier as compared to the coupled damage models [26]. Johnson Cook [27], Modified Mohr-Coulomb [28], Hosford-Coulomb [29], Lemaitre [30], Cockroft-Latham [31], and Gurson [32], are some examples of damage models that can be implemented in FEM simulations. Each model consider damage variable in terms of different material-dependent or independent parameters. For example, Johnson Cook model considers the effects of stress triaxiality, strain rate and temperature [27], Modified Mohr-Coulomb and Hosford-Coulomb models consider the effects of stress triaxiality and lode angle [28], [29], Lemaitre model considers the critical damage in uniaxial tension test [30], Cockroft-Latham model considers the maximum principal stress [31], Gurson model considers the void volume fractions [32]. Depending on

how these parameters affect the formability of the sheet metal, the most feasible damage model can be selected.

In this study, a TRIP-aided DP steel (DH780) has been tensile tested in terms of three different deformation modes (uniaxial, plane stress and shear) in order to test the material in three different stress triaxiality and lode angles. The flow curve in uniaxial tension and the elongation values in three different deformation modes have been used to obtain the parameters of the Hollomon hardening model and the Modified Mohr-Coulomb damage models. Tensile test simulations have been carried out in order to validate the hardening and damage model parameters.

## II. EXPERIMENTAL METHODS

### 2.1. MATERIAL

In this study, DH780 TRIP-aided DP steel in 1.9 mm thickness was used. The microstructure of the steel consists of ferrite, martensite, bainite and retained austenite structures [33]. The chemical composition of the steel is given in Table 1 [34]. Uniaxial, Plane Stress and Shear test specimen geometries were cut from the sheet metal by water jet cutting method. The dimensions of the cut specimens are shown in Figure 1. Zwick/Roell uniaxial tension machine was used to test each samples. The test speed was 25 mm/min for each test samples. A strain extensometer with a gauge length of 50 mm was used to record the strain changes in the samples.

*Table 1. The chemical composition of DH780 steel [34]*

C	Si	Mn	P	S	Al	Nb	Cr	Ti	Cu	Ni	Mo	V
0.159	0.301	1.83	0.018	0.003	0.668	0.002	0.242	0.005	0.022	0.036	0.039	0.007

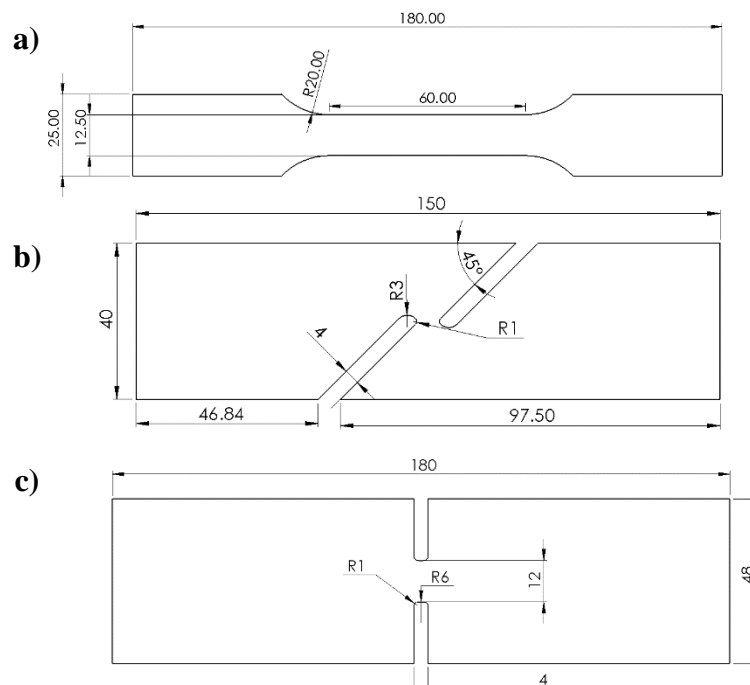


*Figure 1. The dimensions of the a) uniaxial, b) shear and c) plane stress test specimens*

## 2.2. HARDENING AND DAMAGE MODEL

The Hollomon hardening model was used in the simulations to predict the flow behaviour of the sheet metal. Hollomon hardening model is a model that is frequently used for its simplicity to predict the flow behaviour of sheet metals at room temperatures. The hardening model is given in Equation 1. The hardening parameter,  $K$ , and the strain hardening exponent,  $n$ , is found from the slope of log true strain and log true stress curve as given in Equation 2. and shown in Figure 2.

$$\sigma = K\epsilon^n \quad (1)$$

$$\log \sigma = n \log \epsilon + \log K \quad (2)$$

where  $\sigma$  is equivalent stress.

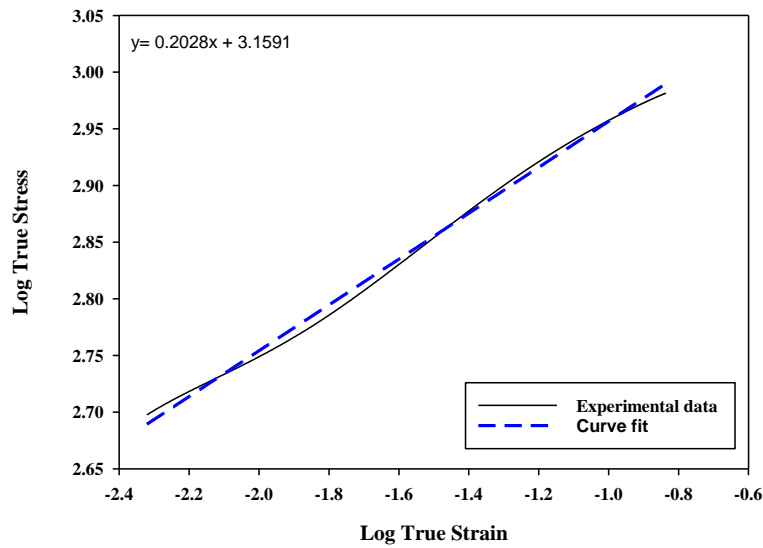


Figure 2. The slope of Log true strain and log true stress graph of DH780 steel

Modified Mohr-Coulomb (MMC) damage model was used to predict the onset of fracture for the sheet metal. MMC damage model considers the effects of stress triaxiality and the lode angle parameter on the formability of sheet metal to predict the onset of fracture. The stress triaxiality is known as one of the important factors impacting the ductility of sheet metals, especially under high stress triaxiality values. However, in recent studies, it has been shown that under low stress triaxiality values lode angle parameter has a significant effect on the ductility of sheet metals [35]. Geometrically, the lode angle can be described as the smallest angle in between the pure shear stress state and the projection of the stress tensor on the deviatoric plane. The lode angle value ranges in between  $0^\circ < \theta < 60^\circ$  and the normalized lode angle parameter  $-1 < \bar{\theta} < 1$ . In case of uniaxial, plane stress and shear stress states, the lode angle parameter, respectively, takes the values of 1, 0 and 0 [35]. The formulations of the stress triaxiality, lode angle, normalized lode angle or lode angle parameter, and the MMC damage model are given in Equations 3-6., respectively.

$$\eta = \frac{\sigma_m}{\sigma_{vM}} \quad (3)$$

$$\theta = \frac{1}{3} \arccos(\zeta) \quad (4)$$

$$\bar{\theta} = 1 - \frac{6\theta}{\pi} = 1 - \frac{2}{\pi} \arccos(\zeta) \quad (5)$$

where  $\eta$ ,  $\sigma_m$  and  $\sigma_{vM}$  respectively represent the stress triaxiality, mean stress and von mises stress,  $\theta$ ,  $\zeta$ , and  $\bar{\theta}$  represent the lode angle, normalized deviatoric invariant and lode angle parameter, respectively.

$$\bar{\epsilon}_f = \left\{ \frac{A}{c_2} \left[ C_\theta^S + \frac{\sqrt{3}}{2-\sqrt{3}} (C_\theta^{ax} - C_\theta^S) \left( \sec\left(\frac{\bar{\theta}\pi}{6}\right) - 1 \right) \right] x \sqrt{\frac{1+C_2^2}{3}} \cos\left(\frac{\bar{\theta}\pi}{6}\right) + c_1 \left( \eta + \frac{1}{3} \sin\left(\frac{\bar{\theta}\pi}{6}\right) \right) \right\}^{-\frac{1}{n}} \quad (6)$$

where  $\bar{\epsilon}_f$  represent the failure strain, the parameters A and n represent the parameters in the hardening model,  $c_1$  describes the dependency of fracture strain on the triaxiality,  $c_2$  influences the height of the fracture surface,  $C_\theta^S$  describes the amount of lode angle dependency of the fracture surface,  $C_\theta^{ax}$  controls the asymmetry of fracture surface with respect to lode angle parameter and is taken as 1 for  $\bar{\theta} > 0$ .

### 2.3. FINITE ELEMENT ANALYSIS MODEL

In this study, Simufact Forming 2023.2 was used to simulate the tensile tests. Test specimen geometries and the grips that are used to hold the specimens were exported to the software as shown in Figure 3. Specimens were meshed with sheet meshes in 0.87 mm size, meshes in the gauge sections of the specimens were refined by two times to create a fine mesh geometry. The through-thickness direction of the specimens was discretised by three mesh elements. Glue type contact was used in between the grips and the specimens. The upper grip, holding the specimen, was used to stretch the specimens at 25 mm/min velocity.

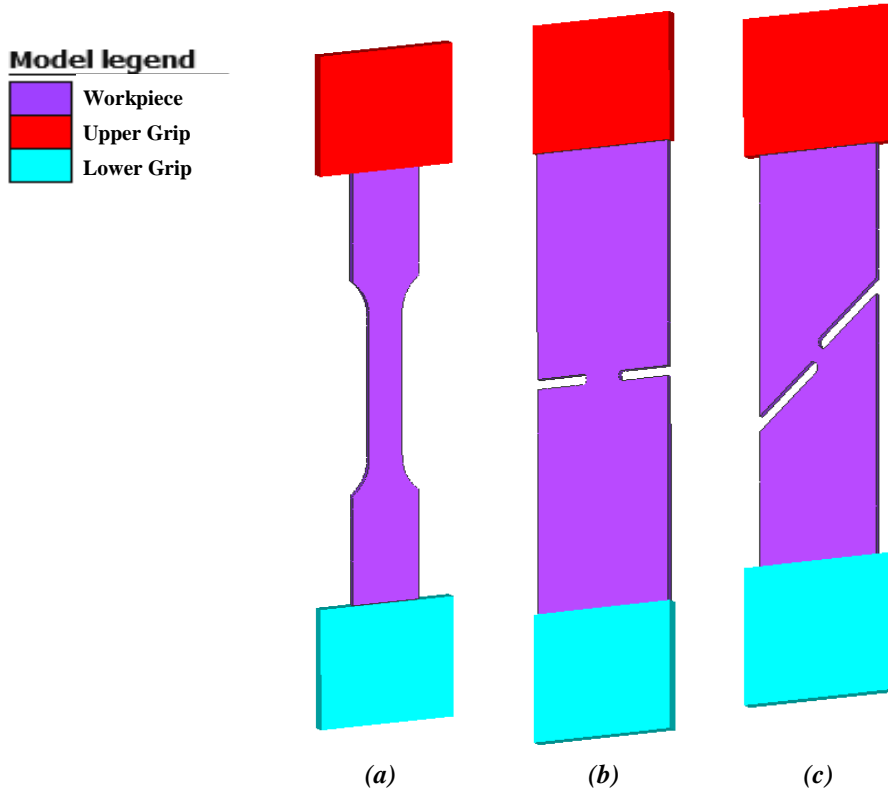


*Figure 3. Simulation model used in the analysis for a) uniaxial, b) plane stress, c) shear specimens*

## III. RESULTS AND DISCUSSIONS

### 3.1. HOLLON HARDENING MODEL

A hardening model is used to predict the flow behaviour of sheet metal. Thus, its correct input is essential to simulate the real sheet metal flow during the forming operation. The initial values of the hardening parameters that are obtained through Figure 2., may not directly result in true flow

behaviour. Thus, it is necessary to use the reverse analysis method to find the optimum hardening parameters that represent the flow behaviour of the sheet metal. In order to evaluate the fitness of the hardening model, tensile test experiments are conducted in the FEM simulations and the obtained force-displacement curves are compared with the experimental values. The obtained hardening model parameters are as follows:  $K= 1305$ ,  $n= 0.166$ , and the comparison graphs of the simulated and the experimental force-displacement curves are shown in Figure 4. It can be seen that the Hollomon hardening model that is implemented in the simulation is sufficient to accurately predict the flow behaviour of DH780 steel for uniaxial, plane stress and shear test specimens.

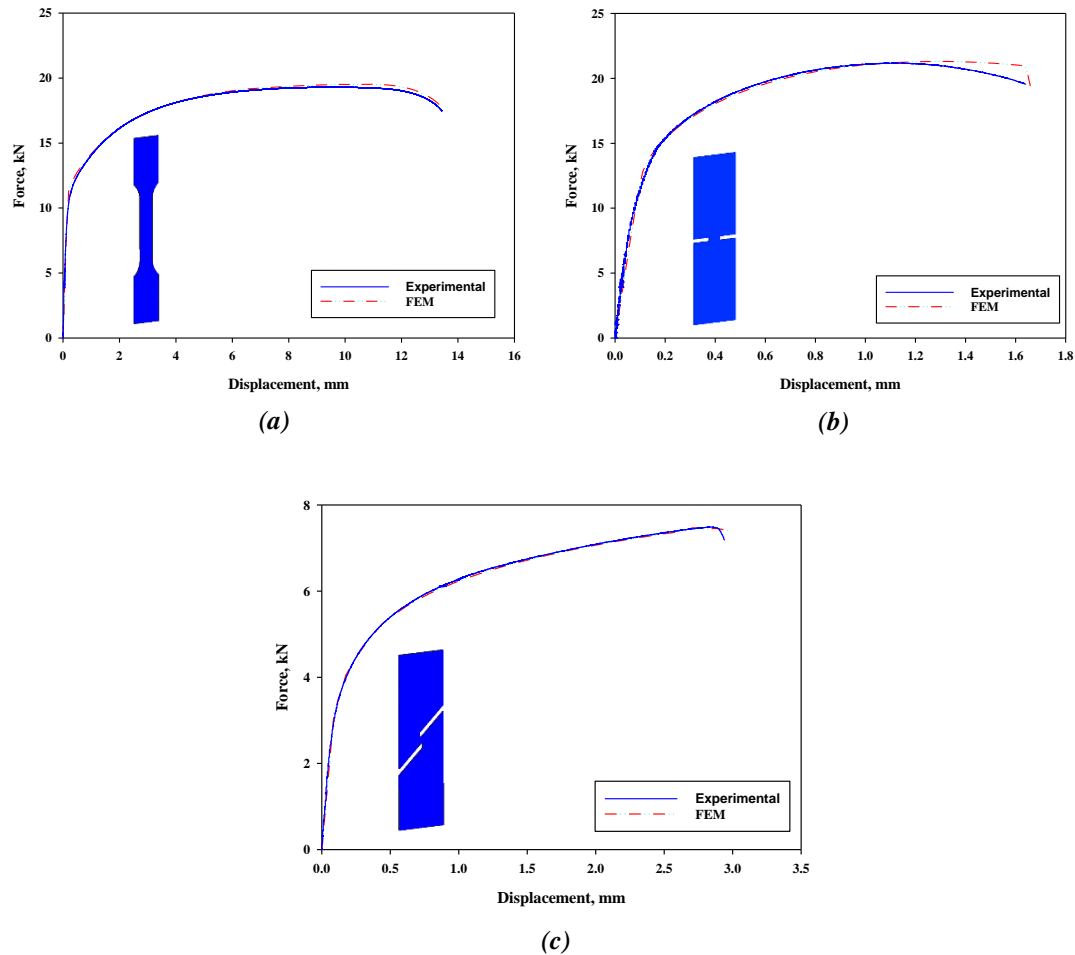


**Figure 4.** The force-displacement curves for **a)** uniaxial, **b)** plane stress and **c)** shear test specimens

### 3.2. MMC DAMAGE MODEL

Damage models in FEM analysis are used to inspect the regions in the sheet metal where the failure is likely to occur. In many studies, it is mentioned that the stress triaxiality and the lode angle have a significant effect on the formability of sheet metals [36], [37]. Thus, in this study, the MMC damage model, which considers the effects of stress triaxiality and lode angle, is used to determine its parameters for DH780 steel. For this reason, FEM simulations have been carried out for uniaxial, plane stress and shear test specimens and the critical elements, which the crack first initiates, have been tracked to determine the critical strain, average stress triaxiality and the lode angle parameters. The variation of the lode angle parameter in uniaxial, plane stress and shear specimens at the critical element has been shown in Figure 5. It can be seen that the lode angle parameter value for the uniaxial specimen has been  $\bar{\theta} = 1$ , while the values for plane stress and shear specimens have varied around  $\bar{\theta} \approx 0$ . The variation of the stress triaxiality values in uniaxial, plane stress and shear specimens at the

critical element have been shown in Figure 6. It can be seen that the stress triaxiality value for the uniaxial specimen has been  $\eta = 0.33$ , while the stress triaxiality values for plane stress and shear specimens have varied around  $\eta \approx 0.56$  and  $\eta \approx 0$ , respectively. The average stress triaxiality, lode angle parameter and the critical strain values have been given in Table 2. Using the values in Table 2., the parameters of the MMC damage model have been obtained and the values have been optimized by the reverse analysis method. The optimised MMC damage model parameters and the fracture surface have been given in Table 3., and Figure 7., respectively. The fractured simulation results in uniaxial, plane stress and shear modes have been shown in Figures 7, 8 and 9, respectively. The fracture initiation or the mesh separation has started at the centre of all the specimens. It is seen that the optimized MMC damage model parameters for DH780 steel have been able to accurately predict the onset of fracture in all the specimens.

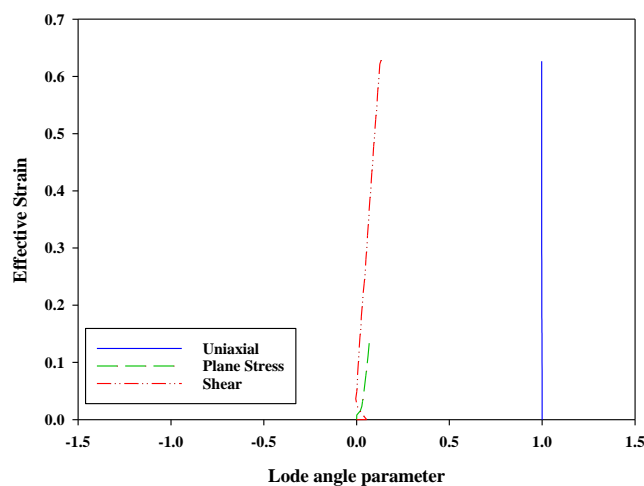


**Figure 5.** The variation of the lode angle parameter at the critical element in uniaxial, plane stress and shear tests.

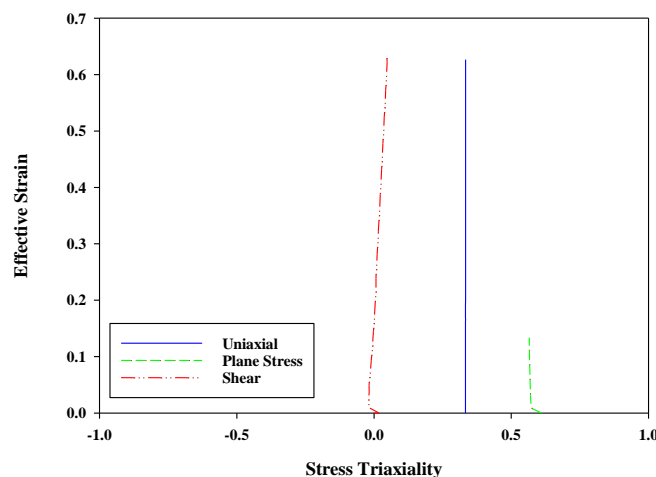


**Figure 6.** The variation of the stress triaxiality at the critical element in uniaxial, plane stress and shear tests.

**Table 2.** The average stress triaxiality, lode angle parameter and the critical strain values for uniaxial, plane stress and shear test specimens

Specimen	Stress Triaxiality	Lode angle Parameter	Critical Strain
Uniaxial	0.33	1	0.75
Plane Stress	0.57	0.08	0.26
Shear	0.05	0.15	0.76

**Table 3.** The optimized MMC damage model parameters used in the simulations.

<b>A</b>	<b>n</b>	<b>c<sub>1</sub></b>	<b>c<sub>2</sub></b>	<b>C<sub>θ<sup>s</sup></sub></b>	<b>C<sub>θ<sup>ax</sup></sub></b>
1305	0.166	0.1526	735.648	1.0302	1

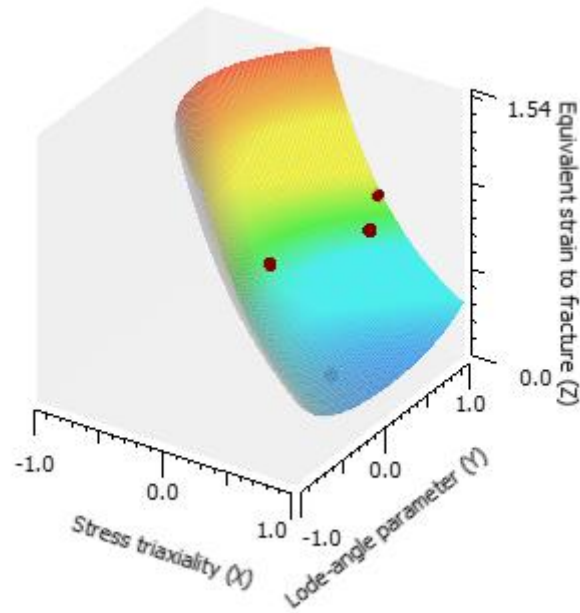


**Figure 7.** The fracture surface of MMC damage model obtained for DH780 steel

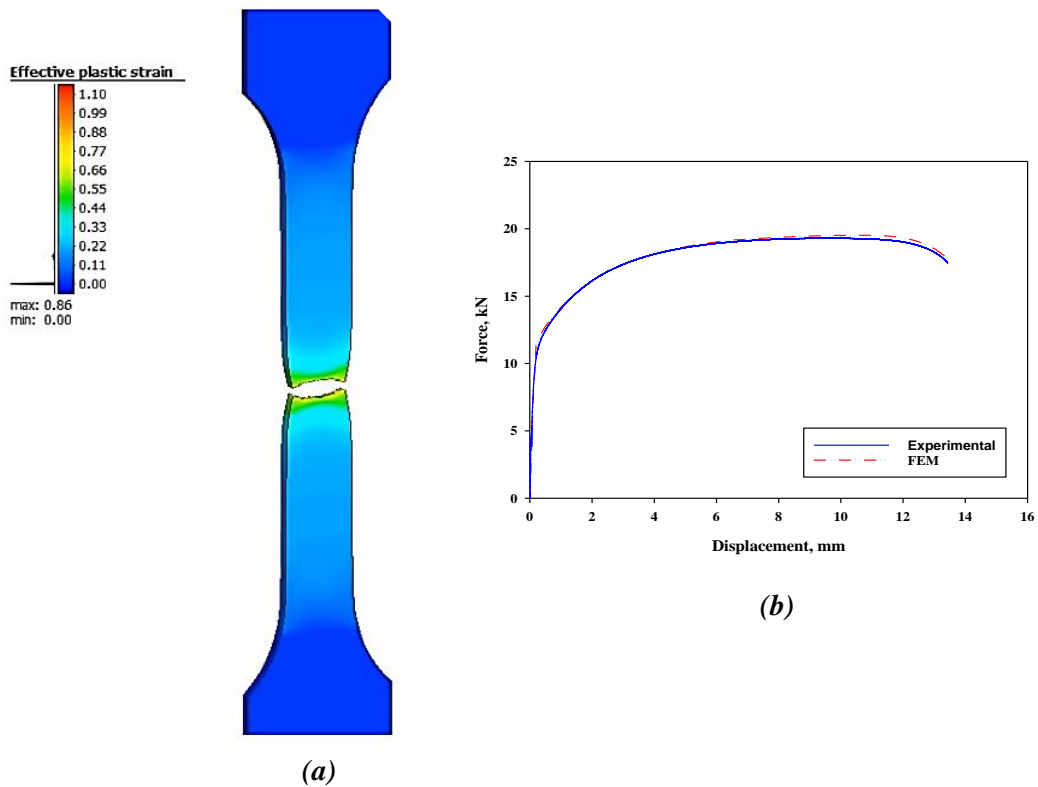


**Figure 8.** (a) The fracture image of the uniaxial test specimen and (b) the respective force-displacement curve

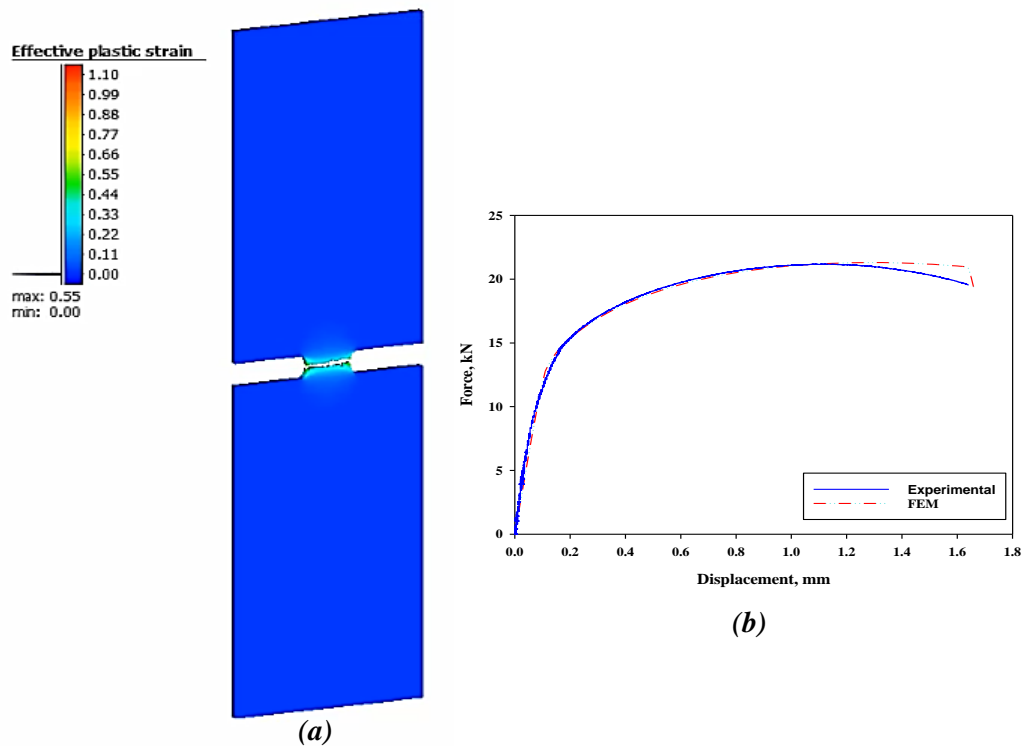


Figure 9. (a) The fracture image of the plane stress test specimen and (b) the respective force-displacement curve

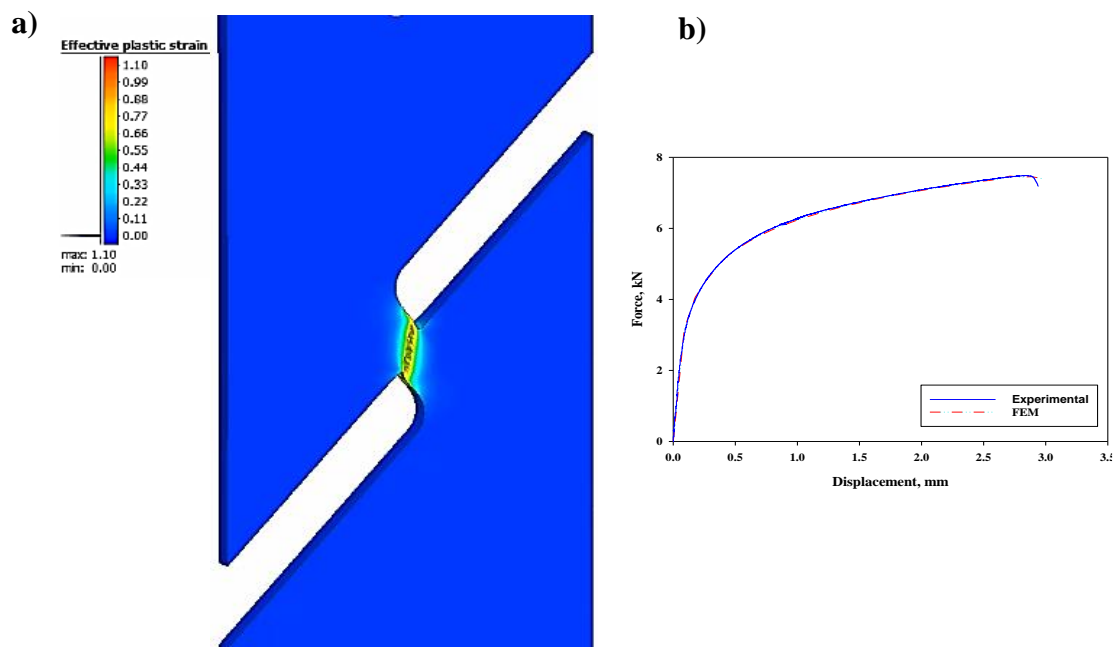


Figure 10. (a) The fracture image of the plane stress test specimen and (b) the respective force-displacement curve



## **IV. CONCLUSION**

In this study, finite element analysis has been carried out to determine and calibrate the parameters of Hollomon hardening model and the Modified Mohr-Coulomb damage model for a TRIP-aided DP steel (DH780). The following conclusions can be drawn from the study:

- The determined Hollomon hardening model parameters have been able to describe the flow behaviour of the DH780 steel for uniaxial, plane stress and shear test specimens.
- The lowest elongation has occurred in the plane stress test sample.
- The determined Modified Mohr-Coulomb damage model parameters have been able to predict the onset of fracture in all the tests.
- Obtained MMC fracture surface has indicated that the effect of stress triaxiality has had a more prominent effect on the formability of DH780 steel than the lode angle parameter.

**ACKNOWLEDGEMENTS:** This work was supported by The Scientific and Technological Research Council of Turkey (TUBITAK) (Project No: 222M321). The authors would like to thank TUBITAK for the financial support given to the project.

## **V. REFERENCES**

- [1] T. Altan and A. E. Tekkaya, *Sheet Metal Forming*. Ohio, United States: ASM International, 2012, pp. 1-201.
- [2] J. Hu, Z. Marciniak, and J. Duncan, *Mechanics of sheet metal forming*. Oxford, United Kingdom: Elsevier, 2002, pp. 1-204.
- [3] H. S. S. Aljibori and A. M. Hamouda, "Finite element analysis of sheet metal forming process," *European Journal of Scientific Research*, vol. 33, no. 1, pp. 57-59, 2009.
- [4] N. Şen, T. Civek, Ö. İlhan, Ö. Erdem Yurt, M. H. Çetin, and H. Şimşir, "Prediction of Flow Behavior and Deformation Analysis of AA5754 Sheet Metal at Warm and Hot Temperatures", *J. Mater. Eng. Perform.*, pp. 1–12, 2023.
- [5] M. Joun, I. Choi, J. Eom, and M. Lee, "Finite element analysis of tensile testing with emphasis on necking", *Comput. Mater. Sci.*, vol. 41, no. 1, pp. 63–69, 2007.
- [6] B. M. Chaparro, M. C. Oliveira, J. L. Alves, and L. F. Menezes, "Work hardening models and the numerical simulation of the deep drawing process", *Materials Science Forum*, vol. 455, pp. 717–722, 2004.
- [7] W. Jia, S. Xu, Q. Le, L. Fu, L. Ma, and Y. Tang, "Modified Fields–Backofen model for constitutive behavior of as-cast AZ31B magnesium alloy during hot deformation", *Mater. Des.*, vol. 106, pp. 120–132, 2016.
- [8] J. Shen, L. Hu, Y. Sun, Z. Wan, X. Feng, and Y. Ning, "A comparative study on artificial

neural network, phenomenological-based constitutive and modified Fields–Backofen models to predict flow stress in Ti-4Al-3V-2Mo-2Fe alloy", *J. Mater. Eng. Perform.*, vol. 28, pp. 4302–4315, 2019.

[9] H. Zhang, C. Xu, T. Gao, X. Li, and H. Song, "Identification of strain hardening behaviors in titanium alloys using tension tests and inverse finite element method", *J. Mech. Sci. Technol.*, vol. 37, no. 7, pp. 3593–3599, 2023.

[10] J.-H. Kim, A. Serpantić, F. Barlat, F. Pierron, and M.-G. Lee, "Characterization of the post-necking strain hardening behavior using the virtual fields method", *Int. J. Solids Struct.*, vol. 50, no. 24, pp. 3829–3842, 2013.

[11] G. Rousselier, F. Barlat, and J. W. Yoon, "A novel approach for anisotropic hardening modeling. Part I: Theory and its application to finite element analysis of deep drawing", *Int. J. Plast.*, vol. 25, no. 12, pp. 2383–2409, 2009.

[12] Y. Zhang, Y. Duan, P. Fu, S. Qi, and J. Zhao, "Constitutive modeling based on non-associated flow rule for anisotropic sheet metals forming", *Mater. Today Commun.*, p. 107086, 2023.

[13] K. Gök, H. Taş, A. Gök, and M. A. Alkan, "Investigation using finite element analysis of effect to earing of anisotropy parameters in deep drawing process", *Int. J. Mod. Manuf. Technol.*, vol. 15, no. 1, 2023.

[14] P. Fu *et al.*, "Finite element simulation and experimental study of non-blank holder forward and backward composite deep drawing earing test", *Int. J. Adv. Manuf. Technol.*, pp. 1–16, 2023.

[15] A. Sanrutsadakorn, W. Lawong, and W. Julsri, "Numerical Study of Predicting Forming Process Based on Different Hardening Models in Advanced High Strength Steel Sheets", *Key Eng. Mater.*, vol. 951, pp. 21–32, 2023.

[16] M. U. Sikandar and M. Usama, "A Case Study in Deep Drawing Process: Numerical Simulation and Analysis of Material Behavior and Hardening Models", *Young*, vol. 7, pp. 10–19.

[17] A. Rouzbeh, R. Hashemi, and M. Sedighi, "Experimental and numerical study of microstructure, mechanical characteristics, and forming limit curve for Al 1050/Mg-AZ31B two-layer sheets manufactured via roll bonding technique", *J. Alloys Compd.*, vol. 942, p. 169059, 2023.

[18] M. Habibi, R. Hashemi, A. Ghazanfari, R. Naghdabadi, and A. Assempour, "Forming limit diagrams by including the M–K model in finite element simulation considering the effect of bending", *Proc. Inst. Mech. Eng. Part L J. Mater. Des. Appl.*, vol. 232, no. 8, pp. 625–636, 2018.

[19] M. Habibi, A. Ghazanfari, A. Assempour, R. Naghdabadi, and R. Hashemi, "Determination of forming limit diagram using two modified finite element models", *Mech Eng*, vol. 48, no. 4, pp. 141–144, 2017.

[20] T. Pepelnjak and K. Kuzman, "Numerical determination of the forming limit diagrams", *J. Achiev. Mater. Manuf. Eng.*, vol. 20, no. 1–2, pp. 375–378, 2007.

[21] K. Achineethongkham and V. Uthaisangsuk, "Analysis of forming limit behaviour of high strength steels under non-linear strain paths using a micromechanics damage modelling", *Int. J. Mech. Sci.*, vol. 183, p. 105828, 2020.

[22] S. K. Paul, "Theoretical analysis of strain- and stress-based forming limit diagrams", *J. Strain Anal. Eng. Des.*, vol. 48, no. 3, pp. 177–188, 2013, doi: 10.1177/0309324712468524.

[23] C. H. M. Simha, R. Grantab, and M. J. Worswick, "Computational analysis of stress-based

forming limit curves", *Int. J. Solids Struct.*, vol. 44, no. 25–26, pp. 8663–8684, 2007.

[24] P. F. Liu and J. Y. Zheng, "Recent developments on damage modeling and finite element analysis for composite laminates: A review", *Mater. Des.*, vol. 31, no. 8, pp. 3825–3834, 2010.

[25] C. Y. Tang, J. P. Fan, and T. C. Lee, "Simulation of necking using a damage coupled finite element method", *J. Mater. Process. Technol.*, vol. 139, no. 1–3, pp. 510–513, 2003.

[26] P.-O. Bouchard, L. Bourgeon, S. Fayolle, and K. Mocellin, "An enhanced Lemaitre model formulation for materials processing damage computation", *Int. J. Mater. Form.*, vol. 4, pp. 299–315, 2011.

[27] M. E. Korkmaz, "Verification of Johnson-Cook parameters of ferritic stainless steel by drilling process: experimental and finite element simulations", *J. Mater. Res. Technol.*, vol. 9, no. 3, pp. 6322–6330, 2020.

[28] H. Talebi-Ghadikolae, H. Moslemi Naeini, M. J. Mirnia, M. A. Mirzai, S. Alexandrov, and H. Gorji, "Experimental and numerical investigation of failure during bending of AA6061 aluminum alloy sheet using the modified Mohr-Coulomb fracture criterion", *Int. J. Adv. Manuf. Technol.*, vol. 105, pp. 5217–5237, 2019.

[29] M. B. Gorji and D. Mohr, "Predicting shear fracture of aluminum 6016-T4 during deep drawing: Combining Yld-2000 plasticity with Hosford–Coulomb fracture model", *Int. J. Mech. Sci.*, vol. 137, pp. 105–120, 2018.

[30] A. Kumar, A. K. Singh, A. Shrivastava, S. Mishra, and K. Narasimhan, "Shear modified Lemaitre damage model for fracture prediction during incremental sheet forming", *Int. J. Solids Struct.*, vol. 252, p. 111822, 2022.

[31] G. Fang, P. Zeng, and L. Lou, "Finite element simulation of the effect of clearance on the forming quality in the blanking process", *J. Mater. Process. Technol.*, vol. 122, no. 2–3, pp. 249–254, 2002.

[32] M. M. Shahzamanian and P. D. Wu, "Study of forming limit diagram (FLD) prediction of anisotropic sheet metals using Gurson model in MK method", *Int. J. Mater. Form.*, vol. 14, pp. 1031–1041, 2021.

[33] Z. Hu, K. Wang, and J. Guo, "Microstructure and mechanical property of a novel hot dip galvanized dual phase steel with high ductility", in *Journal of Physics: Conference Series*, vol. 2368, no. 1, pp. 12021, 2022.

[34] SSAB, (2023,12,21) *Docol 800DH Data Sheet* [Online]. Available: <https://www.ssab.com>

[35] K. Danas and P. Ponte Castañeda, "Influence of the Lode parameter and the stress triaxiality on the failure of elasto-plastic porous materials", *Int. J. Solids Struct.*, vol. 49, no. 11–12, pp. 1325–1342, 2012.

[36] Y. Bao, "Dependence of ductile crack formation in tensile tests on stress triaxiality, stress and strain ratios", *Eng. Fract. Mech.*, vol. 72, no. 4, pp. 505–522, 2005.

[37] T. Güzelderen, "Investigation of variation of triaxiality and lode angle parameter values in sheet metal forming processes", M.S. thesis, Mechanical Engineering, Middle East Technical University, Ankara, Türkiye, 2022.



# Düzce University Journal of Science & Technology

Research Article

## Surface Analysis of Magnesium AZ31 Samples Immersed in Various Aqueous Solutions

 Erdem Şahin<sup>a\*</sup>,  Meltem Alp<sup>a</sup>,  Ahmed Şeref<sup>a</sup>

<sup>a</sup> Department of Metallurgical and Materials Engineering, Faculty of Engineering, Muğla Sıtkı Koçman University, Muğla, TURKEY

\* Corresponding author's e-mail address: [erdemsahin@mu.edu.tr](mailto:erdemsahin@mu.edu.tr)

DOI: 10.29130/dubited.1371973

### ABSTRACT

Rapid degradation in body fluids is known to be the main shortcoming of the AZ31 magnesium alloy that is aimed to be controlled in this study by chemical conversion of its surface in various phosphate and chloride solutions. Deposited layers on the surface of bare alloy plates were subjected to compositional and morphological analyses to assess their performance as barriers to degradation. Also changes in the mass of the samples and pH of the solutions were monitored during 21 day immersion periods. Formations of prismatic, platelike, needlelike crystals of various compositions including calcium phosphates, magnesium phosphates, magnesium chlorides were observed by scanning electron microscopy and their atomic compositions were determined by EDX and quantitative XRD analyses. The results indicate that a layer of ceramic of various thicknesses can stably form on the base alloy by simple adsorption of the particles suspended in the solution or by nucleation and growth of the products of reactions between dissolved ions and the metal ions released from the surface. These deposition layers that are solely induced by the electrochemical potential of the species in the solution offer facile surface modification methods and novel phases to control the degradation of magnesium alloys in aggressive environments such as body fluids or marine environments.

**Keywords:** AZ31 magnesium alloy, Coating, Magnesium phosphates, Calcium phosphates, Phase analysis.

## Çeşitli Sulu Çözeltilerde Tutulan Magnezyum AZ31 Numunelerinin Yüzey Analizi

### ÖZ

Vücut ortamında hızlı bozunduğu bilinen AZ31 magnezyum alaşım yüzeyinin bu eksikliğini çalışmamızda çeşitli fosfat ve klorür çözeltilerinde kimyasal dönüşüme maruz bırakılarak giderilmesi amaçlanmıştır. Alaşım plakaların yüzeyinde biriken katmanlar bozunmaya karşı bariyer performanslarını değerlendirmek için kimyasal ve morfolojik analizlere tabi tutulmuştur. Ayrıca numunelerin kütledeki ve çözeltilerin pH'ındaki değişiklikler 21 günlük daldırma süreleri boyunca izlenmiştir. Kalsiyum fosfatlar, magnezyum fosfatlar, magnezyum klorürler gibi çeşitli bileşimlerdeki prizmatik, plakamsı ve iğnemsı kristal oluşumları taramalı elektron mikroskobu ile incelenmiş ve bunların atomik bileşimleri EDX ve kantitatif XRD analizleri ile belirlenmiştir. Sonuçlar alaşım üzerinde çeşitli kalınlıklarda bir seramik tabakasının, basit adsorpsiyon ve çözünmüş iyonlar ile yüzeyden salınan metal iyonları arasındaki reaksiyon ürünlerinin çekirdeklenmesi ve büyümesi yoluyla kararlı bir şekilde oluşabildiğini göstermektedir. Yalnızca çözeltideki türlerin elektrokimyasal potansiyeli ile oluşan bu birikim katmanları, vücut sıvıları veya deniz ortamları gibi agresif ortamlarda magnezyum alaşımının bozunmasını kontrol etmek için sade bir yüzey modifikasyon yöntemi ve yeni fazlar sunmaktadır.

## **I. INTRODUCTION**

Inherently biocompatible magnesium (Mg) is a safe biomaterial that has ideal properties for non-load bearing maxillofacial applications except for its surface reactivity in contact with aqueous solutions. Various elements have been added to Mg matrix to improve its corrosion resistance and mechanical stability [1-5]. Mg and its alloys possess good specific strength and mechanical properties and biocompatibility behavior. The high strength/weight ratio [6] of Mg alloys make them attractive for widespread application including implantation *in vivo*. The degradation of Mg alloys is beneficial in hard tissue implants unlike steel or titanium implants which need second surgical operation to remove the implant. Controlled spontaneous degradation of Mg can mimic the tissue growth of bones and to deliver safe and nontoxic ions to the body [7-8].

AZXX family of Mg alloys are produced by incorporating aluminum, zinc and manganese for the purposes of improving the corrosion resistance, mechanical properties, and deformability. Still, rapid degradation in body fluids is found to be the main shortcoming of the AZ31 Mg alloys [9-11]. Hence, a rich literature on coating and converting Mg alloy surfaces has formed based on the motivation to improve their stability *in vivo*. Common strategies include coating with physically adsorbable inert suspensions of inorganic particles [12-13], grafting a chemically compatible reactive suspension [14], electrodeposition of an inert layer from solutions [15-17], sputtering with ceramic particles under high energy [18-19] and chemically converting the surface in reactive bath solutions [11, 20-21]. The hybrid approach between simple adsorption of aqueous suspensions, grafting and chemical conversion is an unexplored route with promising results as evident from the literature on coating of metallic implants with calcium phosphate and polymeric cements [2, 22-25]. Our approach focuses on such reactive coating layers, not for enhancing bonding with the bone tissue but to passivate the surface in contact with the body fluids. Such cementitious coatings on Mg alloys can be applied directly before implantation and let fully develop *in vivo* or they can be applied and dried up during the manufacturing stage, and continue development after the implantation by utilizing the body fluid as the solvent. The latter *in situ* approach offers a dynamically evolving surface microstructure that can beneficially counteract the natural biodegradation process that is detrimental to Mg based implants.

Coating of AZ31 surfaces with concentrated suspensions of multiple components that facilitate the desired *in situ* passivation mechanisms necessitates a detailed analysis of singular and synergistic effects of the solute reagents. Solutions of NaCl and MgCl<sub>2</sub> are known to disrupt the passivating hydroxide layer on the surface and help the transformation of the surface especially in alkaline solutions [5]. The pitting corrosion effect of chloride ions is aimed to be balanced by the dissolution inhibiting effect of the extra Mg<sup>2+</sup> ions supplied by MgCl<sub>2</sub>. Samples immersed in NaCl solutions are known to develop Mg oxychloride phases with a porous structure of needle-like crystals. Here a more compact layer of Mg or calcium phosphates is aimed to replace oxychloride phases by supplying high concentrations of PO<sub>4</sub><sup>3-</sup> ions from the particles in coating suspension, similar to a cement reaction. Therefore AZ31 plates were tested in solutions of phosphate salts for their anticipated positive effect while chloride salts were employed for their adverse effects on surface stability. Initially the effects of single component solutions were investigated that provide a continuous supply of phosphate and chloride anions that are the precursors to Mg phosphate and Mg oxychloride cement products. The results provide a baseline reference for the subsequent studies on immersion in multiple component solutions and suspensions as a cementitious coating to control the degradation rate of Mg alloys.

## **II. MATERIAL AND METHODS**

AZ31 alloys were cut into rectangular samples of around 2 cm<sup>2</sup> area and immersed in aqueous solutions of various compositions at ambient conditions (20 °C and atmospheric pressure). Alloy samples were placed statically in glass beakers with 200 mL of solutions for 21 days and analyzed at specific intervals (1, 3, 7, 14, 21 days) by gravimetry to account for the change in their mass. Also the solution pH was monitored at the same intervals. Test media included deionized water (DIW), 3.5 wt% NaCl, 3.5 wt% MgCl<sub>2</sub> solutions and DIW saturated with phosphate salts: monocalcium phosphate (MCP), dicalcium phosphate (DCP), tricalcium phosphate (TCP), and potassium dihydrogen phosphate (PDP). All chemicals were commercially obtained analytical grade reagents. DIW was obtained from a Merck millipore Q3 machine. Immersion tests were completed after 21 days of monitoring the mass and pH variations. Extracted samples were dried in air at ambient conditions. The surfaces of the dried plates were characterized using SEM, EDX and XRD to identify the final composition.

Morphological analysis was done by using a FEI QUANTA 250 FEG scanning electron microscope. A secondary electron (SE) detector was used to capture micrographs at an accelerating voltage of 3.00 kV and a wedge distance of 10 mm. An electron dispersive X-ray detector coupled with a backscattered electron (BSE) detector was used for elemental analysis of the sample surface. The images were obtained at an accelerating voltage of 20 kV and a wedge distance of 5 mm. XRD analysis was conducted by using a Philips X'Pert Pro powder diffractometer with Cu K $\alpha$  radiation at a generator voltage of 45 kV and a tube current of 40 mA. All XRD patterns were obtained at a scan step size of 0.05 and 4 seconds per step. Rietveld refinement method was employed for the quantitative XRD analysis. Profex software from Doebelin.org and XRD references from Crystallography Open Database were used for phase identification and quantification.

## **III. RESULTS AND DISCUSSIONS**

The overall variation of sample weights in both aqua and aqueous solutions of single components is given in Figure 1. While DIW minimally affected the chemical stability of the alloy surfaces, they transformed gradually in all solutions. Generally calcium phosphate solutions resulted in relatively thinner depositions due to their lower solubility in water. Saturated PDP solution formed an especially thick layer which can be further compacted by the addition of various other phases. NaCl and MgCl<sub>2</sub> solutions also resulted in a thick Mg oxychloride layer that is loose due to the needle-like crystal morphology. Therefore chloride salts should not be added to multiple component solutions in high concentrations, its amount should be kept at an optimum level for the purpose of activating the alloy surfaces in alkaline condition induced in DCP or TCP solutions.

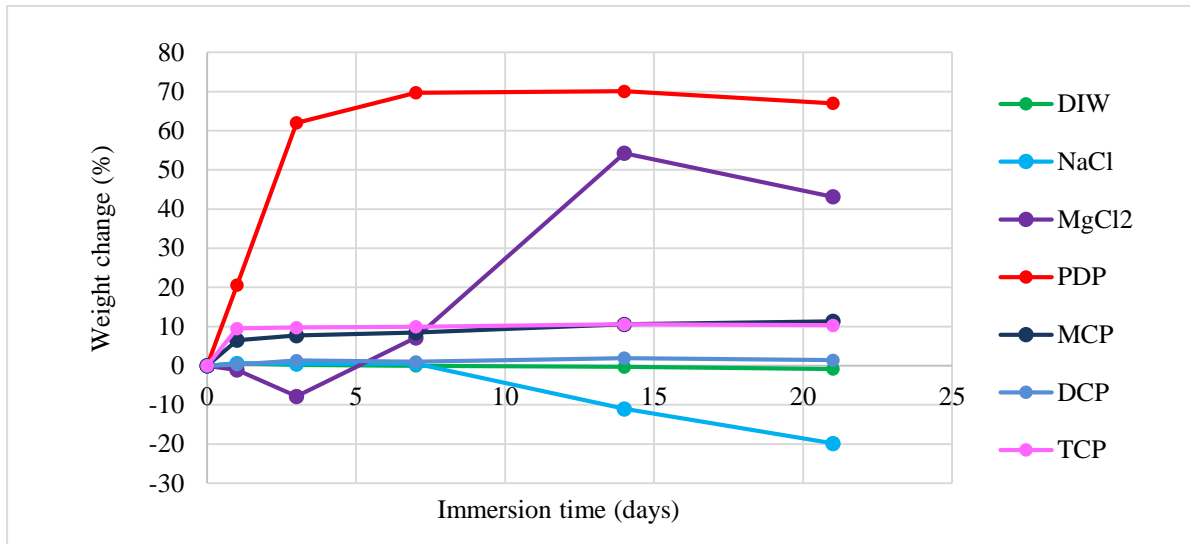


**Figure 1.** Variation of the weight of samples immersed in solutions of single components with time.

Variation of pH of the single phase solutions during immersion tests is given in Figure 2. The solutions were initially acidic in the presence of NaCl, PDP and MCP but all gradually became alkaline. It is an indication of early rapid dissolution of the surface, presumably at growing pits. Subsequent supersaturation build up of Mg hydroxide starts to passivate the surface gradually by the formation of either simple  $Mg(OH)_2$  or more complex hydroxide compounds according to the species in the solution. In acidic MCP, NaCl and PDP solutions a passivating hydroxide layer cannot form on the surface of the alloys initially, rather Mg is exposed in a reactive form before transforming to products of reactions [5]. Chloride addition to these systems is not necessary due to their already reactive surfaces. Instead species that can slow down ion transport and dissolution like polymeric hydrogels and hydroxy carboxylic acid salts can produce a more controlled deposition.

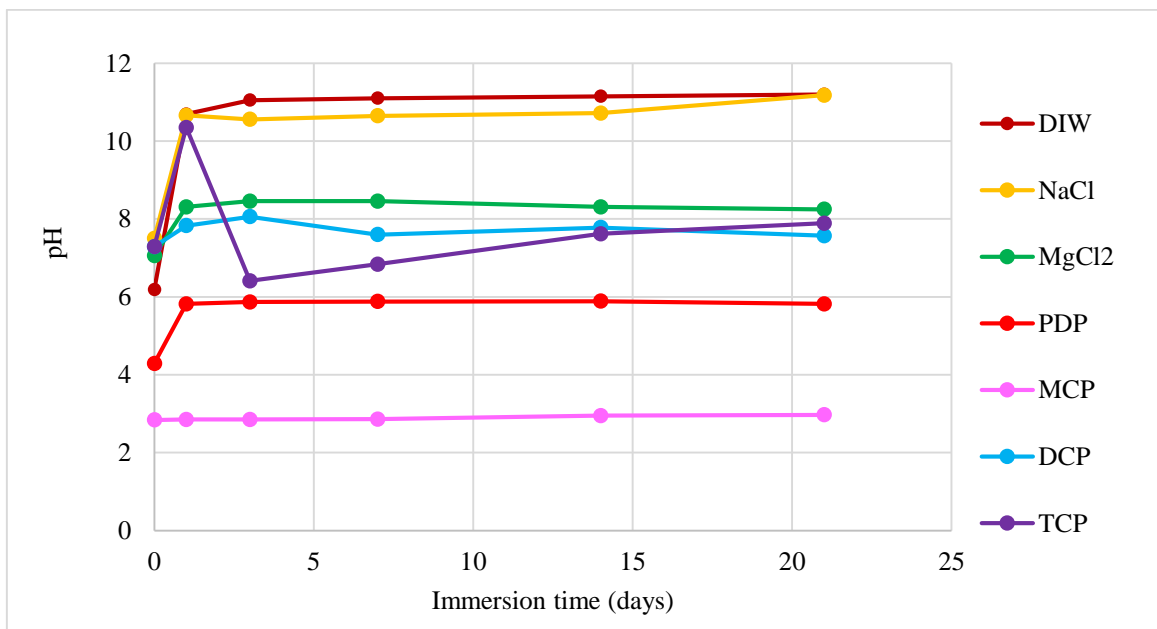


**Figure 2.** Variation of solution pH in deposition systems containing single components.

The degradation behavior of AZ31 in DIW serves as a baseline reference for other immersion tests. It is seen that the weight loss and depositions are negligible in pure water. According to the morphological and compositional analysis of these samples given in Figures 3 and 4, Mg metal and hydrotalcite

( $\text{Mg}_6\text{Al}_2\text{CO}_3(\text{OH})_{16}\cdot 4\text{H}_2\text{O}$ .) were the detected phases on the surface of AZ31. As seen in Figure 4b, hydroxalcite peaks are broad and intense which indicates that these crystals are nanoscale and cover the surface uniformly. The BSE detector image in Figure 4a revealed the presence of bright spots that are homogeneously distributed on the surface. These inclusions that are also visible in Figures 3a and 3b, are composed of Mn, Zn, Al and Mg in some form of intermetallic compound that is oxidized as well, according to the point EDX analysis on one of them (spectrum 25). These are known to form during the alloying process and function as passivation points by binding elements that can cause micro-galvanic corrosion [26]. Figures 3c, 3d and 4a show that these phases form a microporous structure on the surface, that likely originates from the degradation of the grain boundaries of the elongated surface grains.

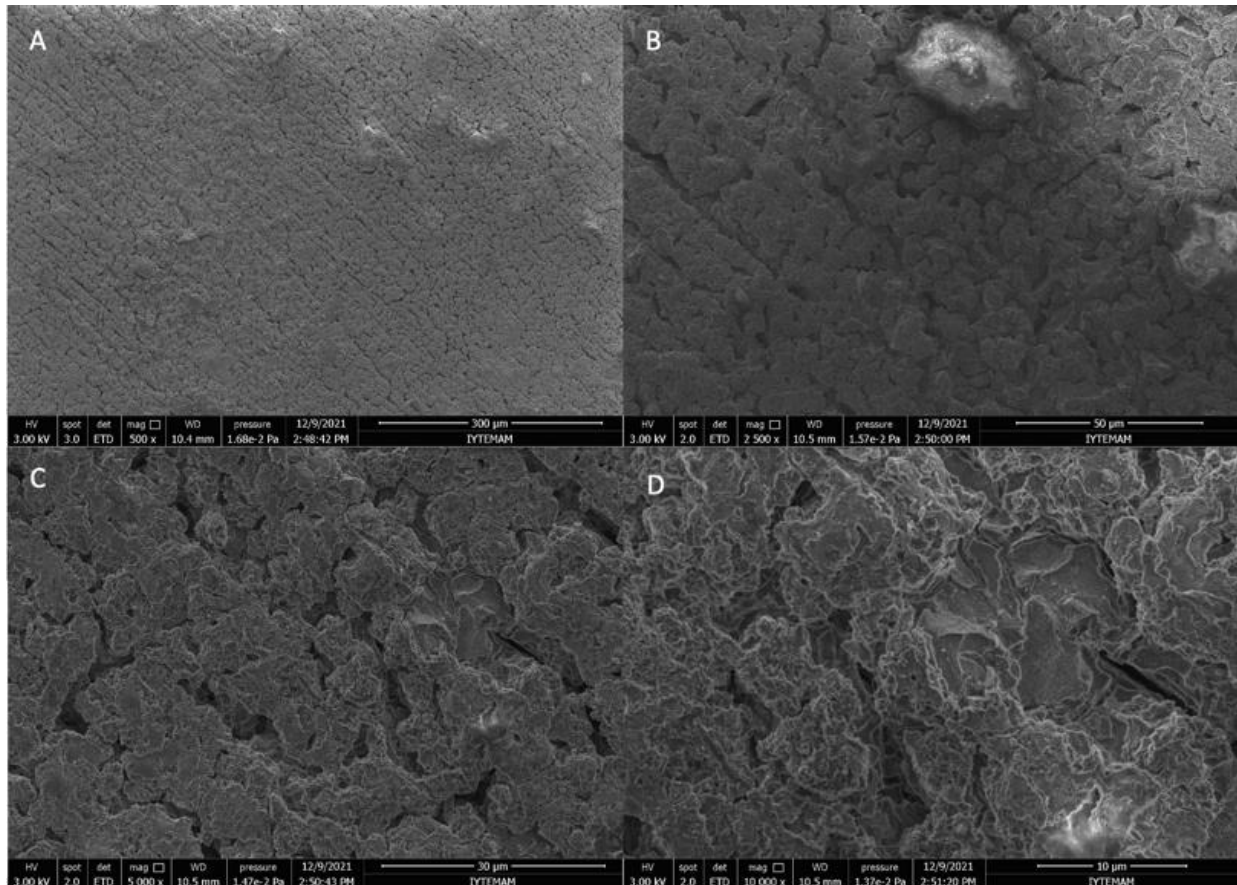


**Figure 3.** Microstructure of AZ31 surfaces immersed in pure water, imaged using a SE detector at a magnification of: (A) 500x, (B) 2500x, (C) 5000x, (D) 10000x.



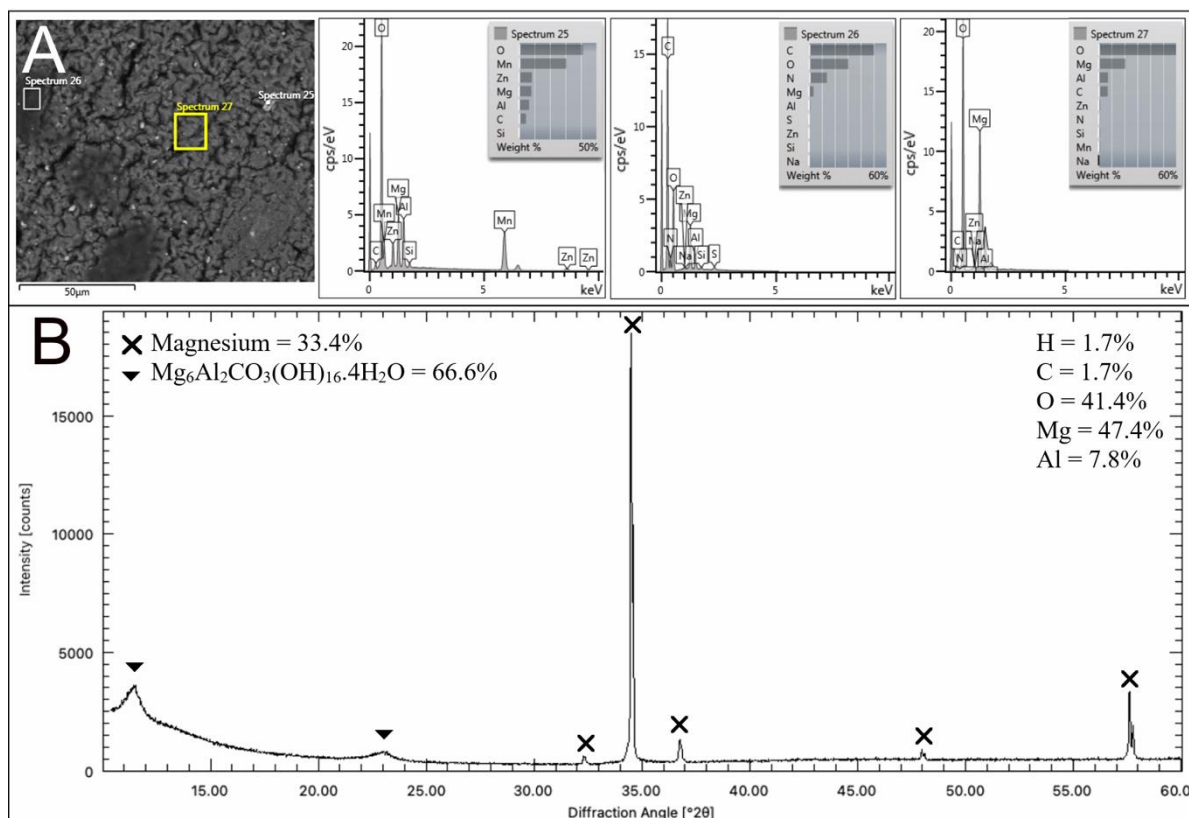


**Figure 4.** Compositional analysis of AZ31 samples immersed in DIW for 21 days: **A)** EDX analysis results from an area imaged with a BSE detector (spectra depict weight ratios), **B)** Quantitative XRD analysis results (percentages of the compounds and elements are based on weight).

It was observed that AZ31 rapidly degraded in NaCl solution with the formation of a thick Mg oxychloride layer. This is reflected in the morphological and phase analysis given in Figures 5e,f and 6a. Bush-like formations of oxychloride needles create loosely interpenetrating layers. MgO, Mg(OH)<sub>2</sub> and various Mg oxychloride stoichiometry were detected by EDX analysis. The elemental ratio of Mg/Cl was found between 4 to 2 and Mg/O was found close to 1/3 in the needles which point to the formations of 5Mg(OH)<sub>2</sub>·MgCl<sub>2</sub>·8H<sub>2</sub>O, also known as the 5-1-8 phase in Mg oxychloride cement literature. The higher ratio of Mg/O at region 8 indicates some of the X-ray signals are coming from deeper parts where Mg metal is present. These observations were further confirmed by quantitative XRD of the dry surfaces after deposition (Figure 6b). Mg was found in abundance and the rest of the surface (excluding gold coating) was 5-1-8 phase.

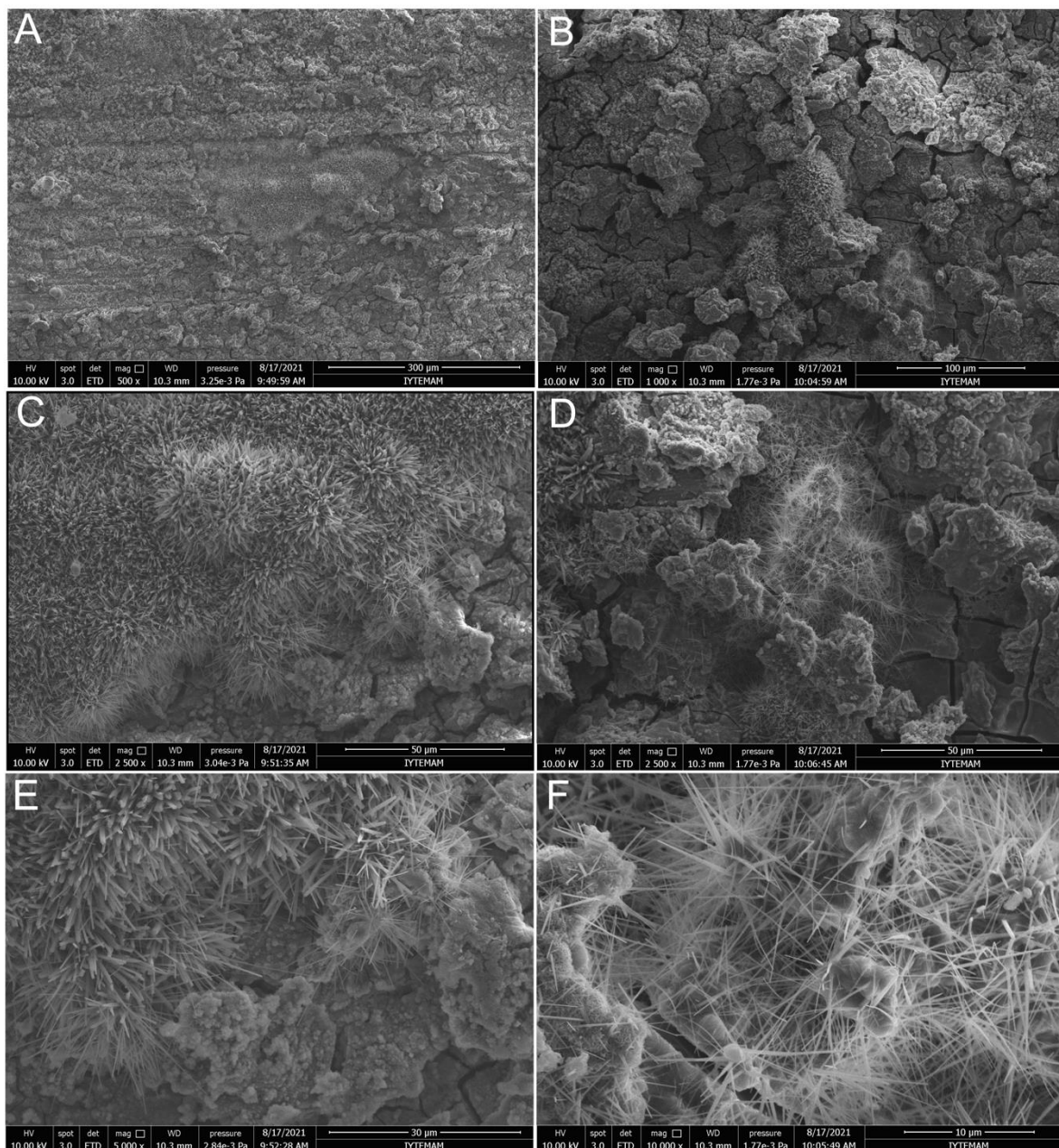


**Figure 5.** Microstructure of AZ31 surfaces immersed in 3.5 wt% NaCl solution, imaged using a SE detector at a magnification of: (A) 500x, (B) 1000X, (C, D) 2500X, (E) 5000X, (F) 10000X.

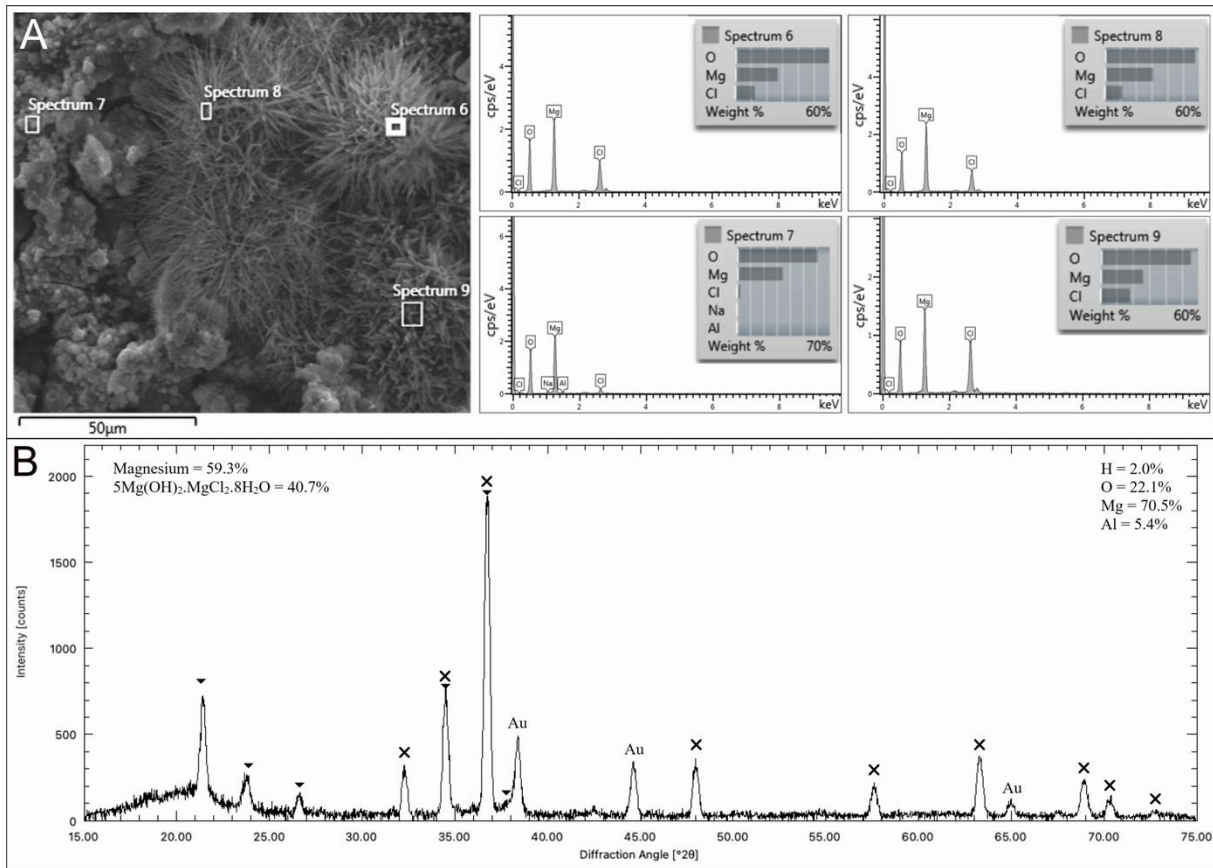


**Figure 6.** Compositional analysis of AZ31 plate immersed in 3.5% sodium chloride solution: **A**) EDX analysis results from an area imaged with a BSE detector (spectra depict weight ratios), **B**) Quantitative XRD analysis results (percentages of the compounds and elements are based on weight).

The effect of Mg chloride was also investigated by EDX and gravimetric analysis. The elemental composition given in Figure 7 shows similar stoichiometric ratios as the NaCl solution. The ratio of Mg/Cl was found around 3 in spectrum 1 while it was around 2 in the second and third regions. The O/Mg ratio in all three regions was around 4. The stoichiometry of regions 2 and 3 corresponds to 3-1-8 phase ( $3\text{Mg}(\text{OH})_2 \cdot \text{MgCl}_2 \cdot 8\text{H}_2\text{O}$ ) that is detected in XRD analysis to be around 11%. The stoichiometry obtained from region 1 is most likely the 5-1-8 phase that was also found on samples immersed in NaCl solutions. It is known to convert to  $3\text{Mg}(\text{OH})_2 \cdot \text{MgCl}_2 \cdot 8\text{H}_2\text{O}$  and then to  $2\text{MgCO}_3 \cdot \text{Mg}(\text{OH})_2 \cdot \text{MgCl}_2 \cdot 6\text{H}_2\text{O}$  upon drying in air after the XRD analysis which explains the C peaks in the spectra. Close examination of these regions shows that there are characteristic needle structure of 5-1-8 around the tubular structure that is presumed to be 3-1-8 phase (Figure 8).

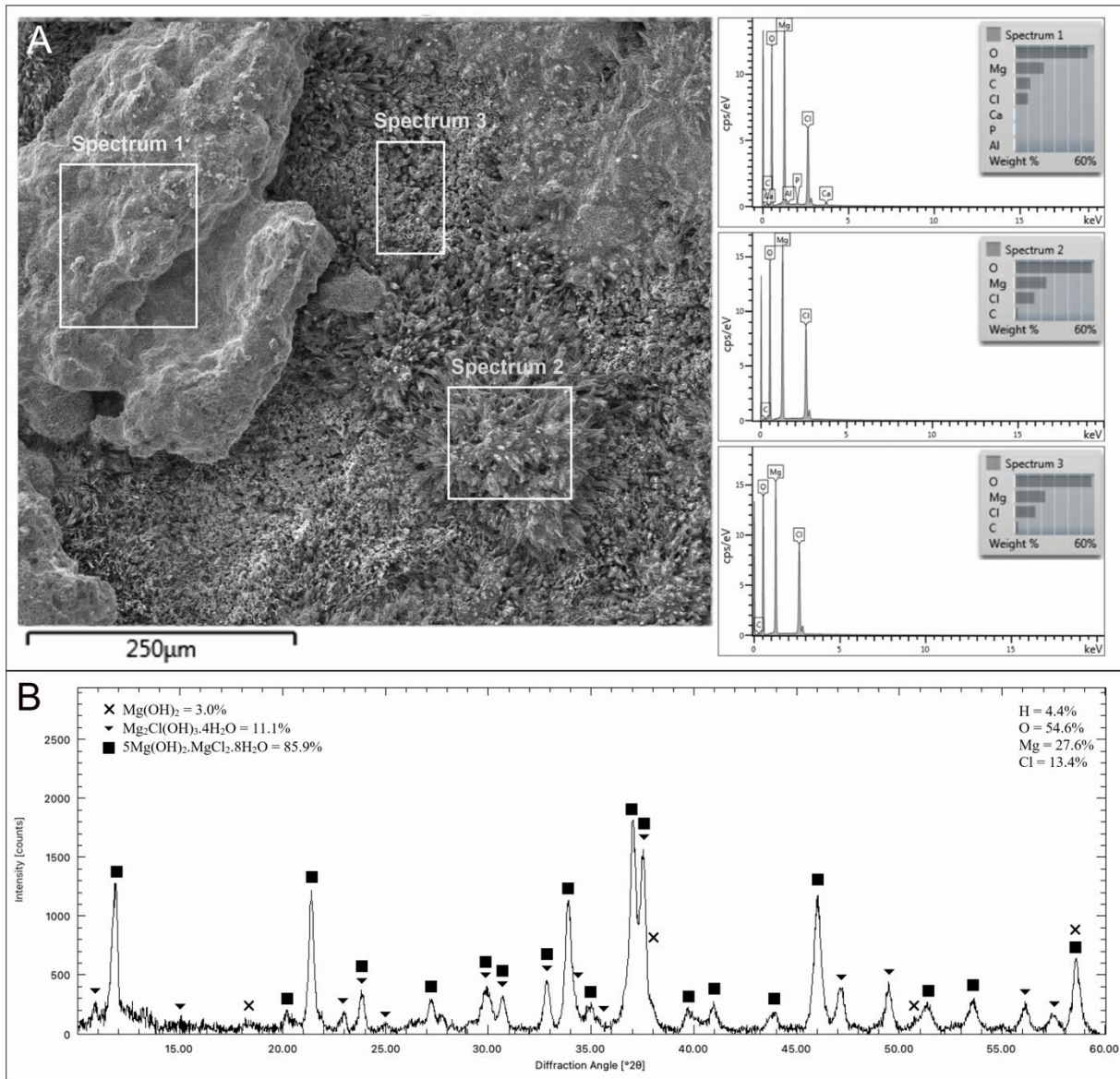


**Figure 7.** Compositional analysis of AZ31 plate immersed in 3.5 wt% Mg chloride solution: **A)** EDX analysis results from an area imaged with a BSE detector (spectra depict weight ratios), **B)** Quantitative XRD analysis results (percentages of the compounds and elements are based on weight).

The variation of sample weight upon immersion in 3.5 wt% Mg chloride and sodium chloride solutions shows a slight difference such that mass loss is detected in the first few days in Mg chloride solution that is followed by significant deposition up to day 14, while NaCl solution immediately caused deposition. There is a significant difference in the initial pH values between the two solutions which stems from higher initial Mg ion concentration and the resulting smaller chemical potential for dissolution in Mg chloride solution. The pH increase seen in Figure 2 for the initial period resulted from the dissolution of Mg hydroxides and the subsequent fall is attributed to the formation of the oxychloride phases.

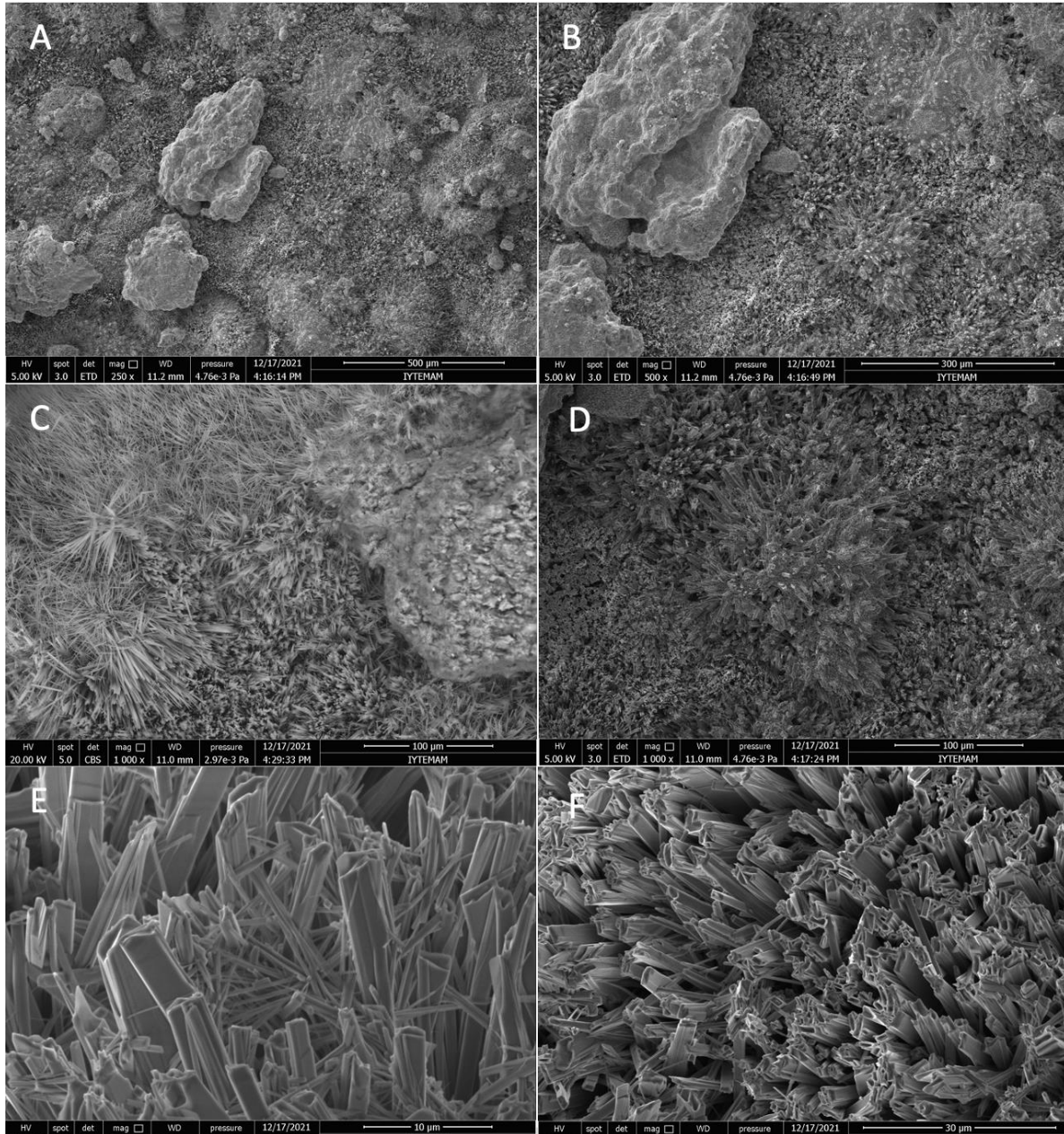


**Figure 8.** Surface morphology of AZ31 sample immersed in saturated MgCl<sub>2</sub> solution for 21 days, imaged using a SE detector at a magnification of: (A) 250X, (B) 500X, (C) 1000X, (D) 1000X, (E) 10000X, (F) 5000X.

The MCP solution is highly acidic and provides a favorable medium for the chemical conversion of Mg alloys. Figure 1 shows that a sudden deposition upon immersion was followed by gradual increase in weight. As a result the solution increased continuously from 2.84 to 2.97. According to phase analysis results, the acidic solution induced the formation of CaHPO<sub>4</sub> and CaHPO<sub>4</sub>·2H<sub>2</sub>O phases that are stable under acidic conditions (Figure 9). Their Ca/P ratio of 1 is more than that of MCP (1/2) which requires some phosphate to stay in solution or to form a Mg phosphate compound. There are no Mg atoms or compounds on the surface according to the surface phase analysis. This is attributed to the inhibiting effect of the acidic medium on Mg hydroxide formation and the competition provided by calcium phosphates to acidic Mg phosphates such as newberyite. The detailed morphology shown in Figure 10 is compact with large calcium phosphate crystals that are characteristic of CaHPO<sub>4</sub>·2H<sub>2</sub>O [27].

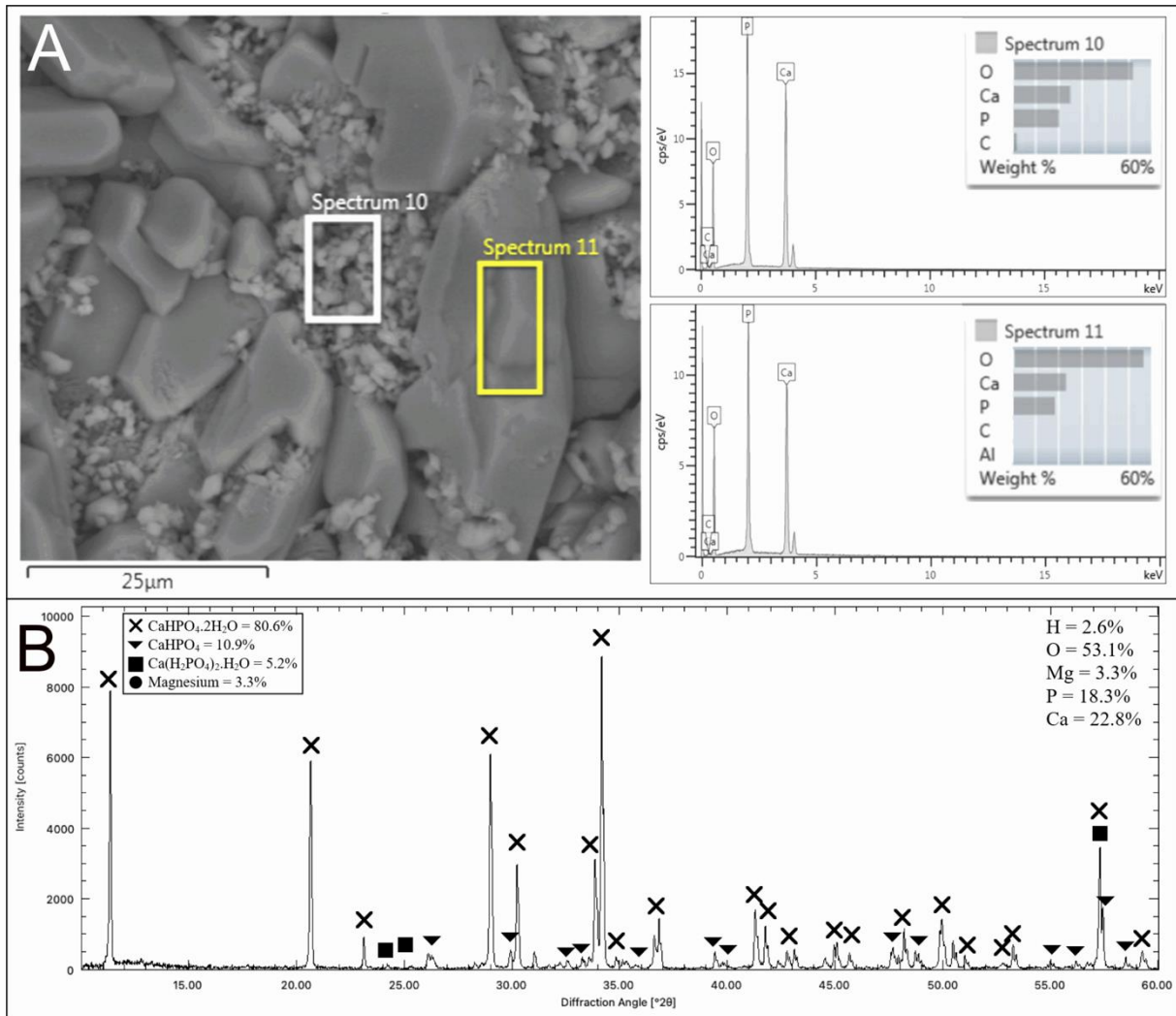


**Figure 9.** Compositional analysis of AZ31 plate immersed in saturated MCP solution: **A)** EDX analysis results from an area imaged with a BSE detector (spectra depict weight ratios), **B)** Quantitative XRD analysis results (percentages of the compounds and elements are based on weight).

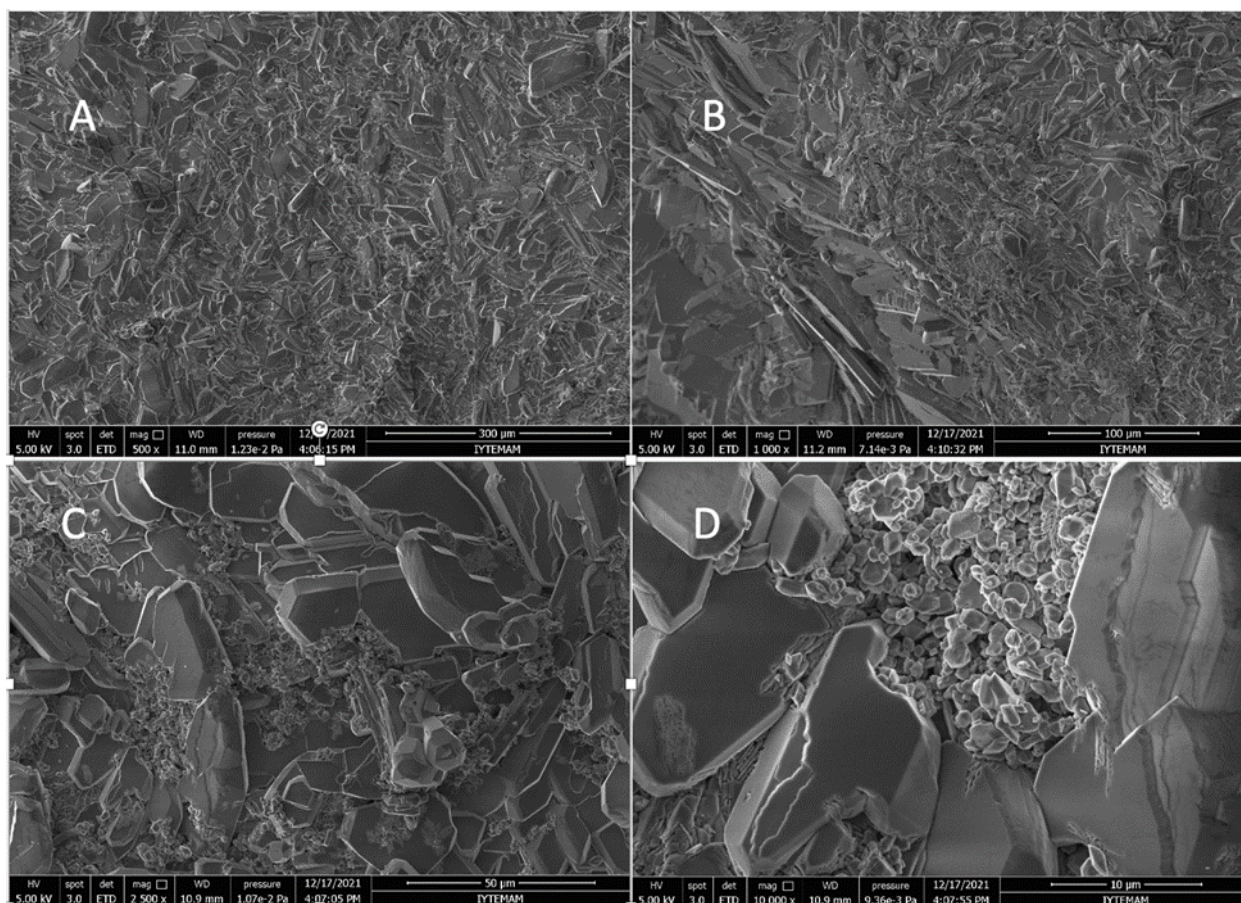


**Figure 10.** Surface morphology of AZ31 sample immersed in saturated MCP solution for 21 days, imaged using a SE detector at a magnification of: (A) 500X, (B) 1000X, (C) 2500X, (D) 10000X.

The saturated solution of DCP contains less calcium and phosphate ions and is less acidic compared to the saturated MCP solution due to its much less solubility in water. As a result, the weight of the sample immersed in this solution only increased by 1% in 21 days. This was accompanied by a parallel change in pH between 7.3-8.1. The surface analysis shows cracked layers of Mg hydroxide and phosphates that are covered with calcium phosphate particles (Figure 11). EDX spectra 8 and 9 reveal that the Ca/P ratio of these particles is around 1 (same as DCP). Therefore these particles are most likely physically adsorbed particles that were excess in solution. Spectrum 7 reveals that the cracked alloy surface contains some phosphate phase of Mg or aluminum, together with Mg hydroxides and carbonates that is stable at neutral pH. Close examination of the surface layer reveals that a sheet-like formation of these phases is present over the alloy surface (Figure 12). Its formation mechanism is thought to be a cementitious reaction, gradual dissolution of the deposited DCP particles in response to solution pH and integration of the phosphate anions with metal cations leaching from the surface. DCP phase is known to be stable at acidic conditions and transform to apatite as pH increases above neutral values [28]. The matching of the shapes of the broken pieces with the grain shapes indicates that they have grown epitaxially on the surface after the cracks have formed which should coincide with the second rise in the pH after 14 days. Interestingly no phosphate compounds were found in XRD analysis as shown in Figure 11b. Only the base alloy and its hydroxide form was detected which means that the DCPD particles occupy a small proportion of the diffracting volume. The thin sheet layer may also be small compared to the alloy surface underneath or it may be a glassy phase that forms as a gel in the nanoscale. An intermetallic protrusion is also seen in Figure 12b.

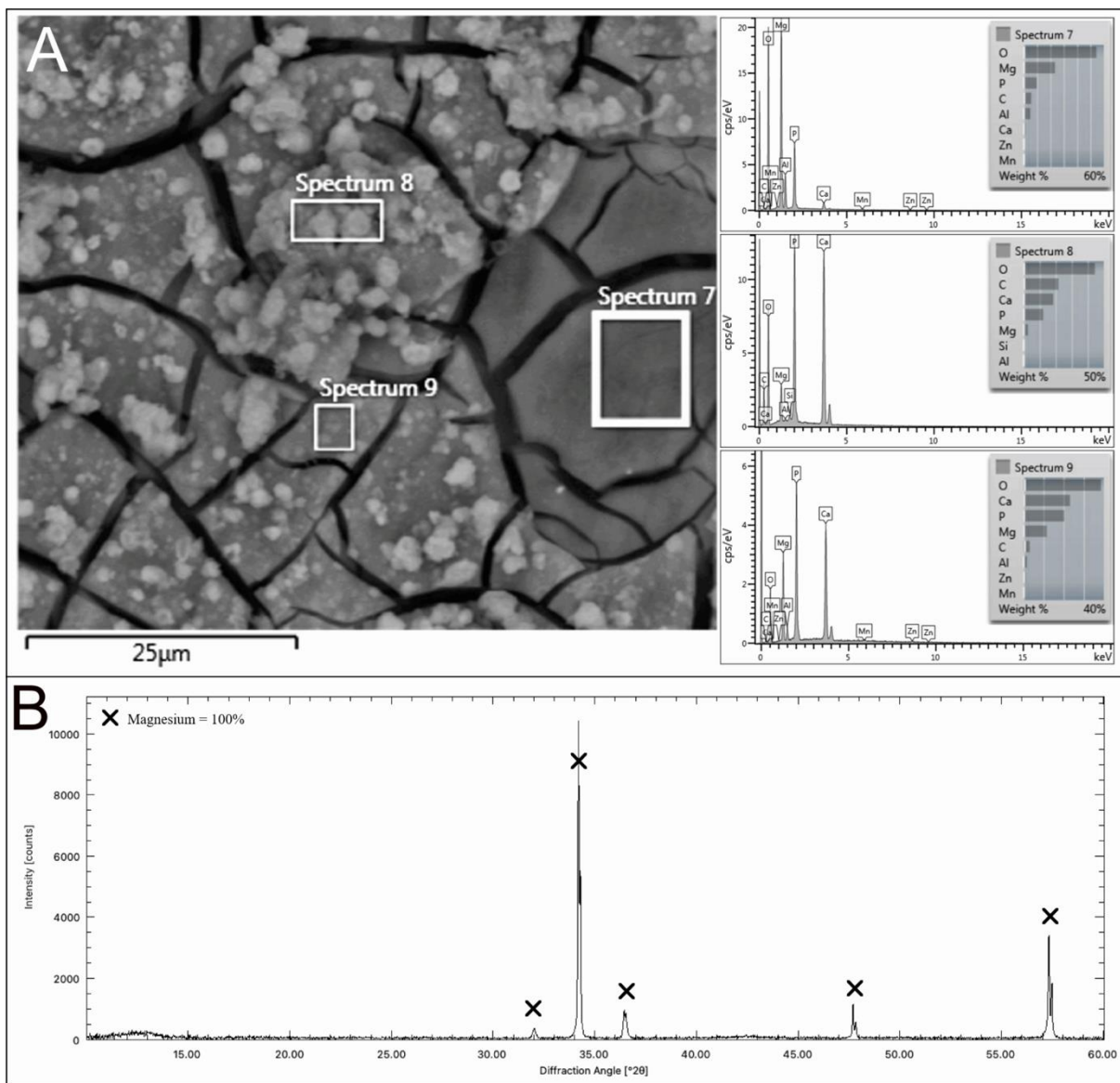


**Figure 11.** Compositional analysis of AZ31 plate immersed in saturated DCP solution: **A)** EDX analysis results from an area imaged with a BSE detector (spectra depict weight ratios), **B)** Quantitative XRD analysis results.



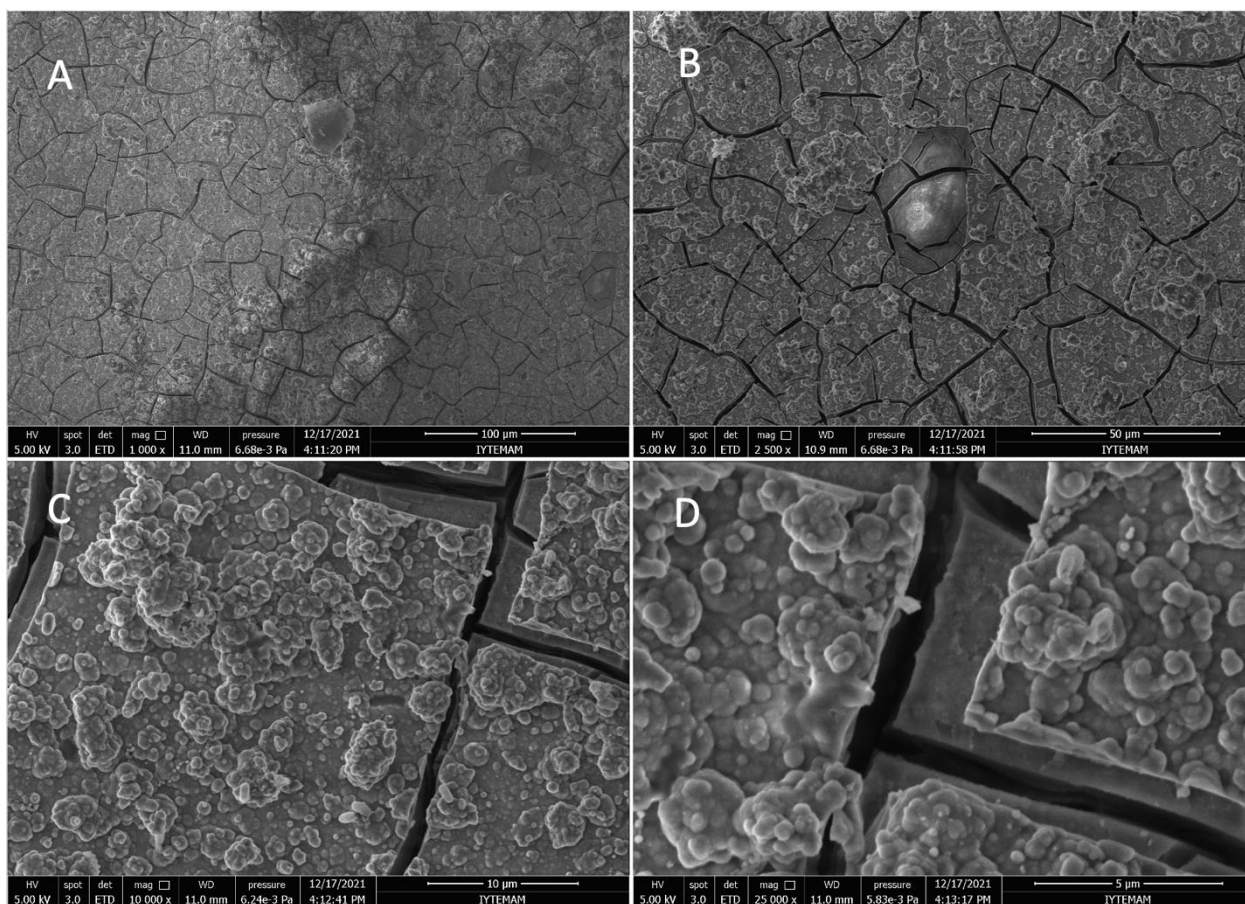


**Figure 12.** Surface morphology of AZ31 sample immersed in saturated DCP solution for 21 days, imaged using a SE detector at a magnification of: (A) 1000X, (B) 2500X, (C) 10000X, (D) 25000X.

AZ31 plates immersed in TCP solution exhibited a sudden increase in weight in the first day but the weight remained relatively constant later (Figure 1). Solution pH fluctuated in a wide range between 6-10 during this abrupt change and then stabilized towards pH=8 (Figure 2). Unlike DCP, the TCP phase is stable under neutral and alkaline conditions but degrade rapidly under acidic conditions. For this reason, combination of MCP and TCP makes an effective bone cement with continuous dissolution of TCP under acidic conditions facilitated by MCP dissolution [28]. Aqueous TCP solution is inert by itself and this is reflected in the relatively constant weight and pH data after the first day. The initial rise in both data is assumed to be due to the covering of the surface by the physical adsorption of particles which may have caused some dissociation of hydroxalcite as well as TCP. EDX analysis of the surface shows that the particle agglomerations have a Ca/P atomic ratio between 1.4 and 1.7 which is close to the stoichiometric ratio of TCP (Figure 13a). Measurement on the bare surface yields a similar composition to the samples immersed in DCP solutions. Therefore the same sheet-like structure seems to be present here as well, with less concentrations of P, C, Al. This may be attributed to the more alkaline solution, smaller phosphate concentration supplied by TCP, less surface dissolution and less epitaxial formation on the hydroxalcite surface. Close examination shown in Figure 14 reveals that particle agglomerates have stably covered the surface. Unlike MCP and DCP, TCP can only form through solid state reactions at elevated temperature and the sintered morphology is its characteristic. XRD analysis of the alloy plate was essentially the same as that immersed in DCP solution (Figure 13b). Monolayers of physically adsorbed particles/agglomerates seem to be too thin for their detection by XRD and the bulk of the alloy plate diffracts at much more intensity. Their XRD pattern is simpler than the AZ31 alloy immersed in DIW, without the hydroxalcite peaks. Homogeneously covering hydroxalcite nanocrystals seem to be the precursor for the sheet structure formed with the physically adsorbed DCP and TCP.

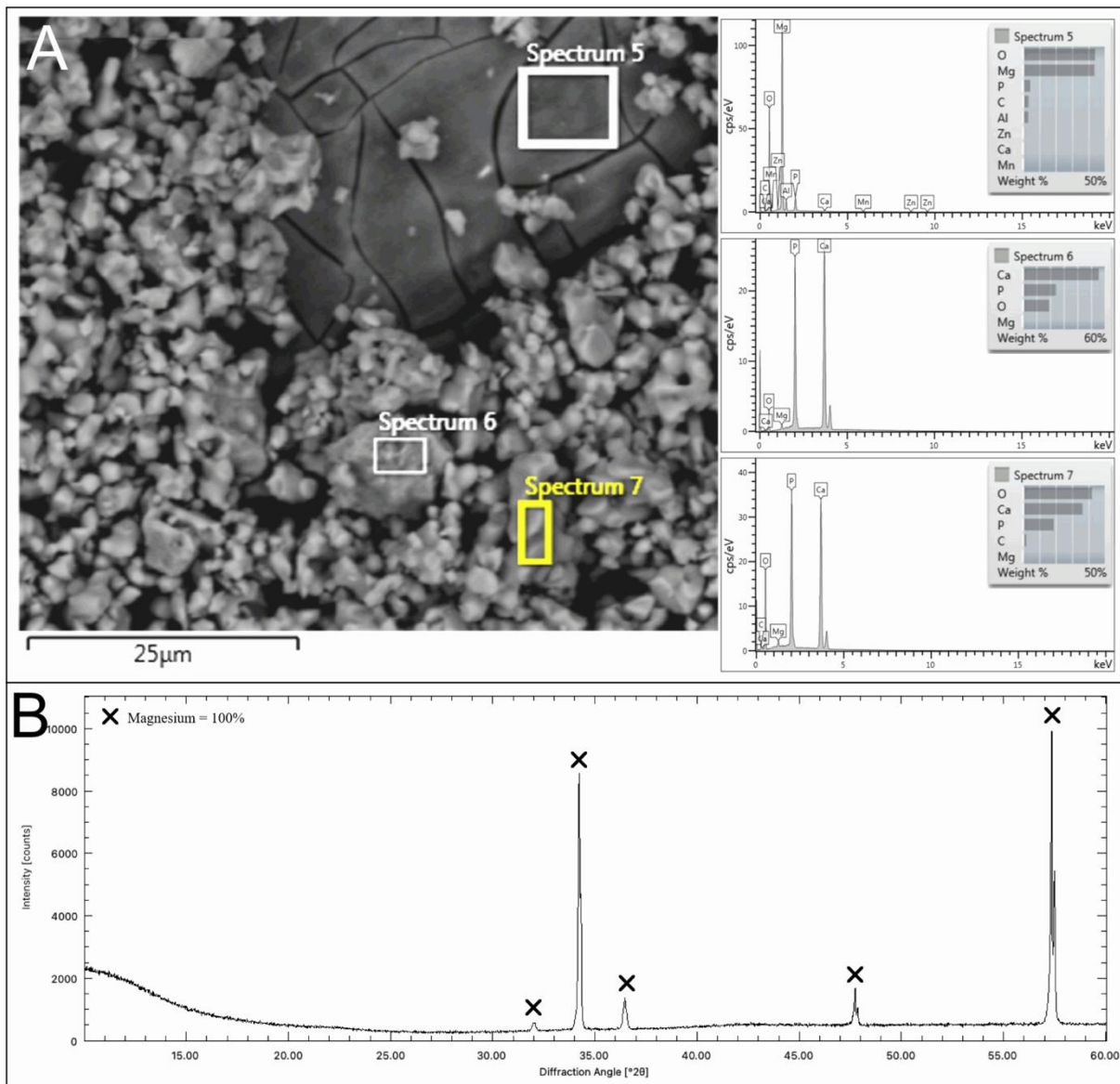


**Figure 13.** Compositional analysis of AZ31 plate immersed in saturated TCP solution: **A)** EDX analysis results from an area imaged with a BSE detector (spectra depict weight ratios), **B)** Quantitative XRD analysis results.

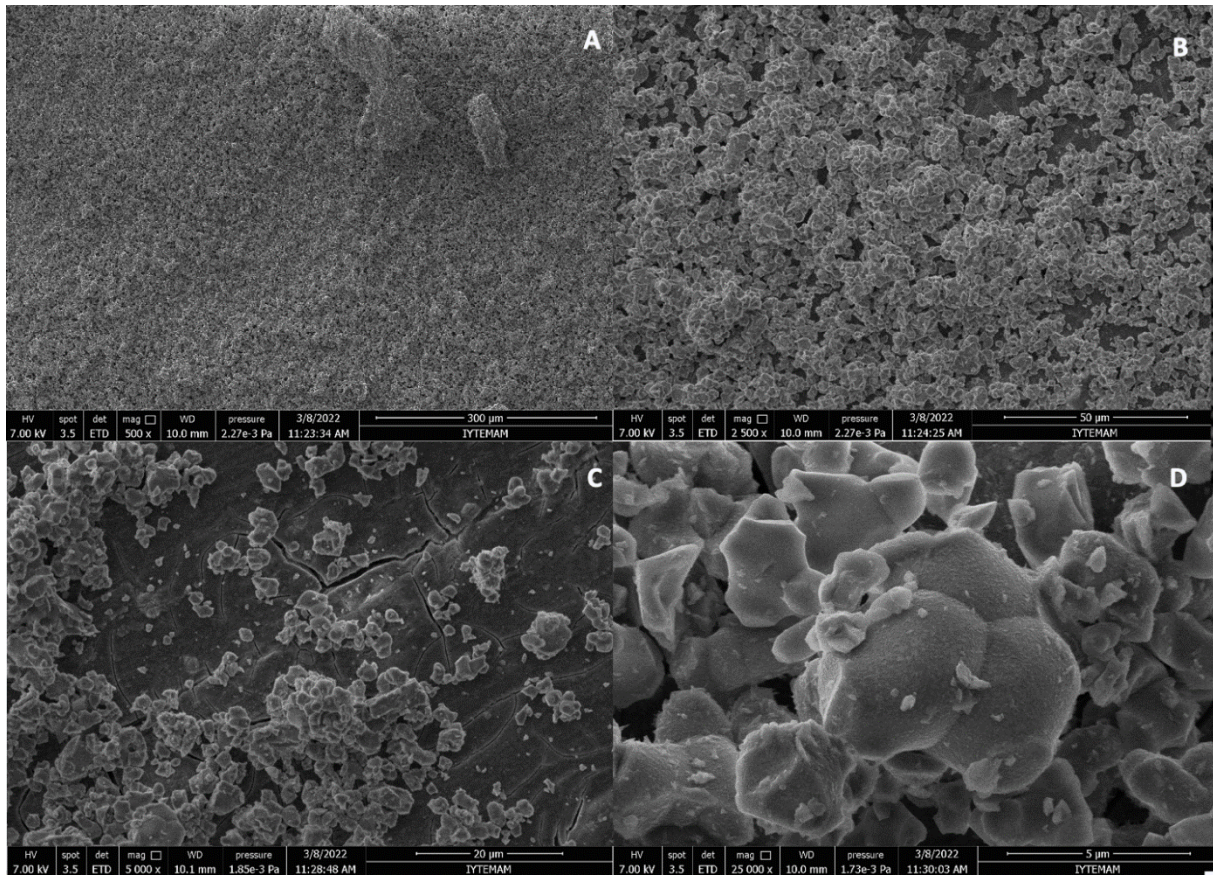


**Figure 14.** Surface morphology of AZ31 sample immersed in saturated TCP solution for 21 days, imaged using a SE detector at a magnification of: (A) 500X, (B) 2500X, (C) 5000X, (D) 25000X.

The saturated PDP solution is expected to form K-struvite ( $\text{MgKPO}_4 \cdot 6\text{H}_2\text{O}$ ) on Mg alloys under alkaline conditions and newberyite ( $\text{MgHPO}_4 \cdot 3\text{H}_2\text{O}$ ) under acidic conditions according to the Mg phosphate literature [29]. It induced a significant deposition in the first three days while the solution pH rose from 4 to 6 in the first day with no further changes in the remaining time. The surface analysis results reveal that a thick layer of newberyite deposited on the surface rather than K-struvite (Figure 15). K is only detected on the delaminated surface, possibly in struvite form as also found in XRD analysis. The thick layer consists of overlapped plates of newberyite according to the elemental ratios. Detailed surface morphology given in Figure 16 indicates a compact microstructure made of monolithic plates stacked next to each other.

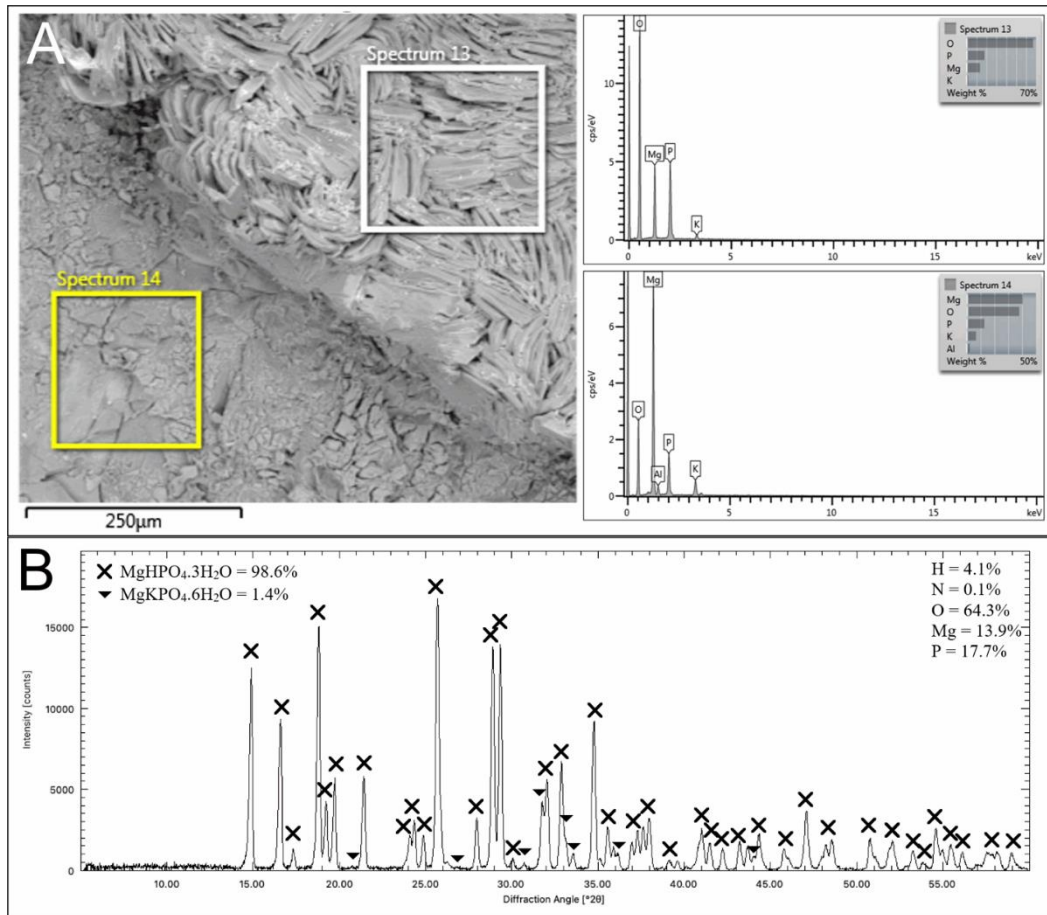


**Figure 15.** Compositional analysis of AZ31 plate immersed in saturated PDP solution: A) EDX analysis results from an area imaged with a BSE detector (spectra depict weight ratios), B) Quantitative XRD analysis results (percentages of the compounds and elements are based on weight).

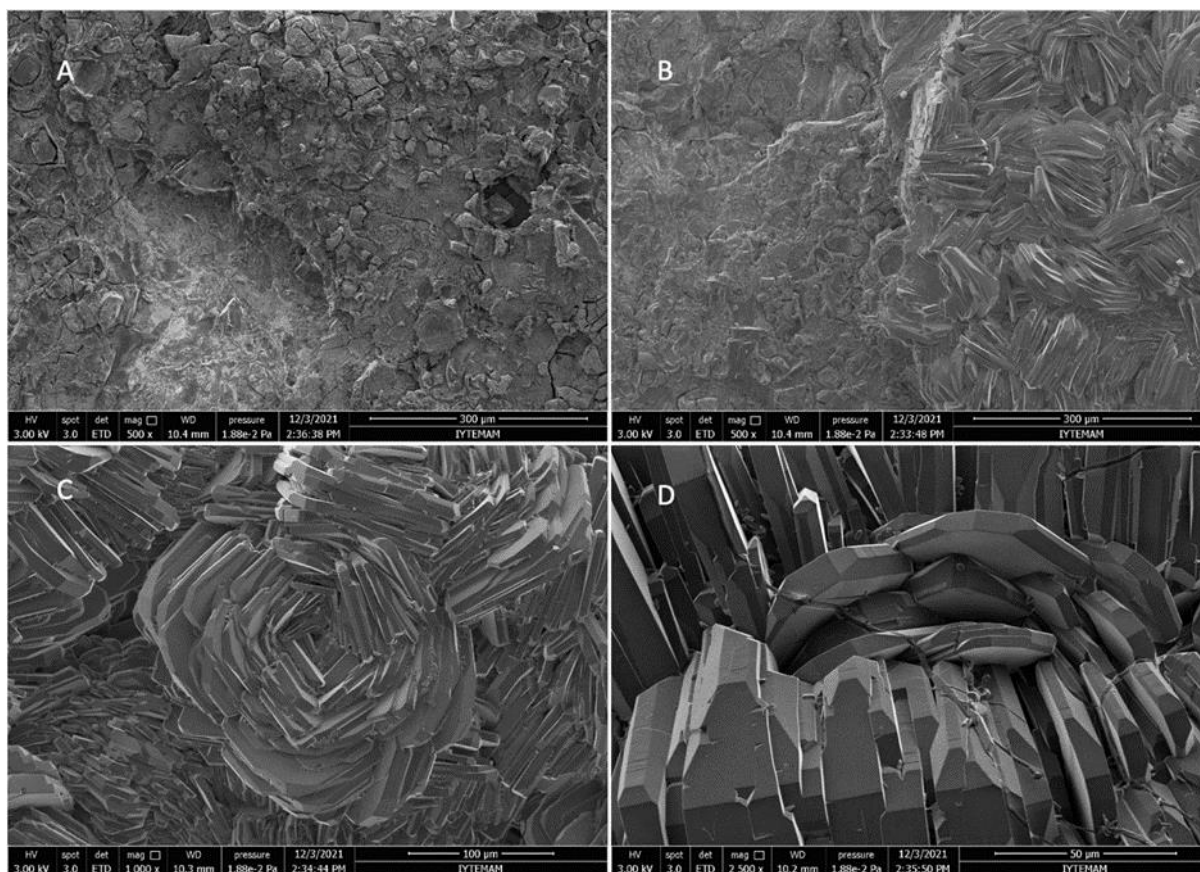


**Figure 16.** Surface morphology of AZ31 sample immersed in saturated PDP solution for 21 days, imaged using a SE detector at a magnification of: (A) 500X, (B) 500X, (C) 1000X, (D) 2500X.

## IV. CONCLUSION

AZ31 surfaces acquired compositions corresponding to the stoichiometries of Mg hydroxide carbonates, Mg phosphates and calcium phosphates upon immersing in various aqueous chloride and phosphate solutions. These are identified through EDX and XRD analyses as  $Mg_6Al_2CO_3(OH)_{16} \cdot 4H_2O$  (hydrotalcite),  $MgHPO_4 \cdot 3H_2O$  (newberyite),  $MgKHPO_4 \cdot 6H_2O$  (struvite),  $CaHPO_4 \cdot 2H_2O$  (brushite or DCPD),  $CaHPO_4$  (monetite or DCPA),  $5Mg(OH)_2 \cdot MgCl_2 \cdot 8H_2O$  (5-1-8 oxychloride phase) and  $3Mg(OH)_2 \cdot MgCl_2 \cdot 8H_2O$  (3-1-8 oxychloride phase).  $Mg(OH)_2$  (brucite) is also detected in small quantities. Detected X-ray diffraction intensity of base Mg matrix was high in the case of thin and physically adsorbed particles while reactive media like chloride and acidic phosphate solutions resulted in a thick layer inhibiting its detection. A thin, sheet-like formation that is assumed to be originating from hydrotalcite formed in DCP and TCP solutions and could not be detected by XRD probably due to its nanostructure. Mg oxychloride morphologies are needle-like clusters with loose structures that are nonideal for barrier performance while newberyite and brushite phases form a dense layer on AZ31 alloy. Further studies are focused on coating with concentrated suspensions of these saturated solutions to induce in situ formation of the barrier layer in contact with such aqueous environments. The initial results confirm their strong resistance against corrosion.

**ACKNOWLEDGEMENTS:** The authors appreciate the financial support from Scientific and Technological Research Council of Turkiye (TUBITAK) (Project No: 2020-119N759). İzmir Institute of Technology Materials Research Center staff is acknowledged for their assistance in characterizations. Doebelin.org and Crystallography Open Database (Crystallography.net) are acknowledged for sharing their XRD analysis software and database.

## **V. REFERENCES**

- [1] X. Li, X. Liu, S. Wu, K. W. K. Yeung, Y. Zheng, and P. K. Chu, "Design of magnesium alloys with controllable degradation for biomedical implants: From bulk to surface," *Acta Biomater.*, vol. 45, pp. 2–30, 2016.
- [2] Z. Ran, W. Dai, K. Xie, and Y. Hao, "Advances of biodegradable magnesiumbased implants for orthopaedics," *Life Res.*, vol. 5, no. 7, pp.1-12, 2022.
- [3] T. Cain, L. G. Bland, N. Birbilis, and J. R. Scully, "A compilation of corrosion potentials for magnesium alloys," *Corrosion*, vol. 70, no. 10, pp. 1043–1051, 2014.
- [4] F. Witte, V. Kaese, H. Haferkamp, E. Switzer, A. Meyer-Lindenberg, C.J. Wirth, and H. Windhagen, "In vivo corrosion of four magnesium alloys and the associated bone response," *Biomaterials*, vol. 26, no. 17, pp. 3557–3563, 2005.
- [5] F. Witte, N. Hort, C. Vogt, S. Cohen, K. U. Kainer, R. Willumeit, and F. Feyerabend, "Degradable biomaterials based on magnesium corrosion," *Curr. Opin. solid state Mater. Sci.*, vol. 12, no. 5–6, pp. 63–72, 2008.
- [6] E. Ghali, "Magnesium and magnesium alloys," *Uhlig's Corros. Handb.*, pp. 809–836, 2011.
- [7] W. D. Müller, M. L. Nascimento, M. Zeddies, M. Córscico, L. M. Gassa, and M. A. F. L. de Mele, "Magnesium and its alloys as degradable biomaterials: corrosion studies using potentiodynamic and EIS electrochemical techniques," *Mater. Res.*, vol. 10, pp. 5–10, 2007.
- [8] Y. Xin, K. Huo, H. Tao, G. Tang, and P. K. Chu, "Influence of aggressive ions on the degradation behavior of biomedical magnesium alloy in physiological environment," *Acta Biomater.*, vol. 4, no. 6, 2008.
- [9] S. Seetharaman, D. Sankaranarayanan, and M. Gupta, "Magnesium-Based Temporary Implants: Potential, Current Status, Applications, and Challenges," *J. Funct. Biomater.*, vol. 14, no. 6, p. 324, 2023.
- [10] A. Carangelo, A. Acquesta, and T. Monetta, "Durability of AZ31 magnesium biodegradable alloys polydopamine aided. Part 2: ageing in Hank's solution," *J. Magnes. Alloy.*, vol. 7, no. 2, pp. 218–226, 2019.
- [11] H. Hornberger, S. Virtanen, and A. R. Boccaccini, "Biomedical coatings on magnesium alloys—a review," *Acta Biomater.*, vol. 8, no. 7, pp. 2442–2455, 2012.
- [12] Y. Wang, Z. Gu, J. Liu, J. Jiang, N. Yuan, J. Pu, and J. Ding., "An organic/inorganic composite multi-layer coating to improve the corrosion resistance of AZ31B Mg alloy," *Surf. Coatings Technol.*, vol. 360, pp. 276–284, 2019.
- [13] Z. Q. Zhang, Y. X. Yang, J. A. Li, R. C. Zeng, and S. K. Guan, "Advances in coatings on magnesium alloys for cardiovascular stents—a review," *Bioact. Mater.*, vol. 6, no. 12, pp. 4729–4757, 2021.
- [14] X. B. Chen, N. Birbilis, and T. B. Abbott, "Review of corrosion-resistant conversion coatings for magnesium and its alloys," *Corrosion*, vol. 67, no. 3, pp. 35001–35005, 2011.
- [15] Y. Song, S. Zhang, J. Li, C. Zhao, and X. Zhang, "Electrodeposition of Ca–P coatings on

biodegradable Mg alloy: in vitro biomineralization behavior,” *Acta Biomater.*, vol. 6, no. 5, pp. 1736–1742, 2010.

[16] J. H. Connor, W. E. Reid, and G. B. Wood, “Electrodeposition of metals from organic solutions: V. Electrodeposition of magnesium and magnesium alloys,” *J. Electrochem. Soc.*, vol. 104, no. 1, p. 38, 1957.

[17] Q. Liu, D. Chen, and Z. Kang, “One-step electrodeposition process to fabricate corrosion-resistant superhydrophobic surface on magnesium alloy,” *ACS Appl. Mater. Interfaces*, vol. 7, no. 3, pp. 1859–1867, 2015.

[18] L. Staišiūnas, P. Miečinskis, K. Leinartas, A. Selskis, A. Grigucevičienė, and E. Juzeliūnas, “Sputter-deposited Mg–Al–Zn–Cr alloys—Electrochemical characterization of single films and multilayer protection of AZ31 magnesium alloy,” *Corros. Sci.*, vol. 80, pp. 487–493, 2014.

[19] G. Bikulčius, P. Miečinskis, A. Ručinskienė, A. Grigucevičienė, A. Selskis, and V. Pakštas, “Improvement of corrosion resistance of magnesium alloy by sputter coating with stainless steel,” *Trans. IMF*, vol. 90, no. 3, pp. 125–128, 2012.

[20] A. R. Shashikala, R. Umarani, S. M. Mayanna, and A. K. Sharma, “Chemical conversion coatings on magnesium alloys—a comparative study,” *Int. J. Electrochem. Sci.*, vol. 3, no. 9, pp. 993–1004, 2008.

[21] J. I. N. Hualan, Y. Xiangjie, and W. Ming, “Chemical conversion coating on AZ31B magnesium alloy and its corrosion tendency,” *Acta Metall. Sin. (English Lett.)*, vol. 22, no. 1, pp. 65–70, 2009.

[22] Y. Su, I. Cockerill, Y. Zheng, L. Tang, Y. X. Qin, and D. Zhu, “Biofunctionalization of metallic implants by calcium phosphate coatings,” *Bioact. Mater.*, vol. 4, pp. 196–206, 2019.

[23] H. M. Wong, K. W. K. Yeung, K. O. Lam, V. Tam, P. K. Chu, K. D. K. Luk, and K. M. C. Cheung “A biodegradable polymer-based coating to control the performance of magnesium alloy orthopaedic implants,” *Biomaterials*, vol. 31, no. 8, pp. 2084–2096, 2010.

[24] P. Tong, Y. Sheng, R. Hou, M. Iqbal, L. Chen, and J. Li, “Recent progress on coatings of biomedical magnesium alloy,” *Smart Mater. Med.*, vol. 3, pp. 104–116, 2022.

[25] L. Y. Li, L. Y. Cui, R. C. Zeng, S. Q. Li, X. B. Chen, and Y. Zheng, “Advances in functionalized polymer coatings on biodegradable magnesium alloys—A review,” *Acta Biomater.*, vol. 79, pp. 23–36, 2018.

[26] Y. Chen, Z. Xu, C. Smith, and J. Sankar, “Recent advances on the development of magnesium alloys for biodegradable implants,” *Acta Biomater.*, vol. 10, no. 11, pp. 4561–4573, 2014.

[27] E. Şahin and M. Çiftçioğlu, “Monetite promoting effect of citric acid on brushite cement setting kinetics,” *Mater. Res. Innov.*, vol. 18, no. 3, pp. 138–145, 2014.

[28] E. Şahin, “Calcium phosphate bone cements,” in *Cement Based Materials*, London, United Kingdom, IntechOpen, 2018 vol. 191, pp. 191–219.

[29] E. V Musvoto, M. C. Wentzel, and G. A. Ekama, “Integrated chemical–physical processes modelling—II. simulating aeration treatment of anaerobic digester supernatants,” *Water Res.*, vol. 34, no. 6, pp. 1868–1880, 2000.



# Düzce University Journal of Science & Technology

Research Article

## Evaluation Of Foreign Object Damage On The Fan Blades with Microscopic Techniques

 Ayhan İsmail KIRCA <sup>a</sup>,  Seyid Fehmi DİLTEMİZ <sup>b</sup>,  Sezer YUMRUKAYA <sup>a</sup>,  Aykut BATAR <sup>a</sup>

<sup>a</sup> 1'inci Hava Bakım Fabrika Müdürlüğü, Eskişehir, TURKEY

<sup>b</sup> Department of Aeronautical Engineering, Eskişehir Osmangazi University, Eskişehir, TURKEY

\* Corresponding author's e-mail address: [ayhanismailkirca@gmail.com](mailto:ayhanismailkirca@gmail.com)

DOI: 10.29130/dubited.1374721

### ABSTRACT

Foreign object damage (FOD) is a common problem in gas turbine engines, particularly in the fan and compressor blades. FOD generally occurs when hard body particles are ingested into an aero-engine fan and compressor blade. High-speed impact on fan titanium alloy blades leads to foreign object damage, which weakens the fatigue performance of the blades. It is important to note that FOD can also cause damage that is not visible to the naked eye, such as internal cracks or fatigue damage. Therefore, regular inspections and maintenance are crucial to detect and prevent FOD damage in gas turbine engines. Also using a microscope for the inspection of blades is important. Proper examination of blades damaged by foreign or domestic object can shed light on blade status and prevent further damage in the future. Here are some of the benefits of using a microscope for blade inspection:

Microscopes can provide high magnification and resolution, allowing for detailed inspection of the blade surface and any defects or damage.

Microscopes can help detect and identify small cracks, chips, or other forms of damage that may not be visible to the naked eye.

Microscopes can provide accurate measurements of the blade's dimensions, which can be important for quality control and maintenance purposes.

Microscopes can help identify the root cause of any damage or wear on the blade, which can inform future design and manufacturing decisions.

Microscopes can provide visual documentation of the blade's condition, which can be useful for tracking changes over time and for communicating with other stakeholders.

Overall, using a microscope for blade inspection can help ensure the safety, reliability, and performance of gas turbine engines and other equipment that relies on blades.

In this study, a comparison was made between visual inspection, borescope control, stereo microscope and SEM-EDX microscope methods used in the detection and removal of foreign material damage. The advantages and disadvantages of these 4 methods are comparatively examined and presented to the attention of the reader.

**Keywords:** SEM-EDX, Foreign object damage (FOD), Stereo microscope

## Mikroskopik Tekniklerle Pale Hasarının Değerlendirilmesi

### ÖZ

Yabancı cisim hasarı (FOD), gaz türbini motorlarında, özellikle fan ve kompresör kanatlarında yaygın bir sorundur. FOD genellikle, sert cisim parçacıkları bir uçak motoru hava alığından girdiğinde oluşur. Titanyum alaşımlı kanatlar üzerindeki yüksek hızlı darbe, kanatların yorulma performansını zayıflatan yabancı cisim hasarına yol açar. FOD'nin iç çatlaklar veya yorulma hasarı gibi çıplak gözle görülemeyen hasarlara da neden



olabileceğini unutmamak gerekir. Bu nedenle, gaz türbini motorlarında FOD hasarını tespit etmek ve önlemek için düzenli denetimler ve bakım çok önemlidir. Bladelerin incelenmesi için mikroskop kullanılması da önemlidir. Harici veya dahili nesne tarafından hasar görmüş bladelerin uygun şekilde incelenmesi, bladelerin durumuna ışık tutabilir ve gelecekte oluşabilecek daha büyük hasarları önleyebilir. Rotor Blade muayenesi için mikroskop kullanmanın faydalarından bazıları şunlardır:

Kanatçık yüzeyinin ve herhangi bir kusur veya hasarın ayrıntılı olarak incelenmesine izin vererek yüksek büyütme ve çözünürlük sağlar.

Çıplak gözle görülemeyebilecek küçük çatlakları, talaşları veya diğer hasar biçimlerini tespit etmeye ve tanımlamaya yardımcı olur.

Kalite kontrol ve bakım amaçları için önemli olabilecek boyutlarının doğru ölçümlerini sağlar.

Kanatçık üzerindeki herhangi bir hasarın temel nedenini belirlemeye yardımcı olur ve bu da gelecekteki tasarım ve üretim kararları için bilgi sağlar.

Kanatçık durumunun görsel olarak belgelenmesini sağlar ve bu, zaman içindeki değişiklikleri izlemek ve diğer paydaşlarla iletişim kurmak için yararlı olur.

Genel olarak, kanat muayenesi için mikroskop kullanmak, gaz türbini motorlarının güvenilirliğini ve performansını arttırmaya yardımcı olur.

Bu çalışmada yabancı madde hasarının tespitinde ve izalesinde kullanılan göz kontrolü, boroskop kontrolü, stereo mikroskop ve SEM-EDX mikroskop yöntemleri arasında karşılaştırma yapılmıştır. Kullanılan bu 4 yöntemin avantaj ve dezavantajları karşılaştırmalı olarak incelenmiş ve okuyucunun dikkatine sunulmuştur.

**Anahtar Kelimeler:** : SEM-EDX, Yabancı cisim hasarı (FOD), Stereo mikroskop

## **I. INTRODUCTION**

Gas turbine engines are motors that operate on the principle of producing thrust or rotational energy through the combustion of pressurized gases and the expansion effect that occurs after combustion. After the primitive version developed by Heron of Alexandria, who produced power with steam reaction before the Common Era, gas turbine engines have made significant progress in modern times [1]. The gas turbine engines used today operate based on the principles of the Brayton Cycle, as formulated by George Brayton (1830-1892) [2].

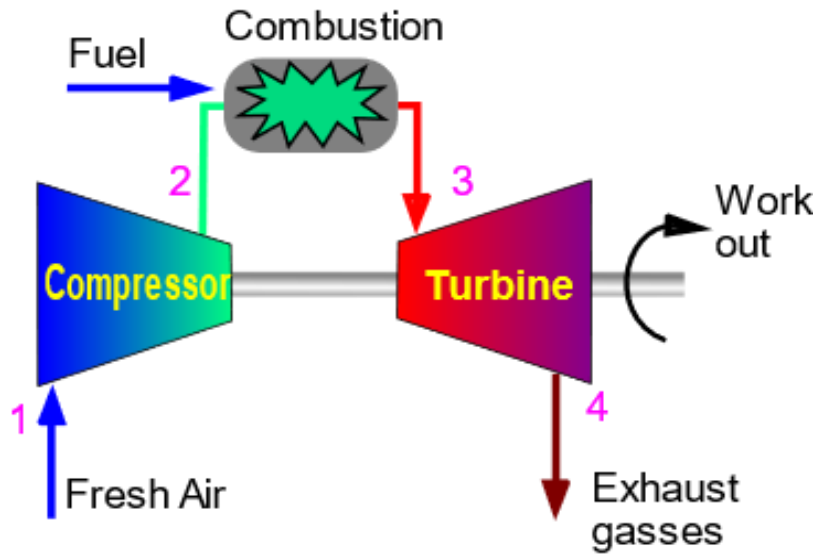


**Figure 1.** Gas Turbine Engine [1]

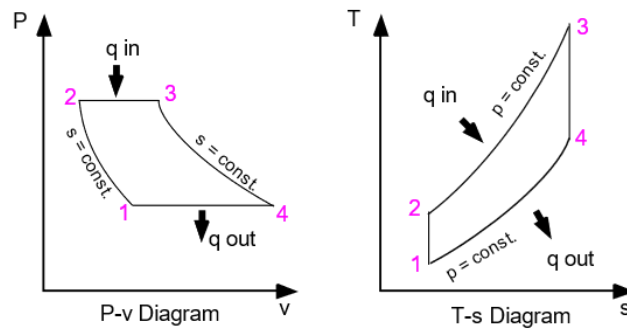


*Figure 2. Brayton Cycle [2]*

The utilization of the Brayton Cycle in aviation marked the beginning of the production of engines closely resembling today's modern counterparts [3]. These engines can generate higher power compared to piston engines and operate effectively at higher altitudes [4]. The specific fuel consumption of jet engines exhibits a decrease in correlation with a reduction in outside air temperature, while maintaining constant revolutions per minute (RPM) and true airspeed (TAS). Pilots can optimize fuel economy and attain the most advantageous cruise speed by operating at elevated flight levels during high-altitude flights [5], [6]

Gas turbine engines aim to efficiently extract work from the intake of air under atmospheric conditions, producing rotational energy or thrust. These engines generally consist of three main sections: the compressor, combustion chamber, and turbine, arranged sequentially from front to back [1]. Compressors can be axial or centrifugal, both serving the purpose of compressing air. During compression, as pressure increases, volume decreases, and the temperature rises due to the compressive effect. In the combustion chamber, compressed air is mixed with fuel and ignited under constant pressure, increasing the temperature and volume of the air. In the turbine section, the high-energy air is converted to mechanical energy to obtain rotation and is used as thrust power at the turbine outlet [5].

Gas turbine engines need to intake a large volume of air to generate high amounts of power. The ingested air may contain substances with sizes that vary based on ambient conditions [5]. This situation can lead to issues such as erosion, corrosion, and foreign object damage [7][8], [9][10]

## **II. THEORETICAL INFORMATION**

### **A. FOD AND DOD**

Gas turbine engines operate by intaking varying amounts of air depending on the engine type, but the ingested air always enters the engine at high speed. The environment from which this air is drawn can vary based on the engine's operating conditions and the mission profile of the aircraft. Depending on changing conditions, aircraft can pull in materials of different sizes, such as sand, gravel, tools, bolts, safety wires, clothing fragments, and even small animals, sometimes on the ground and sometimes during flight [11]. The materials drawn into the engine from the air intakes, especially rotor and stator components, can cause damage. Foreign Object Damage (FOD) refers to the smallest potential damage-causing materials drawn into the engine intakes [11]. When these materials negatively affect the safe operation or performance characteristics of the engine, it is defined as foreign object damage (FOD) [2]. Materials that strike rotor and stator components and cause damage can be from external sources or may be parts of the engine itself that are damaged and detached [12]. Such damages are referred to as

Domestic Object Damage (DOD). Examples include coating peels, breakage of rotor or stator blades, and components like safety wires or loose nuts falling into the airflow path [11].

Despite precautions such as runway cleanliness and meticulous maintenance and repair practices to prevent FOD damage, Foreign Object Damage remains a common type of damage in gas turbine engines due to its inherent nature. [7]

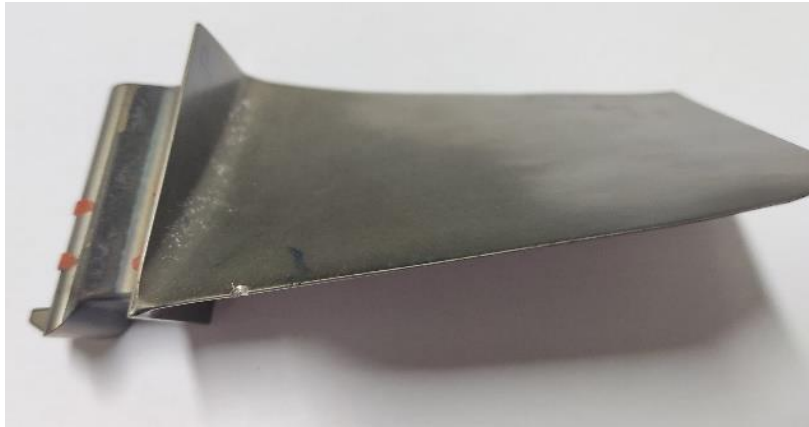


*Figure 3.* A blade with FOD damage

FOD damage can be within acceptable limits or reach a level that prevents the engine from continuing flight. Repairing the damage often incurs high costs and time loss. Therefore, evaluating FOD on the engine is a crucial aspect.

Various methods are employed to detect FOD damage on the engine and the removed damaged part. These include visual inspection, inspection with a borescope, stereo microscope examination, and scanning electron microscopy with energy-dispersive X-ray spectroscopy (SEM-EDX) [10], [12].

## **B. VISUAL INSPECTION**

The human eye can perceive an object of approximately 0.02 mm in size from a distance of 25 cm in a well-lit environment [13]. Visual inspection, which holds a significant place in FOD detection, can aid in identifying foreign objects during aircraft maintenance and cleaning. Visual inspection can be employed to detect foreign materials in critical areas of aircraft engines, such as fan blades, propellers, rims, tires, wings, and other vital components [14].

Visual inspection can be implemented not only by specialized engine personnel but also by all personnel in the aircraft, on the runway, in the aircraft hangar, and in maintenance workshops. In military areas, this visual inspection method, known as "FOD walk," involves personnel walking along taxiways and runways, inspecting the ground [15].

Visual inspection can be seen as a preventive measure against damage rather than a post-FOD occurrence check. However, there are numerous incidents where FOD is visually detected in post-flight inspections after damage has occurred [16].

Despite its advantages in terms of application speed and cost, this method has weaknesses due to the necessity of the application area being open and visually accessible, operator-dependent nature of the method, and its low precision.

### C. BORESCOPE INSPECTION

Borescope is an optical and electronic tool used to visualize areas that are not accessible to the naked eye. Typically, it consists of a flexible or rigid tube with a camera at its end that can capture images and has the capability of optical and digital zoom. Additionally, it includes a screen that transmits the captured image to the operator.



*Figure 4. HPT blade borescope image [17]*

Different manufacturing companies can introduce borescope devices with evolving technical features thanks to rapidly advancing technology, and these devices find broader applications. Currently, in borescope devices, while inspections are carried out by operators, devices capable of detection through deep learning with the aid of artificial intelligence are being developed [18].

Existing borescope devices can capture images in wet or dry areas that are inaccessible to the naked eye and can perform limited measurements. For devices without measurement capabilities, a wire with a known measurement can be extended to the area for comparative measurements [19]

Inspections with a borescope are a fast and cost-effective control method. During the design of engines, various areas of the engine can be visualized through borescope ports or various openings placed for this purpose. Routine inspections often lead to the initial detection of FOD using these devices.

### D. STEREO MICROSCOPE

Unlike other light microscopes, it can create a three-dimensional visual of the examined sample due to both its illumination path and oblique illumination. Besides this feature, it shares similar characteristics with other light microscopes within the framework of physical laws. Its resolution is typically limited to an average of 200-250 nm. In other words, distinguishing points closer than 200 nm is directly impossible in all light microscopes, including stereo microscopes.

The general light source of light microscopes lies within the visible spectrum, ranging from 400 nm to 700 nm. On the other hand, like other light microscopes, sample preparation is straightforward. Placing the sample on the microscope stage is sufficient to start the examination [20]. Typically, the sample is visualized at magnifications ranging from 10X to 50X. The energy source creating the image is white light through a halogen or LED bulb [21]

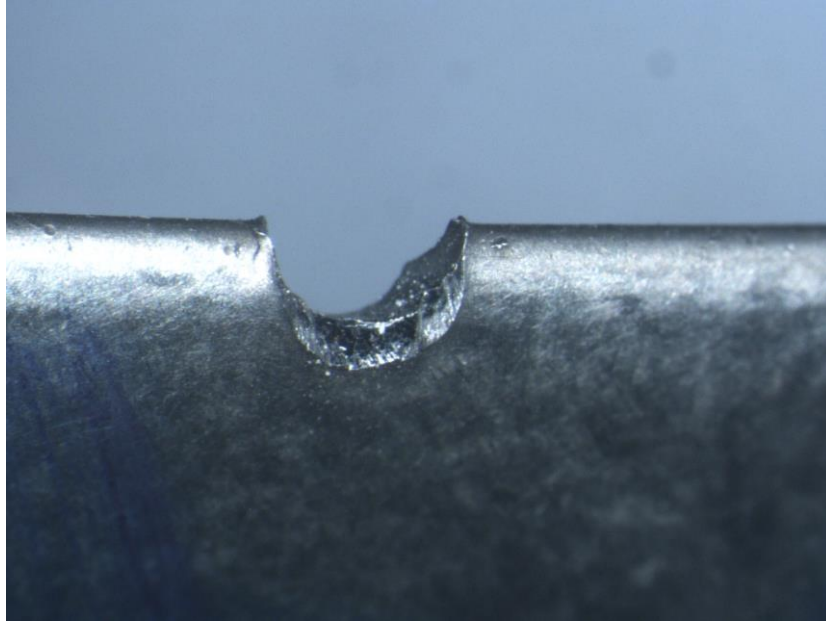


*Figure 5. FOD image at 16X magnification.*

## **E. SEM-EDX**

SEM-EDX microscope is a type of microscope that surpasses the resolution limit of approximately 200 nm observed in light microscopes, allowing for nanometer-level magnification. Instead of bulbs, an electron gun is used to create the image. The resolution of electron microscopes is below 1 nm, thanks to the shorter wavelength of electrons compared to visible light [22].

In FOD examinations, electron microscopes can benefit from the Secondary Electron (SE) detector, Backscatter Electron (BSD) detector, and the Energy Dispersive X-Ray (EDX) unit that can be added to the electron microscope. These detectors and the unit are particularly useful in diagnosing the foreign object.

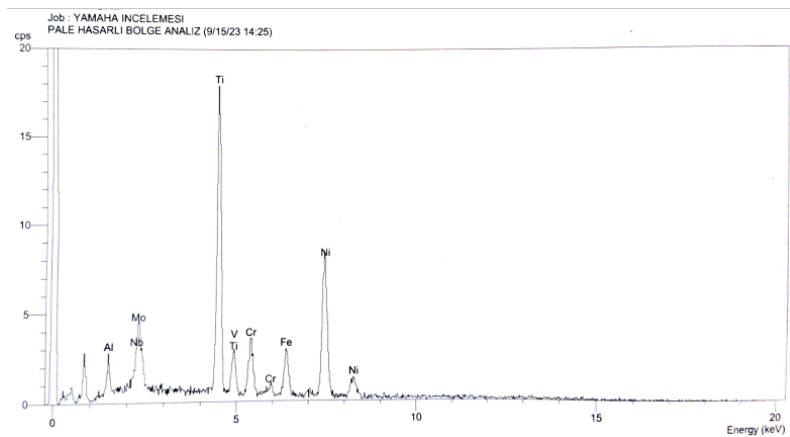


*Figure 6. Elemental analysis made with EDX*

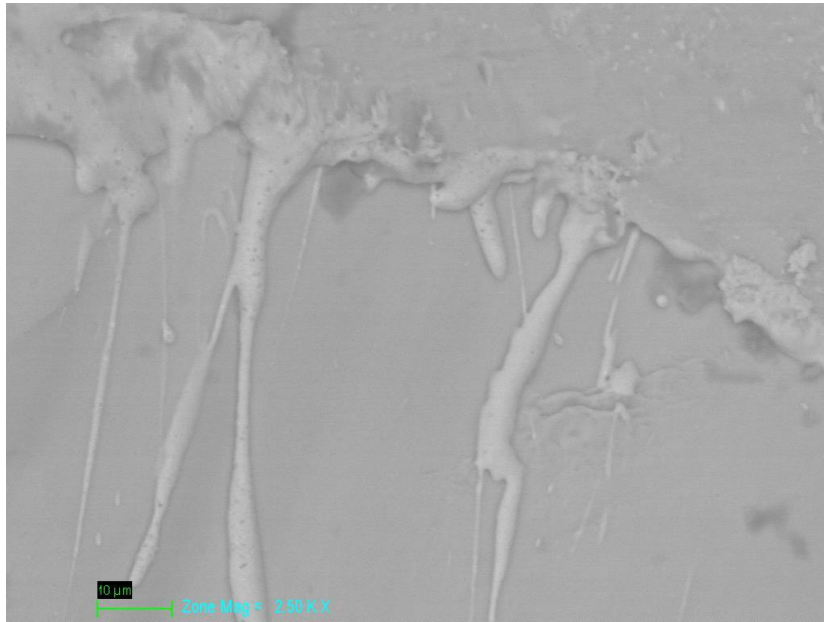


**Figure 7.** Blade SEM (BSD) image

SEM-EDX microscopes, providing information that cannot be obtained with other methods in FOD examinations due to their high-resolution imaging and elemental analysis capabilities, come with disadvantages such as operational complexity and sample size limitations.

### **III. COMPARISON**

In our study, a comparative evaluation of the examination methods will be conducted in terms of FOD detection and assessment. The comparison will be made under five main categories (speed, cost, precision, subjectivity, accessibility) as discussed separately above.

The compared versions of the methods are presented in the table below, rated from 1 to 5, with 1 being the best and 5 the worst.

**Table 1.** Comparison of inspection methods

	Visual Inspection	Boroscope Control	Stereo Microscope	SEM-EDX Microscope
Speed	3	5	2	2
Cost	4	4	3	2
Precision	2	2	4	5
Subjectivity	2	2	4	4
Accessibility	5	4	3	2
Total Point	16	17	16	15

## **A. INSPECTION SPEED**

In both civilian and military aviation applications, providing a quick response to encountered problems is crucial for the continuity of operations and cost control. The borescope method is an application that can be implemented without detailed disassembly, requiring only the removal of borescope plugs or parts such as sensors blocking access to the area. For the inspection of hot-section parts like HPT, it is necessary to wait for the engine to cool down [17]. In visual inspection, only the first stages of the compressor or fan part of the engine can be inspected. However, considering FOD, most damage is expected to occur in the first stages. A pre-inspection FOD check by entering through the air intake, if necessary, is crucial. Inspecting the internal parts of the engine requires disassembly, making the borescope method slower in terms of speed. On the other hand, inspections with Stereo and SEM-EDX microscopes are the slowest methods. In many cases, even assembly disassembly may not be sufficient, and part disassembly may be required.

## **B. INSPECTION COST**

Inspection cost is evaluated not only as the cost incurred during the examination of the part but also includes examination time, pre-inspection disassembly, and sample preparation costs. In this regard, the most expensive method is SEM-EDX microscopy because maintaining the microscope constitutes a separate cost item. The maintenance costs of stereo microscopes are relatively low, but the costs of sample preparation and examination are also very low. In addition to the initial investment cost, the costs incurred due to the time spent on the arrival of the damaged part to the stereo microscope and disassembly processes constitute the basic costs of examining with the stereo microscope. Similarly, borescope devices have routine maintenance costs and are prone to damage due to working conditions. It may seem that visual inspection is cost-free, but the training of personnel to perform the inspection and maintaining their high awareness create costs. Moreover, in areas where disassembly is required for visual inspection, waiting and disassembly costs also arise.

## **C. INSPECTION SENSITIVITY**

Among imaging and analysis techniques, the SEM-EDX unit is one of the most sensitive methods, providing an approximate resolution of 1 nm. The analysis resolution of the SEM-EDX technique can be improved by using a higher accelerator voltage that increases the penetration depth of the electron beam and optimizing sample preparation to reduce surface roughness and loading effects. Thanks to the SEM-EDX technique's ability to allow both material surface morphology and material element analysis, the characteristics of the object hitting the sample surface can be largely determined. Therefore, the SEM-EDX technique plays a significant role as a tool in determining ways to prevent FOD. Stereo microscopes usually magnify between 10X and 50X and have an approximate resolution of 200 nm. They can provide information about the direction and even the depth of FOD due to their ability to create three-dimensional images and easily change the direction of the specimen. The resolution of borescopes depends on the device used, camera length, camera diameter, and image sensor. The resolution of borescopes is usually expressed in pixels, ranging from 640 x 480 pixels to 10,000 pixels. As of yet, the measurement accuracy has not reached aviation standards. Borescopes with stereo cameras capable of creating three-dimensional images are available. With advancing technology, it is expected that devices capable of much clearer measurements will be produced in the coming years. Although research has been conducted on the resolution of the human eye, it is not possible to evaluate it as a fixed camera, and a clear resolution value has not been reached. However, a well-trained and precise human eye can yield surprising results.

## **D. SUBJECTIVITY**

Human factors are the most important in FOD formation [23]. Similarly, in the assessment of FOD, the operator is the most critical factor. However, systems like deep learning may change this situation in the future. All mentioned inspection methods require well-trained personnel, emphasizing the importance

of human factors in aviation applications. If a ranking is to be made among the methods, visual inspection is the most subjective method, often relying on a person's experiences. If possible, supporting this method with a measuring instrument will significantly reduce the problem. One of the biggest problems encountered in borescope inspections in the field is different evaluations between operators. Especially in inspections conducted with a flexible cable, the camera's approach angle, light intensity, screen resolution, and operator experience can lead to the incorrect assessment of FOD.

## **E. ACCESSIBILITY**

Due to the difficulty of maintenance, cost, and low frequency of use, it would not be effective to have an SEM-EDX microscope at every center where an aircraft is located. Because not every FOD incident may require action; only those beyond limits need to be removed. Similarly, stereo microscopes, and even borescope devices, may not be present at every airport. Visual inspection, on the other hand, is a quick and widespread control type performed by both the mechanic and flying personnel before and after each flight.

## **IV. CONCLUSION**

The detection of FOD damage is crucial for flight safety. Visual inspection and borescope examinations stand out as methods with application speed and ease in damage detection. Failure to detect FOD or DOD material at the right time can compromise the material's durability, leading to significant damages, including loss of life. When evaluating the importance of these two methods and their dependence on implementing personnel, the relationship between FOD and awareness becomes apparent.

After the detection of FOD, detailed evaluations highlight the control methods with Stereo microscopes and SEM-EDX microscopes. The Stereo microscope is essential in FOD inspections due to its relatively easy application, measurement precision, and reporting capabilities. SEM-EDX microscopes, while having the most challenging application, can provide highly accurate results that other methods may not reach. Moreover, they can offer insights into the source of FOD in ways not possible with other methods. Accurate efforts to eliminate FOD sources will only be possible through the correct examination of FOD.

## **V. REFERENCES**

- [1] Wikipedia. (2023, May 10) *Gas Turbine*. [Online]. Available: [https://en.wikipedia.org/wiki/Gas\\_turbine](https://en.wikipedia.org/wiki/Gas_turbine)
- [2] "Brayton Cycle," *Brayton Cycle*, "A-to-Z Guide to Thermodynamics, Heat and Mass Transfer, and Fluids Engineering, 2008.
- [3] J. Massih. (2023, April 5) *An Overview of Brayton Cycles | Turbomachinery blog*. [Online]. Available: <https://blog.softinway.com/an-overview-of-brayton-cycles>
- [4] Power Engineering International. (2023, Nov. 25). *Technology for gas turbines operating in harsh environments* [Online]. Available: <https://www.powerengineeringint.com>
- [5] G. F. C. R. H.I.H. Saravanamuttoo, H. Cohen and P. V. S. A.C. Nix, "Gas Turbine Theory SEVENTH EDITION Gas Turbine Theory," p. 606, 2017.
- [6] HighSkyFlying. (2023, Nov. 25). *Why Are Jet Engines More Efficient at Higher Altitudes?* [Online]. Available: <https://www.highskyflying.com/why-are-jet-engines-more-efficient-at-higher->



altitudes

- [7] T. Chauhan, C. Goyal, D. Kumari, and A. K. Thakur, "A review on foreign object debris/damage (FOD) and its effects on aviation industry," *Mater Today Proc*, vol. 33, pp. 4336–4339, Jan. 2020, doi: 10.1016/J.MATPR.2020.07.457
- [8] A. Hamed, W. Tabakoff, and R. Wenglarz, "Erosion and deposition in turbomachinery," *J Propuls Power*, vol. 22, no. 2, pp. 350–360, 2006, doi: 10.2514/1.18462.
- [9] M. W. Reedy, T. J. Eden, J. K. Potter, and D. E. Wolfe, "Erosion performance and characterization of nanolayer (Ti,Cr)N hard coatings for gas turbine engine compressor blade applications," *Surf Coat Technol*, vol. 206, no. 2–3, pp. 464–472, Oct. 2011, doi: 10.1016/J.SURFCOAT.2011.07.063.
- [10] Z. H. Li, Y. H. Lu, C. Hong, Y. G. Zhao, W. D. Zhang, and T. Shoji, "Effects of foreign object damage on high-cycle fatigue behavior of Inconel Alloy 690TT steam generator tubes," *Eng Fract Mech*, vol. 292, p. 109660, Nov. 2023, doi: 10.1016/J.ENGFRACTMECH.2023.109660.
- [11] THE FOD CONTROL. (2023, Nov. 25) *What is FOD? | Foreign Object Debris & Damage Examples* [Online]. Available: <https://www.fodcontrol.com/what-is-fod>
- [12] S. Spanrad and J. Tong, "Characterization of foreign object damage (FOD) and early fatigue crack growth in laser shock peened Ti-6AL-4V aerofoil specimens," *Procedia Eng*, vol. 2, no. 1, pp. 1751–1759, Apr. 2010, doi: 10.1016/J.PROENG.2010.03.188.
- [13] Wikipeđi. (2023, 25 Kasım). *Yabancı madde hasarı*. [Çevrimiçi]. Erişim: [https://tr.wikipedia.org/wiki/Yabancı\\_madde\\_hasarı](https://tr.wikipedia.org/wiki/Yabancı_madde_hasarı)
- [14] Thang, V.D. (October 14, 2021). *How to Detect FOD (Foreign Object Debris) | FOD Check* [Online]. Available: <https://www.aerosweep.com/blog/how-to-detect-fod-foreign-object-debris>
- [15] THE FOD CONTROL. (2023, Nov 25). *A Guide for Annual FOD Walk Downs | FOD Walk Meaning* [Online]. Available: <https://www.fodcontrol.com/annual-fod-walk/>
- [16] Wikipedia. (2023, Nov. 25) *Air France Flight 4590* [Online]. Available: [https://en.wikipedia.org/wiki/Air\\_France\\_Flight\\_4590](https://en.wikipedia.org/wiki/Air_France_Flight_4590)
- [17] Z. Yuan, "Borescope inspection for HPT blade of CFM56-7B engine," *IOP Conf Ser Mater Sci Eng*, vol. 382, p. 032028, Jul. 2018, doi: 10.1088/1757-899X/382/3/032028.
- [18] M. T. Barakat, M. Girotra, and S. Banerjee, "Initial application of deep learning to borescope detection of endoscope working channel damage and residue," *Endosc Int Open*, vol. 10, no. 01, pp. E112–E118, Jan. 2022, doi: 10.1055/a-1591-0258.
- [19] C. L. Ofstead and K. M. Hopkins, "Sterilization Central: The Value of Borescopes in Detecting Damage, Soil, Fluid, and Foreign Objects in Flexible Endoscopes," *Biomed Instrum Technol*, vol. 54, no. 2, pp. 146–152, Mar. 2020, doi: 10.2345/0899-8205-54.2.146.
- [20] *ASM Metals Handbook*, vol. 12 Fractography. ASM International, 1992.
- [21] *ASM Metals Handbook Metallography and Microstructure*, vol. 9, 1985.
- [22] K. Morrison, "Microscopy techniques," *Characterisation Methods in Solid State and Materials Science*, pp. 4-1-4–25, Oct. 2019, doi: 10.1088/2053-2563/AB2DF5CH4.



[23] R. Hussin, N. Ismail, and S. Mustapa, "A study of foreign object damage (FOD) and prevention method at the airport and aircraft maintenance area," *IOP Conf Ser Mater Sci Eng*, vol. 152, p. 012038, Oct. 2016, doi: 10.1088/1757-899X/152/1/012038.



# Düzce University Journal of Science & Technology

Research Article

## Experimental Analysis of The Impacts of Biodiesel-Diesel Fuel Mixtures on Engine Vibration, Noise and Combustion

 Suat SARIDEMİR<sup>a</sup>,  Fikret POLAT<sup>a,\*</sup>

<sup>a</sup> Department of Mechanical Engineering, Faculty of Engineering, Düzce University, Düzce, TÜRKİYE

\* Corresponding author's e-mail address: fikretpolat@duzce.edu.tr

DOI: 10.29130/dubited.1377079

### ABSTRACT

The restricted reserves of fossil-based fuels and the regulations imposed on emission standards increase the importance of renewable fuels. Biodiesel is one of among peripherally friendly and renewable disjunctive fuels and contributes to the reduction of exhaust emissions. Biodiesel fuels have distinctive chemical frames and fuel features compared to conventional diesel fuels based on their substance and production method. Ignition delay, pressure increase rate, and combustion characteristics generate mechanical noises and vibrations in the engine. In compression-ignition engines, high noise and vibration eventuating from the explosive burning have negative effects on the environment and living beings. In this search, the impacts of various proportions of biodiesel fuel and conventional diesel fuel blends on the in-cylinder pressure, vibration, and noise of a three-cylinder water-cooled diesel engine were experimentally investigated. The peak max in-cylinder pressure values for all test fuels were obtained at 15 Nm. For all test fuels, the largest vibration value was obtained at 15 and 60 Nm and the smallest vibration value was obtained at 45 Nm. The engine noise level is reduced up to 45 Nm and increased at 60 Nm. The highest noise level was obtained with conventional diesel fuel (D) at all engine loads. The addition of biodiesel to the test fuels reduced the noise level at all loads. The average noise values of all test fuels are 90.58, 90.28, 90.35, and 90.09 dBA for 15, 30, 45, and 60 Nm loads, respectively.

**Keywords:** Engine Vibration, Noise, Combustion

## Biyodizel-Dizel Yakıt Karışımlarının Motor Titreşimi, Gürültü ve Yanma Üzerindeki Etkilerinin Deneysel Analizi

### ÖZ

Fosil bazlı yakıtların rezervlerinin kısıtlı olması ve emisyon standartlarına getirilen düzenlemeler yenilenebilir yakıtların önemini artırmaktadır. Biyodizel yakıtlar, çevre dostu ve yenilenebilir ayrık yakıtlardan biridir ve egzoz emisyonlarının azaltılmasına katkıda bulunur. Biyodizel yakıtlar, içeriklerine ve üretim yöntemlerine bağlı olarak geleneksel dizel yakıtlara kıyasla farklı kimyasal yapı ve yakıt özelliklerine sahiptir. Yakıtın tutuşma gecikmesi süresi, basınç artış hızı ve yanma özellikleri motorda mekanik sesler ve titreşimler oluşturur. Dizel motorlarda patlamalı yanma sonucu oluşan yüksek gürültü ve titreşim, çevre ve canlılar üzerinde olumsuz etkilere sahiptir. Bu çalışmada, farklı oranlarda biyodizel yakıt ve geleneksel dizel yakıt karışımlarının üç silindirli, su soğutmalı bir dizel motorun yanma basıncı, titreşimi ve gürültüsü üzerindeki etkileri deneysel olarak incelenmiştir. Tüm test yakıtları için maksimum silindir içi basınç değerleri 15 Nm'de elde edilmiştir. Tüm test yakıtları için en büyük titreşim değeri 15 ve 60 Nm'de, en küçük titreşim değeri ise 45 Nm'de elde edilmiştir. Motor gürültü seviyesi 45 Nm'ye kadar azalmış ve 60 Nm'de artmıştır.

**Anahtar Kelimeler:** Motor Titreşimi, Gürültü, Yanma

# **I. INTRODUCTION**

The fact that fossil-based fuels have limited reserves and emit harmful emissions. For these reasons, it is important to develop renewable and eco-friendly fuels that can replace fossil-based fuels. Renewable energy sources being sustainable will reduce the need for fossil-based fuels. Biodiesel fuels are renewable alternative fuels derived from animal and vegetable fats and oils, and waste oils by transesterification method. The oxygen content of biodiesel fuels reduces the exhaust emissions of diesel engines. Biodiesel is a fuel composed of a mixture of long-chain carboxylic acid ester alkyls and can be mixed with conventional diesel fuel in any blend ratio [1-4]. Biodiesel fuels can be used in diesel engines without requiring any modification to the engine since their features are similar to those of petroleum-derived diesel [5-8].

Engine vibration is a factor affecting vehicle vibration and is important for fault detection and driving comfort. Vibration amplitude has negative effects on engine parts and noise has negative effects on life. The main causes of engine vibrations and noise are combustion, knocking, and movement of engine parts. Diesel engine noise consists of exhaust, intake, and combustion noises and mechanical noise from engine components. Mechanical noise due to factors such as piston clearances, deformation, and friction is affected by the end combustion pressure. In diesel engines, the conventional combustion process, which depends on engine load, speed, and fuel features, is the most significant source of noise [9]. Burning noisiness is extremely based on fuel combustion and is a consequence of the harshness and unevenness of fuel self-ignition. Since the end-combustion pressure forces and combustion speed depend mainly on the injection strategy, fuel specifications like cetane number, calorific value, kinematic viscosity, and density play an important role in reducing these forces [10]. The pressure and mechanical forces generated during combustion cause vibration on the engine block. The amplitude of the maximum vibration gives information about the combustion intensity. Early ignition of the fuel and rich mixture increases the vibration amplitude. Late ignition, injector failure, and compression leaks reduce the vibration amplitude [11]. Large vibration amplitude could also damage the electronic and mechanical components of vehicles. Large vibration amplitude will reduce engine life due to the knocking phenomenon and detonation during combustion, which may also degrade the thermal efficiency [12]. Knocking in diesel engines is a phenomenon that also depends on fuel features. The loudness level of ICE depends on the mechanical forces acting on the moving parts, which vary depending on the biggest in-cylinder pressure and the heat release rate. The in-cylinder pressure acting on the combustion chamber and piston surface creates vibration in the engine block. As a result of vibration, noise is emitted into the environment. The combustion process, which is subject to fuel type, engine specifications, and engine operating specifications, is the most important source of vibration and noise [13]. In spite of there are various searches in the books and articles examining the influence of biodiesel-mixed fuels on engine performance and emissions, it has been observed that studies examining the impact of biodiesel-mixed fuels on engine noise and vibration are limited. In the study by Sarıdemir and Ağbulut, the impact of varied ratios of conventional diesel-cotton oil methyl ester on engine vibration and noise under several loads at a steady engine rotation of 1500 rpm was investigated. The least mean vibration value was achieved with B20 test fuel. It was reported that the noise values of the experiment fuels were near to one another at the same engine load [13]. In a study by Patel et al., vibration and noise values of a single-cylinder engine were studied in relation to load. Karanja biodiesel (KB100), KB20, and pure diesel fuel were used as test fuels. The highest noise and vibration values in the vertical direction were obtained with KB20 fuel [14]. In the study by Uludamar and Aydın, the influence of diesel fuel and diesel fuel sunflower, canola, and corn oil biodiesel fuel mixtures on engine noise and vibration depending on engine speed was investigated. The results showed that the noise and vibration of the engine decreased with increasing biodiesel ratio until pure biodiesel usage [15]. In the study by Çelebi et al., the acoustic and vibration effects of biodiesel and its blends were investigated. The experimental engine was fed with conventional diesel, sunflower, and canola biodiesel blends at 20% and 40% by volume. In addition, natural gas was supplied through the intake manifold at 5 L/min, 10 L/min, and 15 L/min. The results showed that sunflower and canola biodiesel reduced the sound pressure level and vibration of the test engine compared to conventional diesel fuel [16]. In the study by Çalık, the effects of conventional diesel, pure waste oil biodiesel, and hydrogen addition to these fuels

on engine vibration were investigated. It was reported that pure biodiesel and hydrogen addition to pure biodiesel and conventional diesel reduced engine vibration [17]. Alisarai et al. examined the impacts of neat diesel fuel, waste biodiesel fuel (B100), and biodiesel-diesel fuel blends (B20, B40, B60, B80) on combustion and vibration. It is stated that maximum vibration values are obtained with B20 and B40 and minimum vibration values are obtained with D100 and B80 [18]. Redel-Macías et al. enquired about the effect of palm oil biodiesel and olive pomace oil biodiesel on engine noise. It was reported that POME and OPME fuels reduced noise and the lowest noise level was obtained with PME50 [19]. Manienyan and Sivaprakasam enquired about the impact of conventional diesel and Mahua biodiesel fuels on engine vibration at a stable speed of 1500 rpm and different loads. It was reported that biodiesel fuel increased the vibration level in the cylinder head and reduced the vibration of the lower part of the engine [12].

Canola oil has a wide production potential in our country. In the books and articles, there are studies investigating the effects of biodiesel fuel blends obtained from various vegetable and waste oils on engine vibration and noise. Vibration and noise are important factors affecting driving comfort. In the literature, it has been observed that the studies investigating the impacts of canola oil biodiesel on engine vibration and noise are limited. Therefore, in this study, the impacts of different ratios of canola oil biodiesel and conventional diesel fuel blend on combustion, vibration, and noise were experimentally investigated.

## II. MATERIAL AND METHOD

Biodiesel fuel was manufactured from refined canola oil by transesterification with the production procedure shown schematically in Figure 1. The produced canola methyl ester was blended with conventional diesel fuel at 10, 30, and 50% by volume just before the experiments to obtain B10, B30, and B50 test fuels.

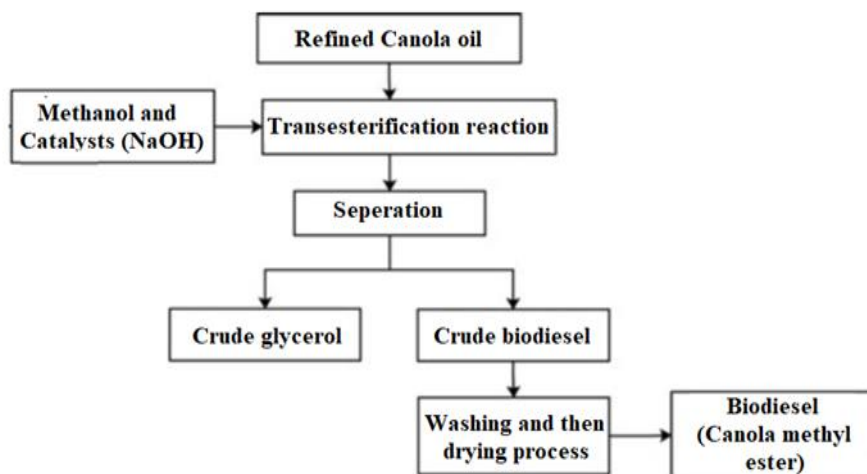


*Figure 1. Canola oil methyl ester production scheme.*

Some of the primary features of the test fuels are given in Table 1.

*Table 1. Some main characteristics of the test fuels.*

Property	D	C10	C30	C50
Density (kg/m <sup>3</sup> ; 25 °C)	844	848	852	861
Lower heating value (MJ/kg)	44.86	44.30	43.14	42.31
Viscosity, (cSt @40 °C)	2.68	3.07	3,38	3.61
Cetane number	54	53	51	49

The tests were handled with a three-cylinder, water-cooled diesel engine whose specifications are given in Table 2. All experiments were started under the same conditions when the engine oil temperature approached 50 °C.

**Table 2.** Tech. features of the test engine.

Model	Lombardini LDW 1003
Engine type	Four-stroke, direct injection (DI)
Number of cylinders	3
Total cylinder volume	1028 cm <sup>3</sup>
Bore–stroke	75 mm–77.6 mm
Compression ratio	22.8:1
Maximum engine power	19.5 kW (26.5 Hp)
Maximum engine speed	3600 rpm
Maximum engine torque	67 Nm/@2000 rpm
Cooling type	Water-cooled
Valve timing (IVO/IVC)	16 BTDC/36 ABDC °CA
Valve timing (EVO/EVC)	36 BBDC/16 ATDC °CA

During the experiments, engine oil and exhaust degree of heat were measured with K-type NiCr-Ni coated thermocouples. All experiments were performed at a stable engine speed of 2000 rpm under loads ranging from 15-60 Nm with 15 Nm intervals. The engine was uploaded by a Kemsan brand electric dynamometer with a maximum power absorption capacity of 22 kW. The speed and torque values of the engine under all loads were measured with a Kistler Rotor type 4550A model magnetic torque meter. In-cylinder pressure values varying with crank angle were measured with an Oprant AutoPSCI-TC model fiber optic pressure sensor fastened up on the glow plug seat of the engine. The engine crank angle was measured with a Kübler-Sendix model encoder. Figure 2 shows a diagrammatic view of the probatory setup.

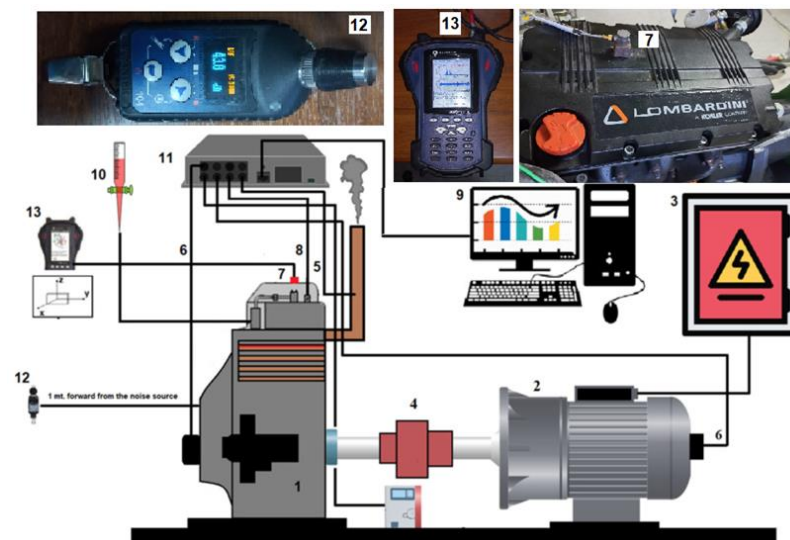


**Figure 2.** The schematically view of experimental-setup. 1. Test engine 2. Dynamometer 3. Control panel 4. Torque metre 5. Exhaust temperature point 6. Encoder 7. Accelerometer 8. Cylinder pressure sensor 9. Computer 10. Fuel consumption level 11. Mainboard 12. Noise measurement device 13. Vibration measurement device

The data from the pressure sensor and encoder were transferred to the Febris combustion analysis software. With this software, in-cylinder pressure data were obtained for each experiment as a function

of crank angle by averaging 1000 cycles of the engine. According to the in-cylinder pressure data obtained, the heat release rate was estimated with the consecution equation.

$$HRR = \frac{\gamma}{\gamma-1} P \frac{dV}{d\theta} + \frac{1}{\gamma-1} V \frac{dP}{d\theta} \quad (J/^{\circ}CA) \quad (1)$$

where HRR,  $\gamma$ , P, and V are heat release rate (J/ $^{\circ}$ CA), rate of specific heat (-), in-cylinder pressure (bar), and volume of cylinders (cm<sup>3</sup>), respectively.

The totality uncertainty percentage of the consequences is found with the consequent equation.

$$W_R = \left[ \left( \frac{\partial R}{\partial x_1} w_1 \right)^2 + \left( \frac{\partial R}{\partial x_2} w_2 \right)^2 + \dots + \left( \frac{\partial R}{\partial x_n} w_n \right)^2 \right]^{1/2} \quad (2)$$

In Eq. (2),  $W_R$  shows the total uncertainty (%) of the results,  $w$  and  $R$  are dimensional shape factors and the uncertainty function, respectively. In addition,  $w_n$  are the uncertainties in the independent variables. Table 3 presents a detail for the equipment. For noise measurement, Svantek 104 model noise meter (dosimeter) was used. For noise measurement, the device was placed 1 m away from the engine block in conformity with ISO 362-1:2007. Vibration measurement data were taken with a four-channel VIBROTEST 80 model FFT analysis data acquisition device with a 4527 model uniaxial piezoelectric accelerometer. The instrument has a Brüel&Kjaer program and hardware system. The data were filtered and analyzed at 6400 precision with the Hanning filtering method. Vibration inputs up to 5 kHz were taken in the tests. The sum amplitude mean of the vibration input was specified by the root mean square (RMS) method. The unit of vibration amplitude is (m/s<sup>2</sup>). Time domain vibration data were recorded for 1.28 seconds at the specified sampling frequency. For every test, a sum of 16384 data was acquired from the accelerometer.

**Table 3.** Measurement ranges, units, and accuracy of the experimental apparatus

Measuring Instrument	Range	Accuracy
Pressure (Optrand Auto PSI-TC)	0-3000 psi	±1 %
Encoder (kübler sendix)	0-360°	0.1° CA
Torque Measuring Unit (Kistler Rotortype 4550A)	0 ± 100 to 0 ± 5000	0.01 %
Svantek SV 104	55 dBA RMS ÷ 140.1 dBA Pik	0.7 %

The vibration amplitude values obtained with all experimental fuels at different engine loads were analyzed comparatively. For this purpose, the root mean square (RMS) values of the vibration amplitude values measured with the accelerometer were calculated. The measured time domain amplitude values were calculated with the equation given in Equation 3 [15, 18].

$$a_{RMS} = \sqrt{\frac{1}{n} \sum_k^n a_k^2} \quad (3)$$

Here;

$a_{RMS}$  : Root mean square root of acceleration values (m/s<sup>2</sup>),

$a_k$ : The  $k_{th}$  value of the time domain data (taken numerically from the accelerometer in the time domain),

$n$ = Number of time domain acceleration inputs ( $n = 16384$  for 1.28 s duration)

Vibration data were taken in one direction (vertical) for all test fuels.

### III. RESULTS AND DISCUSSION

In this study, canola methyl ester was produced from the oil obtained from the canola plant, which grows abundantly in our country. The produced canola methyl ester was mixed with conventional diesel fuel at different ratios by volume to obtain C10, C30, and C50 fuel blends. The test fuels were tested under the same conditions at a stable engine speed of 2000 and variable loads of 15, 30, 45, and 60 Nm. The results addressed the variation of the test fuels on combustion, engine vibration, and noise behavior. The experiment was carried out with an overall uncertainty of 2.4% and the results of the experiment are described in the subsections of this chapter in relation to cause and effect.

#### **A. COMBUSTION CHARACTERISTICS**

The experimental engine, whose technical specifications are given in Table 1, has an abnormal combustion chamber. Since the pressure sensor in the test engine is jointed in the pre-combustion chamber through the glow plug housing, the pressure values acting on the pre-combustion chamber can be measured. Figure 3-6 shows the in-cylinder pressure and heat release rate values of the test fuels for all engine loads (15, 30, 45, 60 Nm) at a stable engine revolution of 2000 rpm, varying with crank angle. In pre-combustion chamber diesel engines, the fuel is sprayed into the pre-combustion chamber by a one-hole nozzle and the initial combustion starts in the pre-combustion chamber where turbulence is very high and continues with its spread to the main combustion chamber. Therefore, as seen in the pressure graphs, the first stage pressure increase occurred due to the start of pilot combustion in the abnormal combustion chamber. As shown in Figure 3-6, as combustion starts in the pre-combustion chamber at all engine loads, the in-cylinder pressure values start to increase. As the flame front spreads into the main combustion chamber, the second stage pressure increase occurs. In-cylinder pressure and heat release rate values are experimental data that provide information about engine noise and vibration values. The peak maximum in-cylinder pressure values for all test fuels were obtained at 15 Nm. As seen in Figure 3, the maximum in-cylinder pressure value at 15 Nm engine load rose subject to the biodiesel ratio in the test fuels increased. The maximum in-cylinder pressure values of the test fuels are 57.98, 59.37, 59.73, and 60.79 bar for D, C10, C30, and C50 fuels, respectively. As seen in Table 1, biodiesel-containing test fuels have smaller lower heating values and cetane numbers, and larger viscosity and density than conventional D fuel. The lower cetane number of biodiesel-containing fuels boosts the ignition delay time. This causes more fuel to accumulate in the combustion chamber along the ignition delay time. With the sudden combustion of more fuel accumulated along the ignition delay time, the test fuels increased the maximum in-cylinder pressure value and HRRmax values subject to the biodiesel content at 15 Nm load. In addition, the high density of biodiesel-containing fuels causes low atomization, which contributes to a longer ignition delay time. The high O<sub>2</sub> content of biodiesel-containing fuels also increased combustion efficiency, max. combustion pressure and HRRmax.

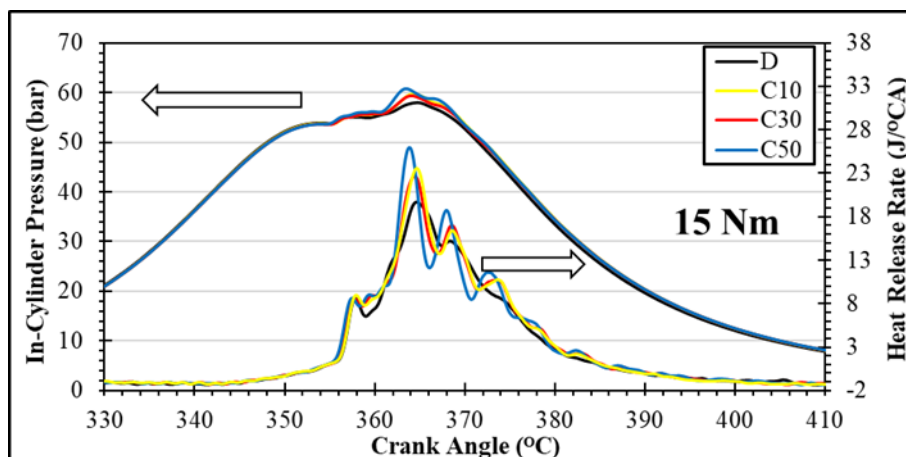


*Figure 3. Combustion pressure and HRR graphs of test fuels at 15 Nm load.*



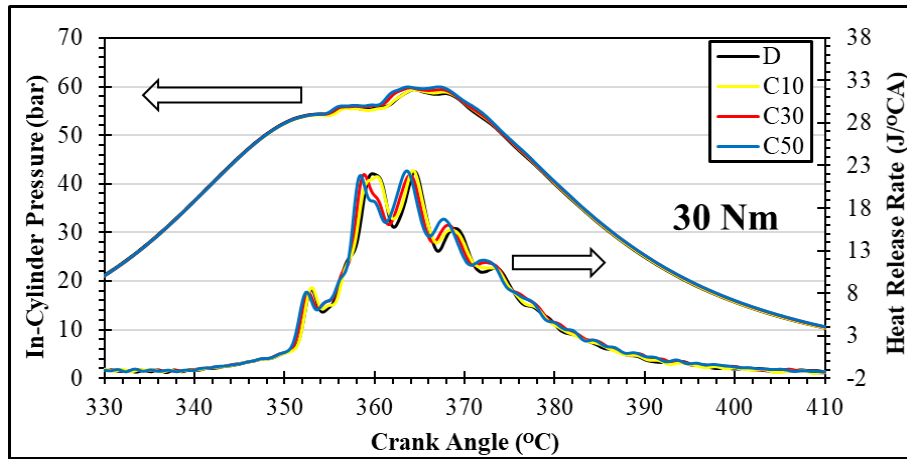


Figure 4. Combustion pressure and HRR graphs of test fuels at 30 Nm load.

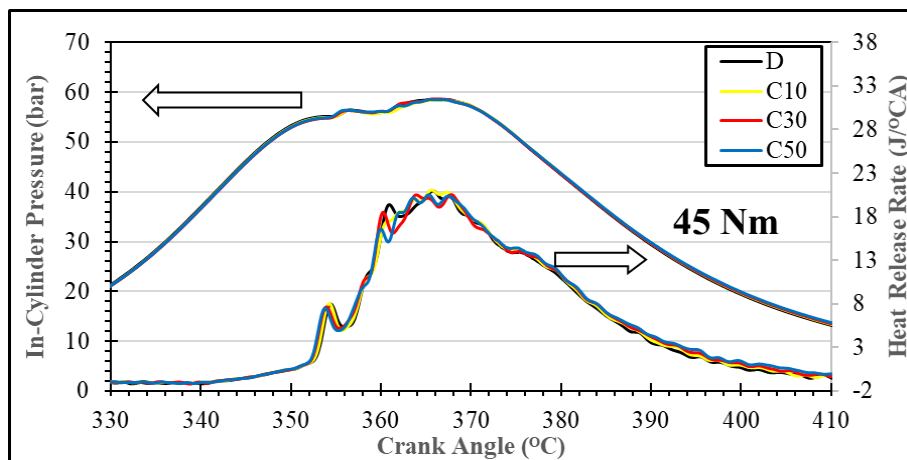


Figure 5. Combustion pressure and HRR graphs of test fuels at 45 Nm load.

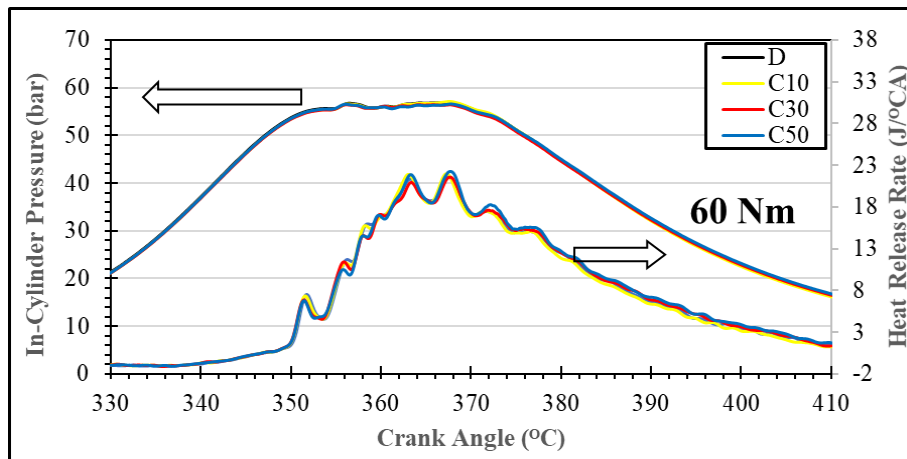


Figure 6. Combustion pressure and HRR graphs of test fuels at 60 Nm load.

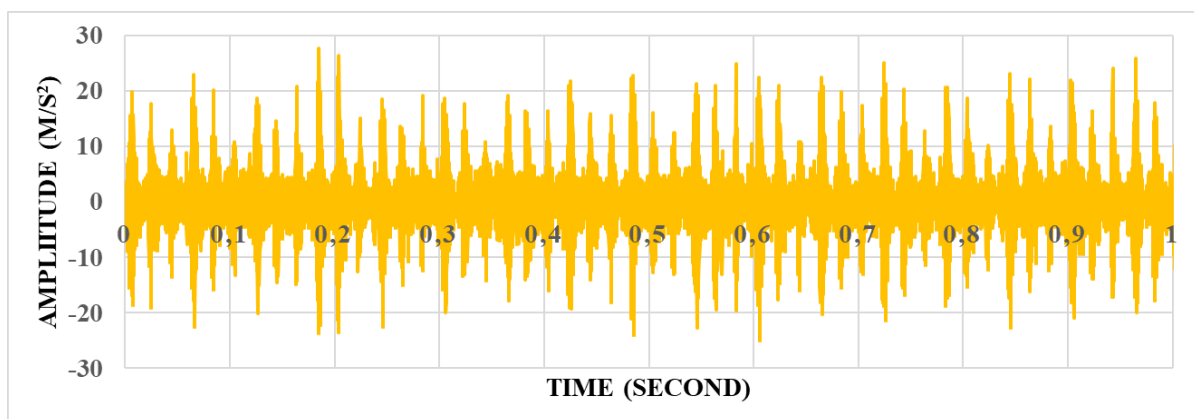
In the literature, it is stated that the maximum combustion pressure values of single-cylinder and direct-injection engines increase with engine load. However, since the test engine used in this study has an abnormal combustion chamber, the maximum combustion pressure values for all test fuels decreased with engine load. This was due to increasing combustion temperatures with increasing engine load shortened the ignition delay time for all test fuels. At higher engine loads, there was less fuel deposition in the combustion chamber during the shorter ignition delay time. Therefore, while the maximum combustion pressure value decreased for all test fuels due to the increase in engine load, the combustion

duration increased due to the increase in the amount of fuel injected from the injectors. Additionally, due to the increase in combustion duration, the piston moves away from the top dead center and combustion takes place in a larger volume depending on the increase in engine load. As seen in Figure 4-6, although more fuel is sprayed from the injector depending on the engine load, the increased combustion duration due to increasing load decreased the maximum in-cylinder pressure value. For these reasons, the maximum combustion pressure and heat release rate values for all test fuels were highest at 15 Nm and these values decreased with engine load. Biodiesel-containing fuels, which have a lower calorific value than conventional D, were injected into the combustion chamber in larger quantities in order to obtain the same torque value. For this reason, close pressure and heat release values were obtained with all test fuels depending on the increase in engine load.

## B. VIBRATION AND NOISE CHARACTERISTICS

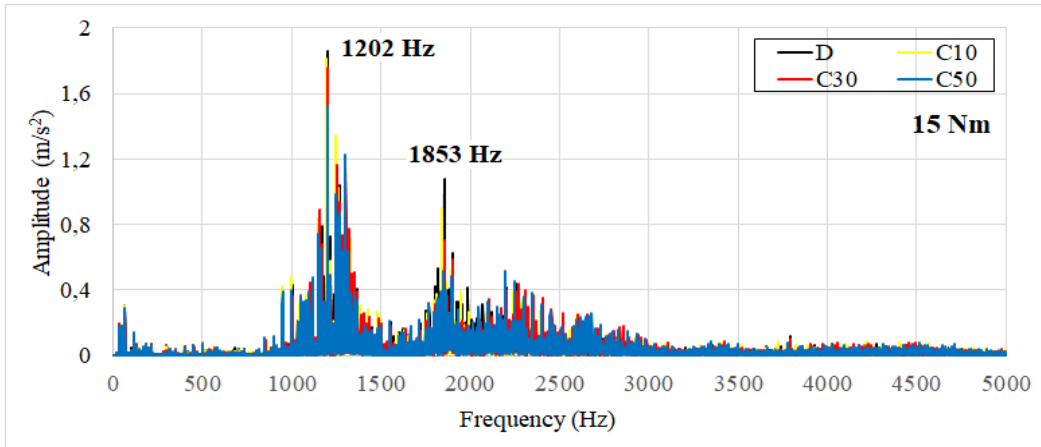
The pressure generated by combustion primarily generates pushing on the piston in the vertical direction. Therefore, only vibration data in the vertical direction were analyzed. The pressure wave generated by combustion impresses the combustion chamber surfaces, causing vibrations in the engine block.

Figure 7 shows the time domain vibration amplitude measured on the vertical axis as a function of time (1 second) with conventional D fuel at 60 Nm load. The time domain vibration amplitude shows the vibration amplitude obtained by injecting fuel from each injector for 1 second. The rotation speed of the engine per minute (2000 rpm) divided by 60 gives the revolutions per minute of the crankshaft around its axis in 1 second (33.33). In four-stroke engines, the injector sprays fuel 1 time in 2 rotations of the crankshaft around its axis. Therefore, 1 injector sprays fuel 16.67 times in 1 second. Since the test engine has 3 cylinders, as a consequence of the combustion caused by every injector spraying fuel in 1 second,  $16.67 \times 3 = 50$  vibration amplitude zones are formed as shown below. There are differences in the maximum amplitude values due to the mounting of the accelerometer on cylinder 1 and combustion irregularities.



*Figure 7. Time domain vibration amplitude graph for D fuel at 60Nm (1 second duration)*

Figures 8-11 show the frequency spectrum of vibrations obtained by converting the time domain data to frequency domain data by Fast Fourier Transform (FFT) analysis for all loads. As seen in Figures 8-11, two peak amplitude values were obtained at all engine loads. Dominant frequency was observed about at half of the experimental speed. This is mainly due to the combustion of fuel were occurred at this frequency. These peak values were obtained at frequencies close to each other at 15, 30, and 60 Nm. At 45 Nm, the peak values are obtained at different frequencies. In addition, the first peak value is the smallest at 45 Nm. This can be attributed to the fact that the smallest HRRmax value is obtained at 45 Nm as seen in Figure 5. In addition, the largest peak values were obtained at 15, and 60 Nm, and the smallest peak values were obtained at 45 Nm. This can be attributed to the smallest HRRmax value at 45 Nm and the lower rate of pressure increase during combustion.



*Figure 8. The frequency spectrum of vibrations of test fuels at 15 Nm.*

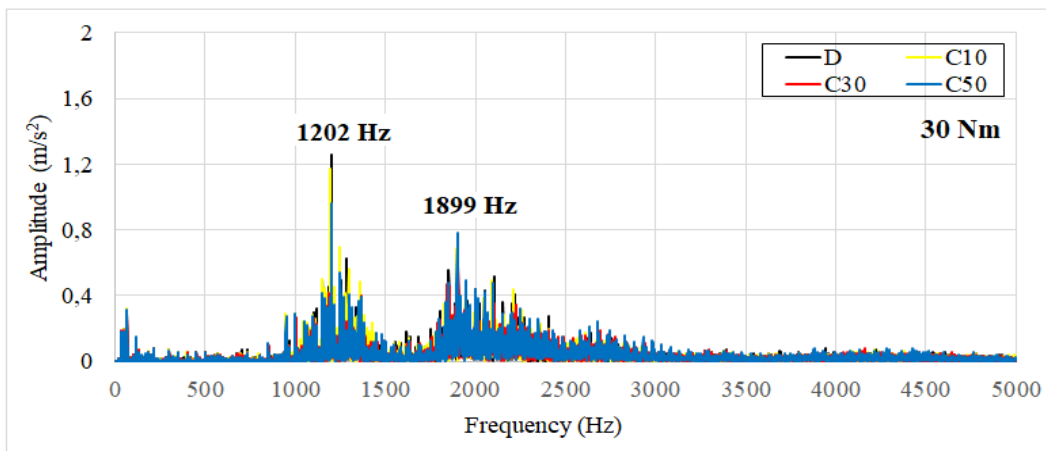


*Figure 9. The frequency spectrum of vibrations of test fuels at 30 Nm.*

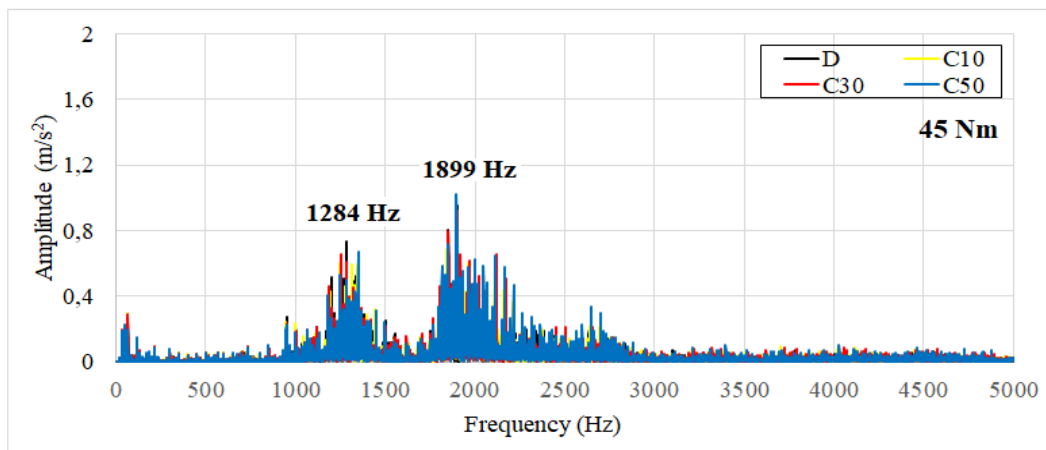


*Figure 10. The frequency spectrum of vibrations of test fuels at 45 Nm.*

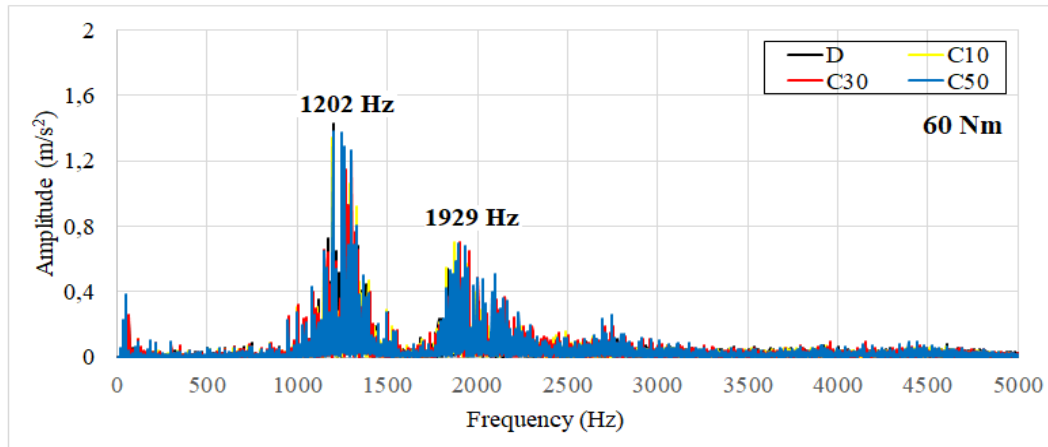


Figure 11. The frequency spectrum of vibrations of test fuels at 60 Nm.

The noise and vibration degree in internal combustion engines depends on the maximum in-cylinder pressure and the mechanical forces that vary with the rate of heat release and pressure rise. The increase in in-cylinder pressure primarily impresses the combustion chamber wall and gives rise to vibrations in the engine block. The consequent vibration creates noise. The in-cylinder combustion process is one of the most important noise sources. The maximum cylinder pressure rise rate, which is also influenced by fuel characteristics, affects the combustion speed. Figure 12 shows the Root Mean Square values ( $a_{RMS}$ ) of the acceleration values of the test fuels as a function of engine load. The average  $a_{RMS}$  values of all test fuels are 4.9, 4.5, 4.17, and 4.83  $m/s^2$  for 15, 30, 45, and 60 Nm loads, respectively.

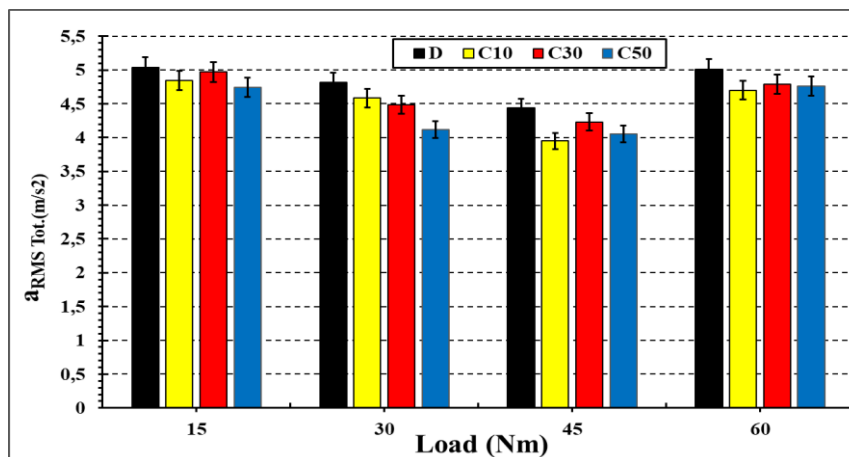


Figure 12. Root mean square values ( $a_{RMS}$ ) of test fuels as a function of load.

At 15 Nm, due to the lower combustion chamber temperature, the ignition delay time of all test fuels was longer than at other loads, which improved the combustion speed and the rate of pressure increase. At 60 Nm, more fuel injected through the injectors also increased the rate of pressure increase and the duration of combustion. At 45 Nm the HRRmax values of all test fuels are the smallest. For these reasons, the biggest vibration value for all test fuels was obtained at 15 and 60 Nm and the smallest vibration value was obtained at 45 Nm, as shown in Figure 12. As seen in Figure 12, the largest  $a_{RMS}$  values were obtained with conventional D and the smallest  $a_{RMS}$  values were obtained with C50 at all loads. The addition of biodiesel to conventional D fuel reduced engine vibration and the  $a_{RMS}$  values at all loads were 4.83, 4.52, 4.62, and 4.42  $m/s^2$  for D, C10, C30, and C50 fuels respectively. This can be attributed to the reduced rate of increase in gas pressure in the cylinder due to the biodiesel content in the test fuel and less pressure fluctuations during the combustion phase. The cetane number, flash point, viscosity, lubricating features, thermal features, physical features, and chemical and molecular structure of the fuel affect vibration variations [20]. The level of combustion noise depends on the rate of increased combustion pressure, which in turn depends on parameters such as injection timing and

ignition delay. The high viscosity and low cetane number of biodiesel-containing fuel blends reduce engine noise emissions. The average noise values of the test fuel at 2000 rpm as a function of engine load are given in Figure 13. The highest noise level was obtained with conventional diesel fuel (D) at all engine loads. The addition of biodiesel to the test fuels reduced the noise level at all loads. The reduction in noise level with biodiesel-containing test fuels is associated with reduced engine vibration. Therefore, in parallel with the decreasing trend in engine block vibration, the noise level also decreased with biodiesel-containing fuels. The average noise values of all test fuels are 90.58, 90.28, 90.35, and 90.09 dBA for 15, 30, 45, and 60 Nm loads, respectively. As seen in Figure 13, the noise level decreases up to 45 Nm and increases at 60 Nm. This can be attributed to the fact that the increased combustion chamber temperature due to engine load decreases the ignition delay time and increases the combustion efficiency. At 60 Nm, the increase in combustion duration due to the maximum amount of fuel injected also increased the noise level.

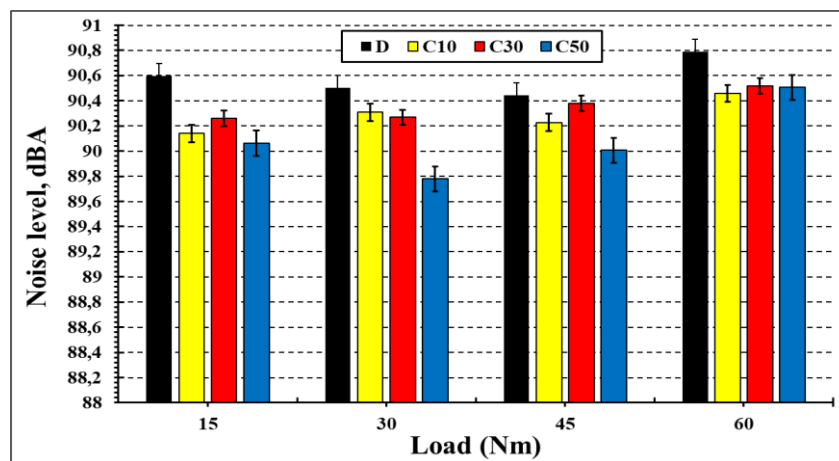


Figure 13. The noise levels of the test fuels as a function of engine load.

## IV. CONCLUSION

The biodiesel fuel used in this study was produced from refined canola oil. The produced canola oil methyl ester was mixed with conventional diesel fuel at different ratios by volume to obtain test fuels. The following results were obtained for the combustion, noise, and vibration characteristics of canola biodiesel and its blends compared to conventional diesel fuel in a three-cylinder engine using a mechanical fuel injector.

- The highest maximum in-cylinder pressure values for all test fuels were obtained at 15 Nm.
- At 15 Nm, the maximum in-cylinder pressure and HRR<sub>max</sub> values heightened subject to the biodiesel content in the test fuels.
- As a consequence of the combustion caused by each injector injecting fuel, 50 vibration amplitude zones are generated in 1 second.
- The average  $a_{RMS}$  values for all test fuels are 4.9, 4.5, 4.17, and 4.83 m/s<sup>2</sup> for loads of 15, 30, 45, and 60 Nm, respectively.
- For all test fuels, the largest vibration value was obtained at 15 and 60 Nm and the smallest vibration value was obtained at 45 Nm.
- The largest  $a_{RMS}$  values were obtained with conventional D fuel and the smallest  $a_{RMS}$  values with C50 fuel at all loads.
- The highest noise level was obtained with conventional fuel D at all engine loads. The addition of biodiesel to the test fuels reduced the noise level at all loads.
- The engine noise level is reduced up to 45 Nm and increased at 60 Nm.

ACKNOWLEDGEMENTS: This work is supported by the Düzce University Scientific Project (Project No: 2020.07.04.1133).

## **V. REFERENCES**

- [1] G. Knothe, “Biodiesel and renewable diesel: A comparison,” *Progress in Energy and Combustion Science*, vol. 36, no. 3, pp. 364–373, 2010.
- [2] A. Woo Go, S. Sutanto, L. Ki Ong, P. Lan Tran-Nguyen, S. Ismadji, and Y.-H. Ju, “Developments in in-situ (trans) esterification for biodiesel production: A critical review,” *Renewable and Sustainable Energy Reviews*, vol. 60, pp. 284-305, 2016.
- [3] J.M. Marchetti, V.U. Miguel, and A.F. Errazu, “Possible methods for biodiesel production,” *Renewable and Sustainable Energy Reviews*, vol. 11, no. 6, pp. 1300-1311, 2007.
- [4] A. Abbaszaadeh, B. Ghobadian, M.R. Omidkhah, and G. Najafi, “Current biodiesel production technologies: A comparative review,” *Energy Conversion and Management*, vol. 63, pp. 138-148, 2012.
- [5] D. Agarwal, S. Sinha, and A.K. Agarwal, “Experimental investigation of control of NOx emissions in biodiesel-fueled compression ignition engine,” *Renewable Energy*, vol. 31, no. 14, pp. 2356-2369, 2006.
- [6] A.K. Agarwal, “Biofuels (alcohols and biodiesel) applications as fuels for internal combustion engines,” *Progress in Energy and Combustion Science*, vol. 33, no. 3, pp. 233-271, 2007.
- [7] K. I. Reksowardojo, H. L. Ichsan, M. Wishnu, P. T. Brodjonegoro, H. T. Soerawidjaja, W. Arismunandar, N. N. Dung, and H. Ogawa, “Performance and Exhaust Gas Emissions of Using Biodiesel Fuel from Physic Nut (*Jatropha Curcas L.*) Oil on a Direct Injection Diesel Engine(DI).,” *SAE Technical Papers*, pp. 11–19, 2007.
- [8] M.M. Islam, M.A. Chowdhury, M.A. Sayeed, E. A. Hossain, S.S. Ahmed, and A. Siddique, “Finite element analysis of steel fiber-reinforced concrete (SFRC): validation of experimental tensile capacity of dog-bone specimens,” *Procedia Engineering*, vol. 90, pp. 89-95, 2014.
- [9] M.F. Russell and R. Haworth, “Combustion Noise from High Speed Direct Injection Diesel Engines,” *SAE Trans*, vol.94, 810–831, 1985.
- [10] A. Albarbar, F. Gu, and A.D. Ball, “Diesel engine fuel injection monitoring using acoustic measurements and independent component analysis,” *Measurement*, vol. 43, no. 10, pp. 1376-1386, 2010.
- [11] S. Jindal, “Vibration signatures of a biodiesel fueled CI engine and effect of engine parameters,” *International Journal of Energy And Environment*, vol. 3, no. 1, pp. 151–160, 2012.
- [12] V. Manienyan and S. Sivaprakasam, “Vibration analysis in DI diesel engine using diesel and biodiesel,” *International Journal of Engineering Trends and Technology*, vol. 4, no. 8, pp. 1821–1826, 2013.
- [13] S. Saridemir and Ü. Ağbulut, “Combustion, performance, vibration and noise characteristics of cottonseed methyl ester–diesel blends fuelled engine,” *Biofuels*, vol. 13, no. 2, pp. 201–210, 2022.

- [14] P. Chetankumar, A. Avinash Kumar, T. Nachiketa, L. Sanghoon, Chang Sik, and L. Sungwook Park, "Combustion, noise, vibrations and spray characterization for Karanja biodiesel fuelled engine", *Applied Thermal Engineering*, vol. 106, pp. 506–517, 2016.
- [15] E. Uludamar, E. Tosun, and K. Aydın, "Experimental and regression analysis of noise and vibration of a compression ignition engine fuelled with various biodiesels," *Fuel*, vol. 177, pp. 326–333, 2016.
- [16] K. Çelebi, E. Uludamar, E. Tosun, Ş. Yıldızhan, K. Aydın, and M. Özcanlı, "Experimental and artificial neural network approach of noise and vibration characteristic of an unmodified diesel engine fuelled with conventional diesel, and biodiesel blends with natural gas addition," *Fuel*, vol. 197, pp. 159–173, 2017.
- [17] A. Çalık, "Determination of vibration characteristics of a compression ignition engine operated by hydrogen enriched diesel and biodiesel fuels," *Fuel*, vol. 230, pp. 355–358, 2018.
- [18] A. Taghizadeh-Alisaraei, B. Ghobadian, T. Tavakoli-Hashjin, S.S. Mohtasebi, A. Rezaei-asl, and M. Azadbakht, "Characterization of engine's combustion-vibration using diesel and biodiesel fuel blends by time-frequency methods: A case study," *Renewable Energy*, vol. 95, pp. 422-432, 2016.
- [19] M.D. Redel-Macías, Pinzi, M.F. Ruz, A.J. Cubero-Atienza, and M.P. Dorado, "Biodiesel from saturated and monounsaturated fatty acid methyl esters and their influence over noise and air pollution," *Fuel*, vol. 97, pp. 751–756, 2012.
- [20] A. Taghizadeh-Alisaraei, B. Ghobadian, T. Tavakoli-Hashjin, S.S. Mohtasebi, "Vibration analysis of a diesel engine using biodiesel and petrodiesel fuel blends," *Fuel*, vol. 102, pp. 414–422, 2012.



# Düzce University Journal of Science & Technology

Research Article

## Inspection of Surface Damage in Composite Materials with Different Techniques

 Seyid Fehmi DİLTEMİZ<sup>a</sup>,  Ersin EROĞLU<sup>a,\*</sup>,  Aykut BATAR<sup>b</sup>,  Sezer YUMRUKAYA<sup>b</sup>

<sup>a</sup> Department of Aeronautical Engineering, Eskişehir Osmangazi University, Eskişehir, TURKEY

<sup>b</sup> 1st Air Maintenance Factory Directorate, Eskişehir, TURKEY

\* Corresponding author's e-mail address: ersineroglu@hotmail.com.tr

DOI: 10.29130/dubited.1373335

### ABSTRACT

Due to their excellent physical properties and high strength and stiffness relative to density, aerospace industry research is producing high-performance structural materials, such as composites, which are used in many critical structural parts like airframes, wings, rotor blades, propellers, and other components. However, during flight, these materials may be damaged by impact, thermal stress, moisture, and ultraviolet radiation. One of the most prevalent issues with composite materials is their challenging nature in terms of flaw detection during both manufacturing and use. When they are employed in the crucial areas that were previously indicated, this becomes a very serious issue. When evaluating the structural integrity of composites and looking for any damage, microscopes are a very useful instrument. Effective methods for identifying and analyzing damage include microscopic procedures like optical microscopy, stereomicroscopy, scanning electron microscopy (SEM), scanning ion microscopy (SIM), and atomic force microscopy (AFM). A variety of methods may be employed with microscopes to examine and identify deterioration in composite materials. It is often possible to examine overt deterioration on the surface of composite materials under the microscope utilizing a number of different approaches and procedures. Determining the kind, extent, distribution, and impact of the damage requires these inspections. Often employed techniques consist of: SEM is a method for high-resolution imaging of surface damage. It entails shining an electron beam onto the sample's surface and capturing pictures. SEM is a useful tool for identifying erosion, delamination, and microcracks. It is also possible to measure things like the damage's breadth and depth. Optical microscopes have a large field of view and look at damaged regions. This makes it possible to find tiny fractures or cracks that are invisible to the unaided eye. Furthermore, details on the degree of harm, the roughness of the surface, and the breadth and depth of the fractures may be acquired. To see damaged objects, optical microscopy is utilized. Cracks and damage locations are visible with optical microscopy. Optical microscopes can identify different kinds of damage by looking at the surface of the material. Damage like delamination, fiber breakage, cracks, and deformations are a few examples of these. This study examines the efficacy of microscopic methods and non-destructive testing in assessing the different kinds of damage that can occur at the interfaces between holes in composite materials. Composite test materials were chosen from glass fiber reinforced phenolic matrix composites that were produced in compliance with aerospace standards. The measurements led to the conclusion that using microscopic techniques has benefits like speed and field suitability. However, the continuous development and improvement of new methods in this field will contribute to a better understanding of layered composite materials and the development of safer and more durable structures.

**Keywords:** Aerospace, Composite materials, Microscopy

## Kompozit Malzemelerde Yüzey Hasarlarının Farklı Tekniklerle İncelenmesi



## ÖZ

Havacılık ve uzay endüstrisinin ticari ve askeri uçakların performansını artırmaya yönelik araştırmalar, yüksek performanslı yapısal malzemelerin geliştirilmesine yol açmaktadır. Kompozit malzemeler, mevcut ve gelecekteki havacılık ve uzay bileşenlerinde önemli bir rol oynayan bu tür malzeme sınıflarından biridir. Kompozit malzemeler, yüksek mukavemet ile sertlik-yoğunluk oranları ve üstün fiziksel özellikleri nedeniyle havacılık ve uzay uygulamaları için özellikle uygulanabilir bir malzeme türü olarak kullanılmaktadır.[1] Uçak gövdeleri, kanatlar, rotor kanatları, pervaneler ve diğer bileşenler gibi birçok kritik yapısal parçada kompozit malzemeler bulunmaktadır. Ancak, uçuş sırasında oluşabilecek darbeler, termal gerilmeler, nem, ultraviyole ışınları gibi faktörler nedeniyle hasarlar meydana gelebilir. Kompozit malzemelerin kullanımı sırasında sık karşılaşılan problemlerden birisi gerek üretim gerekse kullanımları sırasında meydana gelen kusurların tespitinin zor olmasıdır. Özellikle yukarıda değinilen kritik sahalarda kullanımında bu durum daha büyük bir problem olarak öne çıkmaktadır. Mikroskoplar, kompozit malzemelerin yapısal bütünlüğünü değerlendirmek ve potansiyel hasarları tespit etmek için kullanılan güçlü bir araçtır. Optik mikroskopi, stereo mikroskopi, taramalı elektron mikroskopi (SEM), taramalı iyon mikroskopisi(SIM) ve atomik kuvvet mikroskopisi (AFM) gibi mikroskopik teknikler, hasarların belirlenmesi ve analiz edilmesi için kullanılan etkili araçlardır. Mikroskoplar, kompozit malzemelerdeki hasarların tespiti ve analizi için farklı tekniklerle kullanılabilir. Kompozit malzemelerin yüzeyindeki açık hasarların mikroskopi ile incelenmesi, genellikle bir dizi teknik ve yöntem kullanılarak gerçekleştirilir. Bu incelemeler, hasarın türünü, büyüklüğünü, dağılımını ve etkisini belirlemek için önemlidir. Bazı yaygın kullanılan yöntemler şunlardır; SEM, yüzeydeki hasarları yüksek çözünürlükte görüntülemek için kullanılan bir tekniktir. Elektron demeti kullanarak numunenin yüzeyine odaklanır ve görüntüler elde eder. SEM, mikro çatlakları, tabakalaşma ve erozyonu tespit etmek için etkili bir yöntemdir. Ayrıca, hasarın derinliği ve genişliği gibi ölçümler yapılabilir. Optik mikroskoplar, hasarlı bölgeleri geniş bir görüş alanında inceler. Bu sayede çıplak gözle görülemeyen küçük çatlaklar veya kırılmalar tespit edilebilir. Ayrıca, hasar boyutu, yüzey pürüzlülüğü, çatlakların derinliği ve genişliği gibi bilgiler elde edilebilir. Optik mikroskopi, hasar bölgelerini ve çatlakları görselleştirmek için kullanılır. Optik mikroskoplar, malzeme yüzeyini inceleyerek hasar türlerini tespit edebilir. Bunlar arasında delaminasyon (katmanların ayrılması), fiber kırılması, çatlaklar, deformasyonlar gibi hasarlar bulunabilir. Bu çalışmada, tahribatsız muayene ve mikroskopik teknikler kullanılarak, kompozit malzemelerin delik ara yüzeylerinde meydana gelen çeşitli hasar türlerinin değerlendirilebilme etkinliği incelenmiştir. Kompozit malzeme olarak havacılık standartlarında üretilmiş cam fiber takviyeli fenolik matrisli kompozitler seçilmiştir. Ölçümler sonucunda; mikroskopik tekniklerinde, hız ve sahaya uygunluk gibi avantajları ile kullanılabilir olduğu sonucuna varılmıştır. Bununla birlikte, bu alanda sürekli olarak yeni yöntemlerin geliştirilmesi ve geliştirilmesi, katmanlı kompozit malzemelerin daha iyi anlaşılmasına ve daha güvenli ve dayanıklı yapıların geliştirilmesine katkıda bulunacaktır.

*Anahtar Kelimeler: Havacılık, Kompozit malzemeler, Mikroskopi*

## **I. INTRODUCTION**

Composite materials are widely used in the manufacture of aircraft and spacecraft structural parts due to their specific mechanical and physical properties such as high specific strength and high specific stiffness.[2] Other properties of composite materials such as corrosion resistance, excellent surface profiles, improved fatigue resilience and special performance have also contributed significantly to the rapid increase in composite material applications. However, the defects and damages of composite materials and their subsequent repair requirements are currently challenging for composite material users.[3]

Defects and damage to structural components are common occurrences in materials processing, component manufacturing or in service. The impact of the defect or damage on the structural integrity of the composite component is crucial to understanding the defect.[4] Discontinuity, defects or damages are defined as any local change in the physical state or mechanical properties of a material or structure that may affect the structural behavior of the component. There are approximately many different types of defects that composite components are prone to or potentially exposed to. These range from microscopic fiber defects to large, severe impact damage.[5] The damage types in layered composite material in macro and micro dimensions are shown in Figure 1. Also, the separation damage that can occur during drilling operations for layered composite materials is also illustrated in Figure 2.

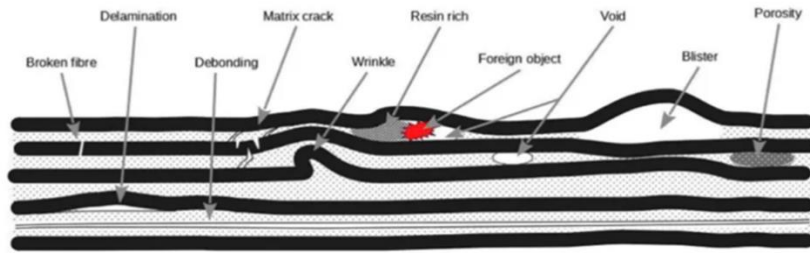


*Figure 1. Types of Damage in Layered Composite Materials [6]*

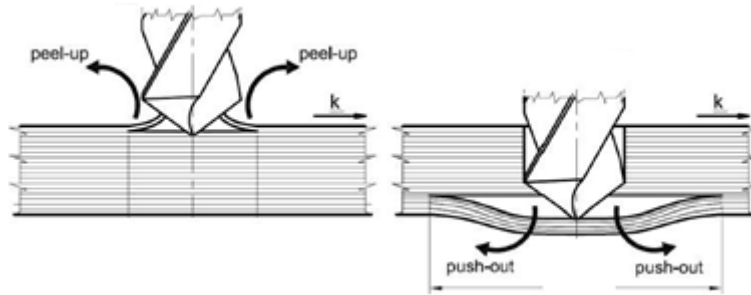


*Figure 2. Damages that can occur during the Drilling Operation*

Composites should be inspected at specified intervals during their production and service life. These inspections are carried out by destructive testing during production and usually by non-destructive testing during their service life. Non-destructive testing (NDI) is a crucial component in the service life cycle of critical structures in aircraft, spacecraft and transportation vessels.[7]

The investigation of composite material manufacturing defects using various control techniques is the focus of this study. Because of their complex behavior, composite materials are used in industries like aerospace and should be well-known.[8] In this study, it is aimed to non-destructively control the surface defects encountered in the drilling operations of polymer matrix glass fiber reinforced composite parts used in aerospace parts, which are pre-impregnated with resin and manufactured by autoclave process in layers, by visual and ultrasonic control methods and to examine the defects encountered.

## **II. MATERIALS AND METHODS**

### **A. MANUFACTURING**

For the selection of materials to be used for this study, glass fiber reinforced pre-resin impregnated materials used in avionic equipment covers, cockpit panels, antenna structures, in the interior and exterior structures of military and civil aircraft were selected[9]. Fiber glass is a special kind of industrial textile material because of its versatility. The fabric form of fiber glass provides an exceptional blend of characteristics, including fire resistance and high strength. The end user can choose the ideal blend of material performance, economy, and product flexibility thanks to the vast array of yarn sizes and weave patterns, which offer endless design possibilities. One engineering material that is dimensionally stable is fiber glass. It is not affected by changes in temperature, either in terms of stretching or shrinking. When exposed to water, it does not absorb moisture or undergo any physical or chemical changes. It is a better material in applications requiring high strength and low weight due to its high strength-to-weight ratio. This strength can be unidirectional or bidirectional in textile form, offering cost and design flexibility. Since it is inorganic, it cannot burn or facilitate combustion. At 1000 °F, it has a strength of roughly 25%. For glass fiber, most chemicals have negligible or no effect. Glass textile fibers that are

inorganic do not decay, rot, or grow mold. Strong alkaline compounds, hot phosphoric acids, and hydrofluoric acids all have an impact on glass fibers. It's a great material for insulating electrical systems. Fiber glass fabrics are perfect as an insulating varnish and printed circuit board reinforcement due to their low dielectric constant, high strength, heat resistance, and low moisture absorption. Compared to asbestos and organic fibers, glass fabrics have a low coefficient of thermal expansion and high thermal conductivity, making them dimensionally stable and able to dissipate heat quickly.

Hexcel HT93 pre-phenolic resin impregnated 7781 style E glass cloth was used as raw material for the production of test panel materials. The pre-impregnated glass fabric was assembled into layered assemblies by hand lay-up and vacuum bag methods in 100.000 class clean room conditions according to ISO 14644. Autoclave process was applied for curing of the phenolic resin and then cured test panel were obtained.



*Figure 3. Composite Test Panel Manufacturing*

## **B. MACHINABILITY OF COMPOSITE MATERIALS AFTER CURING**

During the fabrication of polymer composites, it is more complex to create holes and slots without affecting the reinforcement, in such cases machining is the only technique of choice to create complex shapes and the necessary requirements.[10] Due to their inhomogeneous properties, composite materials show significant differences in machining compared to conventional materials.[11] Also, the cutting mechanism of composite material differs greatly from the cutting mechanism of conventional material.[12] This makes it difficult to analyze their machining performance. Machining of composite material can damage the material surface due to delamination, fiber orientation, fiber cracking and matrix flow.[13] Since it is not economical to process a composite material with most of the conventional processing methods. The performance of fiber-reinforced composites can also be affected by processing conditions, which concerns the lifetime and mechanical performance of polymer composites.[14] Recently composite materials utilize advanced processing techniques such as electrical discharge machining, ultrasonic machining, laser cutting and water jet and abrasive water jet machining.[15] In this study, an investigation has been carried out to understand the processing of composites, especially the drilling process. Our sample materials of layered composites made of glass fiber impregnated with phenolic resin Figure 4 holes were drilled and hole surfaces were examined with

1inç diameter HSS, carbur and seramic composite flat cutting tools, 500-2500mm/min feed rates, 1000-40000 rpm spindle rate and tool speeds on the 5 axes DMG DMU65 Monoblock and 3 axes Spinner VC1000 milling machines.

### C. INSPECTION EQUIPMENT'S

Non-destructive testing (NDI) of composites is a crucial component in the service life cycle of critical structures in aircraft, spacecraft and transportation vessels.[7] Ultrasonic testing (UT) is probably the first method that comes to mind among the many NDI techniques beyond visual inspection and manual tapping hammer testing. Ultrasonic testing is based on the principle of making measurements on the material by using high energy and frequency sound waves. Detection of various defects and properties such as discontinuity, material thickness, etc. on the material is a very sensitive control method. In this study delamination inspection with the GE USN 60 ultrasonic controller and visual inspection up to 40x magnification with the WILD stereo microscope and for higher detailed images were obtained with the ZEISS Ultra Plus SEM.

Stereoscopic microscopes are used in various fields for tasks requiring three-dimensional imaging and fine detail observation. In surface inspection of composite structures, common in aircraft and spacecraft manufacturing, Stereo microscopes allow close inspection of the surface of materials. They can detect defects, faults and irregularities that are invisible to the naked eye.

Scanning Electron Microscopy (SEM) is a technique that uses a focused beam of high-energy electrons to produce various signals on the surface of solid samples. The electrons interact with atoms in the sample, producing a variety of signals that contain information about the surface topography and composition of the sample. SEM has many advantages over conventional microscopes, including a large depth of field, much higher resolution and the ability to image a relatively large area of the sample.[16]

## III. INSPECTION AND RESULTS

Non-destructive control of the composite layered material was firstly carried out with General Electric USD 60 ultrasonic tester using sound receiving and transmitting equipment. Unperforated and perforated surfaces were examined in detail. The sound frequency responses of the non-perforated surface and the perforated surface are compared in Figure 4a and 4b, and separations were detected around the holes machined at high speed and feed rate. Separation could not be detected visually, but all hole surfaces were examined in detail by SEM in Figure 5 and Figure 6, and layers, warping and warping arrangements, matrix and fiber fractures and voids were detected.

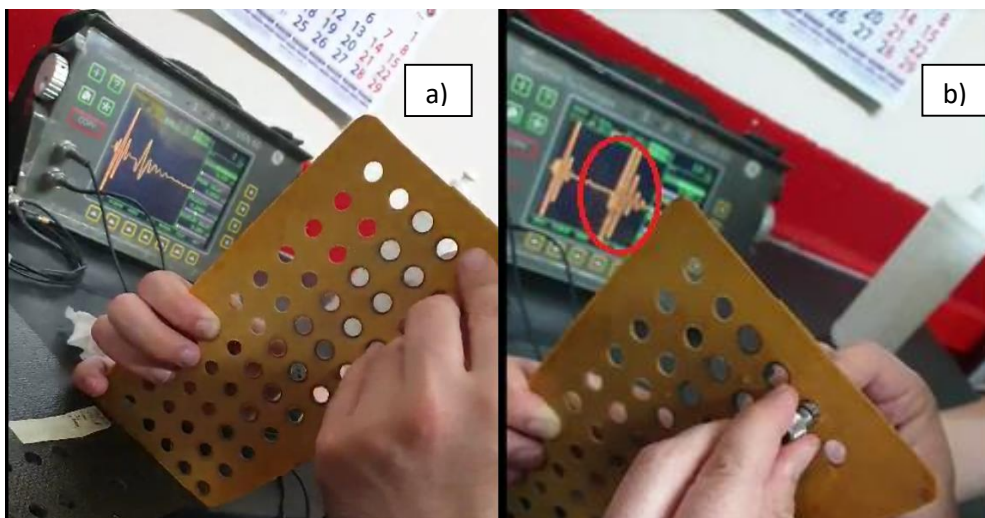


*Figure 4. Ultrasonic controls*

The surface of the hole was examined in detail with 6, 16, and 40 x magnifications in stereo micrograph. With the 6x image, the entire hole perimeter and the fibre openings at the entrance and exit during the milling hole process were detected. With 16x magnification, fibre cross-sections at the exit points of the hole process were detected and with 40x magnification, the arrangement of the layers at the interface, weave directions, matrix agglomerations could be examined.

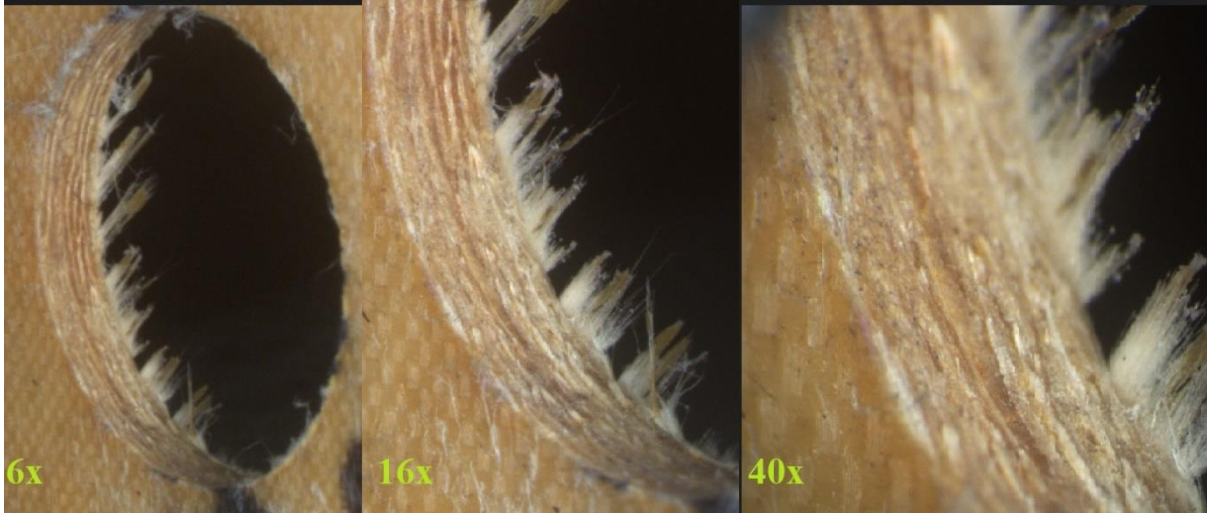


*Figure 5. Stereo microscopic images*

In Figure 6, the weft and warp image of the fibre yarns at the hole interface, the gap between the weft and warp and local regional fibre wrinkles were detected at 54x, 236x and 555x magnifications obtained by SEM.

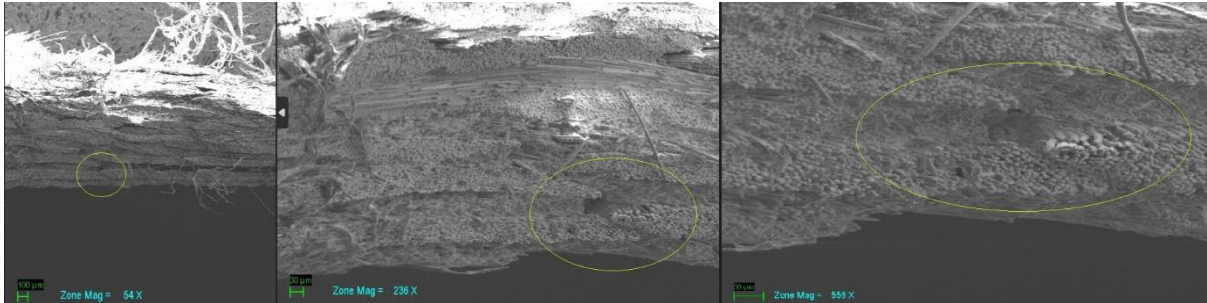


*Figure 6. SEM image of weft and warp*

In the regions marked in Figure 7, weft and warp images of the fibre yarns at the hole interface, fibre matrix fracture and separations were detected at 76x and 451x magnifications obtained by SEM. Fibre yarn thickness measurement can also be made with these images. The surface quality at the entire hole cutting interface can also be determined. The hole or process interfaces of composite materials layered from woven fabrics are not as smooth as metals and do not have the desired low surface roughness.

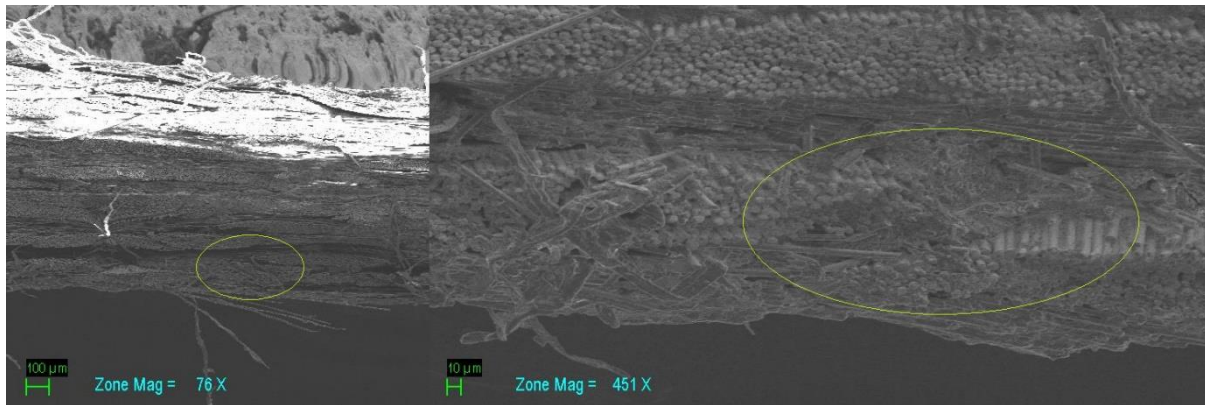


*Figure 7. SEM Matrix Fracture and Cavity*

## **IV. CONCLUSION**

Composite materials are increasingly being researched and used in the manufacture of structural parts for civil and military aerospace structures due to their structural performance, increased efficiency and maintenance advantages. The FAA 20-170B Recommendation on composite structural parts in 2010 emphasized the importance of inspections and testing in the production and processing of composite parts and that requirements should be taken at the factory level. In this study, a detailed experimental study has been carried out on the hole processes required for the connection of composite parts with other structural assemblies with bonding elements, and the hole interfaces of test specimens produced with glass fiber fabric impregnated with phenolic resin were examined by ultrasonic non-destructive control methods and microscopy methods. It has been demonstrated that detailed interfacial controls can be performed successfully and effectively with the microscopy method for layered composite materials, and it is evaluated to be applicable in terms of optimization of hole drilling processes of composite materials and production quality requirements.

## **V. REFERENCES**

- [1] Y. Li, Y. Xiao, L. Yu, K. Ji, and D. Li, "A review on the tooling technologies for composites manufacturing of aerospace structures: materials, structures and processes," *Compos Part A Appl Sci Manuf*, vol. 154, p. 106762, Mar. 2022, doi: 10.1016/J.COMPOSITESA.2021.106762.
- [2] A. M. Abrão, P. E. Faria, J. C. C. Rubio, P. Reis, and J. P. Davim, "Drilling of fiber reinforced plastics: A review," *Journal of Materials Processing Technology*, vol. 186, no. 1–3. pp. 1–7, May 07, 2007. doi: 10.1016/j.jmatprotec.2006.11.146.
- [3] H. Yang *et al.*, "Ultrasonic detection methods for mechanical characterization and damage diagnosis of advanced composite materials: A review," *Composite Structures*, vol. 324. Elsevier Ltd, Nov. 15, 2023. doi: 10.1016/j.compstruct.2023.117554.
- [4] P. Journoud, C. Bouvet, B. Castanié, and L. Ratsifandrihana, "Effect of defects combined with impact damage on compressive residual strength in curved CFRP specimen," *Thin-Walled Structures*, vol. 184, Mar. 2023, doi: 10.1016/j.tws.2022.110484.
- [5] S. L. Ogin, P. Brøndsted, and J. Zangenberg, "Composite materials: constituents, architecture, and generic damage," *Modeling Damage, Fatigue and Failure of Composite Materials*, pp. 3–23, Jan. 2016, doi: 10.1016/B978-1-78242-286-0.00001-7.

- [6] M. Bowkett and K. Thanapalan, "Comparative analysis of failure detection methods of composites materials' systems," *Systems Science and Control Engineering*, vol. 5, no. 1. Taylor and Francis Ltd., pp. 168–177, Jan. 01, 2017. doi: 10.1080/21642583.2017.1311240.
- [7] H. TOWSYFYAN, A. BIGURI, R. BOARDMAN, and T. BLUMENSATH, "Successes and challenges in non-destructive testing of aircraft composite structures," *Chinese Journal of Aeronautics*, vol. 33, no. 3, pp. 771–791, Mar. 2020, doi: 10.1016/J.CJA.2019.09.017.
- [8] A. Zarei, S. Farahani, and S. Pilla, "An experimental study on the manufacturing of engineered defects in composite plates," *Composites Part C: Open Access*, vol. 9, Oct. 2022, doi: 10.1016/j.jcomc.2022.100327.
- [9] C. Jubsilp, P. Mora, C. W. Bielawski, Z. Lu, and S. Rimdusit, "Thermosetting matrix based glass and carbon fiber composites," *Fiber Reinforced Composites: Constituents, Compatibility, Perspectives and Applications*, pp. 341–403, Jan. 2021, doi: 10.1016/B978-0-12-821090-1.00012-0.
- [10] S. O. Ismail, H. N. Dhakal, I. Popov, and J. Beaugrand, "Comprehensive study on machinability of sustainable and conventional fibre reinforced polymer composites," *Engineering Science and Technology, an International Journal*, vol. 19, no. 4, pp. 2043–2052, Dec. 2016, doi: 10.1016/J.JESTCH.2016.07.010.
- [11] A. Hejjaji, D. Singh, S. Kubher, D. Kalyanasundaram, and S. Gururaja, "Machining damage in FRPs: Laser versus conventional drilling," *Compos Part A Appl Sci Manuf*, vol. 82, pp. 42–52, Mar. 2016, doi: 10.1016/J.COMPOSITESA.2015.11.036.
- [12] V. Lopresto, A. Caggiano, and R. Teti, "High Performance Cutting of Fibre Reinforced Plastic Composite Materials," *Procedia CIRP*, vol. 46, pp. 71–82, 2016, doi: 10.1016/J.PROCIR.2016.05.079.
- [13] M. B. Lazar and P. Xirouchakis, "Experimental analysis of drilling fiber reinforced composites," *Int J Mach Tools Manuf*, vol. 51, no. 12, pp. 937–946, Dec. 2011, doi: 10.1016/J.IJMACHTOOLS.2011.08.009.
- [14] A. A. A. Nasir, A. I. Azmi, and A. N. M. Khalil, "Parametric Study on the Residual Tensile Strength of Flax Natural Fibre Composites after Drilling Operation," *Procedia Manuf*, vol. 2, pp. 97–101, Jan. 2015, doi: 10.1016/J.PROMFG.2015.07.017.
- [15] S. Vigneshwaran, M. Uthayakumar, and V. Arumugaprabu, "Review on Machinability of Fiber Reinforced Polymers: A Drilling Approach," *Silicon*, vol. 10, no. 5, pp. 2295–2305, Sep. 2018, doi: 10.1007/s12633-018-9764-9.
- [16] N. Roy and S. Gurusideswar, "Material characterization of polymer nanocomposites for aerospace applications," *Mater Today Proc*, Jun. 2023, doi: 10.1016/j.matpr.2023.05.606.



# Düzce University Journal of Science & Technology

Research Article

## Measuring the Thickness of Fiber Mats Using Light Transmittance via Image Processing

 Burcu YILMAZEL <sup>a,\*</sup>,  Dilara ÖZTÜRK <sup>a</sup>,  Hecan YAVUZTÜRK <sup>a</sup>,  Halit Kaan CAN <sup>a</sup>,  
 Emre KAÇMAZ <sup>a</sup>,  Gamze KARANFİL KAÇMAZ <sup>b,c</sup>

<sup>a</sup> Department of Computer Engineering, Faculty of Engineering, Eskişehir Technical University, Eskişehir, TURKEY

<sup>b</sup> Department of Energy Systems Engineering, Faculty of Engineering, Karamanoğlu Mehmetbey University, Karaman, TURKEY

<sup>c</sup> GMZ Energy Systems Industry and Trade Ltd. Co., Eskişehir, TURKEY

\* Corresponding author's e-mail address: byurekli@eskisehir.edu.tr

DOI: 10.29130/dubited.1371752

### ABSTRACT

Fiber materials possess unique properties, including a large active surface area, high surface-to-volume ratio, high porosity, high mechanical performance, and low density. Consequently, they serve as key components in various applications such as energy production and storage cells, batteries, wastewater treatment membranes, sensors, drug-releasing band-aids, and protective clothing. Electrospinning is a simple and versatile method for producing fiber materials. Despite its simplicity in terms of working principles, it faces challenges in achieving homogeneous thickness (evenly on the entire surface) throughout fiber mats due to inherent bending instability during the process. Non-uniform thickness not only diminishes the efficiency of these mats in applications but also adversely impacts their mechanical functionality. In this study, the aim is to develop a thickness measurement system based on image processing and the principle of light transmittance as a solution to the issues encountered in achieving uniform thickness and thickness control of fiber mats produced by electrospinning devices. To accomplish this, a closed mechanism with a light-impermeable encapsulation method was established. Various fiber mats, produced at different times were placed on the acetate floor built on LED lighting on the base of the mechanism. Using a camera with the adjusted settings positioned at the focal point on top of the mechanism, images of the fiber mats were captured, and image processing techniques were employed to determine threshold value ranges for the mat thicknesses. The actual thicknesses of the fiber mats were verified using an optical microscope, revealing that regions defined with the same color in different samples exhibited similar thicknesses.

**Keywords:** Image processing, Fiber material, Electrospinning method, Thickness measurement

## Fiber Matların Kalınlığının Görüntü İşleme Yoluyla Işık Geçirgenliği Kullanılarak Ölçülmesi

### ÖZ

Fiber malzemeler sahip oldukları geniş aktif yüzey alanı, yüksek yüzey-hacim oranı, yüksek gözeneklilik, yüksek mekanik performans ve düşük yoğunluk gibi özellikleri nedeniyle enerji üretim ve depolama hücreleri, piller, atık su arıtımında kullanılan membranlar, sensörler, ilaç salınımlı yara bantları ile koruyucu giysiler gibi birçok uygulamada ana bileşen olarak kullanılmaktadır. Elektrospon, fiber malzemeler üretmek için kullanılan



basit ve çok yönlü bir yöntemdir. Elektrospın yöntemi her ne kadar çalışma prensibi olarak basit bir yöntem olsa da işlem esnasında ortaya çıkan bükülme dengesizliği nedeniyle homojen kalınlıkta (tüm yüzeyde eşit olacak şekilde) fiber matlar elde edilememektedir. Homojen olmayan kalınlık, bu matların uygulamalardaki verimliliğini azaltmakla kalmaz, aynı zamanda mekanik işlevlerini de olumsuz etkiler. Bu çalışmada, elektrospın cihazı ile üretilen fiber formunda matların homojen kalınlıkta üretimlerinde ve kalınlık kontrolünün sağlanmasında karşılaşılan sorunlara çözüm olarak görüntü işleme ve ışık geçirgenliği prensibine dayalı bir kalınlık ölçüm sisteminin geliştirilmesi amaçlanmıştır. Bu amaç doğrultusunda öncelikle ışık geçirimsiz kapsülleme yöntemiyle kapatılmış bir düzene kurulumu. Düzeneğin zemin kısmında LED aydınlatma üzerine kurulumu asetat zemin üzerine farklı sürelerde üretilmiş çeşitli fiber matlar yerleştirilmiştir. Düzeneğin tepe noktasındaki odak noktasına koyulan çekim özellikleri sabit ayarlanmış bir kamera ile görüntüler elde edilmiş ve mat kalınlıklarına ait eşik değer aralıklarını belirlemek için görüntü işleme teknikleri kullanılmıştır. Fiber matların gerçek kalınlıkları optik mikroskop ölçümüyle doğrulanmış ve farklı numunelerde aynı renkle tanımlanan bölgelerin benzer kalınlığa sahip olduğu belirlenmiştir.

*Anahtar Kelimeler: Görüntü işleme, Fiber malzeme, Elektrospın yöntemi, Kalınlık ölçümü*

## **I. INTRODUCTION**

Fiber materials find widespread applications in diverse fields such as wastewater treatment, energy storage, tissue engineering, drug release, heavy metal detection, and thermal insulation. Their exceptional properties, including a high surface-to-volume ratio, substantial porosity, low density, expansive active surface area, and excellent mechanical performance, make them highly desirable [1]. Electrospinning is a versatile and straightforward technique for fabricating fiber materials. Despite its simplicity in principle, the electrospinning process is influenced by numerous parameters [2-4]. The application of high voltage in electrospinning induces electrical repulsion, leading to bending instability and preventing the production of uniformly thick fibers.

Fiber mats with non-uniform thickness compromise their functionality, resulting in reduced efficiency and inferior mechanical properties in practical applications, such as reduced filtration efficiency or proton permeability [5]. Maintaining the highest functionality necessitates precise knowledge of fiber mat homogeneity and thickness during production.

Several established methodologies for measuring fiber mat thickness involve the utilization of distance measurement sensors, employing diverse technologies to ensure accurate and reliable assessments of distance, thickness, and position. These sensors employ light reflection from object surfaces, facilitating prompt and precise measurements. However, such sensors tend to be costly. A review of the literature reveals that methods employed for measuring fiber mat thickness are often complex and expensive. Image processing techniques are used for different applications in areas such as construction and automotive, where fiber materials are also used extensively. Jiang et al. (2020) have developed a new method to characterize the distribution of the film thickness of asphalt mortar, which is a mixture of binder and fine mineral aggregates, which is considered an important indicator in evaluating the durability of the asphalt mixture, through image processing techniques. Internal images of the samples were scanned and analyzed. Mortar film thickness values were measured along the boundary of each aggregate in the scanned images. To characterize the mortar film thickness distribution, mean values ( $T_m$ ) and standard deviations ( $SD_t$ ) were calculated and the results were compared based on these values [6]. Cruz et al. (2023) developed a new method to analyze some of the disadvantages, such as edge cracking along the sheet thickness resulting from the creation of components with cutting edges, of advanced high-strength steels, which are becoming increasingly popular in the automotive industry due to their high yield and ultimate tensile strengths. When characterizing the formability of sheet metal materials, hole expansion testing is an industry standard method used to evaluate the ductility of their edges. However, visualizing initial cracking accurately is often difficult and subjective, often leading to inconsistent results and low repeatability. In order to find solutions to these problems, they proposed a new digital image processing method to reduce operator dependency and increase the accuracy and efficiency of hole expansion test results. The

proposed approach allows a more precise determination of the hole expansion ratio by detecting the appearance of initial edge cracks by utilizing advanced image processing algorithms [7]. As a result of our research, we have concluded that it is feasible to measure fiber mat thickness at a lower cost using image processing techniques, given the current state of image processing technologies and their successful utilization in numerous industrial applications.

In light of this understanding, our study aimed to develop a thickness measurement system based on image processing, offering a technological solution to challenges encountered in achieving uniform thickness and thickness control in fiber mats produced by electrospinning devices. This system primarily relies on the principle of light transmittance and employs an innovative, light-impermeable encapsulation mechanism. Through this mechanism, we obtained images of fiber mat samples, which were then subjected to various image processing techniques. These processed images were subsequently divided and compared using matrixing methods, leading to the determination of threshold values based on colors. Actual thickness values of the fiber mat samples were measured with an optical microscope, and a color-based thickness scale was established by aligning the threshold value ranges obtained through image processing with the corresponding actual thickness values.

Our study seeks to optimize electrospinning device production parameters by leveraging data collected from the image processing and light transmittance-based thickness measurement system. Achieving uniform thickness distribution in fiber mats produced under optimal conditions is pivotal for sustainability, repeatability, enhanced efficiency, and reduced operational costs through minimized material wastage and energy consumption.

## II. METHODOLOGY

The steps undertaken to implement the solution for measuring the thickness of fiber mats using image processing and light transmission are delineated in Figure 1. Initially, we devised a novel testing mechanism tailored for acquiring images of fiber mats. Subsequently, we captured images of fiber mat samples fabricated on acetate substrates at various time points using this newly developed mechanism. These acquired images were then subjected to rigorous image processing techniques, involving matrixing methods and the determination of threshold values based on color analysis. The true thicknesses of regions corresponding to identical color ranges in distinct fiber mat samples were meticulously measured using an optical microscope. The resultant measurements were then subjected to a comparative analysis. This approach allowed us to draw meaningful conclusions regarding the thickness variations across different fiber mat samples.

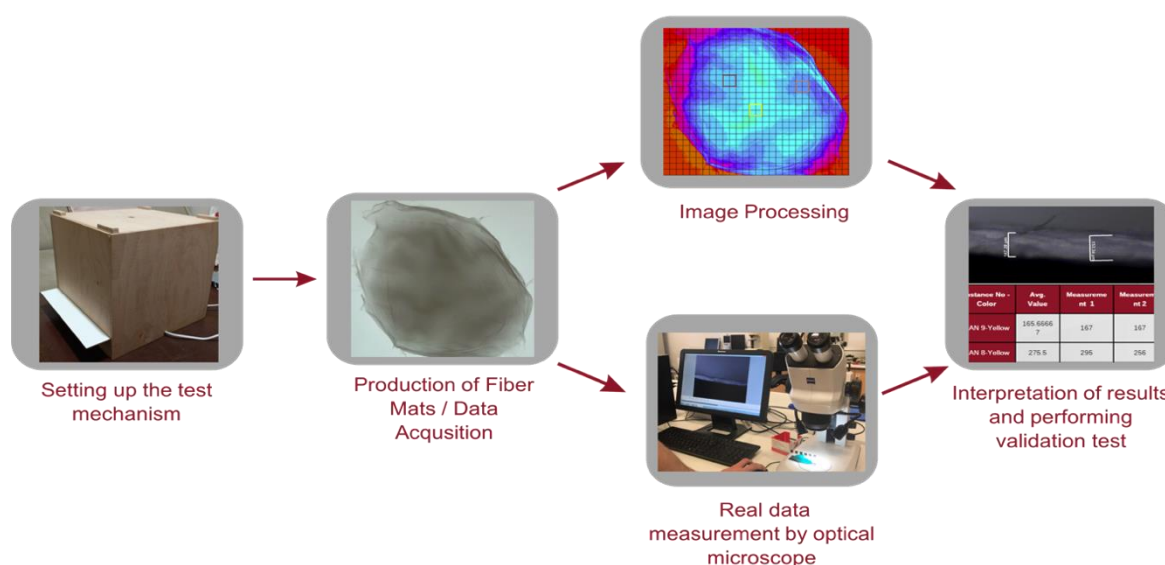


*Figure 1. Experimental workflow*

## A. SETTING UP THE TEST MECHANISM

A new test mechanism enclosed within a light-impermeable enclosure was designed, comprising a camera at the top (with the camera's focal point and shooting parameters set to a fixed configuration) and LED illumination integrated at the base of the mechanism. The schematic representation of the test mechanism is presented in Figure 2, with the finalized version depicted in Figure 3.

Ensuring that the assembly remained impervious to external light was of utmost importance to achieve precise and processable results. Hence, the test mechanism was carefully encapsulated with an opaque material, completely sealing it from external light sources. Additionally, to ensure consistent and valid results, the camera's position within the upper region of the mechanism was standardized for each data collection, maintaining an optimum focal length and consistent shooting parameters for each photograph [8].

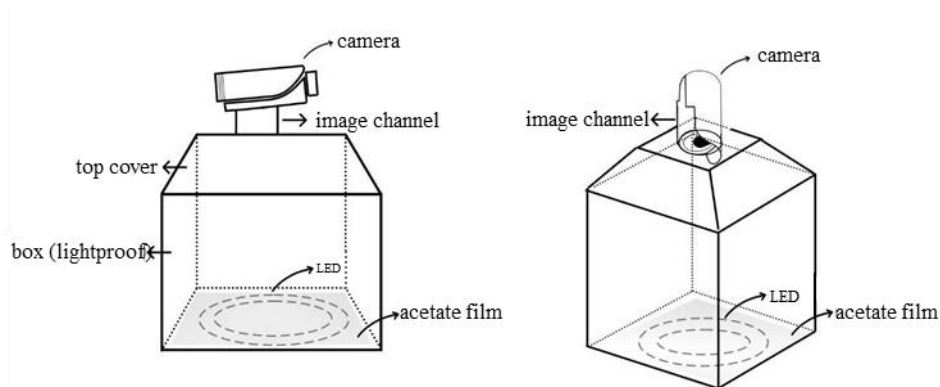


*Figure 2. Drawing of the test mechanism developed for capturing fiber mat images*



*Figure 3. Test mechanism*

## B. PRODUCTION OF FIBER MATS / DATA ACQUISITION AND IMAGE PROCESSING

Initially, GMZ Energy produced a set of 11 different fiber mat samples for this study [9]. Polyacrylonitrile (PAN), the most commonly used polymer, was used for the production of fiber mats. While determining the production conditions, the optimum conditions for PAN nanofibers optimized by GMZ Energy were taken into consideration. In all experiments, 20 kV voltage was applied to 8 wt% PAN solution, 0.5 mL/hour feeding rate was used, and the distance between the needle tip and the collector was kept at 12 cm. Aluminum foil on a metal plate of 25 cm x 30 cm dimensions was used as a collector. Fiber mat production was carried out based on different periods of time.

In the subsequent phase of our research, we acquired images of these fiber mat samples with the test mechanism in Figure 3, where a sample of the obtained data is visually depicted in Figure 4. These acquired images were subsequently subjected to grayscale transformation via image processing. The basic image processing technique for grayscale transformation of an image is to take a color image and convert it into grayscale by averaging the color channels [10, 11].

This grayscale conversion served as the basis for creating a color-coded thickness scale, utilizing thresholding methods [12]. In the grayscale representation, pixel values range from 0 to 255, where 0 corresponds to black, 255 to white, and intermediate values represent varying shades of light or dark gray. As a result, the threshold value for areas with higher light transmission, indicative of thinner sections, tends toward 255 [13].

Following grayscale transformation, we proceeded to apply a colorization technique to these images, assigning distinct color values to predefined threshold ranges, as exemplified in Figure 5 [14]. In order to compare the experimental results with the actual values and to enhance precision in presenting our findings, we diligently annotated the areas having the largest area within each color-coded region, as demonstrated in Figure 6.

To optimize our image processing workflow, we leveraged Python, a widely recognized programming language celebrated for its effectiveness in image processing. Python provides an extensive range of libraries and tools specifically designed for image analysis and manipulation, rendering it the optimal choice for our research. Additionally, we employed the Open-Source Computer Vision Library (OpenCV), a prominent open-source software library encompassing computer vision, machine learning, and image processing capabilities [15]. OpenCV played a pivotal role in establishing the necessary threshold values for our image analysis.



**Figure 4.** Data from the mechanism

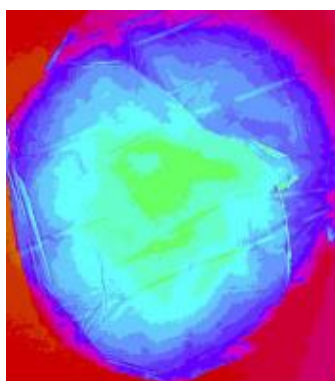


**Figure 5.** The data of PAN-3 after image processing

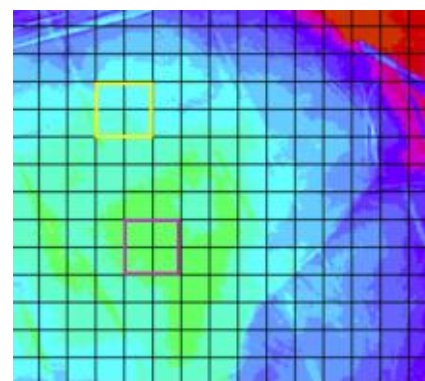


**Figure 6.** PAN-3 grid divided into squares and the largest area marked in regions with the same color

### C. COMPARISON OF IMAGE PROCESSING DATA WITH REAL DATA MEASURED BY OPTICAL MICROSCOPE

The physical fiber mat samples were precisely positioned on the images identified in Section B, and regions corresponding to the same color within different samples were carefully delineated and extracted as illustrated in Figure 7. These extracted regions were securely affixed to coverslips using carbon tape, ensuring they were primed for accurate thickness measurements as depicted in Figure 8.

To ascertain the actual thickness of each sample, measurements were conducted employing a Zeiss Stemi 508 optical microscope as shown in Figure 9. Three measurements were acquired for each sample, and the resultant values were averaged to yield the final thickness measurement (Figure 10).

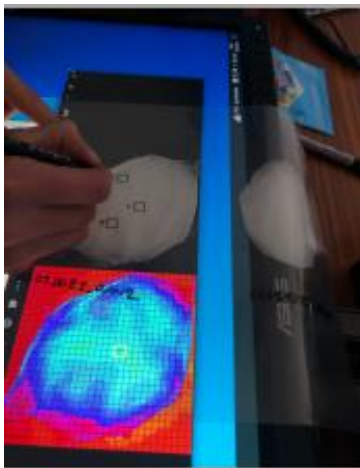


*Figure 7. Marking the measurement areas on real PAN samples*



*Figure 8. Preparation of samples for optical microscopy*



*Figure 9. Optical microscope (Zeiss Stemi 508)*

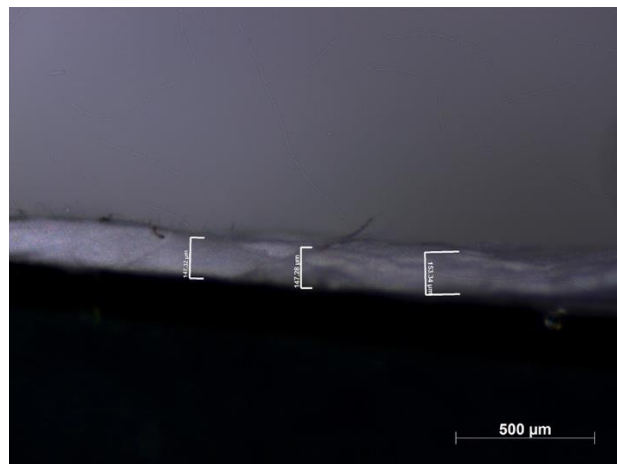


*Figure 10. Thickness measurement with the optical microscope*

## III. RESULTS

After obtaining the actual thickness values of the fiber mat samples using an optical microscope, we established a color-based thickness scale, as presented in Table 1 and Table 2. This scale was derived by aligning the threshold value ranges from our image processing outcomes with the corresponding

actual thickness measurements of specific regions. When the measurement results were examined, it was determined that the margin of error based on the color scale varied between 0.42% and 6.38% and the average margin of error was 3.8%.

**Table 1.** Matching chart of actual thickness values

<i>Instance No / Color</i>	<i>Average Value</i>	<i>Standard Deviation</i>	<i>Measurement 1</i>	<i>Measurement 2</i>	<i>Measurement 3</i>
<i>PAN-7 / Yellow</i>	<b>233.33</b>	32.53	265	235	200
<i>PAN-8 / Yellow</i>	<b>275.5</b>	27.58	295	256	--
<i>PAN-10 / Orange</i>	<b>210.5</b>	21.92	195	--	226
<i>PAN-6 / Orange</i>	<b>191.5</b>	3.54	194	189	--
<i>PAN-3 / Lilac</i>	<b>239.66</b>	23.03	262	241	216
<i>PAN-1 / Lilac</i>	<b>242</b>	6.24	247	244	235

**Table 2.** Color-based thickness scale

<i>Mark Colors</i>	<i>Average Value</i>	<i>Error Margin</i>
<i>Yellow</i>	255	$\pm 11 \mu m$
<i>Orange</i>	202	$\pm 10 \mu m$
<i>Brown</i>	310	$\pm 4 \mu m$
<i>Green</i>	94	$\pm 6 \mu m$
<i>Claret Red</i>	140	$\pm 5 \mu m$
<i>Lilac</i>	241	$\pm 1 \mu m$
<i>White</i>	192	$\pm 11 \mu m$

Our study's results lead to the conclusion that the actual thickness values of regions marked with the same color, extracted from different fiber mats, exhibit remarkable consistency. This consistency enables us to draw meaningful inferences regarding thickness values associated with the chosen colors. For instance, the average thickness measurements of regions identified in lilac color on PAN-10 and PAN-6 were concurrently recorded as 239 and 242 micrometers, as illustrated in Figures 11 and 12. This exemplifies our success in accurately identifying regions of identical thickness within diverse fiber mats.

Moreover, a comparative analysis of measurements taken from identically colored areas reveals consistent results, further affirming the reliability of our approach. Consequently, our study demonstrates that image processing methods can effectively complement manual processes in thickness assessment.

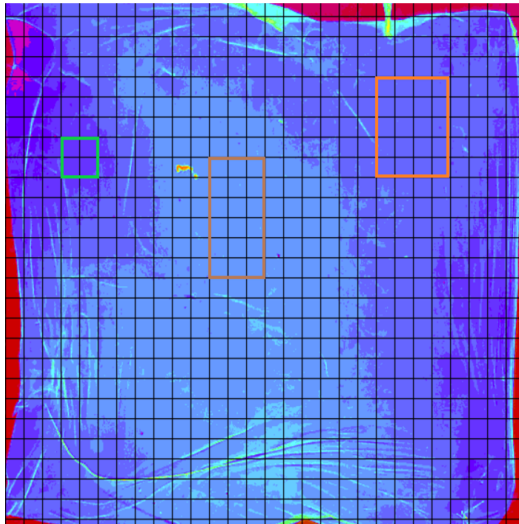


*Figure 11. PAN-10*

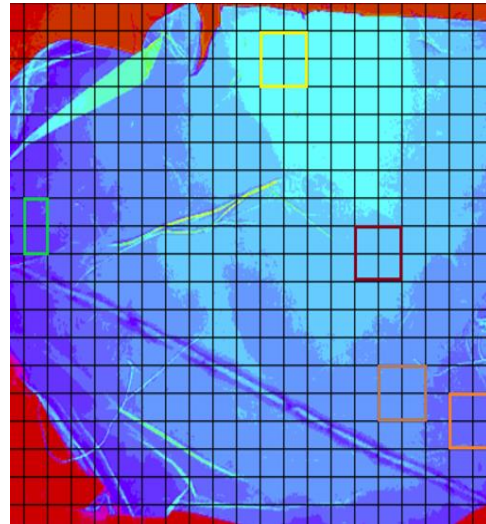


*Figure 12. PAN-6*

## **IV. CONCLUSION AND FUTURE PERSPECTIVES**

Within the scope of this study, we have introduced a novel approach for tackling the significant challenge of thickness measurement in fiber mats produced through the electrospinning method. Our innovative method encompasses a thickness measurement system that leverages image processing techniques based on light transmittance. The results of our measurements revealed a noteworthy alignment between the outcomes derived from image processing techniques and the actual thickness measurements conducted using an optical microscope.

Unlike existing systems, the developed thickness measurement system offers a user-friendly and cost-effective solution for determining the thickness of fiber mats produced via the electrospinning method. In forthcoming research endeavors, we plan to expand the applicability of image processing techniques for measuring the thickness of fiber mats crafted from various polymer materials. Additionally, our vision involves the integration of the developed thickness measurement system into existing electrospinning devices, enabling real-time data acquisition during the fiber mat production process through the use of cameras. Furthermore, we aim to establish a monitoring mechanism that will allow continuous thickness assessment during production by implementing a dedicated application within the electrospinning device.

**ACKNOWLEDGEMENTS:** This study is supported by TUBITAK 2209-B under the grant no: 1139B412202006.

## **V. REFERENCES**

- [1] G. Karanfil, "Preparation and characterization of electrospun sulfonated polysulfone/ZrO<sub>2</sub> composite nanofiber membranes," *Int. J. Mater. Res.*, vol. 113, no. 3, pp. 243-252, 2022.
- [2] G. K. Celep and K. Dincer, "Optimization of parameters for electrospinning of polyacrylonitrile nanofibers by the Taguchi method," *Int. Polym. Process.*, vol. 32, no. 4, pp. 508-514, 2017.

- [3] C. M. Wu, C. H. Hsu, C. I. Su, C. L. Liu, and J. Y. Lee, "Optimizing parameters for continuous electrospinning of polyacrylonitrile nanofibrous yarn using the Taguchi method," *J. Ind. Text.*, vol. 48, no. 3, pp. 559-579, 2018.
- [4] C. F. Wan, T. Yang, G. G. Lipscomb, D. J. Stookey, and T. S. Chung, "Design and fabrication of hollow fiber membrane modules," *J. Membr. Sci.*, vol. 538, pp. 96-107, 2017.
- [5] D. Öztürk, H. Yavuztürk, H. K. Can, E. Kaçmaz, B. Yılmazel, and G. K. Kaçmaz, "Measuring the Thickness of Fiber Mats Using Light Transmittance via Image Processing," in *26th National Electron Microscopy Congress*, Eskişehir, Turkey, 2023, pp. 97.
- [6] J. Jiang, Y. Li, Y. Zhang, H. U. Bahia, "Distribution of mortar film thickness and its relationship to mixture cracking resistance," *Int. J. Pavement Eng.*, vol. 23, no. 3, pp. 824-833, 2020.
- [7] D. J. Cruz, R. L. Amaral, A. D. Santos, J. M. R. S. Tavares, "Application of Digital Image Processing Techniques to Detect Through-Thickness Crack in Hole Expansion Test," *Metals*, vol. 13, no. 7, pp. 1197, 2023.
- [8] H. I. Ryu, M. S. Koo, S. Kim, S. Kim, Y. A. Park, and S. M. Park, "Uniform-thickness electrospun nanofiber mat production system based on real-time thickness measurement," *Sci. Rep.*, vol. 10, no. 1, pp. 1-10, 2020.
- [9] GMZ Energy. (2023, September 10). *Inovative Solutions for Sustainable Production: Smart and Innovative Electrospin Device* [Online]. Available: <https://www.gmzenerji.com/en/>
- [10] C. Saravanan, "Color Image to Grayscale Image Conversion," in *2nd International Conference on Computer Engineering and Applications*, Bali, Indonesia, 2010, pp. 196-199.
- [11] M. Ćadík, "Perceptual Evaluation of color-to-Grayscale Image Conversions," *Computer Graphics Forum*, vol. 27, no. 7, pp. 1745–1754, 2008.
- [12] J. Mukherjee, I. K. Maitra, K. N. Dey, S. K. Bandyopadhyay, D. Bhattacharyya, and T. H. Kim, "Grayscale conversion of histopathological slide images as a preprocessing step for image segmentation," *Int. J. Software Eng. Appl.*, vol. 10, no. 1, pp. 15-26, 2016.
- [13] P. K. Sahoo, S. A. K. C. Soltani, and A. K. Wong, "A survey of thresholding techniques," *Comput. Vision Graphics Image Process.*, vol. 41, no. 2, pp. 233-260, 1988.
- [14] N. Otsu, "A threshold selection method from gray-level histograms," *IEEE Trans. Syst. Man. Cybern.*, vol. 9, no. 1, pp. 62-66, 1979.
- [15] I. Culjak, D. Abram, T. Pribanic, H. Dzapo, and M. Cifrek, "A brief introduction to OpenCV," in *35th International Convention MIPRO*, Opatija, Croatia, 2012, pp. 1725-1730.








# Düzce University Journal of Science & Technology

Research Article

## Structural Health Monitoring Application of Aviation Composite Materials Using Microscopic Techniques

 Seyid Fehmi DİLTEMİZ <sup>a,\*</sup>,  Saliha MUSTAFAOĞLU <sup>b</sup>,  Furkan KAYA <sup>b</sup>

<sup>a</sup> Department of Aeronautical Engineering, Eskisehir Osmangazi University, Eskişehir, TURKEY

<sup>b</sup> Turkish Aerospace, Ankara, TURKEY

\* Corresponding author's e-mail address: [fdiltemiz@ogu.edu.tr](mailto:fdiltemiz@ogu.edu.tr)

DOI: 10.29130/dubited.1374409

### ABSTRACT

Structural Health Monitoring (SHM) is a process that involves the observation and analysis of a system over time using periodically sampled response measurements to monitor changes to the material and geometric properties of engineering structures such as bridges, buildings, and aerospace composite structures. The goal of SHM is to detect changes in the structural behavior or condition that may indicate damage or degradation before a catastrophic failure occurs. SHM involves the implementation of damage detection strategies for structures of high importance. It is commonly used in civil engineering, aerospace engineering, and mechanical engineering applications to ensure the safety and reliability of structures. It improves the safety of aerospace composite structures by detecting damage at an early stage, preventing damage from occurring, improving reliability, and extending the life of the structure. SHM applications enable aircraft to spend less time on the ground and carry more passengers and cargo, thereby reducing operational costs. It can be utilized in various fields such as monitoring the health condition of aircraft tail and wing areas in the aviation industry, preventing damage and deterioration of car parts and components under operating conditions in the automotive sector, monitoring the health condition of bridges and tunnels in the transportation sector, and monitoring the health condition of wind turbines and other structures in the energy sector. Aerospace composite structures can suffer from several complex nonlinear damage modes, including impact damage, delamination, matrix cracking, fiber breakage, and voids. This study provides general and useful information on how structural health applications of aviation composites can be supported by microscopic techniques. In order to better understand the subject, an example aircraft composite structural component containing impact damage, which was mentioned above, was examined using microscopic techniques. In this investigation conducted using Stereo and Scanning Electron Microscopes (SEM), the identification of potential damage sources and the assessment of damage severity are explained in detail.

**Keywords:** Aerospace, Composite materials, Microscopy, Structural Health Monitoring

## Havacılık Kompozit Malzemelerinde Mikroskopik Teknikler Kullanılarak Yapısal Sağlık İzleme Uygulamaları

### ÖZ

Yapısal Sağlık İzleme (YSİ), mühendislik yapıları arasında köprüler, binalar ve havacılık kompozit yapılar gibi yapıların malzeme ve geometrik özelliklerindeki değişiklikleri izlemek için düzenli aralıklarla alınan tepki ölçümlerini kullanarak zaman içinde bir sistemin gözlem ve analizini içeren bir süreçtir. YSİ'nin amacı, yapısal davranışta veya koşullarda meydana gelen değişiklikleri tespit etmek ve felakete sonuçlanmadan önce hasar veya bozulma belirtilebilecek olanları saptamaktır. YSİ, yüksek öneme sahip yapılar için hasar tespiti stratejilerinin uygulanmasını içerir. Genellikle sivil mühendislik, havacılık mühendisliği ve makine mühendisliği uygulamalarında yapıların güvenliği ve güvenilirliğini sağlamak için kullanılır. Havacılık kompozit yapıların

güvenliğini artırarak erken aşamada hasarı tespit eder, hasarın meydana gelmesini önler, güvenilirliği artırır ve yapının ömrünü uzatır. YSİ uygulamaları, uçakların daha az süreyle yerde kalmasını ve daha fazla yolcu ve yük taşımalarını sağlayarak işletme maliyetlerini azaltır. Bu uygulamalar, havacılık endüstrisinde uçak kuyruk ve kanat bölgelerinin sağlık durumunu izlemek, otomotiv sektöründe işletme koşullarında araç parçalarının ve bileşenlerinin hasarını ve bozulmasını önlemek, ulaşım sektöründe köprülerin ve tünellerin sağlık durumunu izlemek ve enerji sektöründe rüzgar türbinleri ve diğer yapıların sağlık durumunu izlemek gibi çeşitli alanlarda kullanılabilir. Havacılık kompozit yapılar, darbe hasarı, delaminasyon, matris çatlama, lif kırılması ve boşluklar dahil olmak üzere çeşitli karmaşık olmayan hasar modlarına maruz kalabilir. Bu çalışma, havacılık kompozitlerinin yapısal sağlık uygulamalarının mikroskopik tekniklerle nasıl desteklenebileceği hakkında genel ve faydalı bilgiler sunmaktadır. Konuyu daha iyi anlamak için yukarıda bahsedilen darbe hasarı içeren bir örnek uçak kompozit yapısal bileşeni, mikroskopik teknikler kullanılarak incelenmiştir. Bu araştırma, Stereo ve Taramalı Elektron Mikroskopları (SEM) kullanılarak potansiyel hasar kaynaklarının tanımlanması ve hasarın şiddetinin ayrıntılı açıklamasını içermektedir.

*Anahtar Kelimeler: Havacılık, Kompozit malzemeler, Mikroskopi, Yapısal Sağlık İzleme*

## **I. INTRODUCTION**

Structural Health Monitoring (SHM) is a systematic process involving the continuous observation and analysis of a system over time, utilizing periodically sampled response measurements to track alterations in the material and geometric characteristics of engineering structures, such as bridges, buildings, and aerospace composite structures. The primary objective of SHM is to discern modifications in the structural behavior or condition that might signify damage or deterioration before an impending catastrophic failure emerges [1], [2]. SHM necessitates the utilization of permanently affixed sensors on the structure, enabling the ongoing collection of data from the structure. Subsequently, this data is subject to analysis to identify changes within the structural system, including structural degradation, damage, and potential hazards. It exhibits the capability to identify various forms of damage modes within aerospace composite structures, encompassing impact-induced damage, delamination, matrix cracking, fiber breakage, and voids. The output from SHM comprises periodically refreshed information concerning the structure's ability to fulfill its intended function considering the inevitable aging and degradation stemming from operational environments. It is widely deployed across domains such as civil engineering, aerospace engineering, and mechanical engineering to ensure the safety and reliability of structural assets [3], [4].

SHM systems have a broad range of applications in real-world scenarios. Their primary purpose is to monitor structural health and promptly detect any signs of damage [5]. These systems are used to continuously monitor the structural health of aircraft components. For example, a real-time SHM system was developed to identify debonding flaws during ground testing of aircraft [6]. It plays a crucial role in monitoring the structural condition of bridges. One notable example is the application of SHM to the Forth Road Bridge in Scotland, where it monitors cable tension and detects any changes that may indicate structural damage [7]. They are also essential for monitoring the structural health of wind turbine components. A typical use case involves the development of SHM systems for wind turbine blades to detect alterations in their structural behavior that may indicate damage [8]. SHM systems are also employed to monitor the structural health of pipelines. An illustrative instance is the development of a SHM system for pipelines, which can identify shifts in their structural behavior signaling potential damage [9].

Aerospace composite structures are susceptible to a range of intricate nonlinear damage modes, all of which can be effectively detected by SHM systems. By detecting damage early, it is possible to take corrective action and prevent further damage, improving the safety and reliability of the aerospace composite structure. Impact damage transpires when a composite structure experiences an external impact, such as a bird strike or hail. This form of damage can instigate delamination, matrix cracking, and fiber breakage [10]. Delamination manifests as the separation of layers within a composite structure. It can occur due to various factors, including impacts, fatigue, or other environmental conditions [6],

[10]. Matrix cracking arises when the resin matrix that binds the fibers within a composite structure undergoes cracking. Matrix cracking can result from fatigue, impacts, or other relevant factors [10], [11]. Fiber breakage takes place when the individual fibers within a composite structure fracture. This type of damage can be attributed to impacts, fatigue, or other contributing factors [12]. Voids represent regions within a composite structure where the resin or fiber is absent. Their presence may stem from manufacturing imperfections or structural damage.

The use of composite components, primarily carbon fiber, in critical areas like aviation where structural health monitoring is necessary, is increasing day by day. Therefore, after the detection of any potential damage on these materials through sensors placed on the structure, a detailed examination is required. This way, damages on the structure can be thoroughly characterized, and a correlation can be established between the type and severity of damage with the information obtained from the sensors on the structure. In various studies, metallographic cross-sections have been prepared to evaluate the condition of the sensors in the composite structure or to examine the damage in detail [13], [14]. However, in situ examination of the damage directly with a stereo microscope provides rapid, useful evaluation.

A composite aircraft structural component containing impact damage is used to demonstrate the capability of microscopic techniques. The damaged part was examined using Stereo and Scanning Electron microscopes (SEM), the identification of potential damage sources and the assessment of damage severity are explained in detail.

This experimental study focuses on demonstrating the application possibilities of SHM using microscopic techniques to detect composite defects on aircraft composite fuselage parts. Using microscopic techniques, it has been shown that not only the severity of defects on composite parts can be determined, but also the type and root cause of damage.

## **II. MATERIALS AND METHODS**

### **A. EXPERIMENTAL PROCEDURE**

This section outlines the procedures employed for assessing the damaged component through microscopic techniques. Initially, a visual inspection and stereo microscope examination were conducted to obtain a comprehensive overview of the damage, providing general information.

Following this, a SEM equipped with an Energy Dispersive X-ray Spectroscopy (EDX) attachment was employed to perform an in-depth assessment of the outer skin. This advanced imaging and elemental analysis technique facilitated a comprehensive characterization and potential identification of the underlying cause(s) of the damage.

### **B. BACKGROUND**

During the service life of an aircraft, a section of the outer skin of the body encountered impact damage. The impact resulted in visible damage, which was subsequently identified during routine inspections. The dimensions of the affected area were measured in terms of width, length, depth, and total area.

Following an assessment in accordance with the pertinent Technical Order (TO) documents, it was determined that the damage exceeded the established usage or repair limits. Consequently, the damaged part was disassembled and disposed of. Subsequently, the part was forwarded to a laboratory for a comprehensive analysis aimed at elucidating the potential root cause(s) and obtaining a more detailed characterization of the type and severity of the damage.

The composite pre-preg material utilized in this study is manufactured by Hexcel™, consisting of an epoxy matrix with plain-weaved carbon fibers. The component is constructed from six layers of 0-900 oriented carbon fibers.

### C. MICROSCOPIC EVALUATION

The component was initially subjected to direct examination under a stereo microscope at its original dimensions. During the inspection, the entire damaged surface was examined at different magnifications ranging from 5 to 50x. The stereo microscope was equipped with an image analyzer, enabling the capture and measurement of images during the inspection process. The accuracy of the measurements made with the image analyzer is periodically verified with calibration blocks.

Following the stereo microscope evaluation, a section of the part surrounding the damaged area was excised for further examination using SEM. A masking procedure was implemented during the cutting process to safeguard the integrity of the damaged surfaces.

SEM/EDX analyses were additionally conducted, wherein the SEM Backscatter detector was employed to gain a deeper insight into elemental distinctions within the component. The accuracy of the analysis performed with the EDX unit is verified by calibrating blocks containing the elements to be measured. EDX measurements are performed at least 3 times to ensure the elemental distribution in the analyzed region.

## III. RESULTS

The general appearance of the damage is illustrated in Figure 1.



*Figure 1. The general appearance of the damage*

Figures 2, depict the damaged area as observed under the stereo microscope. This inspection disclosed that the initial three layers of the composite exhibited damage, with numerous fragmented fiber particles observed on the part's surfaces. The boundaries of the damage were sharply delineated, with no evidence of similar damaged regions detected elsewhere on the surface of the component. The dimensions of the damaged area measured approximately 16.2 mm in maximum length and 4.3 mm in maximum width, with a depth of approximately 0.6 mm. Notably, the damage extends to a depth nearing half of the part's total thickness. It is worth emphasizing that the utilization of stereo microscopes permits a more

comprehensive collection of information and facilitates precise measurements, surpassing the capabilities of on-site visual inspections conducted at the aircraft's location.

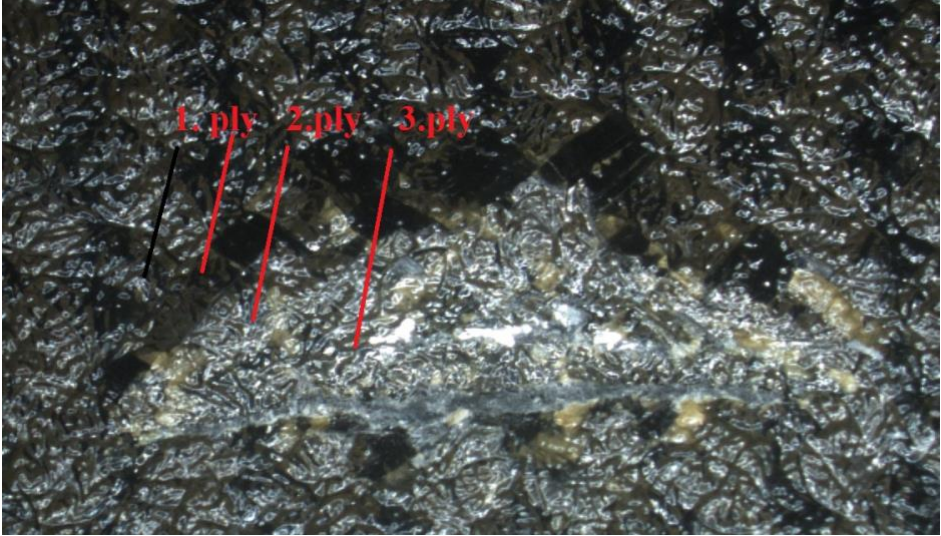
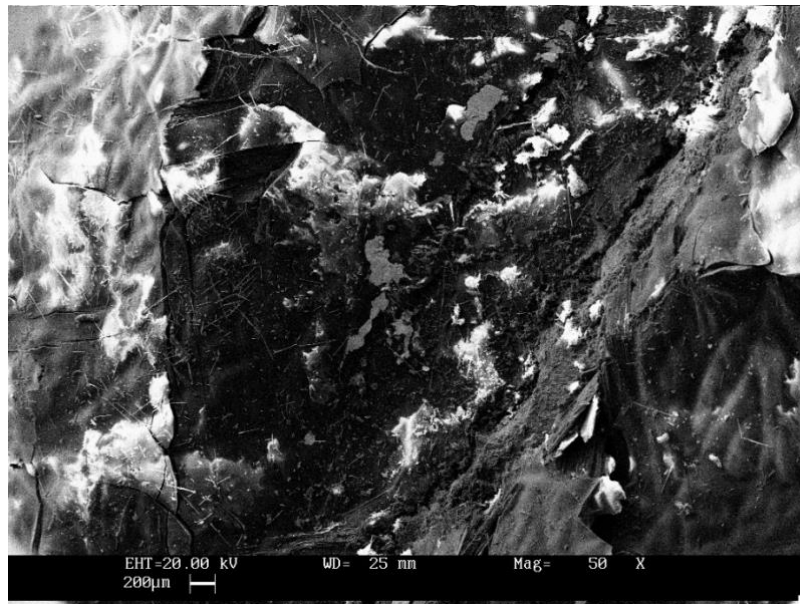


Figure 2. General appearance of the damage\_16x

The SEM examination unveiled the presence of fiber breakage, delamination, and matrix cracking at the site of damage. Additionally, broken fiber particles were observed in SEM Secondary detector images. These specific damages are depicted in Figure 3a and b.



(a)



(b)

**Figure 3.** (a) and (b) the SEM secondary detector images of the damage area\_50x.

Notably, white-colored spots were identified on the damaged surfaces through the backscatter detector, and subsequent EDX micro spot analysis was carried out on these identified spots. The corresponding backscatter images and EDX analysis are presented in Figure 4 and 5, respectively.

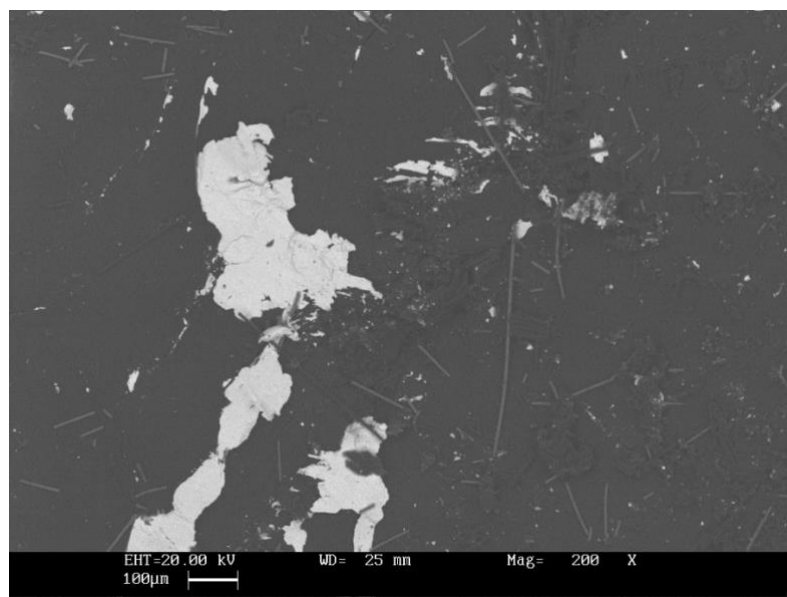


**Figure 4.** Backscatter SEM image from the damage area

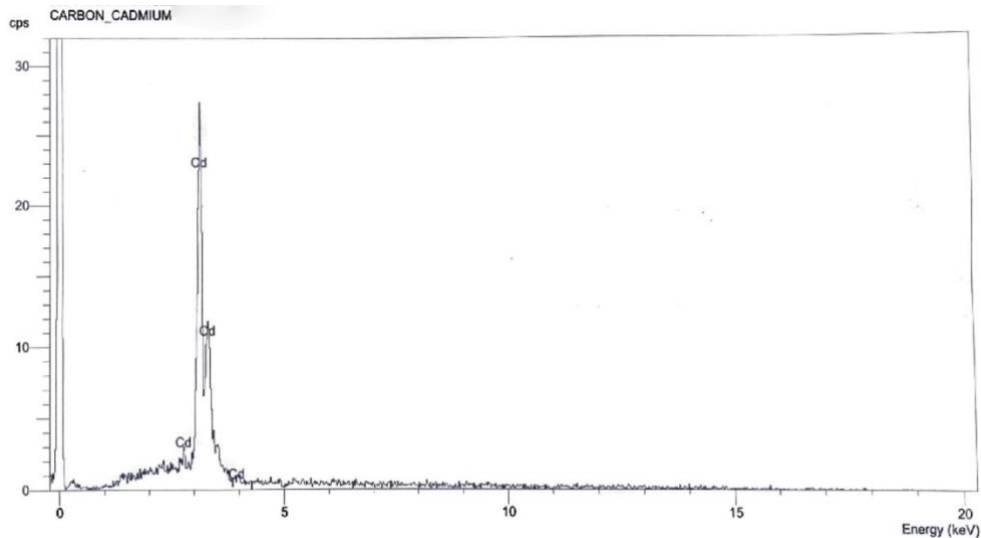


*Figure 5. The EDX analysis*

The investigations conducted on the damaged component have yielded valuable data regarding the mechanism of damage initiation and its effects on the part. The examination using a stereo microscope has provided significant insights. The well-defined and localized boundaries of the damage, coupled with the absence of any external damage in the proximity, suggest that the part has incurred damage characteristic of a hard-body impact.

Furthermore, the preliminary assessment through stereo microscopy, later confirmed by SEM analysis, has revealed that the damage extends to a depth of approximately half the thickness of the part. The SEM examination has also confirmed the presence of fiber breakage, delamination, and matrix cracking within the part.

Moreover, the SEM/EDX examination has detected residues of cadmium on the damaged surfaces. Cadmium is commonly employed as a corrosion-resistant coating in aircraft structural components. Consequently, it can be inferred that the object responsible for the impact damage possesses sharp-edged contours, likely a metallic object associated with possible aircraft structural components.

## **IV. CONCLUSION**

In this study, the utilization of microscopic examination techniques has provided valuable data that can support structural health monitoring of composite components. This data can facilitate correlation studies between sensor data and the type and severity of damage. By examining the impact site with a stereo microscope and SEM, the type of damage could be determined as hard body impact. The determination of the type of damage is of great importance for the implementation of corrective actions such as repair, part replacement, etc. Furthermore, the rapid assessment of composite airframe damage will ensure that the aircraft can be quickly prepared for the next flight. This means significant economic benefits in terms of maintenance costs. The use of SEM/EDX provides useful information about the elemental composition of the impacting object in impact damage events.

The insights gained from this research can contribute significantly to enhancing the effectiveness of future SHM applications. By replicating and expanding upon such studies, we can anticipate more successful outcomes in SHM applications in the future. For example, in future studies, examining impact damage to structures containing sensors such as accelerometers and acoustic emissions with microscopic techniques will provide a detailed examination of the relationship between sensor data and damage.

Consequently, this can lead to improved flight safety, reduced maintenance costs, and extended component lifespans, among other beneficial outcomes.

## **V. REFERENCES**

- [1] “Structural health monitoring - Wikipedia.” Accessed: Sep. 14, 2023. [Online]. Available: [https://en.wikipedia.org/wiki/Structural\\_health\\_monitoring](https://en.wikipedia.org/wiki/Structural_health_monitoring)
- [2] F. G. Yuan, “Preface,” *Structural Health Monitoring (SHM) in Aerospace Structures*, pp. xvii–xviii, Jan. 2016, doi: 10.1016/B978-0-08-100148-6.05001-0.
- [3] P. F. Giordano, S. Quqa, and M. P. Limongelli, “The value of monitoring a structural health monitoring system,” *Structural Safety*, vol. 100, p. 102280, Jan. 2023, doi: 10.1016/J.STRUSAFE.2022.102280.
- [4] K. Diamanti and C. Soutis, “Structural health monitoring techniques for aircraft composite structures,” *Progress in Aerospace Sciences*, vol. 46, no. 8, pp. 342–352, Nov. 2010, doi: 10.1016/J.PAEROSCI.2010.05.001.
- [5] “What is Structural Health Monitoring in Civil Engineering? - The Constructor.” Accessed: Sep. 14, 2023. [Online]. Available: <https://theconstructor.org/digital-construction/structural-health-monitoring-civil-engineering/554160/?amp=1>
- [6] M. Ciminello *et al.*, “Preliminary Results of a Structural Health Monitoring System Application for Real-Time Debonding Detection on a Full-Scale Composite Spar,” *Sensors 2023, Vol. 23, Page 455*, vol. 23, no. 1, p. 455, Jan. 2023, doi: 10.3390/S23010455.
- [7] E. Ozer and M. Q. Feng, “Structural health monitoring,” *Start-Up Creation: The Smart Eco-efficient Built Environment, Second Edition*, pp. 345–367, Jan. 2020, doi: 10.1016/B978-0-12-819946-6.00013-8.
- [8] B. P. Moster *et al.*, “The Application of Structural Health Monitoring in Different Engineering Fields,” *IOP Conf Ser Earth Environ Sci*, vol. 643, no. 1, p. 012164, Jan. 2021, doi: 10.1088/1755-1315/643/1/012164.
- [9] Z. Jiawei, “The Application of Structural Health Monitoring in Different Engineering Fields,” *IOP Conf Ser Earth Environ Sci*, vol. 643, no. 1, Jan. 2021, doi: 10.1088/1755-1315/643/1/012164.
- [10] S. Hassani, M. Mousavi, and A. H. Gandomi, “Structural Health Monitoring in Composite Structures: A Comprehensive Review,” *Sensors (Basel)*, vol. 22, no. 1, Jan. 2022, doi: 10.3390/S22010153.
- [11] V. Giurgiutiu, *Structural Health Monitoring of Aerospace Composites*. Elsevier, 2015. doi: 10.1016/B978-0-12-409605-9.00012-X.
- [12] J. Cai *et al.*, “Structural Health Monitoring for Composite Materials,” *Composites and Their Applications*, Aug. 2012, doi: 10.5772/48215.



- [13] J. Sebastian *et al.*, “Health monitoring of structural composites with embedded carbon nanotube coated glass fiber sensors,” *Carbon N Y*, vol. 66, pp. 191–200, Jan. 2014, doi: 10.1016/J.CARBON.2013.08.058.
- [14] M. Ramakrishnan, G. Rajan, Y. Semenova, and G. Farrell, “Overview of Fiber Optic Sensor Technologies for Strain/Temperature Sensing Applications in Composite Materials,” *Sensors 2016, Vol. 16, Page 99*, vol. 16, no. 1, p. 99, Jan. 2016, doi: 10.3390/S16010099.



# Düzce University Journal of Science & Technology

Research Article

## Microstructural Characterization of Hot Shortness in Steels

 Selçuk Yeşiltepe

Department of Mechanical Engineering, Osmaniye Korkut Ata University, TURKEY  
selcukyesiltepe@osmaniye.edu.tr  
DOI: 10.29130/dubited.1373828

### ABSTRACT

Hot shortness in steels is a macro crack on the steel surface especially on the slab edges of hot rolled steels produced by recycling. Hot shortness in steels is characterized by intergranular cracking of steel on the surface during hot rolling process. The hot shortness damage can be seen by naked eye due to macro cracks on steel surface, after the hot rolling of slab. Although macro cracks can occur due to various parameters such as excessive force or deformed rolls, hot shortness is directly linked to residual elements in the steel composition. Most common and effective residual element for hot shortness is copper. Copper in steel originates from the used scrap in Electric Arc Furnace (EAF) steelmaking. Decreased primary sources and environmental concerns with increased scrap output in the world make the recycling of steel inevitable.

Copper segregates in the austenite grain boundaries during the annealing of steel prior to hot rolling. Liquified copper film decreases the grain cohesion between austenite grains and results in intergranular cracking by the force applied during the rolling. Detection of copper in microstructure is vital to understand mechanism of hot shortness. Common knowledge in the literature of hot shortness suggests that hot shortness mechanism consists of oxidation-segregation-decreased grain cohesion-crack route. In this study, detailed microstructure images of steel surfaces are discussed with optical and scanning electron microscopy examinations. Examined samples of hot shortness are collected from scientific experiments and industrial practice examples. Helpful techniques and etching agents for copper revelation in microstructure are evaluated and explained in this paper.

**Keywords:** Hot shortness, Microstructure, Optical microscopy, Electron microscopy.

## Çeliklerde Sıcak Yırılmanın Mikroyapısal Analizi

### ÖZET

Çeliklerde sıcak yırtılma çelik yüzeyinde oluşan makro çatlakların özellikle slabın kenar bölgelerinde görüldüğü ve sıcak haddelemeye özgü geri dönüştürülmüş malzemelerde ortaya çıkan bir hasar çeşididir. Sıcak yırtılma, sıcak haddeleme esnasında oluşan taneler arası kırılmanın oluşması ile karakterize bir hasardır. Sıcak yırtılma sıcak haddeleme sonrasında gözle görülebilen makro çatlakların oluşumudur. Çelik yüzeyinde sıcak haddeleme sırasında görülebilen makro çatlaklar aşırı haddeleme kuvveti, merdanelerin çarpıklığı gibi farklı nedenlerle meydana gelebilmesine karşılık sıcak yırtılma direkt olarak çelikte bulunan kalıntı elementlerle ilişkilidir. Bakır çeliklerde en çok rastlanan ve sıcak yırtılmada en etkin rolü oynayan elementtir. Elektrik ark fırınında (EAF) kullanılan hurda çelikteki bakırın kaynağıdır. Azalan birincil kaynaklar, çevresel endişeler ve artan hurda miktarları çeliğin geri dönüştürülmesini kaçınılmaz hale getirmiştir.

Bakır sıcak haddeleme öncesindeki tavlama sırasında östenit tane sınırlarında ayrışmaktadır. Sıvı bakır filminin tane sınırlarındaki varlığı taneler arası kohezyonu zayıflatarak sıcak haddeleme sırasında uygulanan kuvvetle birlikte taneler arası kırılmaya neden olmaktadır. Bakırın mikroyapıda tespit edilmesi sıcak haddeleme sırasındaki davranışının anlaşılması için elzemdir. Konu üzerine yazındaki ortak kanı sıcak yırtılma mekanizmasının oksitlenme-ayırışma-taneler arası kohezyonun zayıflaması-çatlama şeklinde olduğunu söylemektedir. Bu çalışmada sıcak yırtılma hasarına uğrayan çeliklerin detaylı mikroyapı görüntüleri optik ve taramalı elektron mikroskopları ile incelenmiştir. İncelenen numuneler bilimsel araştırmada kullanılan ve endüstriyel üretimden alınan sıcak yırtılma örnekleridir. Mikroyapı incelemesinde kullanılan ve bakırın davranışının incelenmesini sağlayan yararlı teknikler ve dağılayıcı ajanlar bu çalışmada açıklanmıştır.

*Anahtar Kelimeler: Sıcak yırtılma, Mikroyapı, Optik mikroskop, Elektron mikroskobu.*

## **I. INTRODUCTION**

Electric Arc Furnace (EAF) steelmaking offers low carbon emissions in steelmaking technology and enables recycling of end-life steel products. [1] Although EAF offers advantageous production process it requires good scrap quality to produce high quality steel products. Scrap steel may contain large amounts of unwanted impurities for desired steel composition. [2] Cu, Sn, As, Sb and Pb are known as tramp elements because in conventional steelmaking refinement of these elements is not possible. [3] These elements, mainly Cu, cause hot shortness problem in hot rolling of steel. [4]

Hot shortness is the crack formation on steel surface during hot rolling process due to Cu in the composition. [5] Oxidation of steel surface causes Cu segregation on steel surface since iron oxides, wustite and magnetite, do not have Cu solubility to form solid solution. [2] Segregated Cu containing phase with low melting temperature elements follows grain boundaries of steel and further penetrates the steel surface. [6] Liquid phase between austenite decreases grain cohesion and causes intergranular cracking of steel during hot rolling. [6]

In this study microstructural characterization methods for hot shortness in steels evaluated. Scientific and industrial examples are investigated with microscopical techniques such as optical and electron microscopy.

## **II. Material and Method**

Steels with hot shortness problem were selected and microstructural characterization applied to specimens. Samples were mounted in bakelite moulds and grinding and polishing applied. Polishing of samples were done with 1 micron Al<sub>2</sub>O<sub>3</sub> suspension. Etching of samples were executed with 3% nitric acid containing Nital and 100 ml FeCl<sub>3</sub> containing ethanol solution of 200 ml for scientific samples and FeCl<sub>3</sub> containing ethanol solution for industrial samples. Chemical composition of steels were determined with Optic Emission Spectroscopy. SEM characterization of microstructure was done with Back Scattered Electron mode. EDS of samples were done to examine the chemical composition of desired areas.

## **III. Results and Discussion**

Optical Emission Spectroscopy results of samples were given in Table 1. Scientific research samples had higher copper content to easily detect the copper segregation and behaviour during the hot rolling, while industrial example had lower amounts of copper to prevent hot shortness.

Table 1. Chemical composition of steels.

Sample	C%	Si%	Mn%	Ni%	Cu%	Sn%
Scientific 1	0.279	0.43	0.45	0.090	0.90	-
Scientific 2	0.263	0.47	0.47	0.090	1.48	-
Industrial	0.026	0.018	0.138	0.088	0.32	0.012

Microstructural view of Scientific 2 sample was given in Figure 1 for both Nital and FeCl<sub>3</sub> based etchants. Both microstructural view were taken with same magnification of X50 and close areas to understand etchant effect on optical microscopy results. Nital etched view did not show any copper related segregation while FeCl<sub>3</sub> based etchant revealed Cu segregation with natural Cu colour. FeCl<sub>3</sub> based etchant was proved to be the best solution for copper segregation research hence the copper has more corrosion resistance and etching of copper with Nital was ineffective. Steel microstructure was revealed with Nital, yet copper was not etched and invisible in optical microscopy.

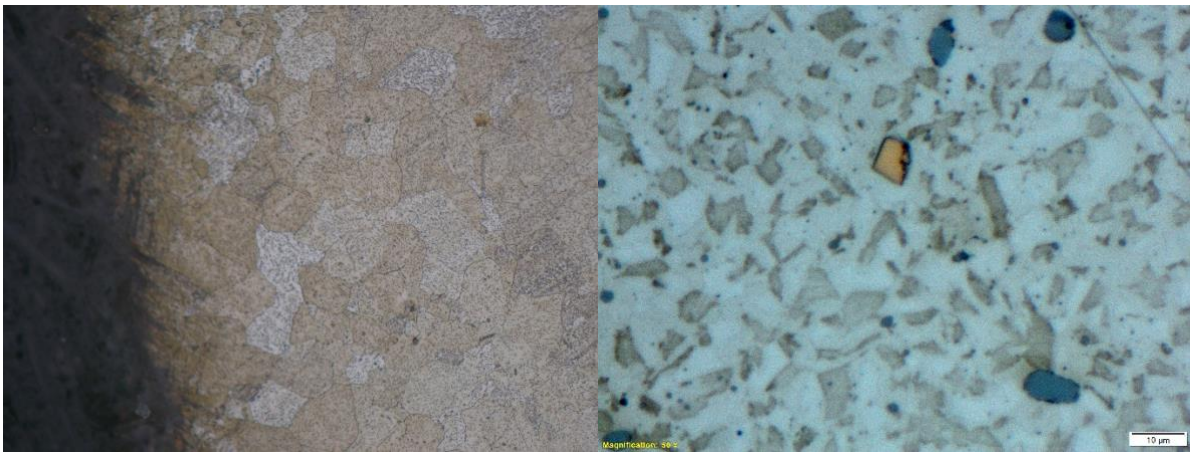


Figure 1. Microstructural view of Scientific 2 (Nital on the left, FeCl<sub>3</sub> on the right).

Scientific 1 sample was further investigated under optical microscopy with FeCl<sub>3</sub> based etchant. Crack propagation points of material were studied. Results showed that, cracks were filled by liquid copper during hot rolling. Cracks were completely filled with copper and solidified copper could be seen in optical microscopy. Microscopical view of Scientific 1 sample was given in Figure 2. Crack path showed intergranular characteristics of cracking.

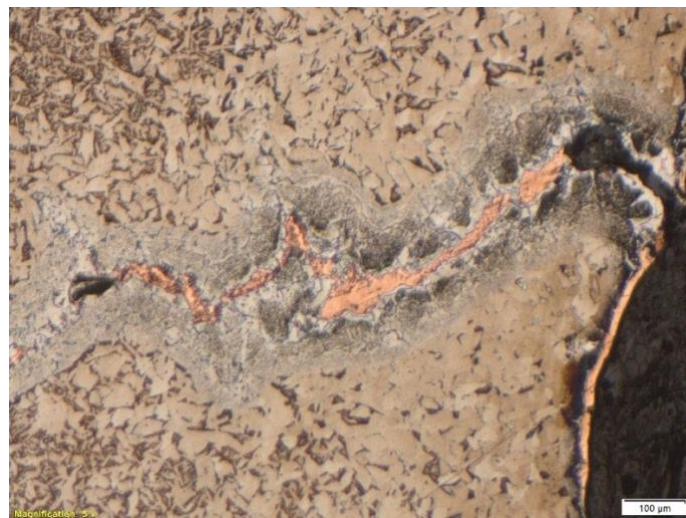
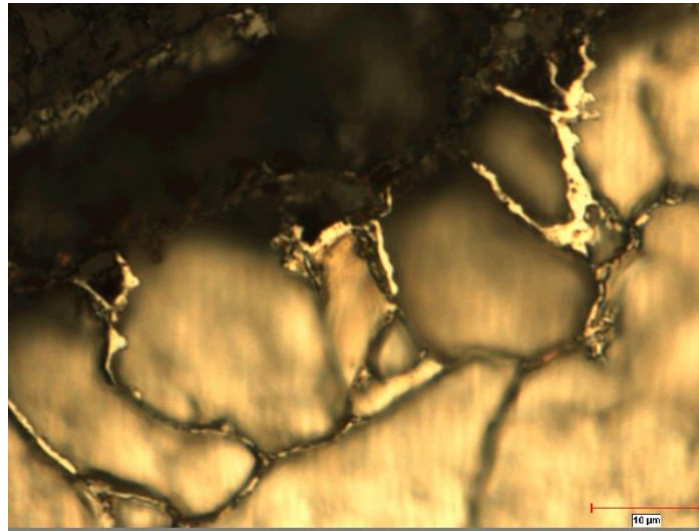


Figure 2. Microstructural view of Scientific 1 etched with FeCl<sub>3</sub> based etchant.

Industrial sample was investigated with FeCl<sub>3</sub> based etchant on optical microscopy. Sample was showing hot shortness properties on macro scale. Investigations revealed segregation phase around the grain boundaries of steel. Yellow colour was used to create contrast in grain boundaries. Intergranular segregation and intergranular cracks were observed. Segregated phase showed characteristics of liquified-solidified phase. Optical microscopy view of sample was given in Figure 3.



*Figure 3. Industrial sample microstructural view of hot shortness.*

Samples were investigated with SEM-EDS techniques to validate optical microscopy views of copper segregation. Back Scattered Electron mode was used during investigations. Back Scattered Electron Imaging had an advantage in SEM characterization of hot shortness because of Cu atomic mass is higher than Fe. Atomic mass difference causes Cu to be seen brighter in imaging and SEM thus EDS areas can be selected easily. SEM image of Industrial sample was given in Figure 4. SEM image was taken from a near region of Figure 3 to validate optic microscopy result. Image showed bright regions around grain boundaries similar to optic microscopy. Point EDS was applied to specimen for characterization of these phases. Results showed that the bright areas were rich in Cu and a segregated phase from steel grains. EDS results are given in Table 2. Copper segregation was found and nickel was found to accompany copper in segregated phase. Unlimited solid solution capacity of copper and nickel was unable to form a segregated phase together. However it was a possible solution offered in literature to decrease hot shortness susceptibility of steel since nickel increases the melting temperature of copper rich segregate.

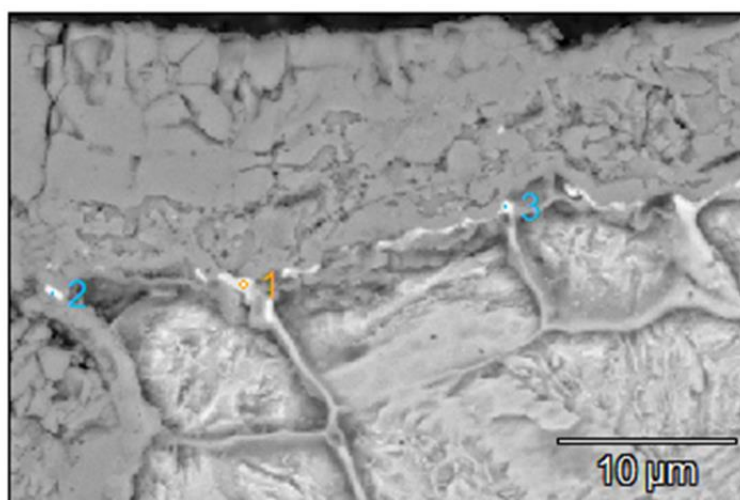


*Figure 4. SEM image of Industrial sample with EDS points.*

*Table 2. EDS point analysis results.*

Point	Cu%	Ni%	Fe%
1	59.91	10.44	29.65
2	30.41	6.92	62.67
3	9.65	1.40	88.95

Industrial sample was further investigated and EDS mapping technique was applied. Results showed that segregation was complete and Cu/Fe boundaries did not show cross-over. SEM image of EDS mapped area and EDS mapping results were given in Figure 5 and Figure 6 respectively.

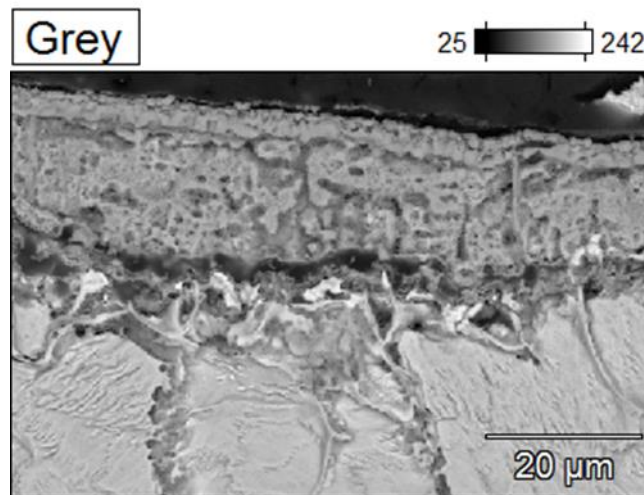


*Figure 5. SEM image of EDS mapped area.*

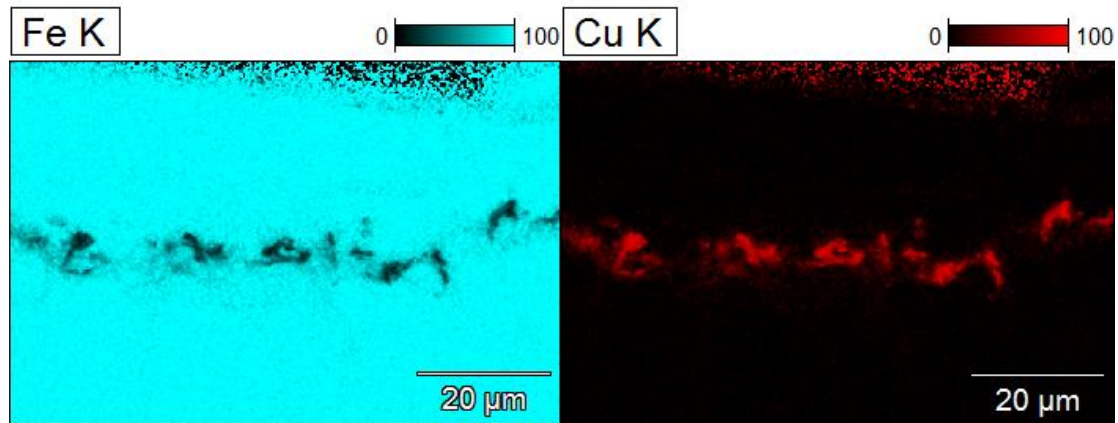


*Figure 6. EDS mapping results.*

## **IV. CONCLUSION**

Microstructural analysis' of samples were done to understand hot shortness mechanism in steels for both scientific and industrial examples of hot shortness. Nital solution for etching was found ineffective in detect the copper segregation in samples. Copper is more noble than Iron by means of etching and FeCl<sub>3</sub> based etchant was able to reveal the copper segregation in samples. Back Scattered Electron mode in SEM imaging was used to acquire microstructure of material and effectively created a contrast between

steel grains and copper due to atomic mass difference. Understanding of mechanism and microstructural view of hot shortness is vital to prevent occurrence of this problem.

**ACKNOWLEDGEMENTS:** This work is supported by MMK Metallurgy Türkiye company financially. Author wants to thank Dr. Özgür Karakaş and MMK Metallurgy Quality Control Department for their support.

## **V. REFERENCES**

- [1] A. C. Ahindra Ghosh, Ironmaking and Steelmaking Theory and Practice, New Delhi: PHI Learning Private Limited, 2008.
- [2] N. K. K. K. Norio Imai, «Effect of Cu and Ni on Hot Workability of Hot-rolled Mild Steel,» ISIJ International, cilt 37, no. 3, pp. 224-231, 1997.
- [3] E. Stephenson, «Effect of Recycling on Residuals, Processing, and Properties of Carbon and Low-Alloy Steels,» Metallurgical Transactions A, cilt 14A, no. March, pp. 343-353, 1983.
- [4] E. S. J. N. S. S. Lan Yin, «The Effects of Nickel/Tin Ratio on Cu Induced Surface Hot Shortness in Fe,» Oxidation of Metals, no. 76, pp. 367-383, 2011.
- [5] M. H. K. Kunishige, «SURFACE HOT-SHORTNESS OF STEELS INDUCED BY A SMALL AMOUNT OF COPPER AND TIN FROM SCRAP STEELS AND ITS SUPPRESSION METHODS,» Materials Science Forum, Cilt %1 / %2539-543, pp. 4113-4118, 2007.
- [6] Y. U. K. K. Y. T. S. H. K. O. Akihiro Takemura, «Surface Hot Shortness of Copper Containing Steel in a Compact Strip Production Process,» Material Transactions, cilt 52, no. 10, pp. 1905-1911, 2011.
- [7] N. K. K. K. Norio Imai, «Effect of Cu. Snand Ni on Hot Workability of Hot-rolled Mild Steel,» ISIJ International, cilt 37, no. 3, pp. 217-223, 1997.



# Düzce University Journal of Science & Technology

Review Article

## Evaluation of Honey Bees within the Scope of Sustainable Development Goals and Ecosystem Services

 Melek YILMAZ KAYA <sup>a,\*</sup>,  Yaşar Selman GÜLTEKİN <sup>b</sup>,  Pınar GÜLTEKİN

<sup>a</sup> Department of Landscape Architecture, Faculty of Forest, Düzce University, Düzce, TURKEY

<sup>b</sup> Department of Forest Engineering, Faculty of Forest, Düzce University, Düzce, TURKEY

\* Corresponding author's e-mail address: melekaya@duzce.edu.tr

DOI: 10.29130/dubited.1383016

### ABSTRACT

Beekeeping is one of the significant activities that contribute to sustainability in environmental, social, and economic aspects. Honeybees provide multifaceted contributions to humanity, with 90% attributed to pollination services and 10% to bee products (honey, propolis, wax, etc.). The preservation of these services plays a key role in achieving ecological and economic sustainability, ensuring a healthy future for human life. According to the Intergovernmental Science-Policy Platform on Biodiversity and Ecosystem Services (IPBES) under the United Nations, more than 80 million beehives contribute to an estimated annual honey production of 1.6 million tons. Honeybees can travel distances ranging from 600 meters to 11.3 kilometers to pollinate in bee forests. The bee products obtained from these areas provide income sources for forest communities, supporting sustainable development. According to the Food and Agriculture Organization of the United Nations (FAO), one-third of global food production relies on pollination services by bees. Pollination services are critical for maintaining food security and increasing agricultural productivity. These services create a significant impact on biodiversity support, landscape diversification, enrichment of forest cover, and expansion of wildlife habitats, as well as erosion control—effects that are often imperceptible to humans. Bees contribute to human well-being and cultural sustainability by providing food, medicine, genetic resources, and related materials. The ecosystem services provided by bees make substantial contributions to achieving Sustainable Development Goals (SDGs) including No Poverty (SDG1), Zero Hunger (SDG2), Good Health and Well-being (SDG3), Affordable and Clean Energy (SDG7), Decent Work and Economic Growth (SDG8), Responsible Consumption and Production (SDG12), Climate Action (SDG13), and Life on Land (SDG15). This study discusses the importance of beekeeping and bee products in terms of ecosystem services for sustainable development and addresses environmental risks.

**Keywords:** Beekeeping, climate change, sustainable development, ecosystem services, life on land.

## Bal Arılarının Sürdürülebilir Kalkınma Hedefleri ve Ekosistem Hizmetleri Kapsamında Değerlendirilmesi

### ÖZET

Arıcılık, çevresel, sosyal ve ekonomik açılardan sürdürülebilirliğe katkıda bulunan önemli faaliyetlerden biridir. Arılar, insanlığa çok yönlü katkılarda bulunur, bunların %90'ı tozlaşma hizmetlerine ve %10'u da arı ürünlerine (bal, propolis, balmumu, vb.) atfedilir. Bu hizmetlerin



korunması, ekolojik ve ekonomik sürdürülebilirliği sağlamak, insan yaşamının sağlıklı bir geleceğini garanti altına almak için kilit bir rol oynar. Birleşmiş Milletler bünyesindeki Biyoçeşitlilik ve Ekosistem Hizmetleri Üzerine Hükümetler Arası Bilim-Politika Platformu'na (IPBES) göre, 80 milyon arı kovana yılda tahmini 1,6 milyon ton bal üretimine katkıda bulunuyor. Arılar, arı ormanlarında tozlaşma yapmak için 600 metre ila 11,3 kilometre arasında mesafeler kat edebilirler. Bu alanlardan elde edilen arı ürünleri, orman toplulukları için gelir kaynakları sağlayarak sürdürülebilir kalkınmaya destek olur. Birleşmiş Milletler Gıda ve Tarım Örgütü'ne (FAO) göre, küresel gıda üretiminin üçte biri arıların tozlaşma hizmetlerine dayanmaktadır. Tozlaşma hizmetleri, gıda güvenliğini sürdürmek ve tarımsal verimliliği artırmak için hayati öneme sahiptir. Bu hizmetler, biyoçeşitliliği destekleme, manzara çeşitlendirmesi, orman örtüsünün zenginleştirilmesi ve vahşi yaşam habitatlarının genişletilmesi, ayrıca erozyon kontrolü gibi, genellikle insanlar için fark edilemeyen etkiler yaratır. Arılar, gıda, ilaç, genetik kaynaklar ve ilgili materyaller sağlayarak insan refahına ve kültürel sürdürülebilirliğe katkıda bulunur. Arılar tarafından sağlanan ekosistem hizmetleri, Yoksullukla Mücadele (SDG1), Açlıkla Mücadele (SDG2), İyi Sağlık ve İyi Olma Hali (SDG3), Uygun ve Temiz Enerji (SDG7), İnsana Yakışır İş ve Ekonomik Büyüme (SDG8), Sorumlu Tüketim ve Üretim (SDG12), İklim Eylemi (SDG13) ve Kara Hayatı (SDG15) dahil Sürdürülebilir Kalkınma Hedefleri'ne önemli katkılarda bulunur. Bu çalışma, arıcılığın ve arı ürünlerinin ekosistem hizmetleri açısından sürdürülebilir kalkınma için önemini ve çevresel riskleri ele almaktadır.

***Anahtar Kelimeler:** Arıcılık, iklim değişikliği, sürdürülebilir kalkınma, ekosistem hizmetleri, karada yaşam.*

## **I. INTRODUCTION**

The mutualistic relationship between bees and people has a crucial importance for sustainability. Bees provide essential ecosystem services through pollination, which directly benefits human agriculture and food production. Bees play a vital role in pollinating plants, including many of the crops that make up a significant portion of our food supply. In turn, humans have historically cared for and benefited from bees by cultivating hives for honey and other bee products. This relationship has evolved over thousands of years and is often referred to as mutualism, where both species gain benefits. Without bees and other pollinators, these services would be severely compromised. The decline in bee populations, as reported by Potts et al. in 2016, is indeed a cause for concern [1].

Bees and flowering plants have co-evolved over millions of years [2]. This co-evolution has resulted in intricate relationships between bees and various plant species, leading to specialized pollination mechanisms that benefit both bees and plants. Bees have evolved to gather nectar and pollen, while plants have developed strategies to allure and reward them for their pollination services. Bees' role as pollinators doesn't exclusively pertain to crops; it extends to wild and native plants, fostering biodiversity and enhancing ecosystem resilience. Safeguarding and conserving bee populations is imperative for maintaining robust ecosystems and providing essential ecosystem services, such as pollination.

While humans directly manage only a modest fraction of bee species (approximately 50 out of around 20,000 documented species), the larger group of bees holds a critical position in ecosystem functionality. There are potentially around 5,000 bee species that are yet to be scientifically described [3]. Fifty bee species are managed by people, of which around 12 are managed for crop pollination [4]. Their dominance among pollinators and their importance in crop pollination underscore their vital contributions to both natural ecosystems and human well-being [5]. Acknowledging and preserving these crucial species is fundamental for sustainable development and environmental conservation.

The decline in natural habitats significantly impacts bee colonies. Profound impact of habitat loss and the destruction of natural environments on bee colonies, which, in turn, can have significant ecological

and agricultural consequences. In Millennium Ecosystem Assessment (MEA) (2005); globally, human-induced changes in land use are a major cause of species endangerment. The primary causes of environmental degradation include monoculture farming, reduced biodiversity, overgrazing, extensive irrigation, and deforestation. The extinction of natural flora poses a threat to bee colonies, as bees rely on diverse and interconnected floral habitats. Small, fragmented habitats limit bees' foraging range, nesting opportunities, and access to food sources [6],[7].

The decline in bee populations can be attributed to various factors including habitat loss, pesticide application, increasing prevalence of parasites, changes in the availability and diversity of forage, changes in land use and climate, and increased species competition [8],[9],[10]. These factors interact in intricate ways. For instance, intensified agricultural practices driven by market demands have restricted bees' access to forage resources while simultaneously heightening their exposure to potentially harmful agrochemicals [9],[10]. Both managed and wild pollinators are inevitably affected by the wide-ranging impacts of industrial agriculture, as they grapple with the dual challenges of habitat destruction resulting from agricultural activities and the detrimental consequences of intensive farming practices, given that the natural habitats of pollinators often intersect with industrial agricultural landscapes [11],[12],[13].

People have the potential to make a positive impact on ecosystem functioning by implementing bee-friendly policies and participating in efforts to conserve bees [1],[14],[15]. In addition to their role in food production, bees offer a diverse array of advantages to society [14]. For instance, they support the livelihoods of farmers and beekeepers, embody social and cultural significance, and contribute to sustaining ecosystem stability [16].

There is literature discoursing the decline in bee populations and the effects on agriculture. We argue that the broader significance of bees in fostering connections between the planet and humanity remains relatively understudied, particularly in the context of broader Sustainable Development Goals (SDGs) and Ecosystem Services (ESs).

Ecosystems offer numerous advantages to human beings in the form of various goods and services, including ecosystem processes and components. These ESs can be either direct, such as regulation functions (e.g. gas, climate, disturbance prevention, water regulation, soil retention, water supply, soil formation, nutrient regulation, pollination, biological control), habitat functions (e.g. suitable living place, suitable reproduction habitat), production functions (e.g. food, raw materials, genetic resources), information functions (e.g. aesthetic, cultural, spiritual recreation, science and education) [17],[18],[15]. Biodiversity and ESs can serve as the foundation for strategies aimed at climate change adaptation and reducing disaster risks. Because they can offer advantages and enhance people's ability to withstand and recover from the impacts of climate change. The presence of bees contributes to the diversity and resilience of local plant populations, thereby enhancing their capacity to withstand the impacts of severe weather conditions and other environmental pressures. Bees as pollinators can provide food for a large number of animals, which is extremely important for biodiversity [19].

The SDGs, the Convention on Biological Diversity, and the Committee on World Food Security are identified as avenues for promoting the integration of pollinators and pollination in mainstream discussions. The Aichi targets set by the Convention on Biological Diversity further emphasize the necessity of including pollinators and pollination in policymaking. Among these targets, Target 2 focuses on integrating biodiversity considerations into strategies and processes, Target 7 emphasizes sustainable agriculture, and Target 14 underscores the restoration and protection of ESs, all of which hold particular relevance for the conservation of pollinators and pollination [16].

The biosphere is the foundation for all SDGs. But biodiversity conservation remains a persistent global challenge [21],[22]. Exploring how a specific group of organisms (honey bees) from the extensive global biodiversity can contribute to achieving the SDGs has the potential to bridge sustainable development policies with conservation efforts through the development of integrated solutions. Indeed, the decline

in bee populations has led to an increase in research efforts directed toward understanding the causes of this decline and its effects on the provision of ESs [23].

SDGs can be grouped into six thematic areas: Dignity, People, Planet, Partnership, Justice and Prosperity. These themes, especially planet and prosperity, are comprehensive in achieving sustainability goals. ESs provided by bees, which play an important role in the continuity of biodiversity, significantly affect these scopes. In particular, food production and biodiversity are supported through pollination services.

Given the reliance of humans on bees for crucial ecosystem services, it is important to recognize the reciprocal dependence of bees on humans for their own survival. Many factors that influence the delicate balance of wild bee-human systems are driven by human activities [14]. The SDGs explains these balance, influence and interactions within scope of Dignity, People and Prosperity. Actions taken to access these goals support provisioning, regulating and cultural ESs. In context of sustainable conservation solutions, bee pollinations offers opportunities at reduced costs in agriculture. Regulating ESs is important especially, about SDG- 2 Zero hunger. Despite cultural ESs enables people to understand the importance of bees on the world and to establish relationships with bees at the level of belief and need. But, these ESs are not taken consideration. Whereas, when this pollinators known, conservation start by people. Relationship between SDGs and ESs has been given in shown Figure 1.

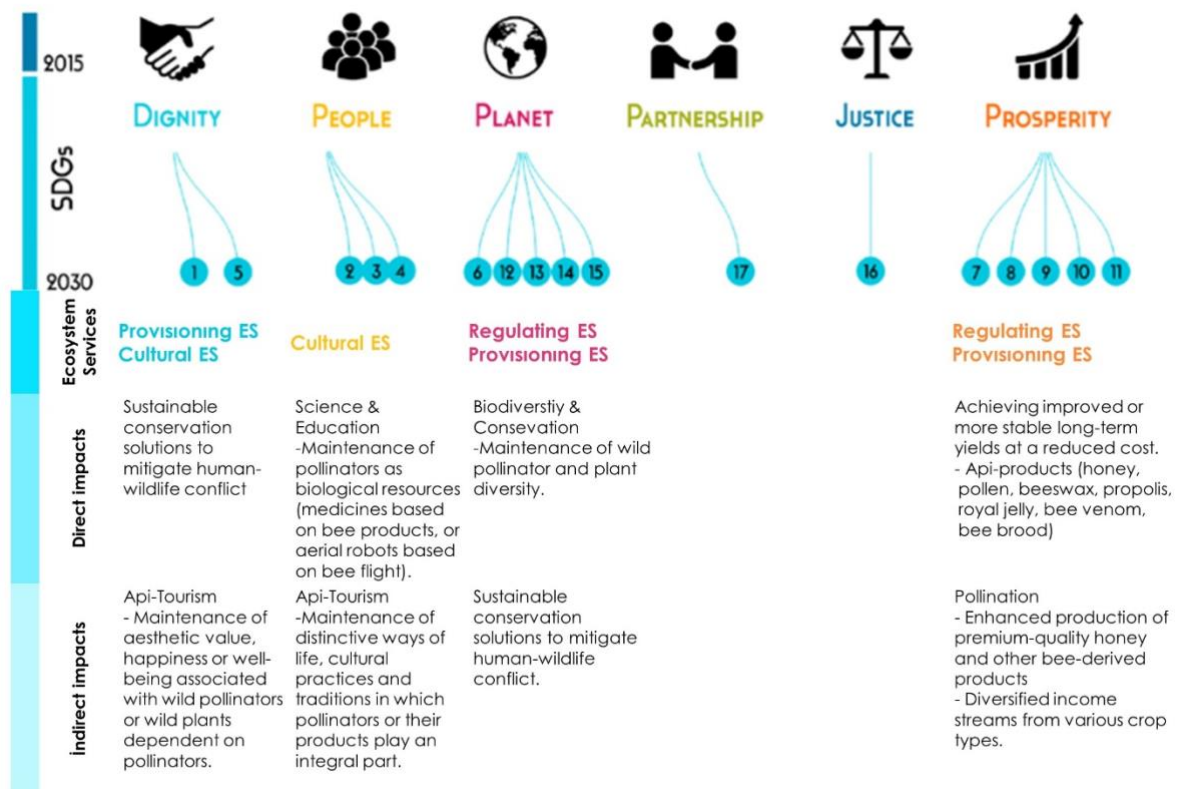


**Figure 1.** Relationship between Sustainable Development Goals and Ecosystem Services provided by honey bee (Prepared with modifications from IPBES,2017; Leal Filho et al., 2018 and Aryal et al., 2020) [16],[22],[15].

We investigate the interrelations between bees, and human communities within the framework of the SDGs and ESs. In this study highlight that the diversity of honey bees has crucial ecological, economic and social importance and crop pollination.

## II. METHOD

We conducted a thorough search of articles through Scopus, Web of Science and Google Scholar using search terms that exclude sustainable honeybees managed, pollination services including ESs and studies of bees with human interaction. Journals had selected in different fields of biochemistry, chemistry, engineering, genetics, molecular biology and environmental.

The report for the SDGs was examined in detail with its themes and sub-goals. Interpretations were made based on reports and articles to define the relationships of beekeeping activities in line with the SDGs. Therefore, publications was analysed based on bee–human interaction and its corresponding services or benefits, its use of livelihood, the social context where bees are found, and benefits from the bees based on SDGs.

We evaluated linkages between SDGs and ESs taken from the Millenium Ecosystem Assessment ESs typology. The services of bees, especially for pollination activities, are arranged and tabulated according to this classification. But the reports of other relevant organizations were examined. These organizations: Ecosystem Services Partnership (ESP), The Economics of Ecosystems and Biodiversity (TEEB), Intergovernmental Panel on Biodiversity and Ecosystem Services (IPBES), UN Sustainable Development Solutions Network (SDSN), and Institute International Sustainable Development. We explained whether the research was examining human and bee interactions through the livelihoods framework and ESs.

## III. RESULTS AND DISCUSSION

Bees contribute either directly or indirectly to most of the SDGs. While maintaining the planet's life support systems, bees offer various ESs that enhance human well-being [14]. ESs inherently contribute to achieving SDGs [24]. Based on literature review, the extent to which bees contribute towards the achievement of the full suite of the SDGs has not been explored in detail.

In literature existing research has highlighted the importance of pollinators in achieving multiple SDGs through the regulation of natural cycles, biological pest control, pollination, seed dispersal, and even as bio-inspiration [25],[26]. Wood et al. (2018) in their study; respondents evaluationed across SDGs and ESs. The most frequently evaluated services were provision of food and water, habitat & biodiversity maintenance, and water quality services (SDG-1 No Poverty, SDG-2 Zero Hunger, SDG-6 Clean Water, and SDG-15 Life on Land) [24]. These substances, which are associated with provisioning and regulating services, can be maintained through pollination. Pollination has been identified as directly contributing to food security (SDG-2) and biodiversity (SDG-15). Bees are important in both food production and economic systems. Bee pollination services effectively have the potential to help meet some of the key SDGs in economics. (SDG-1 (No Poverty), SDG-2 (Zero Hunger), and SDG-8 (Decent Work and Economic Growth)). SDGs linked to bees's services are summarized in Table 1.

*Table 1. Explaining the Relationship Between Ecosystem Services(ESs) and Sustainable Development Goals(SDGs) and Literature Connections[3]*

SDGs	Contributions bees' in achieving the SDG targets	Supported ESs	Some supported literature
1. No Poverty	1.1: Beekeeping can provide economic diversity by offering an additional source of income 1.4: Potential to promote equitable access to economic and natural resources for both men and women	Provisioning ESs and Cultural ESs	[27], [28].

	1.5: Beekeeping can aid in establishing resilient livelihoods for impoverished and vulnerable communities.		
2. Zero hunger	2.2: Enhances the nutritional value of fruits, vegetables and seeds 2.3: Bee pollination increases crop yield	Provisioning ESs and Cultural ESs	[1], [7], [29],[30].
3. Good health and well-being	3.4: Utilized in both traditional and modern medicine for treating non-communicable diseases, including cancer, due to their potent bioactive compounds 3.8: Bee products offer safe and cost-effective medicinal resources 3.9: Bee pollination potentially contributes to the proliferation and variety of plants that play a crucial role in enhancing air quality	Regulating ESs, Provisioning ESs and Cultural ESs	[31], [32], [33].
4. Quality education (knowledge)	4.3, 4.4 and 4.5: Providing vocational training on beekeeping equally for men, women and locals and improving job opportunities	Cultural ESs	[28], [34] [35]
5. Gender equality	5.5: Keeping bees as a hobby or being involved in beekeeping by women can in economic, social and political decision-making processes	Cultural ESs	[28], [34] [35]
6. Clean water and sanitation	6.6: Pollination by bees is important for biodiversity in ecosystems. Appropriate planting studies and designing the urban open-green space system with patch-corridor-matrix approach allow bee activities. Thanks to this design, regional water supply is also supported.	Regulating ESs, Provisioning ESs	[31]
7. Affordable and clean energy	7.2: Bee pollination enhances the yield of oilseed crops used in biofuel production, such as sunflower, canola, and rapeseed	Regulating ESs, Provisioning ESs	[36], [37]
8. Decent work and economic growth	8.1: Bee pollination may contribute to the gross domestic product (GDP) of nations 8.6: Beekeeping can be increased livelihood opportunities in rural areas 8.9:Support nature-based tourism initiatives	Regulating ESs, Provisioning ESs	[38], [28] [30]
9. Industry innovation and infrastructure	Bees are ecosystem services human innovations (e.g., airplane design and computer algorithm development) and new honey-related products	Regulating ESs, Provisioning ESs	[39]
10. Reduced inequality	10.1: Improved livelihoods from beekeeping can support sustainable income growth for lower-income groups 10.2: Promoting social, economic and institutional development.	Regulating ESs, Provisioning ESs	[40], [34]
11. Sustainable cities and communities	11.6: Bees can be useful in air quality in urban ecosystems. Such as pollination of urban green areas can provide improved local air quality. 11.7: Bees can enhance pollination and sustainability of urban green areas and urban open spaces.	Regulating ESs, Provisioning ESs	[41], [42], [43]

12. Responsible consumption and production	12.3: Pollination can contribute to reducing food waste by improving visual shape, size and colour of food and increasing shelf life.	Regulating ESs, Provisioning ESs	[44]
	12.b: Beekeeping can be marketed as sustainable tourism for regional growth.		
13. Climate actions	13.3: Bees can improve understanding of climate impacts on the environment.	Regulating ESs, Provisioning ESs	[45]
14. Life below water	14.4: Bees can serve to production of plant-based sources eaten by fish.	Regulating ESs, Provisioning ESs	[46]
15. Life on land	15.5: Bees contribute to biodiversity by pollinating.	Regulating ESs, Provisioning ESs	[7], [47]
	15.1: Beekeeping can contribute to especially honey forest conservation.		
	15.9: Integrating beekeeping in local planning processes may support reforestation activities based on sustainable regional development.		

### Assessment Regulating Ecosystem Services with Sustainable Development Goals

Pollinators have the greatest share in preserving food and increasing productivity. Moreover; In addition to productivity, the quality of the product due to pollination is also positively affected [48]. This contributes to the regulatory services that bees provide for ecosystems and humans. Today, in conditions where approximately 20 million people are at risk of hunger, ending hunger, safe food and sustainable agricultural activities are aimed within the scope of SDG-2 (Zero Hunger). With this service provided by bees in pollination activities, important solutions can be offered to the safe food problem experienced nowadays. Beyond agricultural pesticides, production and efficiency are possible with natural methods.

Forest ecosystems are areas where pollinator services are most active, especially with the presence of species that attract bees. Preserving these areas where services such as biodiversity, water cycle and carbon sequestration occur is important for sustainability [31]. Especially, within the scope of SDG-15 (Land on Life); Pollinator services of these areas should be supported to achieve the goals of ensuring sustainable forest management and preventing biodiversity loss [29]. Moreover; this pollinator regulating service also indirectly contributes to the supply of non-timber forest products [49]. In this direction, SDG – 8 can be accomplished by rural livelihoods with beekeeping [15].

The issue of efficiency of biofuels in pollination services (SDG-7) has been little noticed. It has been observed that the productivity of oilseed crops, such as canola, increases when pollinated by bees [37].

Bee pollination can be active not only in natural areas but also in the urban open-green space system [50]. The patch-corridor-matrix approach should be adopted in urban planning and design processes and bee-attracting species should be included in these corridor transitions at the planting level. These practices provide a transition within the scope of pollination in achieving the goals of sustainable cities (SDG-11). Such as; the United Kingdom's Protection of Pollinators Bill was proposed to develop a national network of wildflower corridors. Thanks to bee pollination, this corridor can supported SDG-11 and SDG-15 in urban areas [51].

### Assessment Provisioning Ecosystem Services with Sustainable Development Goals

Provisioning services are services used by people as resources. Products obtained from beekeeping activities not only provide these services, but also support the SDG-1 (income diversity) target. People's

use of services from bees dates back thousands of years. It is used in many areas such as food, cosmetics, medicine and fuel. Some bee products are honey, pollen, beeswax, propolis, royal jelly, bee venom, bee brood. In this context; transforming beekeeping activities into a source of income for small farmers will enable the goal to be achieved [15].

Choosing an economy based on bee products directly contributes to the per capita income at home. In line with SDG-8, targeted rural areas can be increased income opportunities in rural areas [3]. Moreover; sustainable tourism activities can be carried out by adding social value other than economy through the initiatives of local people. It provides additional livelihood opportunities through increased tourism activities. For example; Initiatives suitable for these tourism activities are carried out in Slovenia. This offers opportunities to create and purchase original crafts using bee products [38].

### **Assesment Cultural Ecosystem Services with Sustainable Development Goals**

According to literature, the relationship between bees and humans dates back to the Stone Age period [3]. Throughout history, bees have been mentioned in religious texts, mythology, cosmology and iconography.

The existence of bees has become an important figure in many cultures. Beeswax has been used for at least 4000 years. It has been observed that Aboriginal people prefer this product in rock art. It has been determined that the Greek people included bees in their beliefs about life. Immortality is expressed with the bee symbol. In England, in the 19th century, bees were used to tell important events such as birth, death, marriage or long journeys [3].

The most important point in achieving the sustainability goals of cultural services (SDG-1, 4, 5, 8) is education, employment and entrepreneurship. Providing training on beekeeping and providing employment to entrepreneurial farmers should be encouraged with a focus on sustainability. These activities must support gender equality [34].

### **Pressures on Activities of Bees**

According to the literature; there are studies explaining that bee populations are decreasing due to global pollination crises. Reasons such as habitat fragmentation due to land use change, competition between native and invasive species, agricultural activities and climate change negatively affect bee populations [1]. This situation creates pressure towards decreasing efficiency in food production and species losses in biodiversity [15]. These pressures on bees have far-reaching effects that intersect with the SDGs. It is vital to protect and sustain bees, considering the indirect impact they will have on the economy, welfare and the planet.

*Land cover changes:* Increasing urbanization causes the destruction of the habitat required for nesting of fodder in pollination [52]. Destroyed and fragmented many natural habitats prevent bees from nesting and transitioning between species. Apart from the change in open-green areas due to urbanization, the change in aquatic systems also changes bee movements. Bees, which use aquatic plants for pollination, may lose their movement corridor due to changes such as drying of water, being placed under urban construction, or changing their location. Moreover; the loss of plant species specific to the aquatic system due to this change also means the extinction of pollinator species [52].

*Agricultural activities:* One of the most common pressures on pollinators is spraying due to agricultural activities. Exposure to pesticides in intensive agricultural activities and monoculture cropping patterns reduce species richness [52].

*Climate change:* Bee habitats are affected by seasonal changes, extreme weather events and increasing disasters. There is a suitable climate range for each species to survive. It has been demonstrated that those living at the edges of the climate range become more vulnerable to population decline or even extinction. Bees have difficulty in synchronizing and performing spatial displacements because sudden and temporal changes in seasonal transitions also affect migration times. Additionally, this phenological mismatch can lead to pollinator losses.

## **IV. CONCLUSION**

Pollination services sustain all terrestrial ecosystems, being crucial for the reproduction of numerous plants that serve as the foundation of ecosystems worldwide. Therefore, the conservation of pollinators directly or indirectly contributes to most of the SDGs, fostering a more balanced, sustainable, and socially just world. In this context;

- Creating and restoring habitats for pollinators can mitigate the combined impacts of agricultural intensification, climate change, and to some extent, pesticides and pathogens.
- A major challenge during strategic planning at the landscape level is to develop suitable incentives for land managers to collaborate and ensure an effective spatial and temporal network of food and nesting sites for pollinators.
- Urban landscape planning and design should incorporate initiatives to encourage wildlife-friendly gardening and beekeeping, providing better support for pollinators.
- Bee habitats should incorporate a diversity of food sources in both time and space.
- Sowing flowering plants is necessary to minimize temporal and spatial gaps in pollinators' resources.

## **V. REFERENCES**

- [1] S. G. Potts *et al.*, 'Safeguarding pollinators and their values to human well-being', *Nature*, vol. 540, no. 7632, pp. 220–229, 2016, doi: 10.1038/nature20588.
- [2] S. C. Cappellari, H. Schaefer, and C. C. Davis, 'Evolution: Pollen or pollinators - Which came first?', *Curr. Biol.*, vol. 23, no. 8, pp. R316–R318, 2013, doi: 10.1016/j.cub.2013.02.049.
- [3] V. Patel, N. Pauli, E. Biggs, L. Barbour, and B. Boruff, 'Why bees are critical for achieving sustainable development', *Ambio*, vol. 50, no. 1, pp. 49–59, 2021, doi: 10.1007/s13280-020-01333-9.
- [4] J. L. S. Silva *et al.*, *POLLINATION AND FOOD PRODUCTION The assessment report on SUMMARY FOR POLICYMAKERS OF THE ASSESSMENT REPORT OF THE*, vol. 1469, no. 3. 2020.
- [5] J. Ollerton, R. Winfree, and S. Tarrant, 'How many flowering plants are pollinated by animals?', *Oikos*, vol. 120, no. 3, pp. 321–326, 2011, doi: 10.1111/j.1600-0706.2010.18644.x.
- [6] E. Varol and B. Yücel, 'The Effects of Environmental Problems on Honey Bees in view of Sustainable Life', *Mellifera*, vol. 19, no. 2, pp. 23–32, 2019.
- [7] A. M. Klein, V. Boreux, F. Fornoff, A. C. Mupepele, and G. Pufal, 'Relevance of wild and managed bees for human well-being', *Curr. Opin. Insect Sci.*, vol. 26, pp. 82–88, 2018, doi: 10.1016/j.cois.2018.02.011.
- [8] D. Goulson, E. Nicholls, C. Botías, and E. L. Rotheray, 'Bee declines driven by combined Stress from parasites, pesticides, and lack of flowers', *Science (80-. )*, vol. 347, no. 6229, 2015, doi: 10.1126/science.1255957.



- [9] F. Sanchez-Bayo and K. Goka, 'Pesticide residues and bees - A risk assessment', *PLoS One*, vol. 9, no. 4, 2014, doi: 10.1371/journal.pone.0094482.
- [10] D. L. Wagner, 'Insect declines in the Anthropocene', *Annu. Rev. Entomol.*, vol. 65, pp. 457–480, 2020, doi: 10.1038/s43017-023-00478-x.
- [11] P. Hristov, R. Shumkova, N. Palova, and B. Neov, 'Honey bee colony losses: Why are honey bees disappearing?', *Sociobiology*, vol. 68, no. 1, pp. 1–13, 2021, doi: 10.13102/SOCIOBIOLOGY.V68I1.5851.
- [12] A. Kovács-Hostyánszki *et al.*, 'Conservation of Pollinators in Traditional Agricultural Landscapes - New Challenges in Transylvania (Romania) Posed by EU Accession and Recommendations for Future Research', *PLoS One*, vol. 11, no. 6, pp. 1–20, 2016, doi: 10.1371/journal.pone.0151650.
- [13] J. Belsky and N. K. Joshi, 'Impact of biotic and abiotic stressors on managed and feral bees', *Insects*, vol. 10, no. 8, 2019, doi: 10.3390/insects10080233.
- [14] D. M. S. Matias, J. Leventon, A. L. Rau, C. Borgemeister, and H. von Wehrden, 'A review of ecosystem service benefits from wild bees across social contexts', *Ambio*, vol. 46, no. 4, pp. 456–467, 2017, doi: 10.1007/s13280-016-0844-z.
- [15] S. Aryal, S. Ghosh, and C. Jung, 'Ecosystem Services of Honey Bees; Regulating, Provisioning and Cultural Functions', *J. Apic.*, vol. 35, no. 2, pp. 119–128, 2020, doi: 10.17519/apiculture.2020.06.35.2.119.
- [16] IPBES, *The assessment report of the Intergovernmental Science-Policy Platform on Biodiversity and Ecosystem Services on pollinators, pollination and food production*. S.G. Potts, V. L. Imperatriz-Fonseca and H. T. Ngo, (eds)., vol. 325, no. 5940. 2016.
- [17] R. S. De Groot, M. A. Wilson, and R. M. J. Boumans, 'A typology for the classification, description and valuation of ecosystem functions, goods and services', *Ecol. Econ.*, vol. 41, no. 3, pp. 393–408, 2002, doi: 10.1016/S0921-8009(02)00089-7.
- [18] K. J. Wallace, 'Classification of ecosystem services: Problems and solutions', *Biol. Conserv.*, vol. 139, no. 3–4, pp. 235–246, 2007, doi: 10.1016/j.biocon.2007.07.015.
- [19] J. Huang, 'Perspectives Increasing the Number of Bees and Sustainable Development Goal', *iY-1 Perspect.*, vol. 1, no. 1.
- [20] U. Nations, *The-Sustainable-Development-Goals-Report-2023.pdf*. 2023.
- [21] C. Folke, R. Biggs, A. V. Norström, B. Reyers, and J. Rockström, 'Social-ecological resilience and biosphere-based sustainability science', *Ecol. Soc.*, vol. 21, no. 3, 2016, doi: 10.5751/ES-08748-210341.
- [22] A. Leal Filho, W. Azeiteiro, U. Alves, F. Pace, P. Mifsud, M. Brandli, L. Caeiro, SS and Disterheft, 'Reinvigorating the sustainable development research agenda: the role of the sustainable development goals (SDG)', *Int. J. Sustain. Dev. World Ecol.*, vol. 25, no. 1, pp. 131–142, 2018.
- [23] A. Decourtye, C. Alaux, Y. Le Conte, and M. Henry, 'Toward the protection of bees and pollination under global change: present and future perspectives in a challenging applied science', *Curr. Opin. Insect Sci.*, vol. 35, pp. 123–131, 2019, doi: 10.1016/j.cois.2019.07.008.

- [24] S. L. R. Wood *et al.*, ‘Distilling the role of ecosystem services in the Sustainable Development Goals’, *Ecosyst. Serv.*, vol. 29, pp. 70–82, 2018, doi: 10.1016/j.ecoser.2017.10.010.
- [25] F. Sánchez-Bayo and K. A. G. Wyckhuys, ‘Worldwide decline of the entomofauna: A review of its drivers’, *Biol. Conserv.*, vol. 232, no. January, pp. 8–27, 2019, doi: 10.1016/j.biocon.2019.01.020.
- [26] O. Dangles and J. Casas, ‘Ecosystem services provided by insects for achieving sustainable development goals’, *Ecosyst. Serv.*, vol. 35, no. December 2018, pp. 109–115, 2019, doi: 10.1016/j.ecoser.2018.12.002.
- [27] D. R. Amulen *et al.*, ‘Estimating the potential of beekeeping to alleviate household poverty in rural Uganda’, *PLoS One*, vol. 14, no. 3, pp. 1–19, 2019, doi: 10.1371/journal.pone.0214113.
- [28] C. B. Pocol and M. McDonough, ‘Women, Apiculture and Development: Evaluating the Impact of a Beekeeping Project on Rural Women’s Livelihoods’, *Bull. Univ. Agric. Sci. Vet. Med. Cluj-Napoca. Hortic.*, vol. 72, no. 2, 2015, doi: 10.15835/buasvmcn-hort:11423.
- [29] D. Kleijn *et al.*, ‘Delivery of crop pollination services is an insufficient argument for wild pollinator conservation’, *Nat. Commun.*, vol. 6, no. May 2015, 2015, doi: 10.1038/ncomms8414.
- [30] K. Stein *et al.*, ‘Bee pollination increases yield quantity and quality of cash crops in Burkina Faso, West Africa’, *Sci. Rep.*, vol. 7, no. 1, pp. 1–10, 2017, doi: 10.1038/s41598-017-17970-2.
- [31] E. G. Brockerhoff *et al.*, ‘Forest biodiversity, ecosystem functioning and the provision of ecosystem services’, *Biodivers. Conserv.*, vol. 26, no. 13, pp. 3005–3035, 2017, doi: 10.1007/s10531-017-1453-2.
- [32] V. R. Pasupuleti, L. Sammugam, N. Ramesh, and S. H. Gan, ‘Honey, Propolis, and Royal Jelly: A Comprehensive Review of Their Biological Actions and Health Benefits’, *Oxid. Med. Cell. Longev.*, vol. 2017, 2017, doi: 10.1155/2017/1259510.
- [33] A. Easton-Calabria, K. C. Demary, and N. J. Oner, ‘Beyond Pollination: Honey Bees (*Apis mellifera*) as Zootherapy Keystone Species’, *Front. Ecol. Evol.*, vol. 6, no. February, 2019, doi: 10.3389/fevo.2018.00161.
- [34] P. D. M. Mburu, H. Affognon, P. Irungu, J. Mburu, and S. Raina, ‘Gender Roles and Constraints in Beekeeping: A Case from Kitui County, Kenya’, *Bee World*, vol. 94, no. 2, pp. 54–59, 2017, doi: 10.1080/0005772x.2016.1275490.
- [35] G. E. Ekele, T. S. Kwaghgba, and E. N. Essien, ‘Vocational Competencies Required by Youths in Management of Beekeeping for Job creation in North East Zone of Benue State, Nigeria’, *J. Educ. Syst.*, vol. 3, no. 2, pp. 42–49, 2019, doi: 10.22259/2637-5877.0302007.
- [36] T. Perrot, S. Gaba, M. Roncoroni, J. L. Gautier, and V. Bretagnolle, ‘Bees increase oilseed rape yield under real field conditions’, *Agric. Ecosyst. Environ.*, vol. 266, no. December 2017, pp. 39–48, 2018, doi: 10.1016/j.agee.2018.07.020.
- [37] R. Halinski, C. F. Dos Santos, T. G. Kaehler, and B. Blochtein, ‘Influence of wild bee diversity on canola crop yields’, *Sociobiology*, vol. 65, no. 4, pp. 751–759, 2018, doi: 10.13102/sociobiology.v65i4.3467.
- [38] I. K. Arih, ‘Api-tourism: transforming Slovenia’s apicultural traditions into a unique travel experience’, *Sustain. Dev. Plan. VII*, vol. 1, pp. 963–974, 2015, doi: 10.2495/sdp150811.

- [39] Q. Zhang *et al.*, ‘Bioinspired engineering of honeycomb structure - Using nature to inspire human innovation’, *Prog. Mater. Sci.*, vol. 74, pp. 332–400, 2015, doi: 10.1016/j.pmatsci.2015.05.001.
- [40] T. Carroll and J. Kinsella, ‘L’amélioration des moyens d’existence pour les petits apiculteurs au Kenya’, *Dev. Pract.*, vol. 23, no. 3, pp. 332–345, 2013, doi: 10.1080/09614524.2013.781123.
- [41] D. M. Lowenstein, K. C. Matteson, and E. S. Minor, ‘Diversity of wild bees supports pollination services in an urbanized landscape’, *Oecologia*, vol. 179, no. 3, pp. 811–821, 2015, doi: 10.1007/s00442-015-3389-0.
- [42] J. J. M. Van der Steen, J. de Kraker, and T. Grotenhuis, ‘Assessment of the Potential of Honeybees (&i&t;Apis mellifera&i&t; L.) in Biomonitoring of Air Pollution by Cadmium, Lead and Vanadium’, *J. Environ. Prot. (Irvine., Calif.)*, vol. 06, no. 02, pp. 96–102, 2015, doi: 10.4236/jep.2015.62011.
- [43] S. L. Hausmann, J. S. Petermann, and J. Rolff, ‘Wild bees as pollinators of city trees’, *Insect Conserv. Divers.*, vol. 9, no. 2, pp. 97–107, 2016, doi: 10.1111/icad.12145.
- [44] R. H. Lemelin, ‘Entomotourism and the stingless bees of Mexico’, *J. Ecotourism*, vol. 19, no. 2, pp. 168–175, 2020, doi: 10.1080/14724049.2019.1615074.
- [45] K. E. Smith, D. Weis, M. Amini, A. E. Shiel, V. W. M. Lai, and K. Gordon, ‘Honey as a biomonitor for a changing world’, *Nat. Sustain.*, vol. 2, no. 3, pp. 223–232, 2019, doi: 10.1038/s41893-019-0243-0.
- [46] W. Amjad Khan, H. Chun-Mei, N. Khan, A. Iqbal, S. W. Lyu, and F. Shah, ‘Bioengineered Plants Can Be a Useful Source of Omega-3 Fatty Acids’, *Biomed Res. Int.*, vol. 2017, p. 7348919, 2017, doi: 10.1155/2017/7348919.
- [47] C. Mudzengi, C. S. Kapembeza, E. Dahwa, L. Taderera, S. Moyana, and M. Zimondi, ‘Ecological Benefits of Apiculture on Savanna Rangelands’, *Bee World*, vol. 97, no. 1, pp. 17–20, 2020, doi: 10.1080/0005772x.2019.1701797.
- [48] B. K. Klatt *et al.*, ‘Bee pollination improves crop quality, shelf life and commercial value’, *Proc. R. Soc. B Biol. Sci.*, vol. 281, no. 1775, 2013, doi: 10.1098/rspb.2013.2440.
- [49] D. Senapathi, J. C. Biesmeijer, T. D. Breeze, D. Kleijn, S. G. Potts, and L. G. Carneiro, ‘Pollinator conservation - The difference between managing for pollination services and preserving pollinator diversity’, *Curr. Opin. Insect Sci.*, vol. 12, pp. 93–101, 2015, doi: 10.1016/j.cois.2015.11.002.
- [50] E. Stange, D. N. Barton, and G. M. Rusch, ‘A closer look at Norway’s natural capital—how enhancing urban pollination promotes cultural ecosystem services’, *Reconnecting Nat. Cult. Cap. - Contrib. from Sci. Policy*, pp. 235–241, 2018, [Online]. Available: <https://publications.europa.eu/en/publication-detail/-/publication/6a0efd09-0d4d-11e8-966a-01aa75ed71a1/language-en%0Afile:///C:/Users/Saeed/Dropbox/Apps/zotero/zotero/wvg311ca.default/zotero/storage/J57ZS8S8/language-en.html>.
- [51] H. of C. UK Parliament, ‘Protection of Pollinators’, 2017. [Online]. Available: [https://aapco.files.wordpress.com/2015/10/bee\\_label\\_guidance\\_2014.pdf](https://aapco.files.wordpress.com/2015/10/bee_label_guidance_2014.pdf).
- [52] A. J. Vanbergen *et al.*, ‘Threats to an ecosystem service: Pressures on pollinators’, *Front. Ecol. Environ.*, vol. 11, no. 5, pp. 251–259, 2013, doi: 10.1890/120126.



# Düzce University Journal of Science & Technology

Research Article

## Experimental Investigation of the Effects of Paraffin as a Phase Change Material on the Cooling Performance of a Battery Thermal Management System

 Fikret POLAT <sup>a,\*</sup>,  Suat SARIDEMİR <sup>a</sup>

<sup>a</sup> Department of Mechanical Engineering, Faculty of Engineering, Düzce University, Düzce, TURKEY

\* Corresponding author's e-mail address: [fikretpolat@duzce.edu.tr](mailto:fikretpolat@duzce.edu.tr)

DOI: 10.29130/dubited.1379834

### ABSTRACT

Internal combustion engines (ICEs) are largely dependent on fossil fuels, and both the risk of depletion of fossil fuels and the harmful exhaust emissions emitted by ICEs have led researchers to become interested in electric vehicles (EVs). As the EV industry develops day by day, battery thermal management systems (BTMS) have become indispensable in solving the high-temperature problem of batteries, which are the most important component of EVs. The cost and reliability of electric vehicles are affected by parameters such as the life cycle, capacity, charging time, durability, and warranty cost of the battery pack used. The heat produced in the battery pack is removed by gas or liquid cooling in active cooling, and by phase change materials (PCM) in passive cooling. The high energy storage density of PCMs and the fact that there is no need for fan or pump power in cooling using PCMs are some of the reasons why PCMs are preferred for BTMSs. In this study, a battery pack consisting of 18 lithium-ion batteries, 6 in series and 3 in parallel, was first charged and discharged without any cooling system and then with the addition of PCM at a current strength of 1C, and the effect of the BTMS was examined. It has been observed that the BTMS has a positive effect of approximately 8% for charging experiments and 23% for discharge experiments in terms of the maximum temperature value in the battery pack.

**Keywords:** Battery thermal management system, Electric vehicles, Phase change materials

## Faz Değişim Malzemesi Olarak Parafinin Bir Batarya Termal Yönetim Sisteminin Soğutma Performansı Üzerindeki Etkisinin Deneysel Olarak İncelenmesi

### ÖZET

İçten yanmalı motorlar (İYM'ler) büyük ölçüde fosil yakıtlara bağımlıdır ve hem fosil yakıtların tükenme riski hem de içten yanmalı motorların yaydığı zararlı egzoz emisyonları araştırmacıları elektrikli araçlara (EA) ilgi duymaya yöneltmiştir. Elektrikli araç sektörünün her geçen gün gelişmesiyle birlikte, elektrikli araçların en önemli bileşeni olan pillerin yüksek sıcaklık sorununun çözümünde batarya termal yönetim sistemleri (BTYS) vazgeçilmez hale gelmiştir. Elektrikli araçların maliyeti ve güvenilirliği, kullanılan pil paketinin ömrü, kapasitesi, şarj süresi, dayanıklılığı ve garanti maliyeti gibi parametrelerden etkilenmektedir. Batarya paketinde üretilen ısı, aktif soğutmada gaz veya sıvı

soğutmayla, pasif soğutmada ise faz değıştiren malzemeler (FDM) ile uzaklaştırılır. FDM'lerin enerji depolama yoğunluğunun yüksek olması ve FDM'ler kullanılarak yapılan soğutmada fan veya pompa gücüne ihtiyaç duyulmaması, FDM'lerin batarya termal yönetim sistemlerinde tercih edilmesinin nedenlerinden bazılarıdır. Bu çalışmada, 6'sı seri, 3'ü paralel olmak üzere 18 adet lityum iyon pilden oluşan bir pil paketi, önce herhangi bir soğutma sistemi olmadan, ardından 1C akım gücünde FDM ilavesi ile şarj ve deşarj edilmiş ve batarya termal yönetim sisteminin etkisi incelenmiştir. BTYS'nin batarya paketindeki maksimum sıcaklık değeri açısından şarj deneylerinde yaklaşık %8, deşarj deneylerinde ise %23 oranında pozitif etkiye sahip olduğu görülmüştür.

*Anahtar Kelimeler: Batarya termal yönetim sistemi, Elektrikli araçlar, Faz değıştiren malzemeler*

## **I. INTRODUCTION**

In today's world, with the rapid increase in population, the need for energy continues to increase day by day. It is known that most of the energy needs in the world are met by fossil fuels [1-5]. It has been proven that the use of fossil fuels causes many negative factors such as air pollution and depletion of the ozone layer. Regarding this issue, looking at the data published by the World Health Organization in 2020, it is clear that air pollution causes the premature death of an average of 6.7 million people in the world every year and causes great damage to the economies of states [6,7].

As it is known, conventional vehicles that use only internal combustion engines consume fossil fuels and cause the emission of gases such as CO<sub>2</sub>, HC, and NO<sub>x</sub>. HEVs have been developed and implemented in recent years to overcome the environmental and energy crisis problems caused by conventional vehicles. Although HEV technology has improved fuel economy and caused less emissions compared to conventional internal combustion engine vehicles, it has not reached a satisfactory level, especially in terms of environmental concerns. For this reason, hybrid electric vehicles remain only a temporary step in the transition from internal combustion engine vehicles to electric vehicles. Driven by the imperative to decarbonize personal transportation to meet global targets to reduce greenhouse gas emissions and improve air quality in city centers, the electric vehicle revolution has begun to revolutionize the automotive industry. However, the development of battery packs in electric vehicles, which is the technology of today and the future, has become the most important topic. The most serious problem encountered in battery packs is that the battery cells are negatively affected by sudden temperature increases that occur while the batteries are in operation or when charging and discharging [8-10]. If this heat is not distributed homogeneously in the battery pack and cannot be discharged quickly, results such as deterioration of battery cells and reduced lifespan occur.

As the electric vehicle industry is constantly growing and open to development, researchers have concentrated their work on battery thermal management systems in order to solve the above-mentioned problems. Parameters such as cycle life, capacity, charging time, durability and warranty cost of the battery pack used affect the cost and reliability of electric vehicles [11,12]. These important parameters also largely depend on the BTMS. There are two main criteria to evaluate the performance of BTMS: maximum temperature rise and maximum temperature difference of the battery pack. To maintain optimum performance and extend battery life, the temperature of all cells must be maintained within a narrow range between 20 °C and 45 °C, and the maximum temperature difference between cells must be less than 5 °C [13]. On the other hand, operating below 0 degrees also causes its capacity to decrease. BTMSs include active or passive cooling systems. Generated heat in the battery pack; In active cooling, it is removed by gas or liquid cooling. In passive cooling, it is removed with phase change materials. There are battery thermal management systems in which these methods are used separately or together. Each method has advantages and disadvantages relative to each other. Throughout the literature research, it was concluded that it would not be appropriate to directly compare each system due to differences in the battery type, capacity, charging/discharging rate, and other external conditions used in each study. It should be done according to the battery type, the area in which it will be used, the vehicle, and what kind of need it should meet. As a result, it has been understood that the most

appropriate thermal management system to be selected according to criteria such as cost, ease of installation, security risk, and performance will vary depending on the results targeted for the vehicle to be produced.


Phase change materials are materials that show a phase change within a certain temperature range. These materials store or release heat energy during phase change, which ensures that the temperature of the battery remains both homogeneous and at a certain level. PCM-based BTMSs are an innovative approach developed to improve the thermal management of battery technology. These systems provide temperature control of battery packs, increasing the performance of the batteries and ensuring their safety [14-16]. In PCM-based BTMSs, the PCM placed in the battery module begins to melt by absorbing the excessive heat that occurs in the battery during charging and discharging. This process continues until the latent heat value of the PCM is reached. Thanks to the PCM, the temperature is kept constant at the melting point during this time and the temperature rise is also delayed. In other words, the PCM is used as a thermal conductor for the battery pack, thereby increasing system performance. PCMs have been used in the literature due to their advantages such as low operating cost and good temperature homogeneity [17-20].

In a study investigating the effects of PCM thicknesses (3, 6, 9, and 12 mm) around the battery cells on the thermal performance of BTMS, Javani et al found that the maximum temperature and temperature homogeneity in the cell were significantly improved when PCM was used [21]. In another study, researchers analyzed the effects of PCM thickness, melting point, and thermal conductivity on cooling performance by designing different modules consisting of pouch lithium batteries in a computer environment. As a result, they observed that the maximum temperature and maximum temperature deviation decrease, while the thermal conductivity increases when the gap between the modules is increased. In addition, they emphasized that when the melting point of PCM increases, the maximum temperature increases but the maximum temperature deviation decreases [22]. Verma et al. studied the effects of using Capric acid around the battery pack as a PCM. They tested the effect of capric acid as a PCM by conducting research on two ambient conditions, one 294K and the other 323K (desert condition), by forming a PCM layer of different thicknesses, 3mm, 7mm, 9mm, and 12mm, and compared it with conventionally used paraffin. As a result, they declared that the 3 mm thick PCM layer is optimal and reduces the maximum temperature in the battery to 305K [23].

In this study, a battery pack was prepared using 18 lithium-ion batteries purchased from a commercial company. The batteries are connected to each other by spot welding, 6 in series and 3 in parallel. The prepared battery pack was charged and discharged at 1C current power, first without any cooling system, then by adding PCM, and the cooling performance of the battery thermal management system was examined.

## **II. MATERIAL AND METHOD**

In the experimental setup, 18 cylindrical lithium-ion batteries were used. The shape and technical specifications of these batteries can be seen in Figure 1.

	<b>Model</b>	<b>18650 Sony VTC6</b>
	<b>Chemical</b>	Li-ion
	<b>Voltage</b>	3.7 V
	<b>Charging Voltage</b>	4.2 V
	<b>Discharge Voltage</b>	2.75 V
	<b>Capacity</b>	3000 mAh
	<b>Power</b>	13,69 Wh
	<b>Weight</b>	48.50 gr
	<b>Dimensions</b>	18.25 mm x 65.00 mm

*Figure 1. The shape and technical specifications of batteries used in experiments.*

18 batteries, 6 in series and 3 in parallel were punched with the help of strip nickel, and a battery pack was created. In addition, the temperatures of the batteries were measured at the time of charging and discharging with the help of 6 temperature sensors, and data was taken every second via Arduino Nano and recorded on the computer. Power supplies were used to charge the batteries and rheostats were used to discharge them. The final version of the battery pack, charging, and discharging mechanisms are given in Figure 2, Figure 3, and Figure 4, respectively. The created battery pack was enclosed in a battery box obtained with a 3D printer and was made ready for testing. Numbers 1 to 6 in Figure 2 show the location and sequence numbers of the temperature sensors.

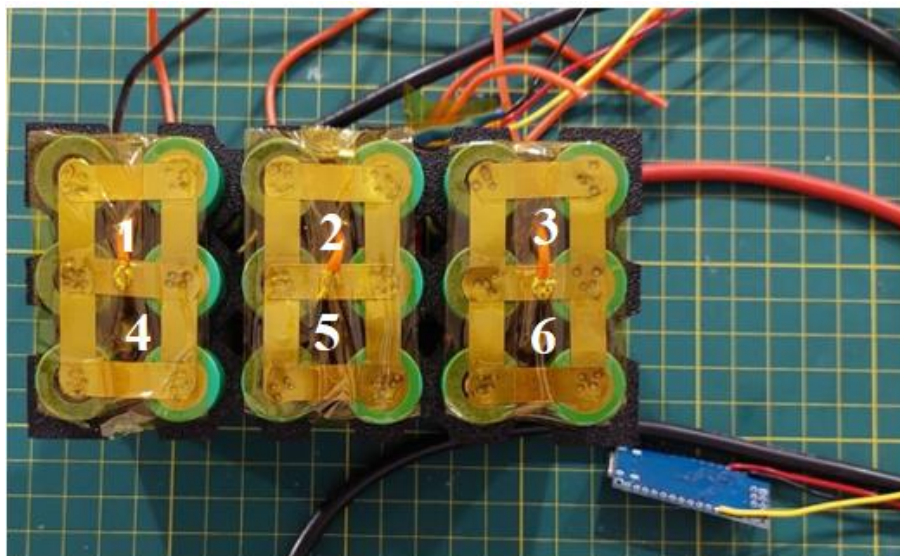


*Figure 2. Final version of battery pack.*

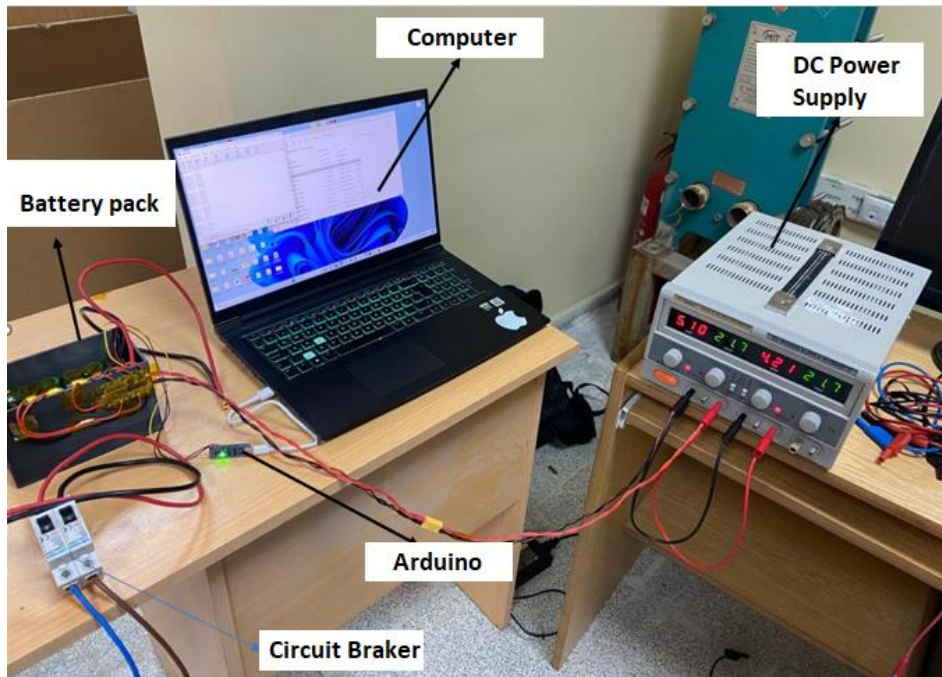


*Figure 3. Experimental setup for charging.*

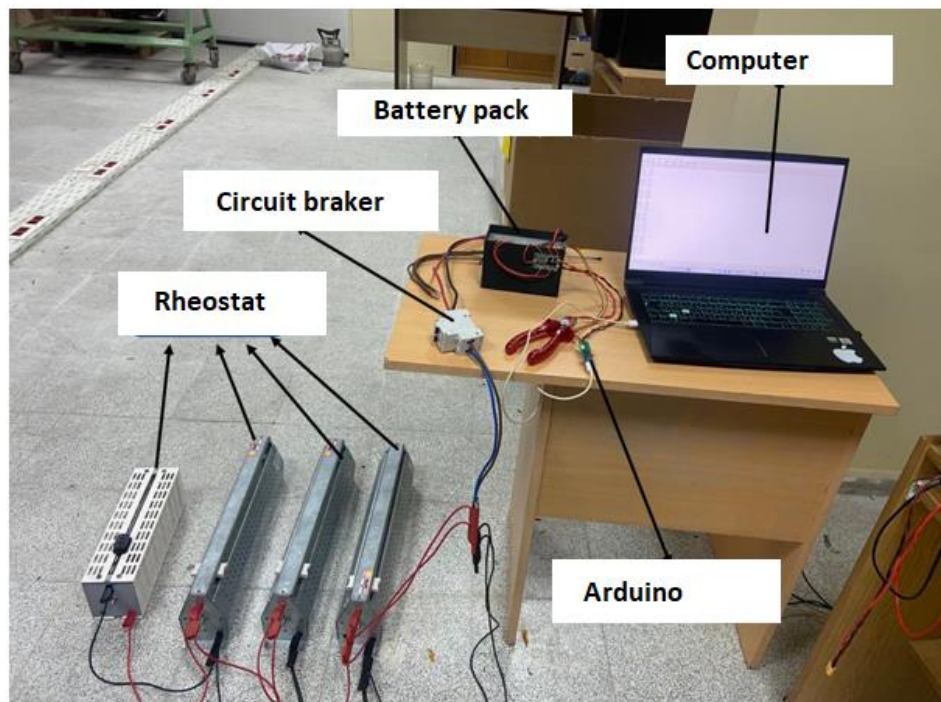


*Figure 4. Experimental setup for discharging.*

First of all, the charging and discharging processes were carried out without any thermal management system, and as mentioned before, the temperature data received from the sensors were recorded on the computer via Arduino. Then, molten paraffin was filled into the battery box and allowed to freeze. After the freezing process was completed, the experiments were repeated under the same conditions as the experiments without paraffin, and the properties of paraffin as a phase change material during the cooling of the batteries were examined. The experiments were carried out at room conditions (22 °C temperature) and 1 C current intensity. Also, the experiments were repeated 3 times and the data were obtained by averaging the results.



In the charging experiments, the battery pack with 18 V voltage was first charged without paraffin, up to the maximum voltage value of 25.2 V. Meanwhile, the current applied to the battery is 4.2 A. DC power supply was used as the charger. The connections were made with xt60 and the charging process continued until the voltage reached 25.2 V and the current value decreased to 0.06 A in both experiments.

The rheostats to be used in the discharge experiments are each rated at 50 ohms and 1000 W, and 4 of them were used. Each rheostat was set to 1.8 ohms and connected to each other in parallel. The equivalent resistor was set to 1 ohm and connected to the fuse to pass high current. In the first discharge process without using PCM, it was observed that the current passing by using a clamp meter was 23 A. The discharge process started at 25.2 V and ended when it reached 17.85 V. In the discharge experiment using PCM, the discharge process started from 25.2 V to 17.75 V. During these experiments, data was recorded every second thanks to Arduino nano. When the current passing through the cables was measured with the help of a clamp meter, it was seen that 23 A current was passing. Since the variable is only PCM, the equivalent resistance in the rheostats was set to 1 ohm in this experiment.

### **III. RESULTS AND DISCUSSION**

The results from the discharge experiments are shown in Figure 5 and Figure 6. Figure 5 shows the experimental results without any battery thermal management system, and Figure 6 shows the experimental results when using the PCM-based battery thermal management system.

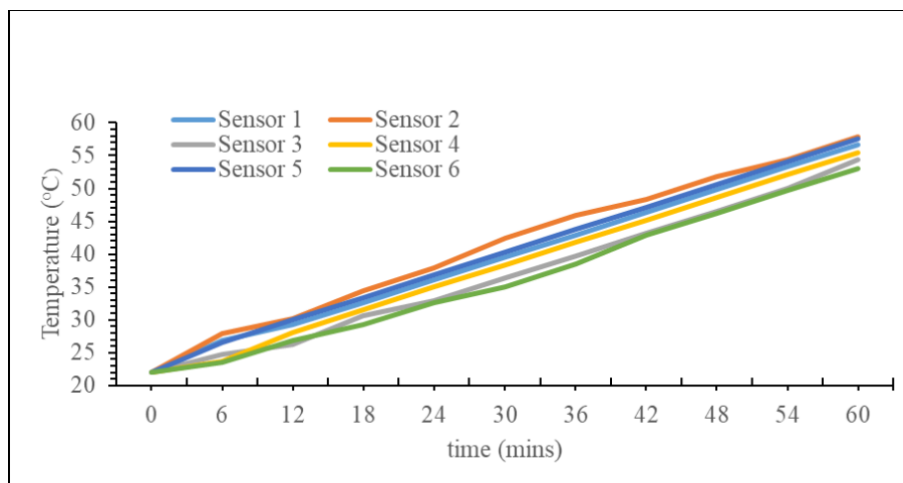


**Figure 5.** Experimental results of discharging without battery thermal management system.

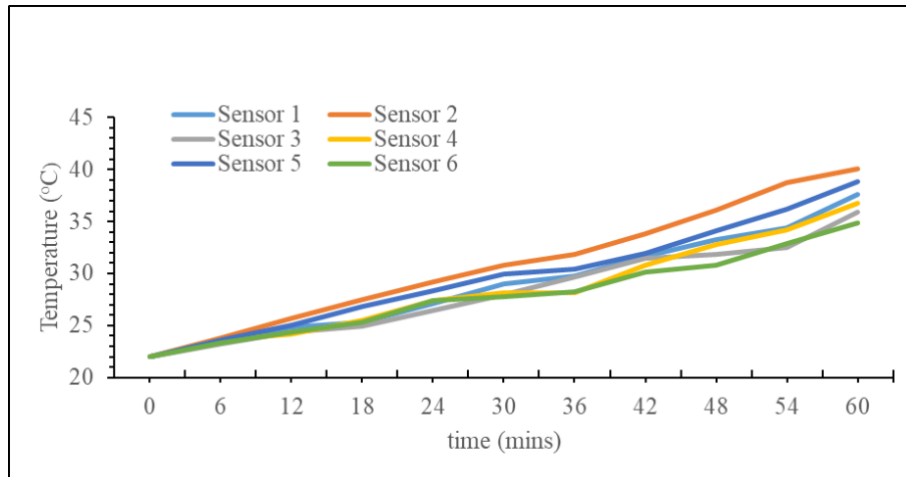


**Figure 6.** Experimental results of discharging with PCM-based battery thermal management system.

In the discharge experiments conducted without PCM and with PCM added, it was observed that the highest temperature values obtained at the end of the discharge process of the battery pack were 57.82 °C and 40.1 °C, respectively as seen in Figure 5 and Figure 6, thanks to the temperature data coming from 6 different sensors. Considering these sensors, it is understood that sensor 2 has reached the highest temperature values. It can be said that the reason for this situation is that this sensor is located in the middle of the battery pack and may be slightly affected by the temperatures of the neighboring battery cells.

The results from the charging experiments are shown in Figure 7 and Figure 8. Figure 7 shows the experimental results without any battery thermal management system, and Figure 8 shows the experimental results when using the PCM-based battery thermal management system.

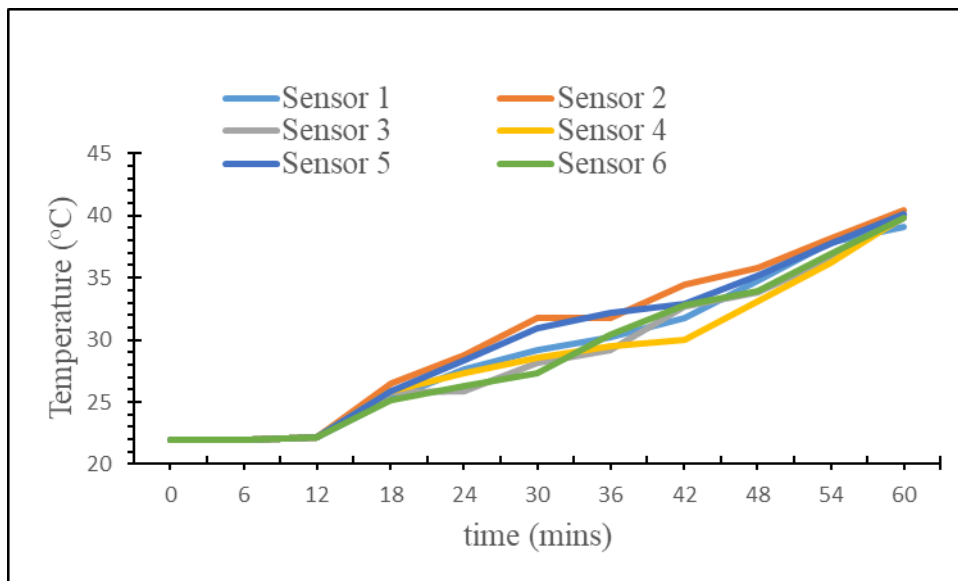


**Figure 7.** Experimental results of charging without battery thermal management system.

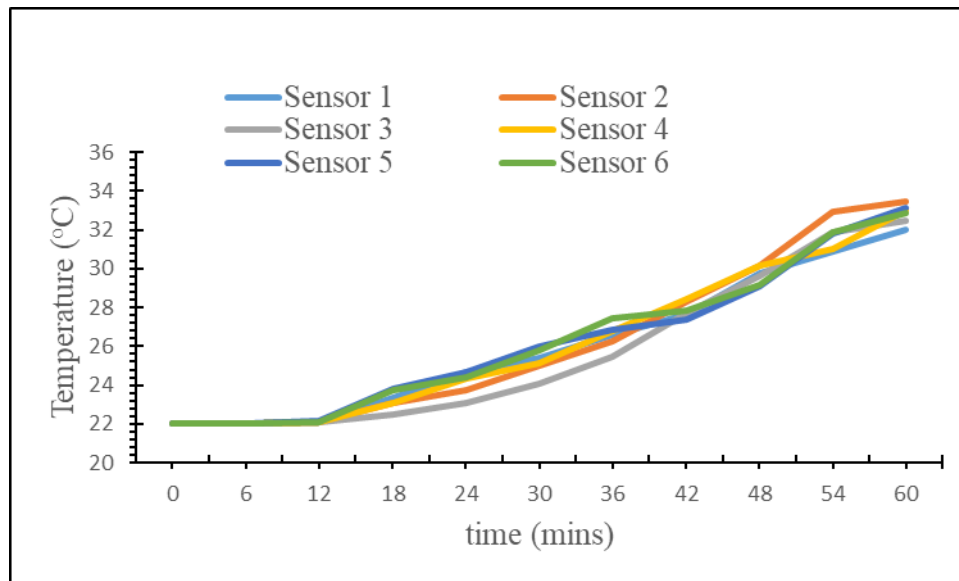


**Figure 8.** Experimental results of charging with PCM-based battery thermal management system.

In the charging experiments conducted without PCM and with PCM added, it was observed that the highest temperature values obtained at the end of the charging process of the battery pack were 40.41 °C and 33.44 °C, respectively as seen in Figure 7 and Figure 8, thanks to the temperature data coming from 6 different sensors.

## **IV. CONCLUSION**

It is known that in electric vehicles, high temperature values occurring in the battery pack during charging and discharging seriously damage the battery cells and directly affect the performance of the battery pack and therefore the performance of the vehicle. For this reason, the necessity of thermal management systems to help battery packs designed for electric vehicles operate efficiently at optimum temperature values has been emphasized by researchers and electric vehicle manufacturers in recent years. In this study, a battery pack was prepared as a prototype and the prepared battery pack was first charged and discharged without any cooling system and then using PCM at 1C current power and the cooling performance of the battery thermal management system was examined. In the literature research on the history and development of battery packs, it was observed that lithium-based batteries provide better results in criteria such as performance, cost, cycle life, capacity, weight and high power. For this reason, lithium ion batteries were used when creating the battery pack in this study. It has been observed that the phase change material-based battery thermal management system positively affects the thermal performance of the batteries. Considering the discharge experiments, it was determined that the maximum battery temperature decreased by approximately 30.65% when a PCM-based battery thermal management system was used. During the charging process, the PCM-based battery thermal management system decreased the maximum temperature by 17.25% compared to without any thermal management system. In addition, it has been observed that thanks to the battery thermal management system, battery temperatures are obtained more homogeneously and the differences between maximum and minimum temperatures are smaller than in experiments without a thermal management system.

## **V. REFERENCES**

- [1] Ağbulut, Ü., Yıldız, G., Bakır, H., Polat, F., Biçen, Y., Ergün, A., & Gürel, A. E. (2023). Current practices, potentials, challenges, future opportunities, environmental and economic assumptions for Türkiye's clean and sustainable energy policy: A comprehensive assessment. *Sustainable Energy Technologies and Assessments*, 56, 103019.
- [2] Çeçen, M., Yavuz, C., Tirmikçi, C. A., Sarıkaya, S., & Yanıkoğlu, E. (2022). Analysis and evaluation of distributed photovoltaic generation in electrical energy production and related regulations of Turkey. *Clean Technologies and Environmental Policy*, 1-16.
- [3] Karagöz, M., Polat, F., Sarıdemir, S., Yeşilyurt, M. K., & Ağbulut, Ü. (2022). An experimental assessment on dual fuel engine behavior powered by waste tire-derived pyrolysis oil–biogas blends. *Fuel Processing Technology*, 229, 107177.
- [4] Polat, F. (2022). Experimental evaluation of the impacts of diesel-nanoparticles-waste tire pyrolysis oil ternary blends on the combustion, performance, and emission characteristics of a diesel engine. *Process Safety and Environmental Protection*, 160, 847-858.
- [5] Çeçen, M., & Yavuz, C. (2022). OBPSO Kullanılarak Dağıtık Güneş Enerji Sistemlerinin Optimum Bağlantı Gücü ve Yerinin Belirlenmesi. *Düzce Üniversitesi Bilim ve Teknoloji Dergisi*, 10(2), 940-952.
- [6] Egerstrom, N., Rojas-Rueda, D., Martuzzi, M., Jalaludin, B., Nieuwenhuijsen, M., So, R., ... & Cole-Hunter, T. (2023). Health and economic benefits of meeting WHO air quality guidelines, Western Pacific Region. *Bulletin of the World Health Organization*, 101(2), 130.
- [7] Połednik, B. (2022). Emissions of Air Pollution in Industrial and Rural Region in Poland and Health Impacts. *Journal of Ecological Engineering*, 23(9).
- [8] Olabi, A. G., Maghrabie, H. M., Adhari, O. H. K., Sayed, E. T., Yousef, B. A., Salameh, T., ... & Abdelkareem, M. A. (2022). Battery thermal management systems: Recent progress and challenges. *International Journal of Thermofluids*, 15, 100171.
- [9] Shchurov, N. I., Dedov, S. I., Malozyomov, B. V., Shtang, A. A., Martyushev, N. V., Klyuev, R. V., & Andriashin, S. N. (2021). Degradation of lithium-ion batteries in an electric transport complex. *Energies*, 14(23), 8072.
- [10] Çetin, İ., Sezici, E., Karabulut, M., Avci, E., & Polat, F. (2023). A comprehensive review of battery thermal management systems for electric vehicles. *Proceedings of the Institution of Mechanical Engineers, Part E: Journal of Process Mechanical Engineering*, 237(3), 989-1004.
- [11] Chen, X., Chu, A., Li, D., Yuan, Y., Fan, X., & Deng, Y. (2021). Development of the cycling life model of Ni-MH power batteries for hybrid electric vehicles based on real-world operating conditions. *Journal of Energy Storage*, 34, 101999.
- [12] Sezici, E., Cetin, I., & Polat, F. (2022). Design and Experimental Investigation of Air-Cooled Battery Thermal Management System for Electric Vehicles. *Journal of Engineering Research and Applied Science*, 11(2), 2062-2077.
- [13] M Lin, J., Liu, X., Li, S., Zhang, C., & Yang, S. (2021). A review on recent progress, challenges and perspective of battery thermal management system. *International Journal of Heat and Mass Transfer*, 167, 120834.

- [14] Luo, J., Zou, D., Wang, Y., Wang, S., & Huang, L. (2022). Battery thermal management systems (BTMs) based on phase change material (PCM): A comprehensive review. *Chemical Engineering Journal*, 430, 132741.
- [15] Hou, J., Meng, X., & Dewancker, B. J. (2021). A numerical study on the effect of phase-change material (PCM) parameters on the thermal performance of lightweight building walls. *Case Studies in Construction Materials*, 15, e00758.
- [16] Faraj, K., Khaled, M., Faraj, J., Hachem, F., & Castelain, C. (2020). Phase change material thermal energy storage systems for cooling applications in buildings: A review. *Renewable and Sustainable Energy Reviews*, 119, 109579.
- [17] J. Luo, D. Zou, Y. Wang, S. Wang, and L. Huang, "Battery thermal management systems (BTMs) based on phase change material (PCM): A comprehensive review," *Chemical Engineering Journal*, vol. 430, p. 132741, Feb. 2022, doi: 10.1016/j.cej.2021.132741.
- [18] C. Roe et al., "Immersion cooling for lithium-ion batteries – A review," *J Power Sources*, vol. 525, p. 231094, Mar. 2022, doi: 10.1016/j.jpowsour.2022.231094.
- [19] J. Lin, X. Liu, S. Li, C. Zhang, and S. Yang, "A review on recent progress, challenges and perspective of battery thermal management system," *Int J Heat Mass Transf*, vol. 167, p. 120834, Mar. 2021, doi: 10.1016/j.ijheatmasstransfer.2020.120834.
- [20] W. Zichen and D. Changqing, "A comprehensive review on thermal management systems for power lithium-ion batteries," *Renewable and Sustainable Energy Reviews*, vol. 139, p. 110685, Apr. 2021, doi: 10.1016/j.rser.2020.110685.
- [21] N. Javani, I. Dincer, G. F. Naterer, and B. S. Yilbas, "Heat transfer and thermal management with PCMs in a Li-ion battery cell for electric vehicles," *Int J Heat Mass Transf*, vol. 72, pp. 690–703, May 2014, doi: 10.1016/j.ijheatmasstransfer.2013.12.076.
- [22] F. Bai, M. Chen, W. Song, Y. Li, Z. Feng, and Y. Li, "Thermal performance of pouch Lithium-ion battery module cooled by phase change materials," *Energy Procedia*, vol. 158, pp. 3682–3689, Feb. 2019, doi: 10.1016/j.egypro.2019.01.891.
- [23] A. Verma, S. Shashidhara, and D. Rakshit, "A comparative study on battery thermal management using phase change material (PCM)," *Thermal Science and Engineering Progress*, vol. 11, pp. 74–83, Jun. 2019, doi: 10.1016/j.tsep.2019.03.003.



# Düzce University Journal of Science & Technology

Research Article

## Comparison of Payback Periods of Solar Power Plant in Türkiye and Europe

 Mohannad GYAM <sup>a</sup>,  İlhan CEYLAN <sup>a</sup>,  Ali Etem GÜREL <sup>b,c</sup>,  Gökhan YILDIZ <sup>d,\*</sup>

<sup>a</sup> Department of Energy Systems Engineering, Technology Faculty, Karabük University, Karabük/TÜRKİYE

<sup>b</sup> Department of Electricity and Energy, Düzce Vocational School, Düzce University, Düzce, TÜRKİYE

<sup>c</sup> Department of Mechanical Engineering, Engineering Faculty, Düzce University, Düzce, TÜRKİYE

<sup>d</sup> Department of Electronics and Automation, Düzce Vocational School, Düzce University, Düzce, TÜRKİYE

\* Corresponding author's e-mail address: gokhanyildiz@duzce.edu.tr

DOI: 10.29130/dubited.1389956

### ABSTRACT

The importance of energy in the world is increasing day by day. Most of the countries' energy needs are met by fossil fuels. Due to the depletion of fossil fuels, their increasing prices and the damage they cause to the environment, researchers have turned to alternative energy sources. The demand for renewable energy sources as alternative energy has increased significantly in recent years. Solar energy is one of the most popular and widely used energy sources among renewable energy sources all over the world. For this reason, efforts are being made to increase the use of solar energy in Türkiye and European countries. Although the amount of solar radiation in Türkiye is high, it has not reached the expected levels. In this study, the payback periods (PBP) of a 1 MW solar power plant (SPP) connected to the grid between Türkiye and European countries were compared. It is assumed that the compared countries use monocrystalline solar panels with an efficiency of 22.6% at their specific solar radiation values. Additionally, due to the impact of the Russia-Ukraine war on energy prices, the PBP of the SPP was determined based on two scenarios. According to the results, in the first scenario, the highest PBP is in Karaman with 2.75 years, followed by Türkiye with 3.17 years. PBPs in Spain, France and Germany are calculated as 3.6, 5.6 and 5.7 years, respectively. In second scenario (after the Russia-Ukraine war), the highest PBPs were determined as Germany with 2.22 years and France with 3.27 years. PBPs in Spain, Karaman and Türkiye were determined as 2.41, 2.75 and 3.17 years, respectively.

**Keywords:** Solar energy, Photovoltaic, Payback period, Solar energy potential

## Güneş Enerjisi Santrallerinin Türkiye ve Avrupa'daki Geri Ödeme Sürelerinin Karşılaştırması

### ÖZET

Dünya'da enerjinin önemi her geçen gün artmaktadır. Ülkelerin büyük bir bölümü ihtiyaç duydukları enerji gereksinimini fosil yakıtlar tarafından karşılanmaktadır. Fosil yakıtların tükenmesi, artan

fiyatı ve çevreye vermiş olduğu zararlardan dolayı araştırmacılar alternatif enerji kaynaklarına yönelmişlerdir. Yenilenebilir enerji kaynaklarına son yıllarda alternatif enerji olarak talep büyük oranda artmıştır. Güneş enerjisi, yenilenebilir enerji kaynakları arasında en popüler ve tüm dünyada yaygın olarak kullanılan enerji kaynaklarından birisidir. Bu sebeple, Türkiye ve Avrupa ülkelerinde güneş enerjisi kullanımı artırılmaya çalışılmaktadır. Türkiye güneş ışınım miktarı yüksek olmasına rağmen beklenen seviyelere ulaşamamıştır. Bu çalışmada, Türkiye ile Avrupa ülkeleri arasındaki şebekeye bağlı 1 MW'lık bir güneş enerjisi santralının geri ödeme süreleri karşılaştırılmıştır. Karşılaştırılan ülkeler, kendilerine özgü solar radyasyon değerlerinde %22,6 verimliliğe sahip bir monokristal güneş panellerinin kullanıldığı varsayılmıştır. Ayrıca, Rusya-Ukrayna savaşının enerji fiyatlarına etkisi nedeniyle güneş enerjisi santralının geri ödeme süresi iki senaryo üzerinden değerlendirilmiştir. Elde edilen sonuçlara göre, birinci senaryoda en yüksek geri ödeme süresi 2,75 yıl ile Karaman'da, ardından 3,17 yıl ile Türkiye gelmektedir. İspanya, Fransa ve Almanya'daki geri ödeme süreleri sırasıyla 3,6, 5,6 ve 5,7 yıl olarak hesaplanmıştır. İkinci senaryoda ise (Rusya-Ukrayna savaşı sonrası), en yüksek geri ödeme süreleri 2,22 yıl ile Almanya ve 3,27 yıl ile Fransa olarak belirlenmiştir. İspanya, Karaman ve Türkiye'de geri ödeme süreleri sırasıyla 2,41, 2,75 ve 3,17 yıl olarak tespit edilmiştir.

**Anahtar Kelimeler:** Güneş enerjisi, Fotovoltaik, Geri ödeme süresi, Güneş enerjisi potansiyeli

## I. INTRODUCTION

The improvement of economic and technological conditions in the world and the increasing population have led to a raise in global energy demand. This energy demand is met by fossil fuels known as coal, oil and gas [1]. These resources are utilized to produce the energy needed in many industrial processes. One of the general problems of fossil fuels is that they release carbon dioxide (CO<sub>2</sub>) into the environment when burned. Since CO<sub>2</sub> is a greenhouse gas, it is one of the factors that increase global warming. Among fossil fuels, coal has the highest CO<sub>2</sub> producer and natural gas has the lowest CO<sub>2</sub> production potential [2]. Interest in fossil fuels is gradually decreasing due to the risk of depletion, the increase in their prices and the increase in greenhouse gases (GHGs) in the ozone layer.

With the decrease in interest in fossil fuels, renewable energy sources (RES) have begun to be used as alternative energy sources [3]. These resources include solar energy, wind, geothermal, hydroelectricity and bioenergy. RES are defined as energy sources that have very little negative impact on the environment. Driven by the need for alternative energy sources and the decrease of carbon footprint, which is the goal of many countries that comply with the UNFCCC global agreements, renewable energy consumption has been increasing steadily since 1950. According to the REN21 2020 report, it was determined that the share of renewable energy in 2018 was around 11% and fossil fuels was 79.9%. Figure 1 shows the distribution of energy resources in 2018 [4].

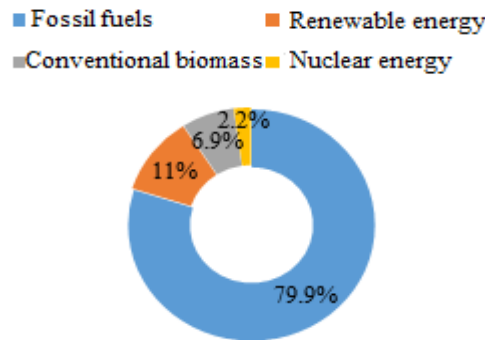


**Figure 1.** Estimated Renewable Share of Total Final Energy [4]

According to the REN21 2020 report, more than 200 GW of new renewable energy generation capacity was installed in 2019, bringing the global total to 2588 GW by the end of the year (Figure 2). Approximately 115 GW of solar PV was added worldwide in 2019. During 2019, 57% of renewable energy capacity additions were solar PV power, followed by wind power (about 60 GW for 30%) and hydropower (about 16 GW for 8%). The remaining 5% of the additions come from bio-energy, geothermal energy and concentrated solar thermal energy (CSE) [4].

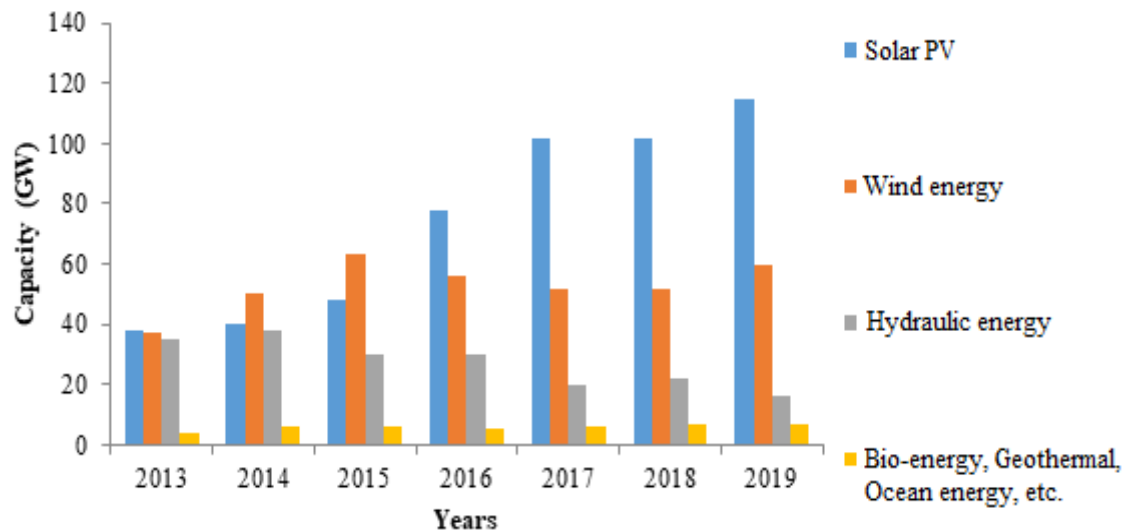


*Figure 2. Annual additions of renewable power capacity, 2013-2019 [4]*

All the advantages of solar energy have led countries, especially energy importers, to turn to solar energy to reduce the import bill in their budgets. For example, in a country like Türkiye, according to the report of TÜRKİYE PETROLLERİ A.O., the ratio of domestic crude oil production to total oil supply was 6.3% in 2019, while this rate became 7.1% in 2020. In other words, Türkiye's dependence on oil imports was 92.9% in 2020. Natural gas consumption amounted to 44.9 billion cubic meters. Net imports of cubic meters in 2020 were approximately 44.4 billion cubic meters [5]. According to Central Bank of the Republic of Türkiye (CBRT) data, Türkiye imported 665 billion 196 million 652 thousand dollars of oil, gas and coal in the 20 years between 2000 and 2019 [6].

The circumstance is no different in the European Union, according to a report in which the European Commission warns about the costs incurred due to the European Union (EU)'s excessive dependence on fossil fuel imports. The Union's energy imports amounted to 331 billion euros in 2018. In 2017 this value was estimated at 266 billion euros, a 26% increase on 2016 (but 34% less than the 400 billion euro peak in 2013). Increasing oil prices accounted for 68% of the total import bill in 2017 with oil, 28% with natural gas and 4% with hard coal [7]. These high figures prompted the EU and Türkiye to turn to solar energy to reduce high energy costs.

According to the report of the International Renewable Energy Agency (IRENA), the EU ranks second in the world after China, and the total capacity of solar photovoltaic energy in the EU reached 152917 MW in 2020. The ratio of solar photovoltaic energy to total electricity consumption in the EU was 6%. Photovoltaic solar energy capacity in Türkiye for 2020 reached 6,668 MW, accounting for 5.9% of the total electricity consumption in Türkiye, where Türkiye ranks sixteenth in the world in terms of solar photovoltaic energy capacity. Table 1 below shows the photovoltaic solar energy capacity and its share in total electricity consumption in the EU and Türkiye [8].

Installing a solar photovoltaic (PV) array is both an environmental and financial decision. Because solar installation is capital intensive, financial arguments often take precedence over environmental factors. Simple Payback Period (SPBP) is an ordinarily stated measure in years of the time between the initial capital outlay on a solar installation and the return on the initial investment. Smets et al.



defined the PBP in solar power plants (SPP), where the PBP is defined in finance as the time required to restore the cost of an investment [9]. The energy PBP in regions with high solar irradiance is significantly shorter than in regions with low irradiance. No matter which PV technology is chosen, the energy PBP is always well below the expected system life, which is usually between 25 and 30 years. Therefore, the energy invested in the PV system is repaid several times throughout the life cycle of the PV system.

**Table 1.** Photovoltaic solar energy capacity and its share in total electricity consumption in the EU and Türkiye [8]

Country or Region	2018		2019		2020		Total consumption share (2020)
	New (MW)	Total (MW)	New (MW)	Total (MW)	New (MW)	Total (MW)	
EU	8147	117530	16599	134129	18788	152917	6.00%
Germany	3000	45158	3889	49047	4736	53783	9.70%
Italy	426	20114	757	20871	729	21600	8.30%
Spain	41	7068	4209	11277	2812	14089	9.00%
UK	313	13073	273	13346	217	13563	4.00%
France	1081	9691	1113	10804	929	11733	2,8%
Netherlands	1697	4608	2569	7177	3036	10213	8.90%
Türkiye	1642	5064	932	5996	672	6668	5.90%

While solar cells were less efficient, it was a correct approach to question the energy return of solar cells. Because the panels were manufactured utilizing electricity obtained from coal, natural gas or nuclear energy, which made solar cells less efficient. Nowadays, solar panels are more efficient and generate more electricity. More efficient production means energy PBPs are reduced to just a few years. In one of the studies conducted in 2018, “Energy payback estimates for rooftop PV systems are 4, 3, 2 and 1 years: 4 years for systems using existing polycrystalline-silicon PV modules, 3 years for existing thin-film modules, 2 years for expected polycrystalline modules and 1 year for expected thin film modules” [10]. With developing technology, solar cells can be made from more efficient materials and production costs can further decrease. With this increased efficiency, PBP will shorten. While the prices of 10 to 100 kWp PV systems in Germany were approximately 14000 EUR/kWp in 1990, at the end of 2020 the price of the same system decreased by 7.4% [11].

SPBP is often evaluated prior to the adoption of solar PV in a residence or business. Although it better reports the value of solar PV electricity from a sustainability perspective, Energy Payback period (EPBP) is rarely utilized to measure the value of an installation [12].

Many studies have been presented before about the PBP in SPPs. Perhaps one of the most important studies conducted recently in Türkiye is a study conducted in 2019 by a group of researchers at Adiyaman University. The results of the study of three identical SPPs in the Adiyaman province of Türkiye, with an installed power of 1025 MW and an installation cost of 1 million USD per SPP, showed that the average annual electricity production was 1696665 kWh. Internal electricity consumption was 10770 kWh. Thus, net electricity production amounted to 1685895 kWh. The average PBP for these SPPs was 5.5 years [13].

In another study conducted by a group of researchers in 2019, the results showed that the PBP of the SPP installed on an area of 20000 m<sup>2</sup> in Aksaray province in Türkiye was 4.5 years, and the profit of the SPP was 501825 USD/year [14].

In another study conducted on the construction of a SPP at Konya Meram Medical Faculty Hospital, the PBP of the SPP was evaluated based on two scenarios in which a 900 kW photovoltaic system was designed. In the first scenario, the circumstance in which there was no support for GHG emission reduction was evaluated and the PBP of the system was found to be 5.1 years. In second scenario, the GHG emission reduction subsidy was accepted as 15 USD per ton of CO<sub>2</sub> and the PBP of the system was determined as 4.8 years [15].

Otovo, a solar platform in Norway, found in a 2019 study that solar PBPs in many Western Europeans have fallen below 10 years and even reached six in some parts of Spain and France. Falling PV panel prices have made solar energy more attractive to consumers in Europe. Otovo has set the system cost at 1800 EUR (2050 USD) per kWp. The study showed that the only country where PBPs fell below six years was France. While this applies to the south and southeast, consumers nationwide can expect PBP between 6 and 7.9 years. While PBPs decrease to 6-6.9 years in central and southern Spain, they can reach up to 10-10.9 years in the north. In Germany, PBP was calculated between 7 and 7.9 years [16].

Based on the literature reviewed, a study comparing the PBP of SPPs in Türkiye and Europe was found. By comparing Türkiye and European countries for the PBPs of SPPs, this study will contribute to knowing the reasons for the delay in the growth of the solar energy sector in Türkiye, even though Türkiye is located in the region with high solar radiation compared to Europe. Additionally, it will contribute to knowing the most important obstacles to the solar energy sector in Türkiye and the reasons for investors' reluctance to invest in SPPs. In this study, it is focused to investigate the PBP of SPPs in Europe and compare it with Türkiye. In addition, it is aimed to evaluate the long-term benefits and costs of electricity production from PV systems and to make recommendations so that this source will provide maximum benefit to the country's economy.

## **II. SOLAR ENERGY POTENTIAL in TÜRKİYE and EUROPE**

### **A. SOLAR ENERGY POTENTIAL IN TÜRKİYE**

Türkiye is located in the Northern Hemisphere, between 36-42 degrees north latitude and 26-45 degrees east longitude. This circumstance has caused the country to be closer to the Equator than to the pole and to be in the temperate zone. Türkiye has a significant solar energy potential due to its geographical location.

According to the Türkiye Solar Energy Potential Atlas (GEPA), the average annual total sunshine duration is 2741 hours and the average annual total radiation value is calculated as 1527.46 kWh/m<sup>2</sup> [20]. Figure 3 shows a map of Türkiye's solar radiation. In Figure 3, the southern regions that benefit from the most solar radiation are shown in light red and dark red, and the northern regions that benefit from the least amount of solar radiation are shown in light blue and dark blue.



**Figure 3.** Türkiye's solar energy potential atlas [19]

Figure 4 shows daily global radiation values for Türkiye on a monthly basis. The global radiation value reaches its highest value in June with 6.57 kWh/m<sup>2</sup>-day, and its lowest value in December with 1.59 kWh/m<sup>2</sup>-day. The average daily solar radiation for Türkiye on a monthly basis is 4.18 kWh/m<sup>2</sup>-day.

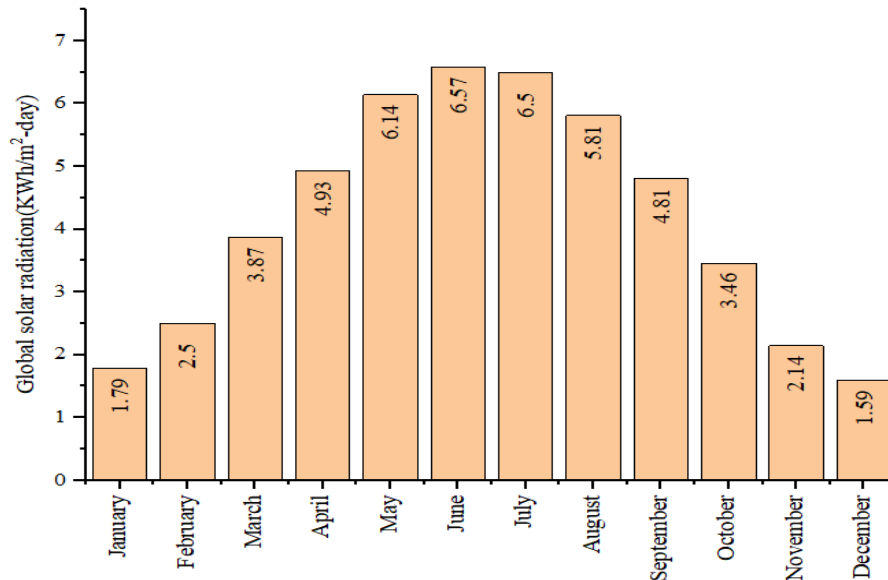


**Figure 4.** Türkiye's global radiation values [19]

Figure 5 shows the sunshine duration on a monthly basis in Türkiye. The highest sunshine duration is in July with 11.31 hours, and the lowest sunshine duration is in December with 3.75 hours. The average daily sunshine duration in Türkiye on a monthly basis is 7.49 hours-day. Considering all these data, it is seen that Türkiye has high solar energy potential.

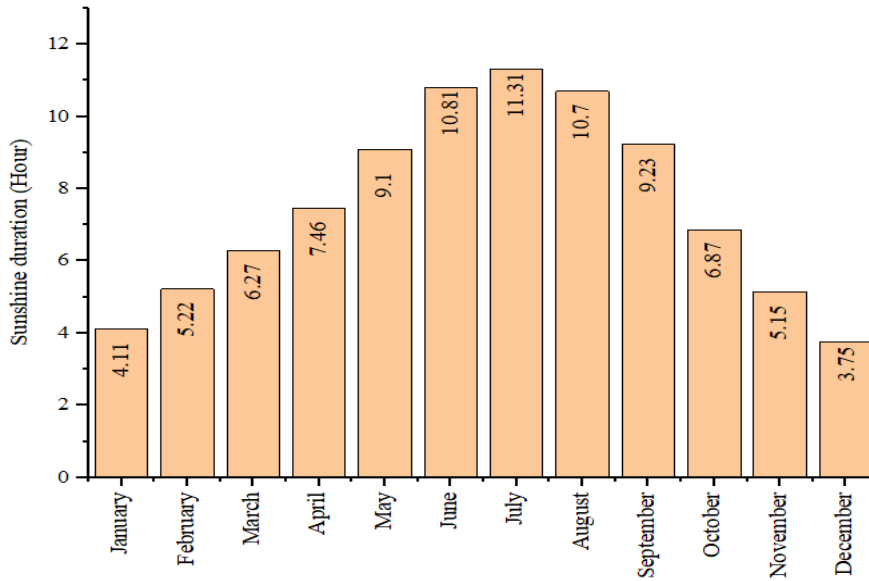


Figure 5. Türkiye's sunshine duration [19]

After examining the solar energy potential map of Türkiye, it was determined that Karaman has the highest average annual total radiation value among Turkish cities. Karaman's average annual total solar radiation is 1661 kWh/m<sup>2</sup> and the average annual total sunshine duration is 3009 hours. Figure 6 and Figure 7 show Karaman's global radiation values and sunshine durations.

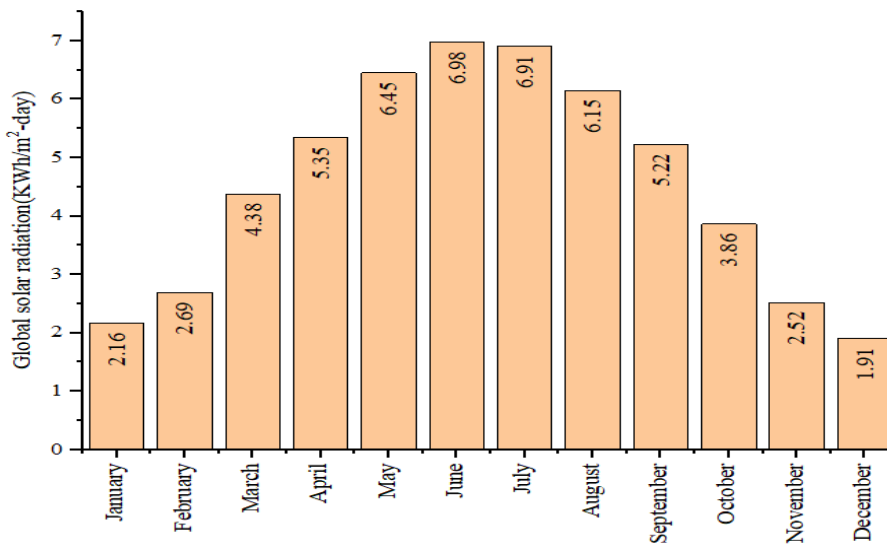


Figure 6. Karaman's global radiation values [19]

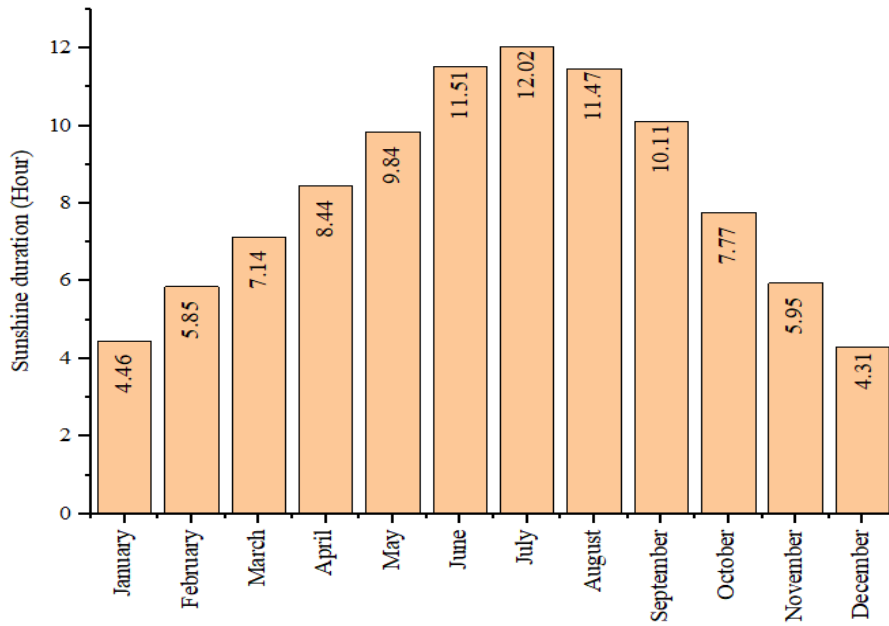


Figure 7. Karaman's sunshine durations [19]

However, among Turkish cities, Hakkari city has the highest sunshine durations. Hakkari's average annual total sunshine duration is 3512 hours and its average annual total solar radiation is 1612 kWh/m<sup>2</sup>. Figure 8 and Figure 9 show Hakkari's global radiation values and sunshine durations.

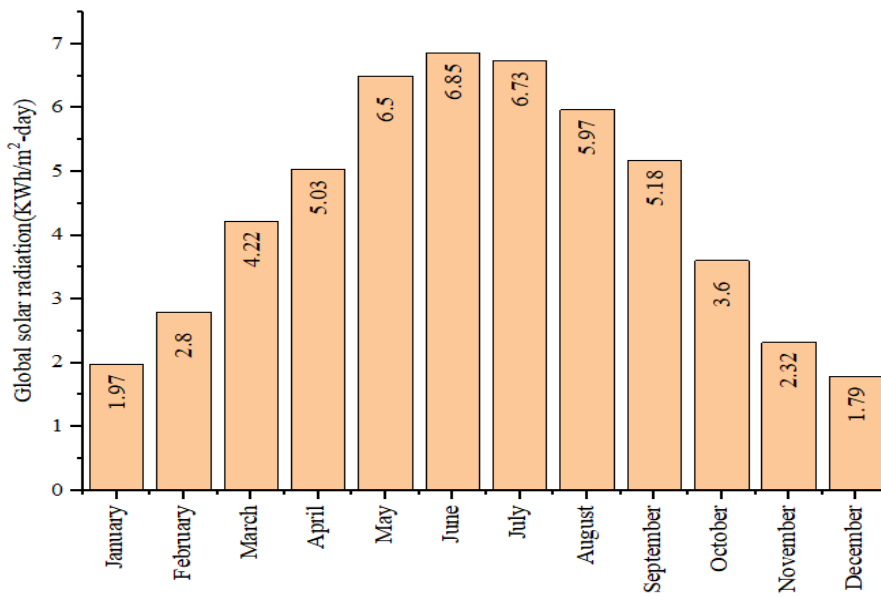


Figure 8. Hakkari's global radiation values [19]

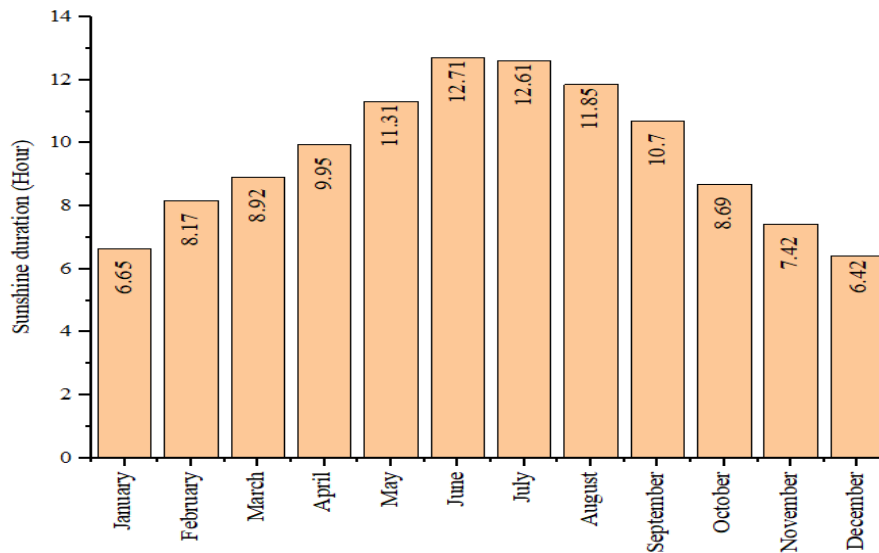


Figure 9. Hakkari's sunshine durations [19]

Due to the higher solar energy potential of cities in the south of Türkiye compared to northern cities, cities in the south are expected to have lower PBP for SPPs.

## B. SOLAR ENERGY POTENTIAL IN EUROPE

Global radiation values vary depending on geographical location and are highest in regions close to the equator. Therefore, annual average global radiation values vary between European regions, with southern regions having much better values than northern regions. The average annual total radiation value in Central Europe is approximately 1100 kWh/m<sup>2</sup> [18].

Figure 10 shows the Solar Energy Potential map of Europe. The average annual total sunshine duration in Europe during the reference period (1983-2012) is 2335 hours [21].

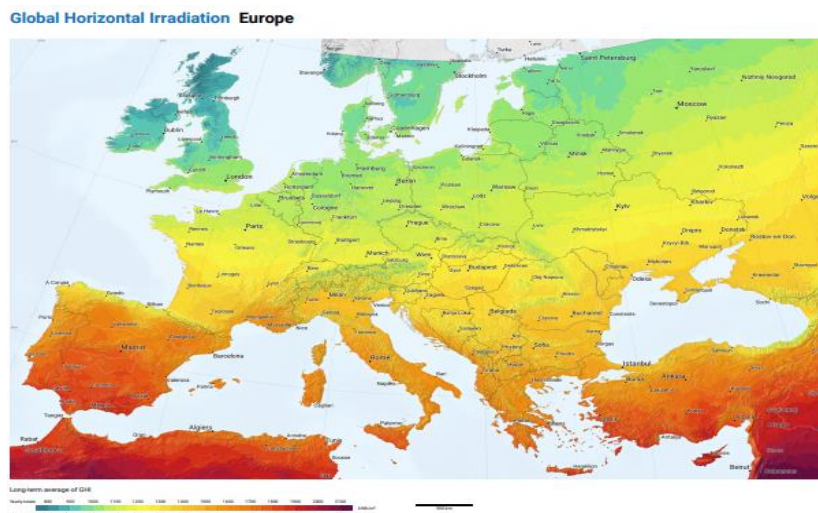


Figure 10. Solar energy potential map of Europe [22]

### B. 1. Solar Energy Potential in Germany

Germany is located in the middle of Europe. Although Germany ranks first in Europe in terms of installed solar PV capacity, Germany's solar energy potential is considered average. Germany's average annual total solar radiation is 1086 kWh/m<sup>2</sup>. Figure 11 shows a map of Germany's solar

radiation for the period 1991-2020. Figure 11 shows that the average annual total solar radiation for Germany for the period 1991-2020 varies between 975 and 1259 kWh/m<sup>2</sup> [23]. Since the southern regions are closer to the equator, the average annual total radiation value increases from north to south.

Figure 12 shows the average monthly global radiation values for Germany. The global radiation value reaches its highest value in June with 165 kWh/m<sup>2</sup>-month, and its lowest solar radiation in December with 17 kWh/m<sup>2</sup>-month. Germany's average monthly radiation value is 90.5 kWh/m<sup>2</sup>-month [23].

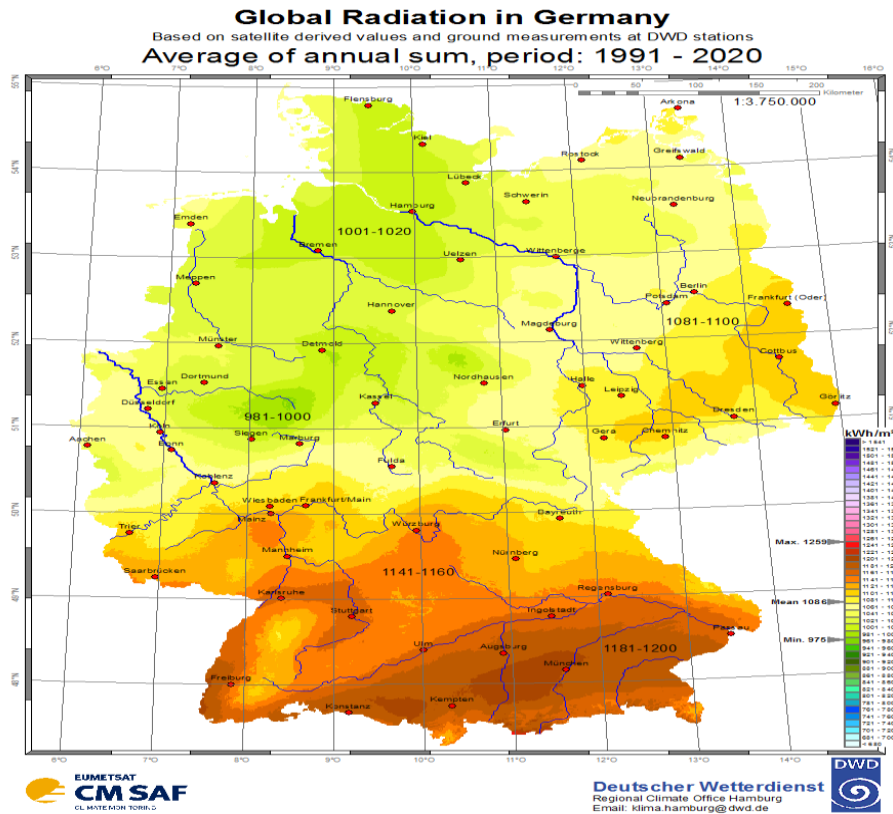


Figure 11. Solar energy potential atlas of Germany [23]

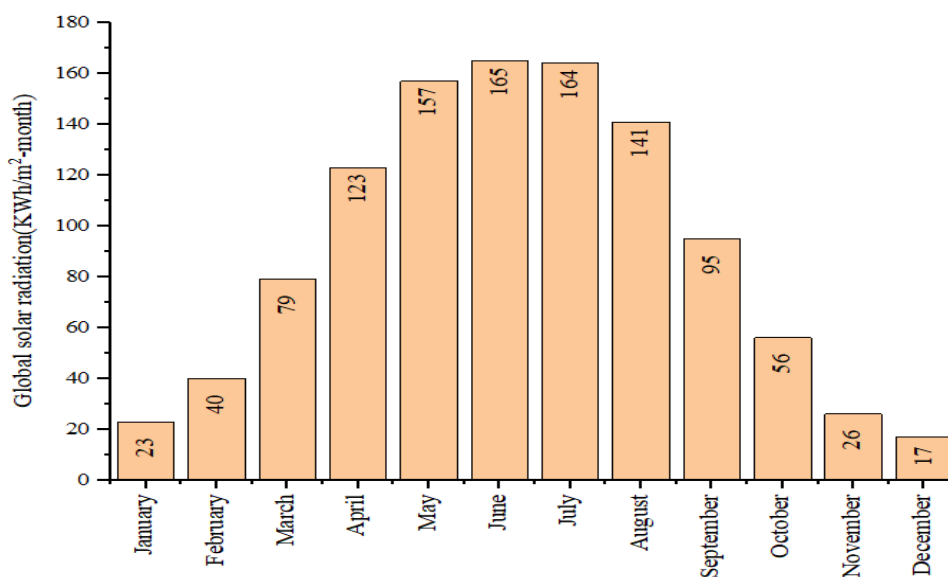


Figure 12. Germany's global solar radiation values [23]

Germany’s total annual sunshine hours for 2021 are 1631 hours. Figure 13 shows the sunshine duration on a monthly basis in Germany. The highest sunshine duration is in June with 8.57 hours, and the lowest sunshine duration is in January with 0.97 hours. For 2021, the daily sunshine duration in Germany on a monthly basis is 4.47 hours-day [24].

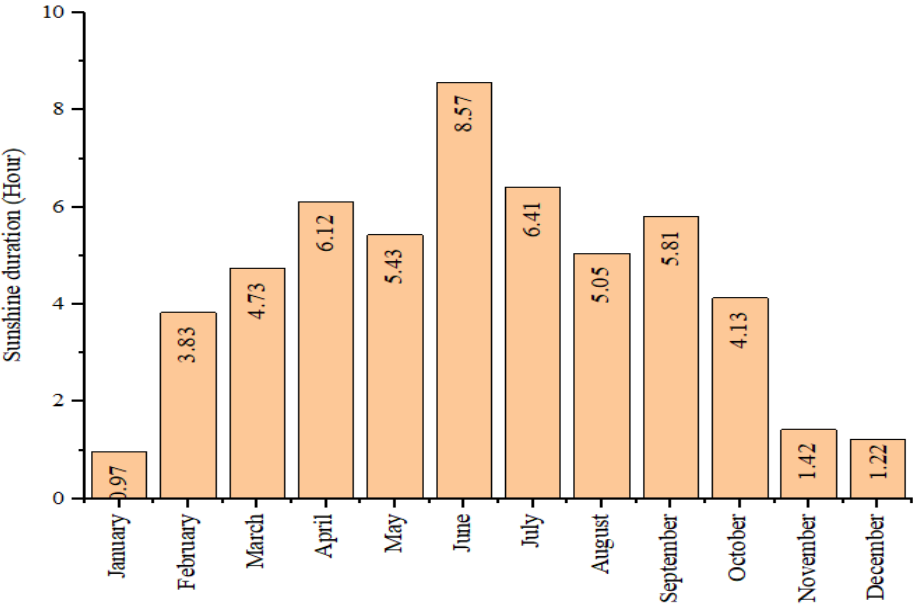


Figure 13. Germany’s sunshine durations

**B. 2. Solar Energy Potential in Spain**

Spain is located in southwestern Europe. Spain’s average annual total solar radiation is 1600 kWh/m<sup>2</sup>. Average solar radiation in the southern regions of Spain varies from 1.5 kWh/m<sup>2</sup> in winter to 7 kWh/m<sup>2</sup> in summer [25]. Figure 14 shows a map of Spain’s solar radiation for the period 2001-2011.

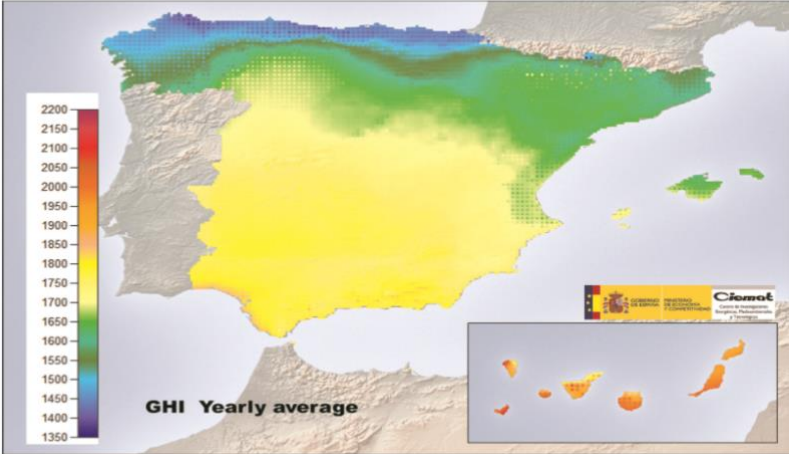


Figure 14. Solar radiation map of Spain for the period 2001-2011 [26]

Among the Spanish cities, Huelva has the highest sunshine hours. Huelva’s average annual total sunshine duration is 2998 hours [27].

**B. 3. Solar Energy Potential in the UK**

The United Kingdom is located in Western Europe. The UK’s average annual total solar radiation is 949 kWh/m<sup>2</sup>, approximately 2.5–3.1 kWh/m<sup>2</sup>-day [28]. Although solar potential in the UK is poor, it



ranks fourth in Europe in terms of installed PV capacity. Among the regions of the United Kingdom, the "Eastbourne" region has the highest sunshine hours. Eastbourne's average annual total sunshine duration is 1888 hours [27].

**B. 4. Solar Energy Potential in France**

France is located in Western Europe. The average annual total radiation value of France is 1274.1 kWh/m<sup>2</sup>. Figure 15 shows the average monthly global solar radiations for France. The global radiation solar radiation reaches its highest value in July with 183.9 kWh/m<sup>2</sup>-month, and its lowest solar radiation in December with 24.9 kWh/m<sup>2</sup>-month. France's average monthly radiation value is 90.5 kWh/m<sup>2</sup>-month [29].

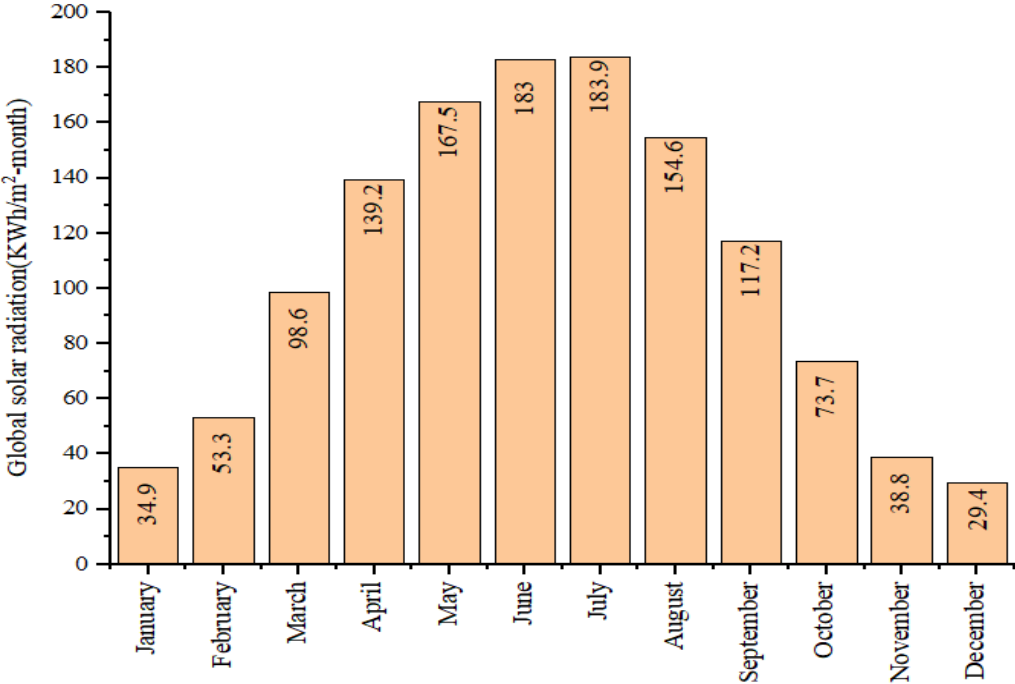


*Figure 15. Global solar radiation values of France*

The highest periods of sunshine occur in the Marseille region in southeastern France. Marseille's average annual total sunshine duration is 2858 hours [27].

**B. 5. Solar Energy Potential in the Netherlands**

The Netherlands is located in the northwest of Europe. The average annual total solar radiation of the Netherlands is 1,000 kWh/m<sup>2</sup> as shown in Figure 16 [9]. The average annual total sunshine duration is between 1400-1700 hours [30].



**Figure 16.** Distribution of solar radiation in the Netherlands [30]

Despite the weak potential of solar energy in the Netherlands, it ranks sixth in terms of installed photovoltaic energy capacity.

### B. 6. Solar Energy Potential in Italy

Italy is located in southern Europe. Italy ranks second in Europe in terms of installed photovoltaic capacity. Italy's average annual total radiation value is 1533 kWh/m<sup>2</sup>. Figure 17 shows the radiation between 2014 and 2017, ranging from a minimum of 990 kWh/m<sup>2</sup> in the northern alpine region to a maximum of 1900 kWh/m<sup>2</sup> in the south [31].

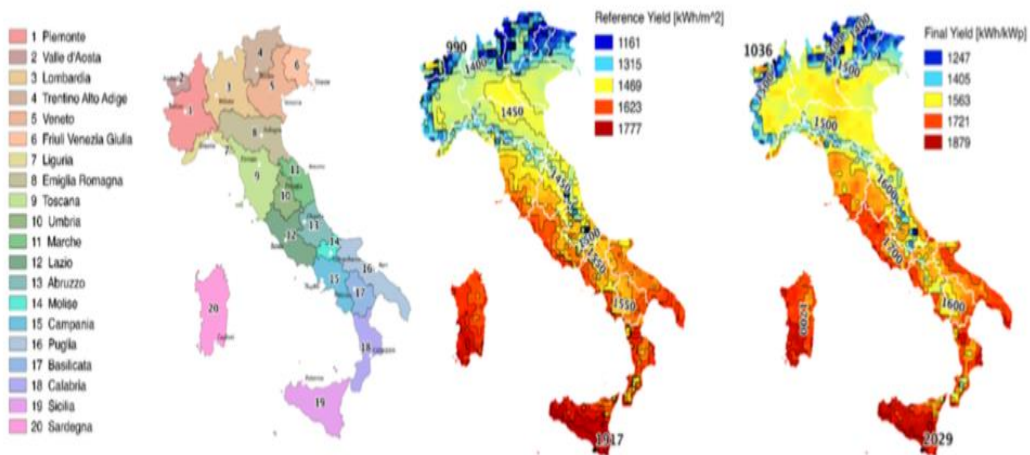


**Figure 17.** Average values of satellite-derived radiation and power estimation between 2014 and 2017 [31]

Among the regions of Italy, the "Ustica Island" region has the highest sunbathing hours. Ustica Island's average annual total sunshine duration is 2660 hours [27].

### **III. PAYBACK PERIOD FOR TÜRKİYE’S 1 MW PHOTOVOLTAIC SOLAR ENERGY POWER PLANT (SPP)**

Türkiye is located in Southeastern Europe and Southwest Asia. Türkiye’s surface area is 783562 km<sup>2</sup> and its population is approximately 85.04 million. The average temperature in Türkiye during the period 1981-2010 was 13.5 °C [32]. Türkiye’s average annual total radiation value is 1527.46 kWh/m<sup>2</sup>.

#### **A. MAKING ENERGY CALCULATIONS TO BE OBTAINED FROM SPP**

In this section, the energy obtained from 1 MW photovoltaic power plant connected to a ground-mounted grid in Türkiye is calculated. It will be assumed that solar panels are used. The solar panels are monocrystalline PERC panels. Table 2 shows the most significant electrical and mechanical data of panels.

*Table 2. The most significant electrical and mechanical data of solar panels [33].*

STC	LXR-400-72M
Nominal Maximum	400 W
Open CIRCUIT Voltage ( $V_{oc}$ )	47.95 V
Module Efficiency	22.60%
Cell Type	Mono-crystalline 157x157 mm
Cell Arrangement	72 (6x12)
Dimensions	1960 x 992 x 40 mm

It is possible to calculate the energy to be obtained from the solar power system as follows:

$$E = A \times R \times H \times PR \tag{1}$$

Here:

E: Energy (kWh)

A: Total Area of Panel (m<sup>2</sup>)

R: Solar Panel Efficiency (%)

H: Average Solar Radiation in Curved Panels (kWh/m<sup>2</sup>)

PR: Performance Rate

The number of solar panels required for a LEXRON-400-72M PERC type 1MW power plant is 2500 (2500 x 400W = 1MW). The area of one panel (1.960 x 0.992) is 1.944 m<sup>2</sup>, thus the total area of solar panels (2500 x 1.944 m<sup>2</sup>) is 4860 m<sup>2</sup>. The efficiency of the solar panel is 22.6% as shown in Table 2. The performance ratio will be calculated as 0.83. The average solar radiation of Karaman province are shown in Figure 6. Türkiye’s average solar radiation values are shown in Figure 4.

Based on Figure 4 and using Equation 1, the results showed that the average amount of electrical energy obtained from the Turkish system in a year is 1392.49 MWh. The average amount of electrical energy to be obtained from the Turkish power plant on a monthly basis is shown in Figure 18.

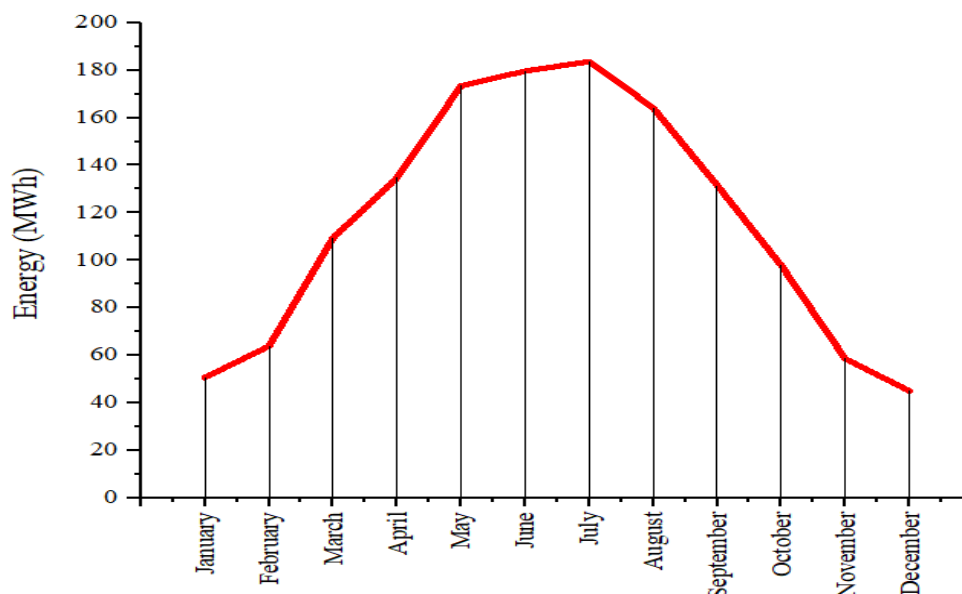


**Figure 18.** Average amounts of electrical energy to be obtained from Türkiye's 1 MW Solar System

According to EPIAŞ Transparency Platform until 17.10.2022, the arithmetic average of market clearing prices was 0.13635 USD/kWh [34]. Therefore, Annual Profit (1392491.02 kWh x 0.13635 USD/kWh) will be calculated as 189866.26 USD.

## B. INITIAL INVESTMENT COST OF PHOTOVOLTAIC SYSTEM

The equipment and prices required for 1 MW SPP installation were predetermined in one of the studies conducted in Van province of Türkiye in 2021, as shown in Table 3. The equipment and fittings listed in Table 3 consist of elements that should generally be included in all 1 MW SPP investments.

**Table 3.** Equipment and prices required for 1 MW SPP installation [35].

Equipment	Explanation	Amount (USD)
Photovoltaic Solar Panel (Monocrystalline silicon)	2,500 units 400 Watt, 47.95 V LEXRON brand, Monocrystalline 72 cells	300000
Inverter	200 units, 5 kW, GoodWe brand	45000
Control and Monitoring System (SCADA)	4 pieces	
Fixed Mounting Structure	1 set	
DC Wiring	21000 m	
AC Wiring	3750 m	
Collection Board	1 set	
Wire Fence and Barbed Wire	750 m	
Landscaping and Earthworks	1500 m <sup>3</sup>	
Lightning Rod and Grounding Systems (Active lightning rod head, 6 m pole, 2×50 mm <sup>2</sup> copper down conductor, 3 m pipe)	1 set	200000

Video Security and Camera Systems (8 cameras (Outdoor, analog HD, NVR recorder (4 TB HDD), 24" screen, cabling)	1 set	
Cable Tray Systems	800 kg	
Solar cable (red and blue)	1x6 mm <sup>2</sup> PVII-F solar cable	6000 m
5x16 mm <sup>2</sup> NYN		400 m
3x35 / 16 mm <sup>2</sup> XLPE cable (36 KV)		3000 m
35 and 16 XLPE cable header		426 and 142 units
MV+LV external panel		70 pieces
Modular cubicle with 100x10 mm <sup>2</sup> copper busbar		1 piece
1250 A current and voltage measurement modular switchgear with switch disconnecter		1 piece
Transformer protection modular switchgear with 1250 breakers		1 piece
Input-output modular cubicle with 1250 A breaker		1 piece
Concrete Kiosk		5 m, with roof
10 kVA dry type transformer		71 pieces
4x63 A TMS+KAKR (300 mA)		104 pieces
3x63 A NH fuse and carrier		74 pieces
0.28 kV, 100 kA B+C surge arrester (AG)		71 pieces
MV surge arrester		1 team
Grounding stake (65x65x7) 1.5 m long		225 pieces
Galvanized strip conductor (30x3.5 mm)		600 m
1x16 mm <sup>2</sup> NYAF ground wire		500 m
Photovoltaic panel construction		1 system
Field lighting equipment		1 team
Total		545000

Due to the difficulty of accessing Türkiye's land prices, land prices will not be included in this study. Other initial investment cost parameters are shown in Table 4.

**Table 4.** Other initial investment cost parameters [35].

Cost Parameters	Amount (USD)
Preparing project and feasibility reports	2000
Construction, transportation, assembly and installation costs of transportation roads to the power plant site and within the power plant	10000
Company formation cost	4000
Administrative building and social area construction	5000
Expenses related to administrative processes (license fee, project approval and acceptance procedures, zoning and EIA decision)	3000
Total	24000

The initial investment cost of a 1 MW Türkiye power plant will be calculated as 569000 USD.

### C. ANNUAL OPERATION AND MAINTENANCE COST

Annual labor costs, solar power insurance fees, distribution system usage fees, commercial, technical and company activity-related transaction costs and other expenses will not be included in maintenance and operation calculations. It is possible to calculate the annual operation and maintenance costs of PV plants as follows:

$$M_t = 0,01 \times I_o \quad (2)$$

Here;

$M_t$ : Annual operating and maintenance costs of PV plants.

$I_o$ : Initial investment for PV plants.

Thus, the annual operation and maintenance costs of the Turkish power plant are expected to reach 5690 USD.

It is assumed that these costs will increase by 3% every year to balance the annual inflation rate and changes in exchange rates [35].

### D. TÜRKİYE'S PAYBACK PERIOD

It is possible to calculate the PBP of PV plants as follows:

$$PBP = \frac{\text{investment amount}}{\text{average annual net profit}} \quad (3)$$

After making the financial calculations shown in Table 5, it was determined that the investment PBP of Türkiye's 1 MW power plant was 3.17 years.

*Table 5. Türkiye's Investment Payback Period.*

Years	Benefit (USD)	Cost (USD)	Net profit (USD)
0	0	569000	-569000
1	189866.26	5690	-384.823.74
2	189866.26	5860.7	-200818.18
3	189866.26	6036.52	-16988.44
<b>4</b>	<b>189866.26</b>	<b>6217.62</b>	<b>166660.2</b>
5	189866.26	6404.15	350122.31
6	189866.26	6596.27	533392.3

## E. KARAMAN'S PAYBACK PERIOD

Karaman is a province located in the south of Türkiye. The surface area of the province is 8,678 km<sup>2</sup>. Karaman has a suitable climate for solar energy installation as it is characterized by mild temperatures in summer and winter. The average highest outdoor temperature of Karaman in the summer months is 31 °C and the average lowest outdoor temperature in the winter months is 3 °C [36]. The average solar radiation values of Karaman province are shown in Figure 6. Karaman has the highest average annual total solar radiation value in Türkiye with 1661 kWh/m<sup>2</sup>. For this reason, Karaman province is considered suitable for installing 1 MW SPP.

Based on Figure 6 and after making calculations using Equation 1, the results showed that the average amount of electrical energy obtained from the Karaman system in a year is 1516803.02 kWh. The average amounts of electrical energy to be obtained from the Karaman power plant on a monthly basis are shown in Figure 19.

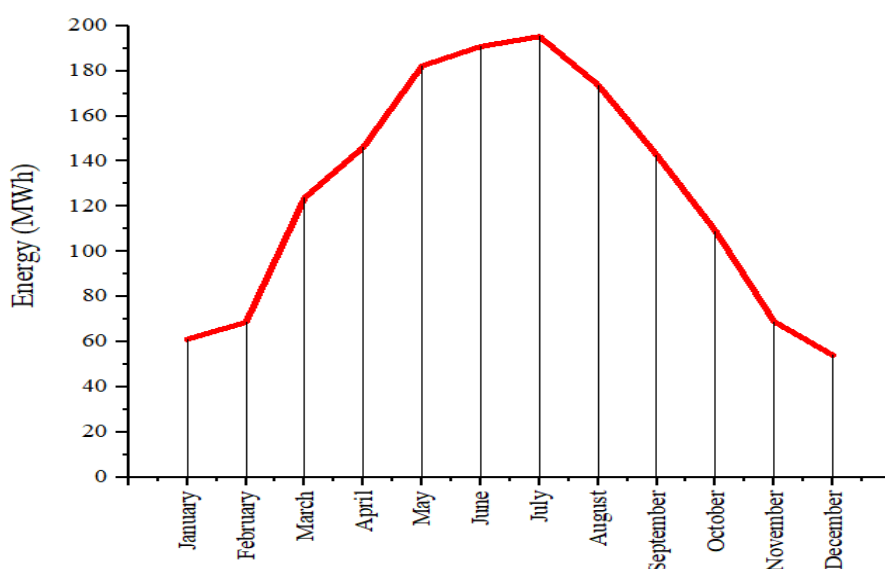


*Figure 19. Average amounts of electrical energy to be obtained from Karaman's 1 MW Solar System*

Annual Profit (1516803.02 kWh x 0.13635 USD/kWh) will be calculated as 206816.09 USD. The initial investment cost of the 1 MW Karaman power plant will be calculated as 569000 USD and the annual operation and maintenance costs will be 5690 USD. After making the financial calculations shown in Table 5, it was determined that the investment PBP of the Karaman 1 MW power plant was 2.75 years.

*Table 6. Karaman's Investment Payback Period.*

Years	Benefit (USD)	Cost (USD)	Net Profit (USD)
0	0	569000	-569000
1	206816.09	5690	-367873.91
2	206816.09	5860.7	-166918.52
<b>3</b>	<b>206816.09</b>	<b>6036.52</b>	<b>33861.05</b>
4	206816.09	6217.62	234459.52
5	206816.09	6404.15	434871.46
6	206816.09	6596.27	637091.28

#### **IV. PAYBACK PERIOD FOR EUROPE'S 1 MW PHOTOVOLTAIC SOLAR POWER PLANT**

In this section, a fixed set of factors will be assumed to compare PBPs between Türkiye and Europe, including the use of solar panels with a system size of 1 MW and a Performance ratio of 0.83. A number of constant factors also include operating and maintenance costs, which increase by 3% annually.

##### **A. GERMANY'S PAYBACK PERIOD**

From Figure 12, which shows the average values of solar radiation on a monthly basis in Germany, and using Equation 1, it was found that the average amount of electrical energy obtained from the German system in a year is 990.04 MWh. Figure 20 shows the average amount of electrical energy to be obtained from Germany's 1 MW Solar System on a monthly basis. The highest average amount of electrical energy is in June with 150.42 MWh, and the lowest average electrical energy generation is in December with 15.49 MWh.

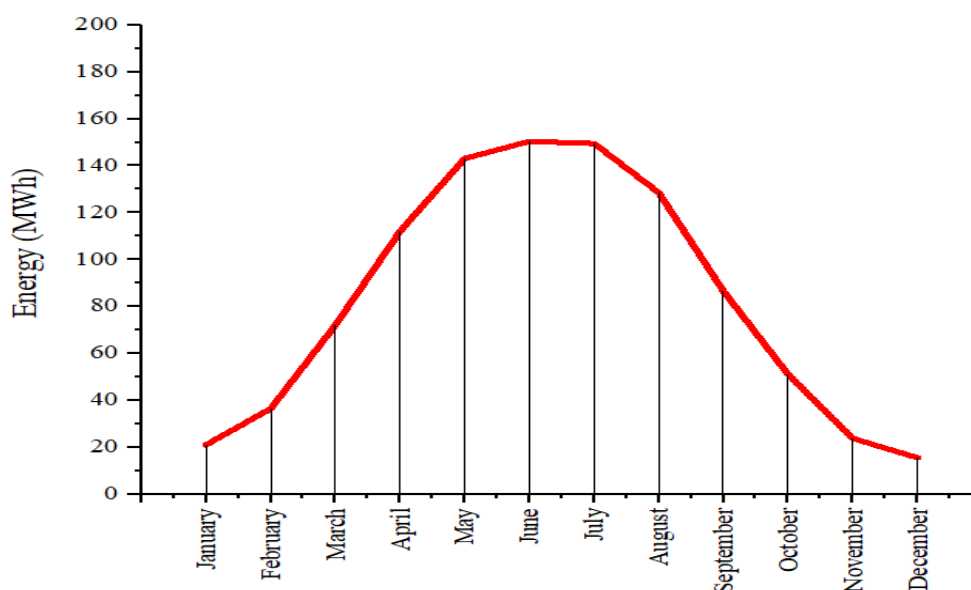


*Figure 20. Average amounts of electrical energy to be obtained from Germany's 1 MW Solar System*



Germany became Europe's largest natural gas consumer, consuming 8.6 billion cubic feet of natural gas daily in 2019. Germany's largest natural gas exporters are Russia, the Netherlands and Norway. Germany has no liquefied natural gas (LNG) terminals, but is well connected to the rest of Europe by natural gas pipelines. Germany imports natural gas from Russia via the Nord Stream pipeline and the Yamal-Europe pipeline [37]. The contribution of gas to electricity generation in Germany in 2021 was approximately 15% [38]. On February 24, 2022, the Russia-Ukraine war broke out, causing a huge increase in gas prices, which in turn caused electricity prices to rise in Europe. According to market clearing prices between 01/01/2021-28/02/2022 in Germany, the average electricity price on a monthly basis was 103.96 EUR/MWh, while the average electricity prices on a monthly basis between 01/03/2022 - 30/09/2022 were 277.08 EUR/MWh [39]. Therefore, two prices will be included to calculate Germany's PBPs during this study. Therefore, the annual profit in the period before the Russian-Ukrainian war (990.04 MWhx103.96 EUR/MWh) will be calculated as 102,924.53 EUR, and the annual profit in the period after the Russian-Ukrainian war will be calculated as (990.04 MWh x 277.08 EUR/MWh) 277320.21 EUR.

According to a report published by the Fraunhofer Institute for Solar Energy Systems in February 2022, the average initial investment cost in Germany for 2020 was 570 EUR/KWp [17]. Thus, the average initial investment cost of a 1 MW PV plant will be 570000 EUR. Using Equation 2, the annual operation and maintenance cost will be determined as 5700 EUR.

After making the financial calculations shown in Table 7 and Table 8, it was determined that the pre-war investment PBP for a 1 MW power plant was 5.7 years, and after the war PBP was 2.22 years.

*Table 7. Pre-war Germany's Investment Payback Period.*

Years	Benefit (EUR)	Cost (EUR)	Net Profit (EUR)
0	0	570000	-570000
1	102924.53	5700	-472775.47
2	102924.53	5871	-375721.94
3	102924.53	6047.13	-278844.54
4	102924.53	6228.54	-182148.56
5	102924.53	6415.40	-85639.43
<b>6</b>	<b>102924.53</b>	<b>6607.86</b>	<b>10677.24</b>
7	102924.53	6806.10	106795.67
8	102924.53	7010.28	202709.92
9	102924.53	7220.59	298624.17
10	102924.53	7437.21	394111.49

*Table 8. Germany's Investment Payback Period after the war.*

Years	Benefit (EUR)	Cost (EUR)	Net Profit (EUR)
0	0	570000	-570000
1	277320.21	5700	-298379.79
2	277320.21	5871	-26930.58
<b>3</b>	<b>277320.21</b>	<b>6047.13</b>	<b>244342.5</b>
4	277320.21	6228.54	515434.17

## **B. FRANCE'S PAYBACK PERIOD**

From Figure 15, which shows the average values of solar radiation on a monthly basis in France, and using Equation 1, it was found that the average amount of electrical energy obtained from the French system in a year is 1161.06 MWh. Figure 21 shows the average amount of electrical energy to be obtained from France's 1 MW Solar System on a monthly basis. The highest average amount of

electrical energy is in July with 167.19 MWh, and the lowest average electrical energy generation is in December with 26.80 MWh.

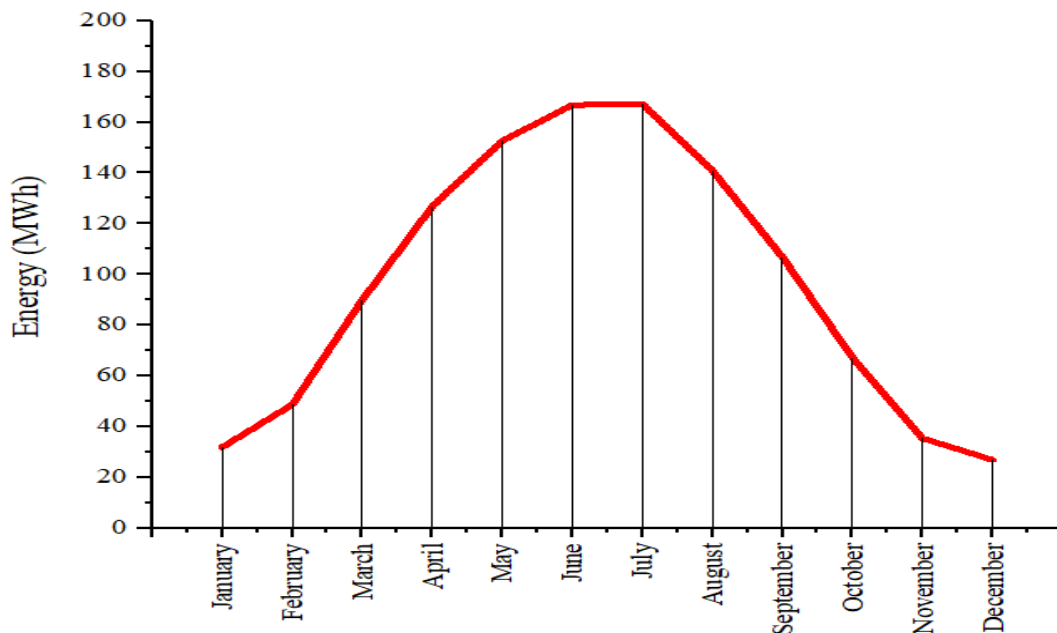


**Figure 21.** Average amounts of electrical energy to be obtained from France's 1 MW Solar System

France's domestic natural gas production is very low. As a result, France imported almost all of its natural gas resources, amounting to approximately 1.4 trillion cubic feet in 2015. France imports natural gas from the Netherlands, Norway and Russia through various cross-border pipelines [40]. Therefore, after the Russian-Ukrainian war in France, electricity prices rose dramatically, as in Germany. According to market clearing prices between 01/01/2021 - 28/02/2022 in France, the average electricity price on a monthly basis was 121.62 EUR/MWh, while the average electricity prices on a monthly basis between 01/03/2022 -22/10/2022 were 305.13 EUR/MWh [39]. Therefore, the annual profit in the period before the Russian-Ukrainian war will be calculated as (1161.06 MWh x 121.62 EUR/MWh) 141208.5 EUR, and the annual profit in the period after the Russian-Ukrainian war will be calculated as (1161.06 MWh x 305.13 EUR/MWh) 354275.21 EUR.

According to a report published by the Fraunhofer Institute for Solar Energy Systems in February 2022, the average initial investment cost in France for 2020 was 768 EUR/kWp [17]. Thus, the average initial investment cost of a 1 MW PV plant will be 768000 EUR. Using Equation 2, the annual operation and maintenance cost will be determined as 7680 EUR.

After making the financial calculations shown in Table 9 and Table 10, it was determined that the pre-war investment PBP for a 1 MW power plant was 5.6 years, and after the war PBP was 2.27 years.

*Table 9. Pre-war France's Investment Payback Period.*

Years	Benefit (EUR)	Cost (EUR)	Net Profit (EUR)
0	0	768000	-768000
1	141208.5	7680	-634471.5
2	141208.5	7910.4	-501173.4
3	141208.5	8147.71	-368112.61
4	141208.5	8392.14	-235296.25
5	141208.5	8643.90	-102731.65
<b>6</b>	<b>141208.5</b>	<b>8903.22</b>	<b>29573.63</b>
7	141208.5	9170.32	161611.81
8	141208.5	9445.43	293968.88
9	141208.5	9728.79	425448.59
10	141208.5	10020.65	556636.44

*Table 10. Investment Payback Period of France after the war.*

Years	Benefit (EUR)	Cost (EUR)	Net Profit (EUR)
0	0	768000	-768000
1	354275.21	7680	-421404.79
2	354275.21	7910.4	-75039.98
<b>3</b>	<b>354275.21</b>	<b>8147.71</b>	<b>271087.52</b>
4	354275.21	8392.14	616970.59

### C. SPAIN'S PAYBACK PERIOD

Spain has the highest solar energy potential in Europe, with an annual average total radiation value of 1600 kWh/m<sup>2</sup>. Using Equation 1, the average electrical energy production from a 1 MW capacity photovoltaic power plant in Spain is expected to be 1458.62 MWh/year.

Spain, Europe's seventh largest consumer of natural gas, burned nearly 1 trillion cubic feet in 2016. Natural gas accounted for approximately 19% of Spain's total energy consumption in 2016. Spain produces almost no natural gas and has negligible reserves, forcing the country to import almost all natural gas to meet demand. Spain imports natural gas from Algeria through two subsea pipelines. In 2016, pipeline imports from Algeria constituted 42% of total natural gas imports. Almost half of Spain's natural gas imports in 2016 (466 Billion cubic feet) were liquefied natural gas (LNG). Spain's three largest LNG suppliers were Algeria, Qatar and Nigeria. In 2016, Algeria supplied approximately 52% of Spain's total natural gas imports [41]. Natural gas accounts for almost a third of electricity production [42]. Due to Spain's lack of dependence on Russian gas, its electrical energy markets were not as significantly affected as those in France and Germany after the outbreak of the Russian-Ukrainian war. In Spain, the average electricity price on a monthly basis according to market clearing prices between 01/01/2021 - 28/02/2022 was 124.25 EUR/MWh, while the average electricity prices on a monthly basis between 01/03/2022 and 31/09/2022 were 181.77 EUR/MWh [43]. Therefore, the annual profit in the period before the Russian-Ukrainian war will be calculated as (1458.62 MWh x 124.25 EUR/MWh) 181233.79 EUR, and the annual profit in the period after the Russian-Ukrainian war will be calculated as (1458.62 MWh x 181.77 EUR/MWh) 265133.74 EUR.

According to a report published by the Fraunhofer Institute for Solar Energy Systems in February 2022, the average initial investment cost in Spain for 2020 was 620 EUR/KWp [17]. Thus, the average initial investment cost of a 1 MW PV plant will be 620000 EUR. Using Equation 2, the annual operation and maintenance cost will be determined as 6200 EUR.

After making the financial calculations shown in Table 11 and Table 12, it was determined that the pre-war investment PBP for a 1 MW power plant was 3.6 years, and the post-war PBP was 2.41 years.

*Table 11. Pre-war Spain's Investment Payback Period*

Years	Benefit (EUR)	Cost (EUR)	Net Profit (EUR)
0	0	620000	-620000
1	181233.79	6200	-444966.21
2	181233.79	6386	-270118.42
3	181233.79	6577.58	-95462.21
<b>4</b>	<b>181233.79</b>	<b>6774.91</b>	<b>85996.67</b>
5	181233.79	6978.16	260252.3
6	181233.79	7187.50	434298.59

*Table 12. Investment Payback Period of Spain after the war.*

Years	Benefit (EUR)	Cost (EUR)	Net Profit (EUR)
0	0	620000	-620000
1	265133.74	6200	-361066.26
2	265133.74	6386	-102318.52
<b>3</b>	<b>265133.74</b>	<b>6577.58</b>	<b>156237.64</b>
4	265133.74	6774.91	414596.47

## V. CONCLUSION

In this study, a fixed number of factors were assumed to compare the PBPs of solar systems in Türkiye and Europe, including the use of solar panels with a system size of 1 MW and a Performance ratio of 0.83. A number of constant factors also include operating and maintenance costs, which increase by 3% annually. In addition, energy prices in Europe increased significantly due to the Russia-Ukraine war that broke out in early 2022, and as a result, the PBPs of photovoltaic power plants were calculated over two periods: before and after the Russia-Ukraine war. At the time of this study, the arithmetic average of market clearing prices in Türkiye after Russia-Ukraine until 17-10-2022 was 0.13635 USD/kWh. As for the period before the Russia-Ukraine war, according to the annex I table of the Law No. 5346 on the Use of Renewable Energy Resources for the Purpose of Electrical Energy Production, if licensed electricity production facilities based on solar energy come into operation until 30/06/2021, for the electrical energy produced from these power plants. A purchase guarantee of 0.133 USD/kWh is provided within the scope of the RES Support Mechanism (YEKDEM) for 10 years [35]. For this reason, the PBP for Türkiye is calculated over one period.

The results in the first period, before the Russia-Ukraine war, found the highest repayment periods in Karaman province with 2.75 years, followed by 3.17 years in Türkiye. In Spain, France and Germany, the repayment periods are 3.6, 5.6 and 5.7 years, respectively. The results of the second period after the Russia-Ukraine war showed that the highest repayment periods were determined in Germany with 2.22 years, followed by France with 3.27 years. In Spain, Karaman province and Türkiye, the PBPs are 2.41, 2.75 and 3.17 years, respectively.

## **VI. REFERENCES**

- [1] A. Ustaoglu, H. Torlaklı, A. Ergün, E. Erdoğan and M. E. Akay, "Advanced exergy analysis of an integrated solid waste fueled cogeneration system based on organic Rankine Cycle for different working fluids", *Energy Conversion and Management*, vol. 270, pp. 116294, 2022.
- [2] A. H. A. Al-Waeli, H. A. Kazem, M. T. Chaicha and K. Sopian, "Photovoltaic/thermal (PV/T) Systems: Principles, design, and applications", Springer Nature, Switzerland, pp. 1-3, 2019.
- [3] A. Ergün and H. Eyiç, "Performance assessment of novel photovoltaic thermal system using nanoparticle in phase change material", *International Journal of Numerical Methods for Heat & Fluid Flow*, vol. 29, no. 4, pp. 1490-1505, 2019.
- [4] REN21, "Renewables 2020 Global Status Report", Paris, 2020.
- [5] TÜRKİYE PETROLLERİ A.O., "Petrol ve Doğal Gaz Sektör Raporu", Ankara, 2020.
- [6] Duvar Gazete, "665 Milyar Doları Nasıl Yaktık?", <https://www.gazeteduvar.com.tr/665-milyar-dolari-nasil-yaktik-makale-1535547>, 2022.
- [7] EUROPEAN COMMISSION, "Energy prices and costs in Europe", Brussels, 2019.
- [8] International Renewable Energy Agency (IRENA), "Renewable capacity statistics 2021", Abu Dhabi, 2021.
- [9] A. H. Smets, K. Jäger, O. Isabella, R. A. Swaaij and M. Zeman, "Solar energy the physics and engineering of photovoltaic conversion, technologies and systems", UIT Berlin, Germany, pp. 726-729, 2015.
- [10] Internet: Clean Technica, "Solar Power Energy Payback Time Is Now Super Short - CleanTechnica", <https://cleantechnica.com/2018/03/25/solar-power-energy-payback-time-now-super-short/>, 2022.
- [11] Fraunhofer Institute for Solar Energy Systems and PSE Projects GmbH, "Photovoltaics Report", Freiburg, 2021.
- [12] W. Kessler, "Comparing energy payback and simple payback period for solar photovoltaic systems", *E3S Web of Conferences.*, vol. 22, pp.80, 2017.
- [13] F. Lüle, T. Koyuncu and A. Kaya, "Payback periods of three identical solar photovoltaic power plants", *Engineering Sciences*, vol. 14, no. 4, pp. 200–206, 2019.
- [14] T. Taner and A. S. Dalkilic, "A feasibility study of solar energy-techno economic analysis from Aksaray city, Turkey", *Journal of Thermal Engineering*, vol. 3, no. 5, pp. 1–1, 2017.
- [15] R. Büyükzeren, H. B. Altıntaş, K. Martin, and A. Kahraman, "Binalardaki fotovoltaik uygulamasının teknik, çevresel ve ekonomik incelenmesi: meram tıp fakültesi hastanesi örneği", *EMO Bilimsel Dergi*, vol. 5, no. 10, pp. 9–14, 2015.
- [16] T. Tsvetomira, "Solar Payback Times in Europe on the Slide - Otovo", <https://renewablesnow.com/news/solar-payback-times-in-europe-on-the-slide-otovo-644921/>, 2022.
- [17] Fraunhofer Institute for Solar Energy Systems and ISE, "Photovoltaics Report", Freiburg, 2022.

- [18] Wild-Scholten, D. and Schottler, M., "Solar as an environmental product. Thin-film modules. Production processes and their environmental assessment", Netherlands, 2009
- [19] Enerji İşleri Genel Müdürlüğü, "GEPA", <https://gepa.enerji.gov.tr/MyCalculator/Default.aspx>, 2022.
- [20] T.C. Enerji ve Tabii Kaynaklar Bakanlığı, "Güneş - T.C. Enerji ve Tabii Kaynaklar Bakanlığı", <https://enerji.gov.tr/bilgi-merkezi-enerji-gunes> 2022.
- [21] Copernicus Climate Change Service (C3S), "Sunshine duration and clouds", <https://climate.copernicus.eu/ESOTC/2019/sunshine-duration-and-clouds>, 2022.
- [22] Global Solar Atlas, "Solar resours map", <https://globalsolaratlas.info/download/europe-and-central-asia>, 2022.
- [23] Deutscher Wetterdienst DWD, "Global radiation (Mean 30-year monthly and annual sums)", [https://www.dwd.de/EN/ourservices/solarenergy/maps\\_globalradiation\\_mv.html#buehneTop](https://www.dwd.de/EN/ourservices/solarenergy/maps_globalradiation_mv.html#buehneTop), 2022.
- [24] RU-GELD.DE, "Sunshine in Germany: the number of sunny days, hours of sunshine quantity in Germany by year, season, month, and also by federated state", <https://ru-geld.de/en/country/weather-and-climate/sunshine.html>, 2022.
- [25] F. G: Montoya, M. J. Aguilera and F. Manzano-Agugliaro, "Renewable energy production in Spain: A review", *Renewable and Sustainable Energy Reviews*, vol. 33, pp. 509–531, 2014.
- [26] J. Polo, "Solar global horizontal and direct normal irradiation maps in Spain derived from geostationary satellites", *Journal of Atmospheric and Solar-Terrestrial Physics*, vol. 130, no. 131, pp. 81–88, 2015.
- [27] Current Results, "Average sunshine a year in Europe", <https://www.Currentresults.com/Weather/Spain/annual-days-of-sunshine.php> (2022).
- [28] R. R. Urs, Z. Ali, M. Marzband, K. Saleem, B. Mohammadi-Ivatloo and A. Anvari-Moghaddam, "A technical assessment on photovoltaic power generation under varying weather profile – Northumbria university pilot", 2020 IEEE 29th International Symposium on Industrial Electronics (ISIE), pp. 811–815, 2020.
- [29] A. Kalyanpur, M. Mercadier and P. Blanc, "Gisement solaire en France : caractérisation de la ressource énergétique, profil de répartition et volatilité", *Environnement & Technique*, vol. 331, pp. 54–59, 2017.
- [30] Y. B. Hinssen and W. H. Knap, "Comparison of pyranometric and pyrheliometric methods for the determination of sunshine duration", *Journal of Atmospheric and Oceanic Technology*, vol. 24, no. 5, pp. 835–846, 2007.
- [31] M. Pierro, D. Moser, R. Perez and C. Cornaro, "The value of PV power forecast and the paradox of the “single pricing” scheme: The Italian case study", *Energies*, vol. 13, no. 15, pp. 3945 2020.
- [32] Çevresel Etki Değerlendirmesi İzin ve Denetim Genel Müdürlüğü, "Çevresel göstergeler", [https://webdosya.csb.gov.tr/db/ced/icerikler/cevresel\\_gostergeler\\_-2021tr-rev-20220622105837.pdf](https://webdosya.csb.gov.tr/db/ced/icerikler/cevresel_gostergeler_-2021tr-rev-20220622105837.pdf), 2022.

- [33] ACS Enerji ve Teknoloji Ltd Sti, "LEXRON-72M Data Sheet", <https://www.acsenerji.com/>, 2022.
- [34] EPIAŞ Şeffaflık Platformu, "Piyasa takas fiyatı ", <https://seffaflik.epias.com.tr/transparenciy/piyasalar/gop/ptf.xhtml> (2022).
- [35] M. Yalılı, "Lisanslı fotovoltaik güneş enerji santrali yatırımının finansal analizi: Van ili örneği", Bitlis Eren Üniversitesi Fen Bilimleri Dergisi, vol.10, no. 3, pp. 1055–1074, 2021.
- [36] Weather Spark, "Karaman iklimi, aylık hava durumu, ortalama sıcaklığı (Türkiye)", <https://tr.weatherspark.com/y/97718/Karaman-Türkiye-Ortalama-Hava-Durumu-Yıl-Boyunca>, 2022.
- [37] U.S. Energy Information Administration (EIA), "Energy sector in Germany", <https://www.eia.gov/international/analysis/country/DEU>.
- [38] Statistisches Bundesamt, "Gross electricity production in Germany", <https://www.destatis.de/EN/Themes/Economic-SectorsEnterprises/Energy/Production/Tables/gross-electricity-production.html> (2022).
- [39] NORD POOL, "DAY-AHEAD PRICES", <https://www.nordpoolgroup.com/en/Market-data1/Dayahead/Area-Prices/de-lu/monthly/?view=table>, 2022.
- [40] U. S. Energy Information Administration (EIA), "Energy sector in France", <https://www.eia.gov/international/analysis/country/FRA>, 2022.
- [41] U. S. Energy Information Administration (EIA), "Energy sector in Spain", <https://www.eia.gov/international/analysis/country/ESP>, 2022.
- [42] International Energy Agency (IEA), "Spain natural gas security policy", <https://www.iea.org/articles/spain-natural-gas-security-policy>, 2022.
- [43] The nominated electricity market operator (NEMO), "Monthly report on the development of the electricity market", <https://www.omie.es/en/publications?page=0>, 2022.